

MAGNETIC AND MORPHOLOGICAL CHARACTERIZATION OF SrFe<sub>12</sub>O<sub>19</sub>/PA12  
COMPOSITES: HARD-MAGNETIC FILAMENT FOR MAGNETIC FIELD  
ASSISTED ADDITIVE MANUFACTURING (MFAAM)

by

Tanjina N. Ahmed, M.S., M.Phil.

A dissertation submitted to the Graduate Council of  
Texas State University in partial fulfillment  
of the requirements for the degree of  
Doctor of Philosophy  
with a Major in Materials Science, Engineering, and Commercialization  
May 2023

Committee Members:

Ir. Wilhelmus J. Geerts, Chair

Gary W. Beall

Jitendra S. Tate

Maggie (Yihong) Chen

Craig Hanks

**COPYRIGHT**

by

Tanjina N. Ahmed

2023

## **FAIR USE AND AUTHOR'S PERMISSION STATEMENT**

### **Fair Use**

This work is protected by the Copyright Laws of the United States (Public Law 94-553, section 107). Consistent with fair use as defined in the Copyright Laws, brief quotations from this material are allowed with proper acknowledgement. Use of this material for financial gain without the author's express written permission is not allowed.

### **Duplication Permission**

As the copyright holder of this work I, Tanjina N. Ahmed, authorize duplication of this work, in whole or in part, for educational or scholarly purposes only.

## **DEDICATION**

To my Ammu & Abbu  
and  
my Teachers ...

Without their effort, my efforts would not have been so fruitful.

## ACKNOWLEDGEMENTS

First of all, I would like to take this opportunity to express my deepest sense of gratitude to my advisor Dr. Ir. Wilhelmus J. Geerts for his endless hours of help, suggestions, ideas, advice, and proper guidance throughout the whole time of my Ph.D. Without his efforts, my efforts would not have been so fruitful. He helped me in numerous ways during the challenging research I was a part of and he is a kind of mentor who sees the best in you and pushes you to believe more in yourself than you could have ever imagined. I am truly grateful and thankful to him for teaching me the art of research.

I would also like to extend my gratitude to the other members of my dissertation committee, Drs. Jitendra S. Tate, Gary W. Beall, Maggie Y. Chen and Craig Hanks for their time, discussion, and input on my dissertation project. I am especially grateful to Dr. Tate, for giving me the opportunity to work in his lab and giving me access to his extruder, the thermal analysis tools and also for his many suggestions and insights from a manufacturing engineering perspective and Dr. Chen for her valuable recommendation for my very first internship opportunity of my life.

I would like to thank SRO staff Dr. Joyce Anderson, Alissa Savage, Dr. Juan Gomez and last but not least Dr. Casey Smith for the technical training on multiple tools of the Analysis Research Service Center. There are many fellow mates of the MSEC program who I want to acknowledge including Dr. Anupam K.C., Jacob Armitage, Binod D.C, and Dean Koehne. I am forever indebted to my fellow-mates Chandan Howlader,

Tuhin Dey, Dr. Mithil Mazumder, Sadia Rab and all my friends of the Bangladeshi Student Association of TXST, for their endless support throughout my Ph.D. life. Their constant encouragement helped me to find ways out and meaning of seeming dead ends. My gratitude and appreciation are not enough for my lab mates Maria Camila Belduque, Oluwasola Arigbabowo, Lauren Henderson, and Kolton Dieckow for their support during my Ph.D. journey. I also like to thank our collaborator Chris Selsor from Texas A&M University and special thanks to my friend Dr. Aditya Mishra from UTD for his guidance and advises whenever I needed it. I am grateful to Dr. Preyom Dey for his endless support and guidance.

I am extremely grateful to our MSEC directors Drs. Sean Kerwin and Jennifer Irvin for their incredible support and encouragement. I am also grateful to Dr. Alex Zakhidov for his mentorship and guidance in the beginning of my MSEC journey. A special thanks to MSEC officials Karla Pizana and Kelsie Crumpton for their constant support and assistance throughout my Ph.D. journey. Furthermore, I would like to acknowledge the help of Dr. Erik Samwel of MicroSense-KLA in implementing the modifications to the VSM software. I must acknowledge NSF through DMRMRI Grants (#1726970 and 2216440), DOD through a HBCU/MI grant (#W911NF2010298), and graduate college of Texas State through dissertation support grant for the financial support of this research.

Lastly, I would like to thank, most sincerely, my wonderful parents and husband, my lovely sisters & supportive family and all my teachers for mentoring, motivating, and guiding me to reach this far in my life.

# TABLE OF CONTENTS

	Page
<b>ACKNOWLEDGEMENTS .....</b>	<b>v</b>
<b>LIST OF TABLES .....</b>	<b>viii</b>
<b>LIST OF FIGURES .....</b>	<b>ix</b>
<b>LIST OF ABBREVIATIONS .....</b>	<b>xviii</b>
<b>ABSTRACT.....</b>	<b>xix</b>
<b>CHAPTER</b>	
<b>1. INTRODUCTION .....</b>	<b>1</b>
<b>1.1 Background .....</b>	<b>1</b>
<b>1.2 Permanent Magnetic Materials.....</b>	<b>4</b>
<b>1.3 Magnetic Properties .....</b>	<b>10</b>
1.3.1 Magnetic Anisotropy.....	11
1.3.2 Saturation Magnetization and the existence of Domains.....	14
1.3.3 Domain Walls .....	14
1.3.4 Single or Multiple Domain .....	16
1.3.5 Magnetic Phase Diagram of Strontium Ferrite .....	20
1.3.6 Magnetic Reversal Mechanism.....	20
1.3.6.1 Coherent Rotation .....	21
1.3.6.2 Incoherent Rotation.....	22
<b>1.4 Magnet Manufacturing Techniques.....</b>	<b>23</b>
1.4.1 Sintered Magnet .....	23
1.4.2 Bonded Magnet.....	23
1.4.2.1 Additive Manufacturing (AM) for Bonded Magnet Fabrication.....	24
<b>1.5 Organization of the Thesis .....</b>	<b>27</b>
<b>REFERENCES .....</b>	<b>29</b>
<b>2. LITERATURE REVIEW AND MOTIVATION OF THE RESEARCH .....</b>	<b>36</b>
<b>2.1 Introduction .....</b>	<b>36</b>
<b>2.2 Broader Impact and Applications of MFAAM.....</b>	<b>37</b>
<b>2.3 Literature Review .....</b>	<b>39</b>

<b>2.4 Challenges and Objective of the Research .....</b>	<b>45</b>
2.4.1 Problem Statement .....	45
2.4.2 Objective and Proposed Solutions .....	46
<b>2.5 Conclusion .....</b>	<b>49</b>
<b>REFERENCES .....</b>	<b>50</b>
<b>3. MANUFACTURING &amp; CHARACTERIZATION TECHNIQUES AND ANALYSIS .....</b>	<b>54</b>
<b>3.1 Introduction .....</b>	<b>54</b>
<b>3.2 Manufacturing Techniques.....</b>	<b>54</b>
3.2.1 Twin-Screw Extruder .....	54
3.2.2 3D Printing or Additive Manufacturing (AM).....	56
3.2.3 Magnetic Field Assisted Additive Manufacturing (MFAAM) .....	57
<b>3.3 Characterization Techniques for Filaments.....</b>	<b>59</b>
3.3.1 Biaxial Vibrating Sample Magnetometer (VSM) and Torque Magnetometer (TM).....	59
3.3.1.1 Theory of VSM Operation .....	60
3.3.1.2 Schematics of MicroSense VSM Head Option .....	61
3.3.1.3 Schematics of Torque Magnetometer (TM) .....	63
3.3.1.4 VSM Data Analysis Software .....	65
3.3.1.4.1 Image Effect Correction .....	65
3.3.1.4.2 Sweep Field Lag Correction.....	66
3.3.2 Optical Microscopy.....	67
3.3.2.1 Optical Microscopy Image Analysis .....	69
3.3.3 Scanning Electron Microscopy (SEM) .....	70
3.3.4 Electron Dispersive X-ray Spectroscopy (EDS).....	72
3.3.4.1 EDS Spectra Analysis.....	73
3.3.5 Imaging Sputter Coater .....	76
3.3.6 Fourier Transformed Infrared Spectroscopy (FTIR) .....	77
3.3.6.1 FTIR Spectra Analysis .....	79
3.3.7 X-Ray Diffraction (XRD).....	81
3.3.7.1 XRD Measurement Analysis.....	82
3.3.8 Thermo-Gravimetric Analysis (TGA) and Differential Scanning Calorimetry (DSC) .....	85
3.3.8.1 TGA Measurement Analysis.....	86
3.3.8.2 DSC Measurement Analysis.....	90
<b>3.4 Conclusion .....</b>	<b>93</b>
<b>REFERENCES .....</b>	<b>94</b>
<b>4. TIME DEPENDENT STUDY.....</b>	<b>100</b>
<b>4.1 Introduction .....</b>	<b>100</b>
<b>4.2 Pristine Filament Time Dependence Study .....</b>	<b>105</b>
4.2.1 Experimental Procedure.....	105
4.2.2 Results and Discussion.....	106
4.2.3 Summary .....	111

<b>4.3 “Field-annealed only” and “Field-annealed and cooled” Filament Time Dependence Study</b> .....	<b>111</b>
4.3.1 Experimental Procedure .....	112
4.3.2 Results and Discussion.....	112
4.3.3 Summary .....	116
<b>4.4 Conclusion</b> .....	<b>117</b>
<b>REFERENCES</b> .....	<b>118</b>
<b>5. TEMPERATURE DEPENDENT STUDY</b> .....	<b>120</b>
<b>5.1 Introduction</b> .....	<b>120</b>
<b>5.2 Dynamic Viscosity of Strontium Ferrite–Nylon Composite Below the Nylon Melting Temperature</b> .....	<b>124</b>
5.2.1 Experimental Procedure .....	125
5.2.2 Quasi Static Magnetic Measurement .....	126
5.2.3 Dynamic Magnetic Measurement .....	130
5.2.4 Data Analysis and Modelling.....	133
5.2.5 Discussion .....	137
5.2.6 Summary .....	139
<b>5.3 Magnetic Behavior and Chaining of Strontium Ferrite-Nylon Composite Above the Melting Temperature</b> .....	<b>141</b>
5.3.1 Experimental Procedure .....	142
5.3.2 Measurement Data and SEM Image Analysis .....	145
5.3.3 Summary .....	151
<b>5.4 Conclusion</b> .....	<b>152</b>
<b>REFERENCES</b> .....	<b>154</b>
<b>6. TORQUE OR ANGULAR DEPENDENT STUDY</b> .....	<b>159</b>
<b>6.1 Introduction</b> .....	<b>159</b>
<b>6.2 Correction Strategy for Systematic Wobble Errors in VSM Torque Curves Measured on Soft Magnetic Samples</b> .....	<b>163</b>
6.2.1 Theory .....	165
6.2.2 Experimental Verification .....	171
6.2.3 Summary .....	176
<b>6.3 Torque Measurements of 3D Printed Sample, Freely Extruded Sample on 3D printer, and Field-Annealed and Cooled Sample</b> .....	<b>177</b>
<b>6.4 Magnetic Anisotropy Measurement of Field annealed Composite Filament Above the Nylon Melting Temperature</b> .....	<b>179</b>
6.4.1 Experimental Procedure .....	179
6.4.2 Measurement Results .....	180
<b>6.5 Conclusion</b> .....	<b>182</b>
<b>REFERENCES</b> .....	<b>183</b>

<b>7. CONCLUSION AND FUTURE APPROACHES.....</b>	<b>185</b>
<b>7.1 Conclusion .....</b>	<b>185</b>
<b>7.2 Suggestions for Future Research.....</b>	<b>189</b>
7.2.1 Flow-induced Anisotropy .....	189
7.2.2 Installing Electromagnet or Permanent Magnet to Make MFAAM Facile.....	190
7.2.3 XRD Pole Figure for Texture Analysis.....	191
7.2.4 Development of MFAAM a Model .....	191
<b>REFERENCES .....</b>	<b>192</b>

## LIST OF TABLES

<b>Table</b>	<b>Page</b>
<b>1.1</b> Price of some raw materials of permanent magnet (updated December 2022) [10, 11, 12] .....	5
<b>1.2</b> Properties of some permanent magnetic materials [1].....	7
<b>3.1</b> Manufactured 3D-printer filament with different concentration of SrFe <sub>12</sub> O <sub>19</sub> in PA12 by twin screw-extruder .....	56
<b>3.2</b> Mass loss ( $\Delta m/m_{\text{initial}}$ ) % of neat PA12 and strontium-ferrite/PA12 composites: .....	89
<b>3.3</b> TGA data of Strontium-ferrite/PA12 composites .....	89
<b>3.4</b> DSC data of Strontium-ferrite/PA12 composites .....	92
<b>5.1</b> Cluster size of pristine and 230 °C field-annealed 5 and 40 wt.% composite .....	151
<b>6.1</b> Magnetic anisotropy of pristine and 230 °C field-annealed 5 and 40 wt.% SrO(Fe <sub>2</sub> O <sub>3</sub> ) <sub>6</sub> /PA12 composite.....	180

## LIST OF FIGURES

Figure	Page
<b>Fig. 1.1:</b> (BH) <sub>max</sub> can be graphically defined as area of the largest rectangle that has drawn in the second quadrant of the B-H loop [3].....	2
<b>Fig. 1.2:</b> Hysteresis loops comparing a (iron-silicon steel) to a soft magnet (permalloy) on the same scale [5].....	2
<b>Fig. 1.3:</b> The crystal structure of SmCo <sub>5</sub> on the left and Sm <sub>2</sub> Co <sub>17</sub> on the right [8].....	5
<b>Fig. 1.4:</b> Neodymium (top) and Cobalt (bottom) prices (USD/lb) past five years (updated December 2022) [10] .....	6
<b>Fig. 1.5:</b> The crystal structure of Nd <sub>2</sub> Fe <sub>14</sub> B [15] .....	6
<b>Fig. 1.6:</b> (a) The Unit cells of hexagonal SrFe <sub>12</sub> O <sub>19</sub> [26] and (b) schematic diagram of Strontium ferrite crystal structure by Granados et al., 2016 [27] .....	8
<b>Fig. 1.7:</b> Hexaferrites with different form factors; (a) Sr-Ferrites platelets [32], (b) Ba-Ferrites “spherical-like” particles [33], (c) Ba-Ferrites fibers [34, 35].....	10
<b>Fig. 1.8:</b> The demagnetizing field HD [36] .....	12
<b>Fig. 1.9:</b> Schematic representation of a 180° domain wall (left) [45] and (right) the change in magnetization within the wall can be gradual as in (a) or abrupt as in (b) [36] .....	15
<b>Fig. 1.10:</b> Schematic illustration of the breakup of the magnetization of an oblate ellipsoid into domains (a) single domain, (b) two domains, (c) three domains, and (d) three domains with closure domains .....	16
<b>Fig. 1.11:</b> Schematically illustrates the size dependence of H <sub>C</sub> of the non-interacting magnetic particles [31].....	18
<b>Fig. 1.12:</b> Magnetic phase diagram of Strontium Ferrite based on Shirk et. al [46] .....	20
<b>Fig. 1.13:</b> (a) Total energy of particle with uniaxial anisotropy as a function of the angle of	

the magnetic dipole moment with respect to the easy axis for a field angle parallel to the easy axis; (b) Calculated hysteresis curve versus field angle $\alpha$ [30] .....	21
<b>Fig. 1.14:</b> Different reversal modes (a) coherent rotation; (b) curling; (c) buckling; (d) fanning; (e) domino effect; Field angle dependence of switching field for coherent rotation (SW) and curling for different aspect ratio particles $S= b/b_0$ [45] .....	23
<b>Fig. 1.15:</b> Types of additive manufacturing processes and technologies [70, 71] .....	25
<b>Fig. 2.1:</b> Identified applications for MFAAM deposition: Superior field homogeneity of 3D printed Halbach cylinders for application in portable MRI equipment compared to currently considered cylinders using discrete magnets [10] .....	37
<b>Fig. 2.2:</b> Identified applications for MFAAM deposition: flux guides for printable electronics and waveguides [8] .....	38
<b>Fig. 2.3:</b> Identified applications for MFAAM deposition: Magnetic robots for biomedical applications [9, 11] .....	38
<b>Fig. 2.4:</b> Magnetic properties of Big Area Additive Manufacturing (BAAM) and Injection Molding (IM) fabricated NdFeB bonded magnets [1] .....	39
<b>Fig. 2.5:</b> Hysteresis measurements for isotropic (no external field $H_0$ ) and anisotropic (maximum external field $H_{max}$ ) printed magnets in all magnetization directions .....	41
<b>Fig. 2.6:</b> Hard axis and easy axis hysteresis loops of the (a) $SrFe_{12}O_{19}$ (Strontium hexaferrite) and (b) $Sm_2Fe_{14}N_3$ 3D printed samples [18] .....	42
<b>Fig. 2.7:</b> Magnetic hysteresis of recycled Sm-Co powder in epoxy measured under applied magnetic field of 3 T at 400 K [20] .....	43
<b>Fig. 2.8:</b> Schematic of in-situ alignment mechanism for the 3D printed magnetic materials [16] .....	44
<b>Fig. 2.9:</b> Magnetic characterization of Nd-Fe-B + Sm-Fe-N/Nylon-12 65 vol.% sample printed at 180 °C nozzle temperature under varying alignment current [16] .....	44
<b>Fig. 2.10:</b> Selection matrix of permanent magnets [31] .....	47

<b>Fig. 3.1:</b> (a) Thermo Fisher Process 11 Twin Screw Extruder [1] (b) Schematic of the manufacturing process .....	55
<b>Fig. 3.2:</b> A water-cooled ROVA 3D printer of ORD solutions and ROVA 3D printer of ORD solutions at Texas State University .....	56
<b>Fig. 3.3:</b> (a) MFAAM sample printed on NdFeB permanent magnets on top of ROVA3D's print bed and schematics of MFAAM printing method for (b) transverse ( $H_{trans}$ ) and (c) longitudinal ( $H_{long}$ ) print-fields. ....	57
<b>Fig. 3.4:</b> (a) Specialized designed 3D printer with electromagnet positioned around the extruder nozzle at Ames laboratory [3] and (b) modified 3D-printer showing the extruder including the nozzle and the flexible fixing unit for the permanent magnets by Suppan et al. [4].....	58
<b>Fig. 3.5:</b> a) Setup of the Bi-axial MicroSense EasyVSM at Texas State University [8]...	62
<b>Fig. 3.6:</b> Diagram of the MicroSense torque magnetometer including sensors, coils, and magnets [9].....	63
<b>Fig. 3.7:</b> Magnetization vs. field plot from MicroSense manual depicting the image effect correction employed at fields above 1.5 Tesla [11].....	66
<b>Fig. 3.8:</b> Hirox Digital Microscope at Texas State University .....	68
<b>Fig. 3.9:</b> (a) MXB-2016 (6-320x) Zoom Lens (left) and (b) MXB-2500 (35-2500x) Zoom Lens (right).....	68
<b>Fig. 3.10:</b> (a) and (b) Optical microscopy images of 40 wt.% Strontium-ferrite/PA12 annealed filament showing periodic pattern of particles .....	70
<b>Fig. 3.11:</b> (a) Schematic diagram of a scanning electron microscope [13] (b) Different type of signal generated from the irradiated spot of the sample along with corresponding depth from the surface [15], (c) FEI Helios NanoLab 400 DualBeam field emission scanning electron microscope of Texas State University [14].....	71
<b>Fig. 3.12:</b> Charging issue under electron microscope before coated with Iridium.....	72
<b>Fig. 3.13:</b> Schematic of EDS systems for detection [18] .....	73

<b>Fig. 3.14:</b> EDS spectra of 5 wt.% filament (cross-section along the radial direction) .....	74
<b>Fig. 3.15:</b> EDS spectra of 40 wt.% filament (cross-section along the radial direction) ....	76
<b>Fig. 3.16:</b> Imaging Sputter Coater of Texas State University .....	76
<b>Fig. 3.17:</b> TEM images for the illustration of the difference between the two coatings based on the grain size of Au and Ir [ARSC document of Texas State University].....	77
<b>Fig. 3.18:</b> (a) FTIR basic operation principle and beam amplification effect of the ATR system (top) [19] (b) Fourier Transformed Infrared Spectroscopy (FTIR) of Texas State University (bottom).....	78
<b>Fig. 3.19:</b> FTIR spectra of (a) neat PA12 and (b) 5, (c) 26, (d) 40, and (e) 70 wt.% SrO(Fe <sub>2</sub> O <sub>3</sub> ) <sub>6</sub> /PA12 composite filament (cross section along the radial direction) .....	80
<b>Fig. 3.20:</b> (a) Diffraction of X-ray at crystal planes (b) Rigaku Smartlab diffractometer of Texas State University [16] .....	82
<b>Fig. 3.21:</b> XRD patterns of (a) neat PA12 and (b) 5, (c) 26, (d) 40, and (e) 70 wt.% SrFe <sub>12</sub> O <sub>19</sub> / PA-12 composite filament (horizontally) .....	83
<b>Fig. 3.22:</b> XRD patterns of (a) neat PA12 and (b) 5, (c) 26, (d) 40, and (e) 70 wt.% SrFe <sub>12</sub> O <sub>19</sub> / PA-12 composite filament (tree trunk) .....	84
<b>Fig. 3.23:</b> An SDT 650 Simultaneous Thermal Analyzer of TA Instruments to perform Thermo-Gravimetric Analysis (TGA) and Differential Scanning Calorimetry (DSC) analysis at Texas State University .....	85
<b>Fig. 3.24:</b> TGA curves of neat PA-12, Strontium-Ferrite/PA-12 (5 and 40 wt.%) composites and multiple temperature cycle annealed Strontium-Ferrite/PA-12 (5 and 40 wt.%) composites.....	87
<b>Fig. 3.25:</b> DSC curves of neat PA-12, Strontium-Ferrite/PA-12 (5 and 40 wt.%) composites and multiple temperature cycle annealed Strontium-Ferrite/PA-12 (5 and 40 wt.%) composites.....	91
<b>Fig. 4.1:</b> A magnetic viscosity experiment at constant field [7].....	102
<b>Fig. 4.2:</b> The time dependence of the magnetization of a ferromagnet [11] .....	103

<b>Fig. 4.3:</b> (a) Major magnetization hysteresis loop for the $\text{Sr}_{0.8}\text{La}_{0.2}\text{Fe}_{11.8}\text{Co}_{0.2}\text{O}_{19}$ hexaferrite (b) Dependence of the magnetic viscosity coefficient $S$ on the applied reverse field by Serletis et al. 2012 [6] .....	103
<b>Fig. 4.4:</b> $M_x/M_s$ (a) and $M_y$ (b) Hysteresis curves of the 5wt.% $\text{SrO}(\text{Fe}_2\text{O}_3)_6/\text{PA12}$ filaments; Time dependence of $M_x/M_s$ (c) and $M_y/M_s$ (d) signals of 5wt.% $\text{SrO}(\text{Fe}_2\text{O}_3)_6/\text{PA12}$ filaments [15].....	106
<b>Fig. 4.5:</b> $ \Delta M_{\text{max}}/M_s $ [16] (a) and $ \Delta M_{\text{max}}/M $ (b) as a function of field angle for 5 wt.% $\text{SrO}(\text{Fe}_2\text{O}_3)_6/\text{PA12}$ composite filaments at room temperature.....	108
<b>Fig. 4.6:</b> $M_x/M_s$ (a) and $M_y$ (b) Hysteresis curves of the 26 wt.% $\text{SrO}(\text{Fe}_2\text{O}_3)_6/\text{PA12}$ filaments; Time dependence of $M_x/M_s$ (c) and $M_y/M_s$ (d) signals of 26 wt.% $\text{SrO}(\text{Fe}_2\text{O}_3)_6/\text{PA12}$ filaments [16].....	109
<b>Fig. 4.7:</b> $ \Delta M_{\text{max}}/M_s $ (a) and $ \Delta M_{\text{max}}/M $ (b) as a function of field angle for 26 wt.% $\text{SrO}(\text{Fe}_2\text{O}_3)_6/\text{PA12}$ composite filaments at room temperature (RT).....	110
<b>Fig. 4.8:</b> $M_x$ hysteresis curves of (a) Pristine 40 wt.% $\text{SrO}(\text{Fe}_2\text{O}_3)_6/\text{PA12}$ filaments; (b) “field-annealed and cooled” and (c) “field-annealed only” at 22 kOe of 40 wt.% $\text{SrO}(\text{Fe}_2\text{O}_3)_6/\text{PA12}$ filaments at 230 °C for 3 minutes .....	112
<b>Fig. 4.9:</b> Time dependence of $\Delta M_x/M_s$ (a) and $\Delta M_y/M_s$ (b) signals of the Pristine 40 wt.% $\text{SrO}(\text{Fe}_2\text{O}_3)_6/\text{PA12}$ filaments .....	114
<b>Fig. 4.10:</b> Time dependence of $M_x/M_s$ (a) and $M_y/M_s$ (b) signals of the “field-annealed and cooled” 22 kOe of 40 wt.% $\text{SrO}(\text{Fe}_2\text{O}_3)_6/\text{PA12}$ filaments at 230 °C 3 minutes.....	114
<b>Fig. 4.11:</b> Time dependence of $M_x/M_s$ (a) and $M_y/M_s$ (b) signals of the “field-annealed only” 22 kOe of 40 wt.% $\text{SrO}(\text{Fe}_2\text{O}_3)_6/\text{PA12}$ filaments at 230 °C 3 minutes .....	115
<b>Fig. 4.12:</b> $ \Delta M_{\text{max}}/M_s $ of (a) field-annealed and cooled and (b) field-annealed only at 22 kOe of 40 wt.% $\text{SrO}(\text{Fe}_2\text{O}_3)_6/\text{PA12}$ filaments at 230 °C 3 minutes .....	115
<b>Fig. 5.1:</b> Schematics of the size region between FFs and MRFs [8] .....	121
<b>Fig. 5.2:</b> Coercive field ( $H_c$ ) as a function of particle mean diameter ( $D$ ) of $\text{SrFe}_{12}\text{O}_{19}$ [10].....	123

<b>Fig. 5.3:</b> 40 wt.% SrO(Fe <sub>2</sub> O <sub>3</sub> ) <sub>6</sub> in PA12 cylindrical-shaped filament secured in Pyrex glass tubes [23] .....	126
<b>Fig. 5.4:</b> Magnetic hysteresis curves above and below the softening temperature of the PA-12 matrix .....	127
<b>Fig. 5.5:</b> Angle dependence of RT hysteresis curves before (a) and after (b) 1 minute anneal at 150 °C in a field of 22 kOe; (c) Angle dependence of hysteresis at 150 °C [23] .....	128
<b>Fig. 5.6:</b> 40 wt.% SrO(Fe <sub>2</sub> O <sub>3</sub> ) <sub>6</sub> /PA12 composite filament (a) pristine filament (left); (b) filament annealed in a field of 22000 Oe at 175 Celsius for one minute (right) and the white arrow indicates the applied magnetic field direction [23] .....	129
<b>Fig. 5.7:</b> Top view of the sample inside VSM chamber (a) Filament samples were annealed in a field of 22,000 Oe at 175 °C for 1 minutes, cooled down in a magnetic field to the measurement temperature; (b) rotated over 90 degrees in the VSM so the magnetic moment of the field annealed sample is perpendicular to the field direction; (c) a step field of 500 Oe was applied at the measurement temperature while the M <sub>x</sub> and M <sub>y</sub> component were monitored as a function of the field temperature .....	130
<b>Fig. 5.8:</b> Angle variation with time (a) at different elevated temperature (b) at 136 °C for different rotation fields of 40 wt.% SrO(Fe <sub>2</sub> O <sub>3</sub> ) <sub>6</sub> in PA12 matrix [23] .....	132
<b>Fig. 5.9:</b> (a) Dynamic viscosity and (b) Shear stress as a function of temperature for 40 wt.% SrO(Fe <sub>2</sub> O <sub>3</sub> ) <sub>6</sub> particles in PA12 matrix [23] .....	136
<b>Fig. 5.10:</b> (a)  M  Vs time of 40wt.% SrO(Fe <sub>2</sub> O <sub>3</sub> ) <sub>6</sub> /PA12 composite filament for different temperatures (left) and (b) comparison between observed $ \vec{M}(t) / \vec{M}_s $ transient on filament and disk sample at 160 °C (right) [23].....	138
<b>Fig. 5.11:</b> (a) SrO(Fe <sub>2</sub> O <sub>3</sub> ) <sub>6</sub> /PA12 cylindrical-shaped filament wrapped with Teflon tape and secured in Pyrex glass tubes with PEEK stoppers and high temperature silicone glue (b) at 230 °C upon melting, without Teflon wrap, filament turn into hollow cylinder .....	143
<b>Fig. 5.12:</b> Top view of the sample inside VSM chamber (a) Filament samples were annealed in a field of 22,000 Oe at 230 °C for 3 minutes, cooled down in a magnetic field;	

(b) rotated over 90 degrees in the VSM so the magnetic moment of the field annealed sample is perpendicular to the field direction; (c) a step field of 500 Oe was applied at the measurement temperature while the  $M_x$  and  $M_y$  component were monitored as a function of the field temperature .....144

**Fig. 5.13:** Magnetic transient upon application of a 500 Oe field perpendicular to the easy axis of 5 wt.% 22 kOe field annealed at 230 °C composite (a) ascending temperature from 150 to 225 °C (left); (b) descending 225 °C to 150 °C (right) .....146

**Fig. 5.14:** Magnetic transient upon application of a 500 Oe field perpendicular to the easy axis of 40 wt.% 22 kOe field annealed at 230 °C composite (a) ascending temperature from 150 to 225 °C (left); (b) descending 225 °C to 150 °C (right) .....146

**Fig. 5.15:** SEM images of Pristine (a) 5 wt.% and (b) 40 wt.%  $\text{SrO}(\text{Fe}_2\text{O}_3)_6/\text{PA12}$  composite .....147

**Fig. 5.16:** (a) Spinning Jeffery orbit for prolate spheroid; (b) tumbling Jeffery orbit for prolate spheroid; (c) spinning Jeffery orbit for oblate spheroid; (d) tumbling Jefferey orbit for oblate spheroid [59].....148

**Fig. 5.17:** Effect of anneal-field on agglomeration: SEM images of zero field and 22,000 Oe field-annealed at 230 °C for 3min for (a) 5 wt.% (top) and (b) 40 wt.% (bottom)  $\text{SrO}(\text{Fe}_2\text{O}_3)_6/\text{PA12}$  filament .....149

**Fig. 5.18:** Effect of anneal-time on agglomeration: SEM images of 1500 Oe field annealed at 230 °C for 5 sec and for 180 sec for (a) 5 wt.% (top) and (b) 40 wt.% (bottom)  $\text{SrO}(\text{Fe}_2\text{O}_3)_6/\text{PA12}$  filament .....150

**Fig. 6.1:** Uniaxial disk sample in a saturating magnetic field produced by an electromagnet (c = easy axis) [2].....160

**Fig. 6.2:** Variation with  $\theta$  of the anisotropy energy  $E$  and the torque  $L$  ( $=dE/d\theta$ ) for a uniaxial crystal [2] .....161

**Fig. 6.3:** For the case where  $M_s$  is not aligned with the field  $H$  [2] .....162

<b>Fig. 6.4:</b> Variation of torque with angle $\psi$ between easy axis $c$ and field $H$ for a uniaxial crystal and the dashed curve is for $H= 2K_1/M_s$ ; solid curve for $H \gg 2K_1/M_s$ [2] .....	163
<b>Fig. 6.5:</b> Biaxial torque curve (left) and true torque curve (middle) for a 2 mm circular mu-metal foil sample misaligned on a 5 mm diameter transvers rod (right) .....	165
<b>Fig. 6.6:</b> Measured $S_{xx}(\theta)$ , $S_{yy}(\theta)$ , $S_{yx}(\theta)$ for a strontium-ferrite/PA-12 filament sample mounted horizontally on a perpendicular rod .....	171
<b>Fig. 6.7:</b> $2\theta$ component of raw torque curve as a function of the reciprocal value of the applied field .....	172
<b>Fig. 6.8:</b> Relative angles of easy axis Nickel wire (TRQ Standard), the field ( $H$ ) and the magnetic moment vector ( $M$ ) for values below 18000 and above 18000.....	172
<b>Fig. 6.9:</b> $M_{y,raw}$ , $M_{y,cor}$ , $M_x$ and corrected torque curves of the Nickel torque calibration standard.....	173
<b>Fig. 6.10:</b> (a) $2\theta$ component of $M_y$ as a function of $1/Ha$ for raw data and data corrected for cross talk and angular sensitivity; (b) Corrected Torque versus $1/Ha$ curve .....	174
<b>Fig. 6.11:</b> (a) $M_{y,raw}$ , (b) $M_{y,cor}(S_{xy})$ , (c) $M_{y,cor}(S_{xy},S_{xx})$ , (d) $M_{x,raw}$ , and (e) torque curves of a Strontium Ferrite PA-12 3D printed filament (7.7 mm long x mm diameter) (f) shows the true torque curve of a similar sample that has a length of 4 mm .....	175
<b>Fig. 6.12:</b> $M_{y,raw}$ and $M_{y,cor}$ (left) and corrected and raw torque (right) .....	176
<b>Fig. 6.13:</b> Freely extruded sample on 3d printer and the shear flow of the molten suspension causes the strontium ferrite platelets to line up with the cylindrical outer surface of the filament resulting in texture .....	178
<b>Fig. 6.14:</b> 3D printed sample have a more complex magnetic anisotropy and a tilted easy axis is observed.....	178
<b>Fig. 6.15:</b> The field-annealed $SrO(Fe_2O_3)_6/ PA12$ cylindrical-shaped filament wrapped with Teflon tape and secured in Pyrex glass tubes with PEEK stoppers and high temperature silicone glue for torque measurement.....	180

**Fig. 7.1:** Small (a) and (b) electromagnet [9] or (c) permanent magnet can be installed on a regular FFF 3D printer in order to make the MFAAM process more facile [10] .....190

## LIST OF ABBREVIATIONS

<b>Abbreviation</b>	<b>Description</b>
AM	Additive Manufacturing
ACS	Auto Calibration Select
ATR	Attenuated Total Reflection
DM	Digital Microscope
DSC	Differential Scanning Calorimetry
EDS	Energy Dispersive Spectroscopy
FDM	Fused Deposition Modelling
FFF	Fused Filament Fabrication
FTM	Film Thickness Monitor
FTIR	Fourier Transform Infrared Spectroscopy
PA12	Polyamide-12
PM	Permanent Magnet
REE	Rare Earth Element
SD	Single Domain
SEM	Scanning Electron Microscopy
SE	Secondary Electron
SP	Super Paramagnetic
SW	Stoner and Wohlfarth
MD	Multi Domain
MFAAM	Magnetic Field Assisted Additive Manufacturing
TM	Torque magnetometer
TGA	Thermogravimetric Analysis
VSM	Vibrating Sample Magnetometer
XRD	X-ray Diffraction

## ABSTRACT

Magnetic polymer composites are being investigated for applications such as permanent magnets, transformers, electrical machines, and magnetic shielding. The particles are dispersed in a polymeric matrix to allow for the realization of magnetic parts of any form with reduced manufacturing cost and weight without significantly sacrificing their magnetic behavior. Materials are manufactured through additive manufacturing (AM) processes such as Fused Filament Fabrication (FFF) to allow for rapid prototyping and highly complex designs compared to magnetic composites manufactured through conventional methods. However, the major concern of permanent magnet AM is, no commercial hard-magnetic 3D-printer filament is yet on the market.

In our work, we manufacture and characterize magnetic polymer composite 3D-printer hard magnetic filament for the development of the Magnetic Field Assisted Additive Manufacturing (MFAAM) technology. The magnetic filaments are made by adding different wt.% of  $\text{SrO}(\text{Fe}_2\text{O}_3)_6$  powders into polyamide-12(PA12) using a twin-screw extruder. In MFAAM 3D printing, an external magnetic field is applied during the printing process, which allows an in-situ magnetic pre-alignment of particles in the molten composite and the magnetic particles to be oriented in a well-defined direction resulting in the realization of magnetic structures with complex well-defined easy axis distributions. This realizes field induced magnetic anisotropy during the extrusion and increases remanence, thus yielding stronger permanent magnets. In this dissertation, we investigate the magnetic hysteresis, magnetic viscosity and magnetic anisotropy of our manufactured composite pristine and field-annealed filaments by a vector Vibrating Sample Magnetometer (VSM). To my best knowledge, these are the first vector magnetic viscosity measurements reported on in literature. The magnetic viscosity is largest along the easy direction. The hysteresis measurements of pristine filaments show that they have a wire texture originating from the flow of the molten composites during the extrusion process. The texture of 3D printed filaments is more complex and originates from shear

flow contributions in the extrusion nozzle and in between the moving nozzle and the stationary printer bed. The magnetic properties of field annealed and MFAAM samples were studied to further the development of the MFAAM deposition process. The objective was to better understand how melt viscosity and packing fraction affect non-spherical particle alignment processes. field-annealed and MFAAM samples have their easy axis parallel to the anneal or print field direction, hence, show strong anisotropy. In this dissertation, a new method is presented to study the rotation of the magnetic particles in a molten suspension using a biaxial VSM. Modelling calculation and the temperature dependent experiment performed with the VSM to explore the orientation of the magnetic particles in a magnetic field and determine their dynamic behavior, melt viscosity, and the rotation of the magnetic moment in a strontium ferrite-PA12 composite “below the matrix melting temperature” and “above the matrix melting temperature”.

Furthermore, biaxial VSM was used to measure the magnetic anisotropy of the samples and anisotropy depends on the field annealing process through induced shape anisotropy contributions originating from agglomerates. Magnetic anisotropy increases with the increase of the field annealing time of the composites. For 22 kOe field-anneals, the measured magnetic anisotropy is larger than an individual particle’s effective anisotropy ( $K_{\text{eff}}$ ), providing evidence for significant agglomeration along the anneal field direction. This conclusion is supported by SEM analysis showing good particle alignment and significant chaining. We also discussed the 3D printed sample’s magnetic anisotropy by VSM and in addition, a Torque magnetometer (TM) has used to measure the anisotropy of the 3D printed sample to do the comparative analysis of TM and VSM results. These magnetic characterization efforts were complemented with SEM, EDS, FTIR, XRD, TGA, and DSC studies for morphological, chemical, structural, and thermal properties analysis.

# 1. INTRODUCTION

*“What we know is a drop, and what we don’t know is an Ocean”.*

-Sir Isaac Newton

## 1.1 Background

The earliest, and for centuries the only, use for a magnet was the needle of a magnetic compass for navigation purposes. Today the applications of magnets in devices and products, in industry, in the home, in the automobile, and in space, form a long list [1]. Magnetic materials are key players for the development and implementation of novel technologies. Currently magnetic materials attract enhanced interest from the materials science and materials manufacturing communities due to a shift to electric devices for transport and energy production. A change is observed in vehicle control from traditional hydraulic, mechanical and pneumatic systems to electric control that requires special magnetic materials in sensors, actuators, and motors. The move to renewable energy sources to reduce greenhouse emission and slow down or stop global warming also requires special magnetic material.

Magnetic materials include the hard-magnetic materials and soft-magnetic materials. The words “hard” and “soft” refer here not to the material’s mechanical properties but to its magnetic properties. For **hard magnetic** materials that are often applied in permanent magnets, a large magnetic field is needed to align the magnetic spins. These materials have in general a large hysteresis and retain their magnetic moment over large time intervals. On the contrary, **soft magnetic** materials are easily magnetized and demagnetized [2] and have a small coercivity and negligible hysteresis.

Whether a ferro- or ferrimagnetic material is magnetically hard or soft depends on the strength of the magnetic field needed to align its magnetic dipole moments. This property is characterized by coercivity ( $H_c$ ) and saturation or anisotropy field ( $H_k$ ). A hysteresis loop (Fig. 1.1) shows the relationship between the induced magnetic flux density  $B$  and the magnetizing force  $H$ . It is often referred to as the  $B$ - $H$  loop, which provides the value of retentivity ( $B_r$ ) and coercivity ( $H_c$ ) of a material. Hard magnetic materials have a high coercivity ( $10^3$ – $10^5$  A/m), and thus retain their magnetization in the

absence of an applied field, whereas soft magnetic materials have low  $H_c$  values ( $10^{-1}$ – $10^2$  A/m) [2].

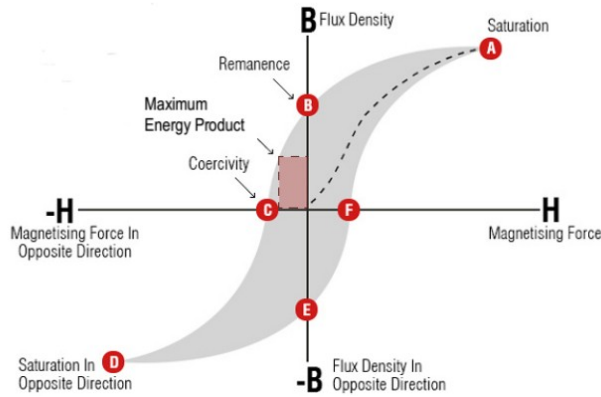


**Fig. 1.1:**  $(BH)_{max}$  can be graphically defined as area of the largest rectangle that has drawn in the second quadrant of the B-H loop [3].

The remanence ( $B_r$ ) and coercivity ( $H_c$ ) are determined from the saturation loop and are related to the maximum energy product, though not directly [3]. In magnetics, the maximum energy product is an important figure-of-merit for the strength of a permanent magnetic material. The maximum energy product denoted by  $(BH)_{max}$  and measured in  $\text{kJ/m}^3$ , is the amount of energy that a material can supply to an external magnetic circuit when operating within its demagnetization curve. In other words, it is the storage energy in a magnet. Generally, a magnet with a higher  $(BH)_{max}$  will be stronger and more stable than a magnet with a lower  $(BH)_{max}$  [4]. Permanent magnets constructed from high  $(BH)_{max}$  materials can be smaller than magnets constructed from low  $(BH)_{max}$  materials.

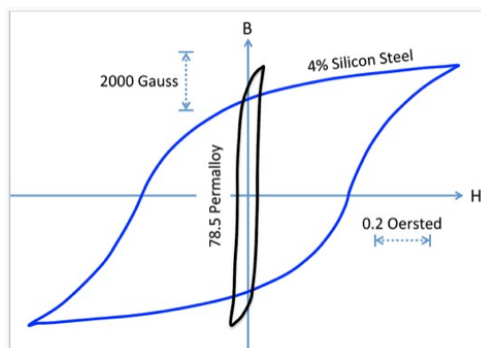


**Fig. 1.2:** Hysteresis loops comparing a (iron-silicon steel) to a soft magnet (permalloy) on the same scale. 4% Silicon steel is harder than the Permalloy.  $H_c$  for permalloy is 0.05 Oe, about 10 times lower than that of the iron-silicon steel. The remanent magnetizations of the two materials are comparable [5].

The Fig. 1.2 compares hysteresis loops for two soft magnetic materials. 4% Silicon steel is used in transformers and although it is a soft magnetic material, is harder than permalloy that is used in hard disk heads. The energy dissipated in magnetizing and demagnetizing the material is proportional to the area of the hysteresis loop. We can see that soft magnets, while they can achieve a high value of  $B_{\text{saturation}}$ , dissipate relatively little energy in the loop. This makes soft magnets preferable for use in transformer cores, where the field is switching 60 times per second. Permalloy, an alloy consisting of about 20% Fe and 80% Ni, is one of the most soft magnetic materials. It has a very high magnetic permeability  $\mu$  (i.e., a large maximum slope of the B vs. H curve) and a very narrow hysteresis loop [1, 5].

Some materials, such as iron metal, can exist as either hard or soft magnetic form. Whether bodycentered cubic (bcc) iron is a hard or soft magnet depends on the crystal grain size and orientation. When crystal grains in iron are sub-micron size, and comparable to the size of the magnetic domains, then the magnetic domain walls are pinned by crystal grain boundaries and the coercivity is large. When iron is annealed, its crystal grains grow and become multi-domain. The magnetic domains are no longer pinned by the grain boundaries and domains become more free to align with an applied magnetic field. This decreases the coercive field and the material becomes a soft magnet [2, 5]. Harder magnetic materials such as  $\text{CrO}_2$ ,  $\gamma\text{-Fe}_2\text{O}_3$ , and cobalt ferrite ( $\text{CoFe}_2\text{O}_4$ ) are used in magnetic recording media, where the higher coercivity allows them to retain the magnetization state (read as a logical 0 or 1) of a magnetic bit over longer periods of time. The coercivity of these materials is in general still low enough so a recording head can change its magnetic moment. Even harder magnetic materials are used in permanent magnets, including in disk drives, refrigerator magnets, electric motors, generators and other applications. For these applications one does not need to change the magnetic moment of the material. The cheap permanent magnetic materials are made of hexa-ferrites. Drive motors for hybrid and electric vehicles nowadays use the hard magnet  $\text{Nd}_2\text{Fe}_{14}\text{B}$  and require up to 1 kilogram (2.2 pounds) of neodymium [5].  $\text{Nd}_2\text{Fe}_{14}\text{B}$  has a much higher energy product than the hexa-ferrites but are also more expensive. Hard-magnetic components are ubiquitous in industrial equipment and consumer goods [6].

## 1.2 Permanent Magnetic Materials

Of the many permanent magnetic materials, four are predominant in use: AlNiCo, Samarium Cobalt (SmCo), Neodymium–Iron–Boron (NdFeB) and hexa-ferrites. **Alnico** is a generic name for a family of alloys that comes from the chemical symbols for aluminum, nickel, and cobalt, even though all alnicos have iron as a major constituent. They were at one time the most widely used permanent magnetic materials but have now been largely replaced by permanent magnets made from ferrites or rare earth-transition metal alloys [1]. Alnicos have a relatively high Curie temperatures i.e. 810 °C and therefore a relatively small temperature dependence of their magnetic properties near room temperature, which is a major advantage in some applications. The permanent magnetic properties of alnico are poor as they have a low energy product 34-80 kJ/m<sup>3</sup> [7]. All the alnicos are hard and brittle, much too brittle to be cold worked. Research on alnico largely ended about 1970, when the remarkable properties of rare-earth-transition metal compounds were discovered. The properties of alnico have improved only marginally since that time [1]. **Samarium Cobalt** (SmCo<sub>5</sub> or Sm<sub>2</sub>Co<sub>17</sub>) is a rare-earth magnetic material and two different materials are being marketed. SmCo<sub>5</sub> has a hexagonal crystal structure and Sm<sub>2</sub>Co<sub>17</sub> has a rhombohedral crystal structure [1]. Samarium is alloyed with Cobalt –a transition metal. So, each magnet is the result of a rare earth metal and a transition metal bonding together. SmCo<sub>5</sub> magnets are comprised of about 65% cobalt, which is one of the three naturally ferromagnetic elements besides iron and nickel. Samarium–cobalt magnets have maximum energy products (BH<sub>max</sub>) that range from 111 to 264 kJ/m<sup>3</sup> and are one of the magnetically strongest (coercivity ~ 750 kA/m) rare earth permanent magnets [8]. SmCo is also well-known for operating at higher temperatures which is important for most electrical machines that operate at about 120-180 °C.

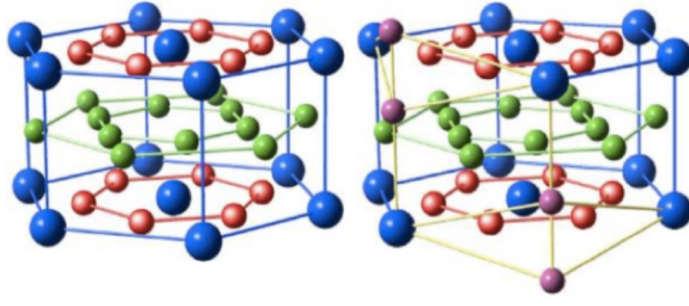


**Fig. 1.3:** The crystal structure of  $\text{SmCo}_5$  on the left and  $\text{Sm}_2\text{Co}_{17}$  on the right [8].

The crystal structure of  $\text{SmCo}_5$  on the left and  $\text{Sm}_2\text{Co}_{17}$  on the right is shown in Fig. 1.3. The notation  $\text{Sm}_2\text{Co}_{17}$  is shorthand for a family of complex compositions that may be expressed as  $\text{Sm}_2(\text{Co}, \text{Fe}, \text{Cu}, \text{Zr}) \approx 15$ . Some alternative production also evolved for producing SmCo magnets by reduction of a rare-earth oxide such as  $\text{Sm}_2\text{O}_3$  while introducing Co, usually using Ca as the reducing agent [1]. Cobalt is expensive though and the world production is limited. It became highly expensive after instabilities in the Congo, the global provider of above 60% of this material in 1979-1982 [9]. **NdFeB** was introduced to the market in the 80's by General Motors, Sumitomo Special Metals Co., Ltd. and by the U.S. Naval Research Laboratory at almost the same time due to the need of independency of US from external sources of Cobalt to produce SmCo magnetic materials.

**Table 1.1:** Price of some raw materials of permanent magnet (updated December 2022) [10, 11, 12]

Metal	Price per lb.
Neodymium (Nd)	\$67.48/ lb.
Cobalt (Co)	\$23.56/ lb.
Strontium Ferrite ( $\text{SrFe}_{12}\text{O}_{19}$ )	\$0.30/ lb.
Aluminum (Al)	\$1.07/ lb.
Iron (Fe)	\$0.07/ lb.
Nickel (Ni)	\$12.28/lb.
Dysprosium (Dy)	\$213.60/lb.
Samarium (Sm)	\$7.61/lb.
Strontium (Sr)	\$2.45/lb.

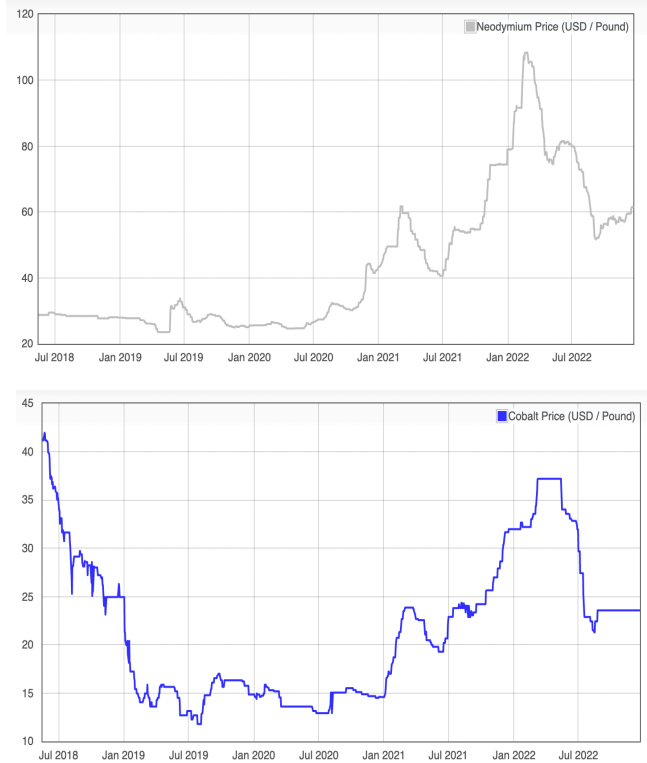


**Fig. 1.4:** Neodymium (top) and Cobalt (bottom) prices (USD/lb.) past five years (updated December 2022) [10].

Although NdFeB was initially cheaper than SmCo magnets [13], over the last two years the Neodymium (Nd) per metric ton has gone up strongly and as of 2022 is almost 2.5 times that of Cobalt [11]. Note that NdFeB magnet contains approximately 30 wt.% Nd while SmCo magnets contain 30 or 75 wt.% Co. In order to keep the manufacturing expenses low one is currently exploring to replace Nd, Pr, and Dy with readily available Ce and La [14].

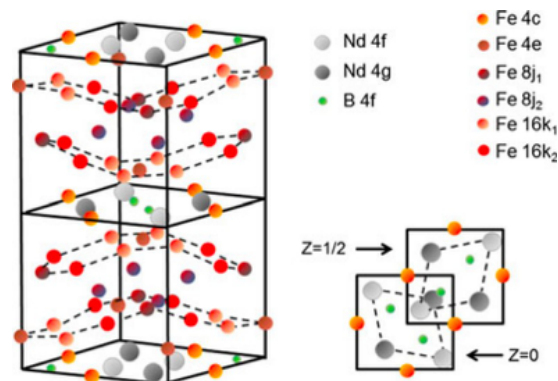


**Fig. 1.5:** The crystal structure of  $\text{Nd}_2\text{Fe}_{14}\text{B}$ . A view looking down the tetragonal c-axis is shown on the right [15].

NdFeB is an intermetallic compound, highly available and magnets have been made with energy products of 388 kJ/m<sup>3</sup> or more [1]. NdFeB is classified as permanent/hard magnetic material. Its hardness highly depends on the microstructure which is a result of the manufacturing process. For instance, a chemical route is not recommended because of its reactivity and highly oxidation behavior [16]. The NdFeB tetragonal crystal structure can be observed in Fig. 1.5, it has 68 atoms and 6 crystallographic distinct iron sites per unit cell and its easy magnetic axis can be found along the c-axis [16]. Some of the drawbacks of NdFeB are their low Curie Temperature ( $T_c$ ) up to 311 °C, their brittle behavior, and their sensitivity to corrosion. To maximize the coercivity at the operating temperature, a fraction of Nd is typically substituted with heavy rare earth elements such as Dy. In particular for permanent magnets in electrical motors the Dy content often exceeds 5 wt.%.

**Table 1.2:** Properties of some permanent magnetic materials [1].

Product	$B_r$ , kG	$H_c$ , kOe	$H_{ci}$ , kOe	$(BH)_{max}$ , MGOe	Max $T$ , °C	Temperature Coefficient, %/°C
Hard ferrite 1	3.8	2.4	2.55	3.4	200	-0.2
Hard ferrite 2	4.0	3.65	4.0	4.0	200	-0.2
Alnico 5	12.5	0.680		5.5	450	-0.02
Alnico 9	11.2	1.375		10.5	450	-0.02
SmCo <sub>5</sub>	8.7	8.50	30.0	18.0	250	-0.04
Sm <sub>2</sub> Co <sub>17</sub>	10.7	9.75	26.0	26.0	300–350	-0.03
NdFeB 1	10.0	9.60	41.0	24.0	150–200	-0.1
NdFeB 2	12.9	12.40	23.0	40.0	150–200	-0.1

**Hard Ferrites**, applied in ceramic magnets, are still the most widely manufactured and distributed permanent magnet material. Various hard ferrites are used in applications including Barium Ferrite (BaFe<sub>12</sub>O<sub>19</sub>) and Strontium Ferrite (SrFe<sub>12</sub>O<sub>19</sub>). Hard Ferrite's have many applications in high technology due to their low materials and manufacturing costs compared to competing materials, such as Alnico, SmCo or NdFeB [18]. Three different groups of ferrite magnetic materials exist based on their crystal structure which depends on the preparation of the material: spinel, garnet, and hexagonal ferrites. The third type of ferrite has the hexagonal crystal structure and is often called the hexa-ferrite material. Based on the crystal structure, hexa-ferrite materials can be divided into six types, namely types M, W, Y, Z, X, and U where M, W, Y, Z, X and U have a slightly different

structure and different substituted elements [19]. M-type hexagonal ferrites ( $MFe_{12}O_{19}$ ) where,  $M = Sr, Ba$  etc, have been widely used as a permanent magnetic material. They show ferrimagnetic ordering and have a large crystalline anisotropy.  $SrFe_{12}O_{19}$  has a slightly higher magnetization and anisotropy field than  $BaFe_{12}O_{19}$  and is known as an important hard magnetic material [18]. Furthermore, strontium can be absorbed as calcium by humans, whereas barium can have toxic effects, making strontium ferrite a better choice for consumer products [20]. The magnetic moment originates from the  $Fe^{3+}$  ions which each carry a magnetic moment of approximately  $5 \mu_B$  [21]. M-type  $SrFe_{12}O_{19}$  was discovered in the 1950s by Philips' laboratories [22]. Due to appropriate magnetic properties, chemical stability, and low cost compared with rare-earth compounds,  $SrFe_{12}O_{19}$  has attracted extensive interests in the past decades [23] and it has been recognized that it can be used as permanent magnets, in recording media, in telecommunication devices, and as components in microwave, high-frequency, and magneto-optical devices [24, 25].

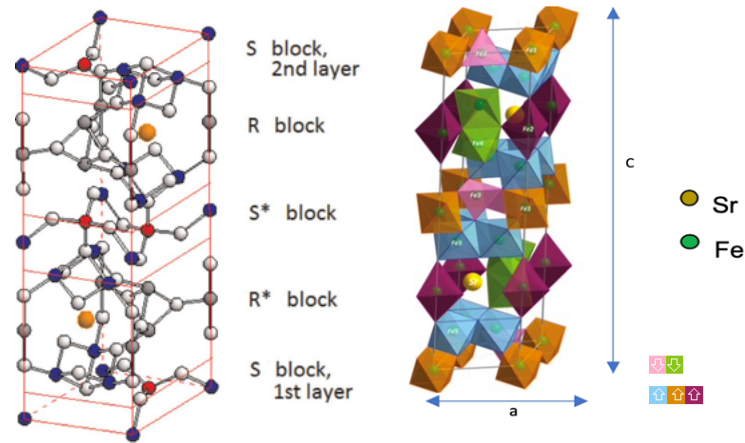


**Fig. 1.6:** (a) The Unit cells of hexagonal  $SrFe_{12}O_{19}$  [26] and (b) schematic diagram of Strontium ferrite crystal structure by Granados et al., 2016 [27].

Ferrites are not susceptible to oxidation or corrosion, which extends their magnetic properties for longer periods of time. They are low-cost and easily manufactured in single domain particles of around  $1.4 \mu m$ , a highly attractive characteristic to obtain large coercivity material [28, 29]. Its high coercivity is also due to its large magnetic anisotropy. The magnetic moment prefers certain directions in the material. These preferred orientations are referred to as easy axis and in zero field the magnetic moment aligns along

these directions. For  $\text{SrFe}_{12}\text{O}_{19}$  the magnetic anisotropy is mainly the result the crystal structure and the shape of the particles, although stress, annealing, deformation, irradiation, and exchange anisotropy can also contribute [30]. The hexagonal lattice of  $\text{SrFe}_{12}\text{O}_{19}$  as displayed in Fig. 1.6, is defined by two parameters, the lattice constants:  $a$ , the width of the unit cell in the hexagonal plane, and  $c$ , the height of the unit cell (Fig. 1.6b). For the hard ferrites, the preferred orientation of the magnetic moment, the easy axis, goes parallel to the  $c$ -axis. This makes the basal plane a hard direction for the magnetic dipole moment. Strontium ferrite has high coercivity, which originates from the large magnetocrystalline anisotropy energy with single easy magnetization axis. Other hexa-ferrites such as most Y ferrites and all the  $\text{Co}_2$  ferrites are ferroplana with a preferred direction of magnetization in the hexagonal basal plane or in a cone at an angle with the  $c$ -axis. These ferrites are mostly soft magnetic as the magnetic moment can now freely rotate in the basal plane [31]. **Soft ferrite** is an iron-oxide-based soft magnetic material. Soft ferrites are ferrimagnetic in nature with cubic crystal structure and they are characterized by chemical formula  $\text{MO}\cdot\text{Fe}_2\text{O}_3$ , where  $M$  is a transition metal ion like iron, nickel, manganese, and zinc. Manganese–zinc ferrites act as softmagnets up to high frequencies of 10 MHz which are easily magnetized and demagnetized, so store or transfer magnetic energy in alternating or other changing waveforms. Soft ferrites are used for transformer cores, switch mode power supplies, inductors, convertors, electromagnetic interference filter and antennas [17]. Although the soft ferrites have a magnetization much lower than soft iron, their high resistivity make them interesting for high frequency applications. The high resistivity of the ferrites originate from the fact that they are semiconductors.

A large number of methods can be used to manufacture ferrites including the salt-melt method, coprecipitation, ion exchange, sol-gel process, citrate synthesis, glass crystallization, combustion method, spray drying, and self-propagating high temperature synthesis [31]. When made in powder form, the shape of single crystalline particles reflect the symmetry of the crystal structure often resulting in non-spherical particles including platelets. Some preparation methods such as the citrate synthesis result in the realization of fibers. The shape of the particles will affect the magnetic properties specifically the magnetic anisotropy. Different volume to surface ratio can also affect the crystal anisotropy of the particles because of surface anisotropy.

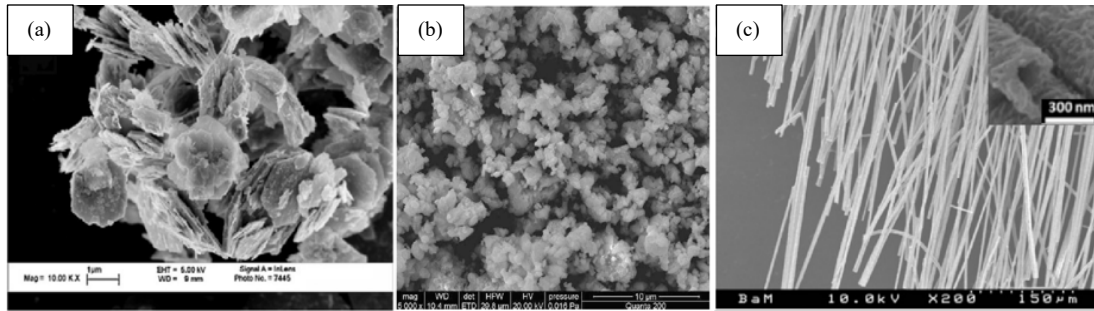


**Fig. 1.7:** Hexaferrites with different form factors; (a) Sr-Ferrites platelets [32] (left), (b) Ba-Ferrites “spherical-like” particles [33] (middle), (c) Ba-Ferrites fibers [34, 35] (right).

### 1.3 Magnetic Properties

The magnetic materials properties, specifically the hysteresis curve, depend on intrinsic and extrinsic properties. Intrinsic properties are the magnetization ( $M_s$ ), the exchange interaction ( $A$ ), and the magnetic anisotropy ( $K$ ). The magnetization is the magnetic dipole moment per unit mass ( $\text{Am}^2/\text{kg}$ ) or volume ( $\text{A/m}$ ). Unpaired spins in atoms will result in individual atoms having a net magnetic dipole moment. These dipole moment on individual atoms can be aligned by an applied magnetic field or by exchange coupling between neighboring atoms. Exchange interaction between atoms results in magnetic order, including ferromagnetic and ferrimagnetic order. In ferromagnets a parallel alignment of magnetic dipoles in neighboring atoms results in the crystal over larger distances to have a non-zero magnetization. For ferrimagnets the magnetic moment on neighboring atoms is aligned anti-parallel and as the magnetic dipole moment on neighboring atoms is unequal the materials still has a non-zero magnetization over larger distances. The strength of the exchange interaction is often determined from the Curie temperature ( $T_c$ ). This is the temperature above which spin order disappears in a magnetic material. The third parameter, the magnetic anisotropy originates from the spin orbit interaction and the crystal structure and couples the magnetic dipole moment in a single crystal with the crystal structure creating preferential directions for the magnetic dipole moment in the crystal. Extrinsic properties are for example impurities, grain boundaries, lattice defects, and texture that all greatly can impact  $M_s$ ,  $A$ , and  $K$  through the material, making those parameters functions of the spatial coordinates. The distribution of these parameters through the material can affect the magnetic reversal mechanism and thus the

hysteresis, remanence, and coercivity. For magnetic composites, extrinsic properties also include the size and shape of the particles, the packing fraction, the distribution of the particles through the polymer matrix, and the orientation of the particles. In this section the physics behind the magnetic properties is discussed.

### 1.3.1 Magnetic Anisotropy

**Magnetic anisotropy** is one of the factors which strongly affects the shape of the M, H (or B, H) hysteresis curve, and controls the coercivity and remanence [25]. This term magnetic anisotropy simply means that the magnetic energy of the sample depends on the orientation of the magnetic moment in the sample. Two different magnetic anisotropy i.e. crystal and the shape of the sample contribute to the anisotropy of the magnetic energy of a hard-magnetic powder [36, 37].

The **crystal magnetic anisotropy** is due to the spin-orbit interaction and the crystalline electric field. The spin orbit interaction couples the magnetic dipole moment with the crystal axes. If the local crystal field around the atom is of low symmetry and the bonding electrons of that atom have an asymmetric charge distribution, the atomic orbitals will interact anisotropically with the crystal field [38]. When an external field tries to reorient the spin of an electron, the orbit of that electron also tends to be reoriented. But the orbit is strongly coupled to the lattice and therefore, resists the attempt to rotate the spin axis. The magnetic moment of the strontium ferrite originates from the spin of the unpaired electrons on the  $\text{Fe}^{3+}$  that are ferrimagnetic coupled through indirect exchange interaction through the oxygen ions. As the spin of the electrons is coupled to the direction of their orbits (spin orbit interaction), rotating the magnetic moment will also rotate the orbits changing the total energy of the magnetized strontium ferrite: the energy is dependent on the direction of the orbit with respect to the crystal structure. The energy required to rotate the spin system of a domain away from the easy direction towards its hard axis, which is called the anisotropy energy, is just the energy required to overcome the spin-orbit coupling [30, 36]. As mentioned in the previous section the easy axis of strontium ferrite is along the c-axis, so the magnetic anisotropy is uniaxial. Assuming that  $\theta$  is the angle between the c-axis and the magnetic dipole moment the magnetic anisotropy

energy of strontium ferrite is given by the following equation:

$$E_{crys} = K_0 + K_1 \sin^2(\theta) + K_2 \sin^4(\theta) \quad (1.1)$$

Where  $K_0$ ,  $K_1$ , and  $K_2$  are the zero, first and 2<sup>nd</sup> order crystal anisotropy constants. Since  $K_0$  is independent of magnetic moment angle and assuming  $K_1 \gg K_2$  we can simplify this expression to:

$$E_{crys} \approx K_1 \sin^2(\theta) \quad (1.2)$$

Where  $K_1$  is approximately 344 kJ/m<sup>2</sup> for strontium ferrite [39].

The **shape anisotropy** [36] is due to the shape of the particle. A magnetized body will produce magnetic charges or poles ( $+\sigma_m$ ,  $-\sigma_m$ ) on its surfaces where  $\vec{M}_s \cdot \hat{n}$  is non-zero. Here  $\hat{n}$  is the normal vector on its surface and  $\vec{M}_s$  is the saturation Magnetization. These magnetic surface charges are sources of the magnetic H field. Outside the materials this H field is referred as stray field but inside the materials the H field is called the demagnetizing field. It is called the demagnetizing field because it is pointing opposite to the magnetization.

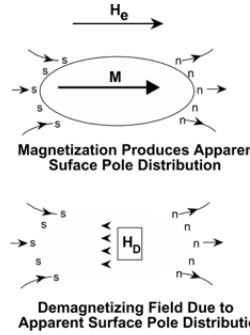


**Fig. 1.8:** The demagnetizing field  $H_D$  [36].

For example, for a magnetized prolate ellipsoid (Fig. 1.8) with its long axis oriented horizontally and its magnetic dipole moment oriented towards the right, the demagnetizing field is directed towards the left. As demagnetizing field and magnetic dipole moment are in opposite directions, the magnetostatic energy of the demagnetizing field  $E_d$  is given by [40]:

$$E_d = -\frac{1}{2} \mu_o \vec{m} \cdot \vec{H}_d \quad (1.3)$$

Where  $\vec{m}$  is the magnetic dipole moment. As  $\vec{m}$  and  $\vec{H}_d$  are opposite to each other  $E_d$  is positive and unequal to zero. The demagnetizing field will be smaller if the object

is magnetized along its long axis and larger if its magnetize along its short axis. Assuming that the demagnetizing field is proportional to dipole moment [41], i.e.

$$\vec{H}_d = -N_d \vec{m} \quad (1.4)$$

the magnetostatic energy from equation (1.3) can be written as:

$$E_d = \frac{1}{2} \mu_o N_d \vec{m} \cdot \vec{m} \quad (1.5)$$

where  $N_d$  is the demagnetizing factor which for non-spherical objects depends on the angle of the magnetic moment in the object. For an oblate spheroid with demagnetizing factors  $N_a$  and  $N_c$  along the long a-axis and the short c-axis, the magnetostatic energy will vary with the angle  $\theta$  the magnetic moment makes with the c-axis as:

$$\begin{aligned} E_d &= \frac{1}{2} \mu_o [M_s^2 \sin^2(\theta) N_a + M_s^2 \cos^2(\theta) N_c] \\ &= \frac{1}{2} \mu_o M_s^2 (N_a + (N_a - N_c) \sin^2(\theta)) \end{aligned} \quad (1.6)$$

Where  $\frac{1}{2} \mu_o M_s^2 (N_c - N_a)$  is referred to as the shape anisotropy  $K_s$ . This produces an easy axis of magnetization along the long a-axis, i.e. along the axis with the smallest demagnetizing factor. The shape anisotropy [42] is caused by the effect of the field of the individual magnetic dipoles on each other. The easy shape anisotropy axis is normally that direction in the sample that will cause the magnetic north and south poles to be positioned far apart from each other. So, for a thin film the easy shape anisotropy axis is in plane. For an elongated cylindrical shaped sample, the easy shape anisotropy axis is along the long axis of the cylinder. A sphere of a material with zero crystal anisotropy, on the other hand, has no shape anisotropy, because the same demagnetizing field will act on its magnetic dipoles in any direction [30]. The magnitude of the shape anisotropy is dependent on the saturation magnetization. For strontium ferrite the saturation magnetization is approximately 380 kA/m. Since the strontium ferrite powder used in this dissertation consists of non-spherical platelets that can be described by oblate ellipsoids that have an average short axis that is approximately 3 times shorter than their long axis the demagnetizing factor is approximately  $N_d = N_c - N_a = 0.64$ , resulting in shape anisotropy of approximately 41 kJ/m<sup>3</sup>. Scanning Electron Microscope (SEM)

micrographs and magnetic measurements indicate that the platelets have a magnetic easy axis along the short axis of the oblate ellipsoids from which one can conclude that the easy axis of the crystal anisotropy (c-axis) is aligned along the short axis of the particles. So, the easy axis of the particle's shape ( $K_s$ ) and crystal anisotropy ( $K_c$ ) are perpendicular to each other and  $K_c \gg K_s$ . Assuming the particles are single crystalline the magnetic anisotropy is given by:

$$E_{eff} = (K_c - K_s)\sin^2(\theta) = K_{eff}\sin^2(\theta) \quad (1.7)$$

Where  $K_{eff}$  is the effective magnetic anisotropy constant which is positive, so the easy axis is when  $\theta=90$  degrees, i.e. lined up with the short axis of the particles. For strontium ferrite platelets that have an aspect ratio of 3 the effective  $K_{eff}=309$  kJ/m<sup>3</sup>. Note that this is the anisotropy constant for a single particle. The actual anisotropy constant of the sample can differ because of the shape anisotropy of the sample, the shape anisotropy of agglomerates in the sample, and the easy axis distribution of the particles in the composite.

### 1.3.2 Saturation Magnetization and the existence of Domains

Even in the absence of external magnetic fields, in ferro and ferrimagnets the magnetic dipole moment is aligned over larger distances because of the exchange interaction. This exchange interaction is from quantum mechanical origin. Usually, an external field is necessary to get all the magnetic moments in a magnetic sample to align with each other, even in materials that are strongly ferro or ferrimagnetic. The reason for such behavior is the presence of magnetic domains or sub-volumes. Each one of these domains possess a saturated (i.e., maximum possible) moment, but different domains may not be aligned with each other. This non-alignment is the cause of unsaturation in zero field for ferro and ferrimagnetic materials [38].

### 1.3.3 Domain Walls

Magnetic domains are separated by domain walls. These are interfaces between regions in which the magnetization has a different direction. In strontium ferrites that

has a uniaxial magnetic anisotropy, within the walls, the magnetization must change direction from up along the c-axis to down along the c-axis. The domain wall width is determined by a trade-off in exchange and magnetocrystalline energy [36]. The schematic representation of the domain wall, shown in Fig. 1.9, illustrates that the dipole moments of the atoms within the wall are not pointing in the easy direction of magnetization and hence are in a higher magnetic anisotropy energy state. In addition, the atomic dipoles within the wall are not parallel to each other and so the magnetic spins in the wall are in a higher exchange energy state as well. Therefore, a domain wall energy is associated with a domain wall which depends on the degree of magnetocrystalline anisotropy ( $K_{crystal}$ ) and the strength of the exchange interaction ( $A$ ) between neighboring atoms. The thickness of the wall will also depend on these parameters. A strong magnetocrystalline anisotropy will result a narrow wall, whereas a strong exchange interaction will result a wider wall. For a material with a uniaxial crystal anisotropy the domain wall energy and width are given by the following expressions [24]:

$$\gamma_{180} = 4 \sqrt{AK_{crystal}} \quad (1.8)$$

$$\delta_{180} = \pi \sqrt{\frac{A}{K_{crystal}}} \quad (1.9)$$

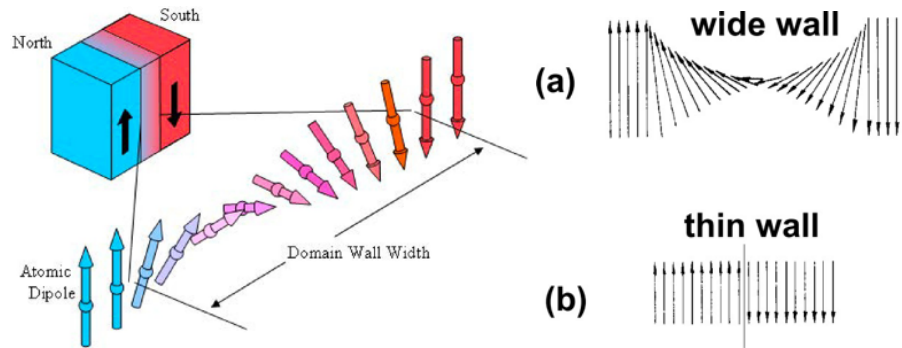


**Fig. 1.9:** Schematic representation of a 180° domain wall (left) [43] and (right) the change in magnetization within the wall can be gradual as in (a) or abrupt as in (b) [36].

Note that the exchange energy acts to keep spins parallel and can be kept small if the 180° rotation takes place over a lot of atomic units. Therefore, a small exchange energy results in a wide wall as shown in Fig. 1.9a and a large exchange energy a thin wall as

shown in Fig. 1.9b. Similarly, a large crystal anisotropy results in thin wall while a small crystal anisotropy in a thick wall. [36].

### 1.3.4 Single or Multiple Domain

Weiss proposed the existence of magnetic domains to explain the fact that ferromagnetic materials with spontaneous magnetization could exist in a demagnetized state. The magnetization within a domain is saturated and typically lies along the easy axis direction when there is no externally applied field.

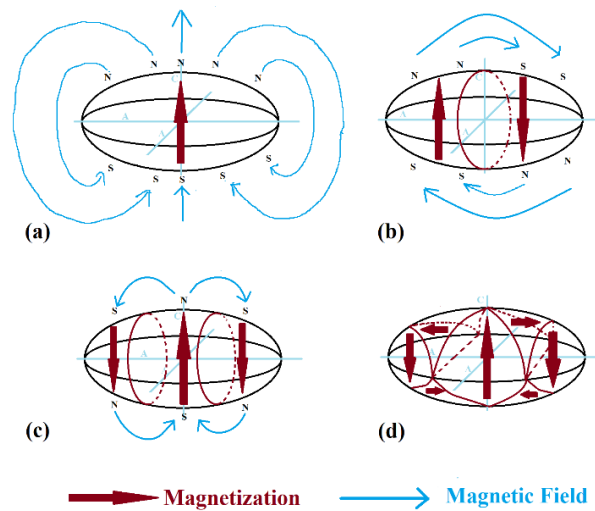


**Fig. 1.10:** Schematic illustration of the breakup of the magnetization of an oblate ellipsoid into domains (a) single domain, (b) two domains, (c) three domains, and (d) three domains with closure domains.

Fig. 1.10 shows possible domain patterns of a large oblate spheroid particle that has a uniaxial magnetic anisotropy in the vertical direction of the drawing. For a uniformly magnetized specimen as shown in Fig. 1.10a, and hence a single domain, magnetic surface charges will form on the top and bottom surfaces due to the normal component of the magnetization. As mentioned above these surface charges are a source of a demagnetizing field ( $H_d$ ) and can result in a significant demagnetizing energy [36].

For the magnetic domain configuration shown in Fig. 1.10b the demagnetizing energy is significantly reduced. The magnetostatic energy can be approximately halved if the magnetization splits into two domains magnetized in opposite directions. This brings

(+) and (-) charges closer together, thus decreasing the spatial extent of the demagnetizing field. If the domain pattern in the oblate spheroid breaks down into  $N$  domains then the demagnetizing energy is roughly reduced by a factor of  $1/N$ , hence Fig. 1.10c has a third of the demagnetizing energy of Fig. 1.10a etc. The demagnetizing energy can be further reduced by eliminating the external field lines by closing the ends with sideway domains (closure domains). Fig. 1.10d shows a closure domain structure where the demagnetizing energy is zero [36, 43]. Note that for a uniaxial material, the closure domains will have their magnetic moment in the hard direction and have a higher crystal anisotropy energy.

Although the demagnetizing energy decreases as the number of domains increases, the material will not continue to split into more and more domains because the introduction of a domain wall also raises the overall energy of the system. This is because the domain wall has an energy associated with it, proportional to its area as was shown equation 1.8 in the previous section [43]. So, the more domain walls in the particle the higher the domain wall energy. So eventually introducing an extra domain wall in the particle will reduce the demagnetizing energy less than it increases the domain wall energy and some type of equilibrium is established.

A minimum energy can therefore be achieved with a specific number of domains within a specimen. This number of domains will depend on the size and shape of the sample (which will affect the demagnetizing energy) and the intrinsic magnetic properties of the material (which will affect the demagnetizing energy and the domain wall energy). The cost of a 180-degree domain wall through the center of an oblate ellipsoid with dimensions  $a$  by  $a$  by  $c$  is surface energy of the wall given above times the surface area of the wall  $\pi ac$  follows from equation 1.8

$$\Delta U_w = 4\sqrt{AK}\pi ac \quad (1.10)$$

Using the approximation given above that a single domain wall will reduce the magnetostatic energy of the particle with a factor 2 and expression 1.5, we see that the decrease in demagnetizing energy will be:

$$\Delta U_{MS} = \frac{4}{3}\pi a^2 c \frac{1}{2}\mu_o M_s^2 N_d \quad (1.11)$$

Setting both equations equal to each other gives for the critical size,

$$a = \frac{12\sqrt{AK}}{N_d\mu_oM_s^2} \quad (1.12)$$

Particles of this size are expected to consist of a single domain (SD), while particles larger than this size might have one or more domain walls in them and are referred to a multiple domain (MD) particles. Assuming that the particles are spherical the expressions for SD  $r_c$  is

$$r_c = \frac{36\sqrt{AK}}{N_d\mu_oM_s^2} \quad (1.13)$$

For particles with an a/c ratio of 3, the demagnetizing factor is approximately 2/3 and the  $r_c$  is approximately a factor 2 smaller. Summarizing the magnetic domain pattern of magnetic particles depends on it size and shape. Below a certain critical radius, the particle is expected to be SD.

The existence of domains in particles is hinted at by the observation that some magnetic properties, and in particular, coercivity and remanence vary greatly with grain size. This is best illustrated in the figure below, which shows the variation of  $H_c$  with particle size.

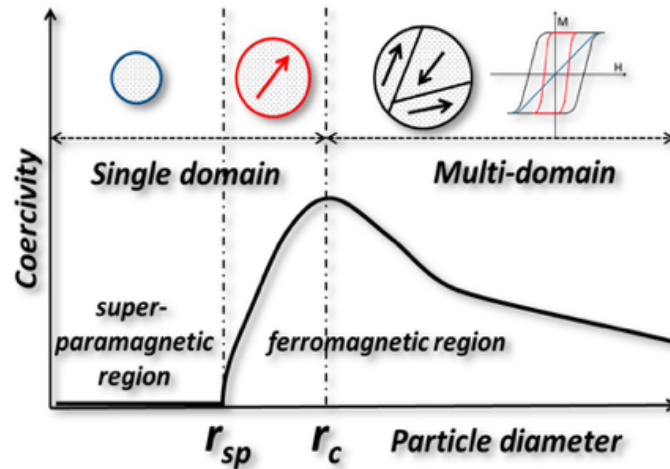


**Fig. 1.11:** Schematically illustrates the size dependence of  $H_c$  of the non-interacting magnetic particles. The maximum coercivity for a given material occurs within its single-domain range at critical radius ( $r_c$ ). For larger grain sizes, coercivity decreases as the grain subdivides into domains. For smaller grain sizes, coercivity again decreases, the latter due to the randomizing effects of thermal energy [31].

There is a relationship between particle size and coercivity ( $H_c$ ) as magnetic reversal by domain wall motion is much easier than magnetic reversal by coherent rotation

of all magnetic spins at the same time. So, the presence of domain walls in the particles implies a much smaller coercivity and much less hysteresis [44, 45]. Larger particles are often multidomain as the domain pattern in the particles lowers the demagnetizing energy significantly. The energy of the domain walls is less than the lowering of the demagnetizing energy. If the particle is smaller than the width of the domain wall, the particle will be single domain as a domain wall no longer fit in such particle. For most materials single domain particles have a much larger coercivity than multidomain particles. Summarizing, magnetic particles would behave as SD or MD depending on particle size and the size of the domain wall. The coercivity of a particle is larger when the particle is single domain. Reversal of the magnetic moment in single domain particles requires nucleation of the magnetic dipole moments of part of the particles or requires to rotate all dipoles through the hard magnetic anisotropy axis. Both of these processes require a large field resulting in a high coercivity. At the particle size of the critical radius ( $r_c$ ), the single domain prefers to be uniformly magnetized along one of its anisotropic easy axes, which leads to a strong enhancement in coercivity, meaning that it is more difficult to reverse its magnetization [36]. For multi-domain particles the reversal of the magnetization can take place by the motion of a domain wall which requires much less field. Below  $r_c$ , the coercivity value decreases with smaller particle size [45] due to the decrease of the magnetic anisotropy energy ( $U_e$ ),

$$U_e = K_e V \quad (1.14)$$

Where  $V$  is volume of the particle, and  $K_e$  is the effective anisotropy of the particle. On reduction of the particle size below  $r_{SD}$ , the anisotropy energy value decreases further and becomes comparable to the thermal energy  $k_B T$  where  $k_B$  is the Boltzmann constant. In this region, the energy barrier for magnetization reversal is dominated by thermal energy. Thus, the magnetic dipole moment of the particle thermally fluctuates like the spins in a paramagnetic material. This leads to a net magnetization of zero; this state is called the superparamagnetic state. Superparamagnetic materials have no coercivity at room temperature due to the randomizing effects of thermal energy. Although the transition from ferromagnetic to ordinary paramagnetic properties in bulk magnets is due to  $k_B T$  over winning the exchange interaction energy, the ferromagnetic-to-superparamagnetic transition in fine particles is solely due to the size effect [46] and

caused by  $k_B T$  getting larger than the magnetic anisotropy energy.

### 1.3.5 Magnetic Phase Diagram of Strontium Ferrite

Using equations 1.13 and the temperature dependence of  $K_1$  and  $M_s$  of Shirk et al. [39] we calculated the magnetic phase diagram of Strontium Ferrite. Results are shown in Fig. 1.13. The blue line shows the critical size below which the single domain particles become superparamagnetic and the orange line the critical size below which the particle is a single domain. The blue line is calculated from setting equation 1.14 equal to  $k_B T$ .

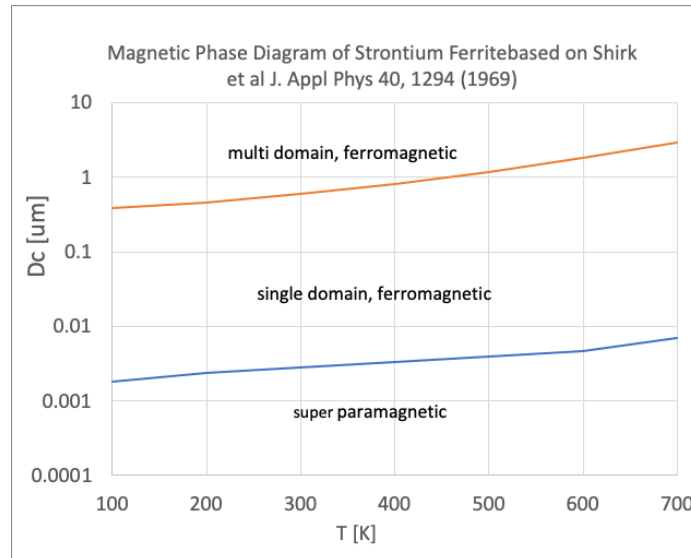


Fig. 1.12: Magnetic Phase Diagram of Strontium Ferrite based on Shirk et. al [39].

### 1.3.6 Magnetic Reversal Mechanism

As shown in the previous section the reversal mechanism in particles can greatly affect the magnetic properties. For single domain particles the reversal of magnetic spins can be in unison with each other (coherent rotation) or in a mode where the spins do not rotate in parallel (incoherent rotation). For the incoherent reversal case the magnetic reversal is affected by nucleation processes that start at the surface of the particle and then propagate through the particle.

### 1.3.6.1 Coherent Rotation

A simple model developed by Stoner and Wohlfarth [47] assumes coherent spin rotation whereby all spins within the SD particle are collinear (the magnetization is uniform) and rotate in unison. Such process of magnetization reversal in a single domain is referred to as coherent rotation due to the absence of a domain wall, according to the Stoner–Wohlfarth (SW) theory. This switching field of reversal by coherent rotation can be calculated from the anisotropy energy (shape and crystal) and the magnetostatic energy of the sample in the magnetic field. The model predicts the field strength necessary to reverse the spin orientation direction or coercivity depending on the effective anisotropy, the saturation magnetization and the orientation of the easy axis with respect to the field direction [46].

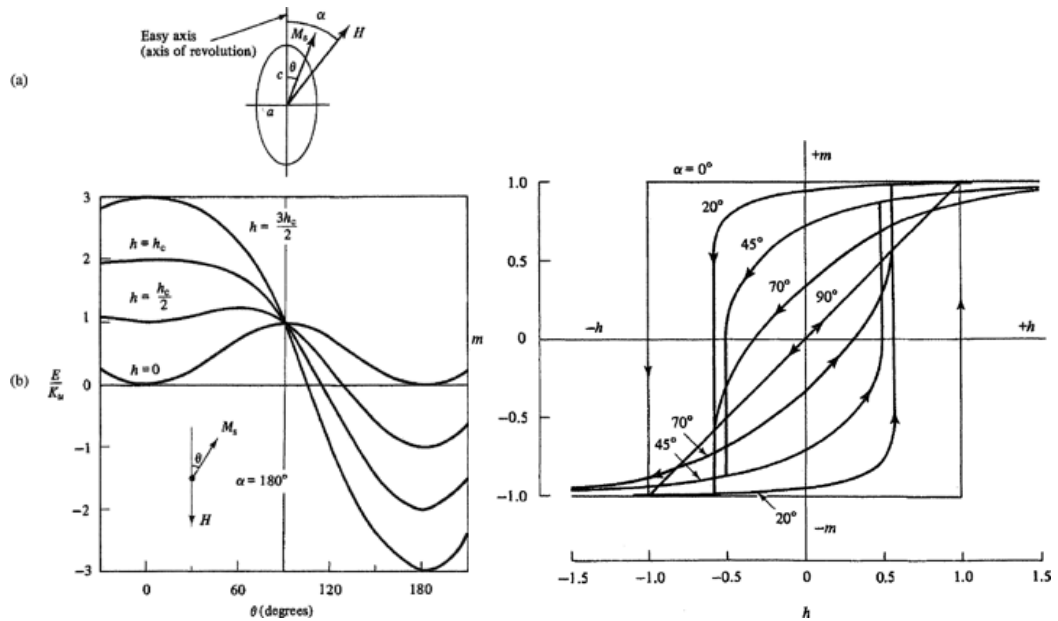


**Fig. 1.13:** (a) Total energy of particle with uniaxial anisotropy as a function of the angle of the magnetic dipole moment with respect to the easy axis for a field angle parallel to the easy axis; (b) Calculated hysteresis curve versus field angle  $\alpha$  [30].

For a particle with a uniaxial anisotropy with anisotropy  $K_e$  and saturation magnetization  $M_s$  the total anisotropy and magnetostatic energy is given by [36]:

$$U = U_a + U_H = K_e \sin^2(\theta) - HM_s \cos(\alpha - \theta) \quad (1.15)$$

Where  $\alpha$  is the angle between the easy axis and the field and  $\theta$  is the angle the magnetic dipole moment vector makes with the easy axis. The  $E(\theta)$  curve contains one or two minima whose  $\theta$  can be calculated from setting  $\frac{\partial U}{\partial \theta} = 0$ ,  $\frac{\partial^2 U}{\partial \theta^2} > 0$  (see Fig. 1.13a). The  $\theta(H)$  can be used to calculate the hysteresis curve along the field direction (see Fig. 1.13b). The two minima in the  $E(\theta)$  curves (Fig. 1.13a) are related to the ground and meta-stable states of the hysteresis curves (Fig. 1.13b). The energy barrier between both states will determine the time dependence of the magnetic moment of the particle and is thus related to the magnetic viscosity.

### ***1.3.6.2 Incoherent Rotation***

The critical field for coherent rotation is high, in particular for particles that have a large anisotropy energy. Above  $r_c$  it is more likely that the magnetic reversal is no longer coherent. Various different modes of incoherent reversal mechanisms have been discussed in literature including domain wall motion [30], curling, buckling, fanning, and domino effect (wall perpendicular to magnetic moment) [48]. Fig. 1.14a below shows the different incoherent reversal mode except for domain wall motion and Fig. 1.14b shows the angular dependence of the nucleation field for the Stoner Wohlfarth coherent rotation and the curling incoherent rotation mode.

For incoherent rotation the reversal is dominated by nucleation at the surface of the particle. Nucleation gives rise to Kondorsky type behavior [49]. From the angular variation of the coercive force of Barium Ferrite it was concluded that the reversal is mainly affected by nucleation at small angles of the field to the easy axis and that coherent rotation determines the hysteresis for particles oriented at large angles to the field [50].

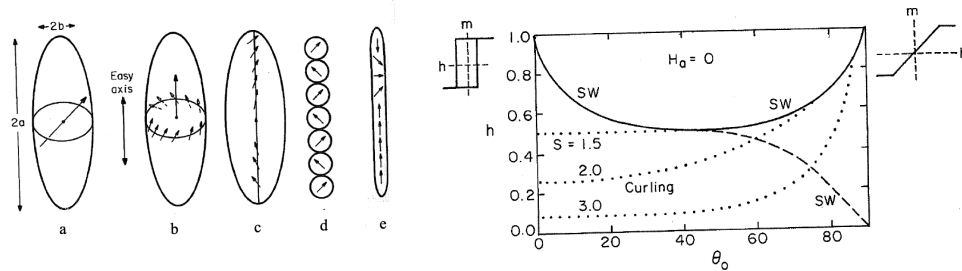


**Fig. 1.14:** Different reversal modes (a) coherent rotation; (b) curling; (c) buckling; (d) fanning; (e) domino effect; Field angle dependence of switching field for coherent rotation (SW) and curling for different aspect ratio particles  $S = b/b_0$  [51].

## 1.4 Magnet Manufacturing Techniques

A permanent magnet (PM) can produce and maintain a magnetic field even in the presence of an opposing magnetic field. In comparison, an electromagnet does not produce a magnetic field on its own. It relies on electric currents to generate the magnetic field. Obviously, energy conversion systems powered by PM's will use less energy than those using electromagnet [52].

There are several processes for making permanent magnets. The conventional permanent magnets are mainly produced by sintering.

### 1.4.1 Sintered Magnet

In this process, a suitable composition is pulverized into fine powder, compacted and heated to cause densification via "liquid phase sintering". Therefore, these magnets are most often called sintered magnets, that have a fill fraction close to 100%. Conventional magnets are mainly produced by sintering, and hence limited in complexity of their shapes and also several mechanical processing steps of manufacturing [53].

### 1.4.2 Bonded Magnet

Due to procedural advantages of plastic technologies, polymer bonded hard magnets enable the manufacturing of complex shapes and features by design flexibility regarding shape and magnetizing structure. The basic form bonded magnets consist of two

components; a hard-magnetic powder and a non-magnetic polymer matrix or rubber binder. The powder may be hard Ferrite, NdFeB, SmCo, AlNiCo, or mixtures of two or more magnetic powders known as hybrids [53]. In general, bonded magnets have a high degree of net-shape formability but a lower energy product [54, 55] as part of the space is occupied by the non-magnetic polymer. Recently, bonded permanent magnets have experienced accelerated industrial applications due to their advantages such as intricate shapes, low weight and cost, minimal or no secondary processing operations, superior mechanical properties and corrosion resistance, etc [53].

Bonded magnets come in rigid or flexible form and typically are manufactured by one of four methods which are calendering, injection molding, extrusion, and compression bonding. Each process and final product benefits from certain characteristics of the raw material magnetic powder such that not all materials are suitable for all products. Ferrite, for example, is too fine powder to use effectively in a compression bonded magnet. Final product characteristics are a function of both the magnet powder and of the binder. Another exciting novel processing technology that has the potential to revolutionize the production of bonded magnets is **3D printing or additive manufacturing (AM)**. 3D printing, is a trending technology for rapid prototyping and fabrication of net-shaped complex components which is being significantly studied for application in the manufacturing of permanent magnets and other magnetic materials [56-61].

#### *1.4.2.1 Additive Manufacturing (AM) for Bonded Magnet Fabrication*

AM is a fast-emerging manufacturing technique that has promise for the manufacturing of bonded magnets [46]. AM is also known as 3D printing, fabricates objects from a three-dimensional (3D), computer-aided design (CAD) model by stacking material in a layer-by-layer arrangement. It's a layer-based manufacturing method, allows to fabricate complex geometries within a short time compared to conventional subtractive manufacturing methods, so it is also known as rapid prototyping [61-63]. The reduction in design limitations shortens the design and manufacturing cycle whilst speeds up the development process that leadsto high-efficiency products, especially for mass-customized items [63, 64]. AM is also cost- effective as it minimizes additional

expenses such as those associated with tooling or molds making it an attractive manufacturing method for customized products, manufacturing on demand, or low volume production products. The higher degree of automation of AM can reduce human error and increase product accuracy. After the invention of the first AM methods, laser-based and photochemical stereolithography (SLA), various other approaches based on layer manufacturing were developed, for instance, selective laser sintering (SLS), powder bed and inkjet head 3D printing (3DP), etc. [63]. Among the several AM methods, one of the most widespread [63], is a fused deposition technique also known as Fused Deposition Modelling (FDM) [65], Fused Filament Fabrication (FFF) [66] or Material Extrusion Additive Manufacturing (MEAM) [67]. The FDM/FFF was first developed by S. Scott Crump, co-founder of Stratasys, in 1988 [68]. The reasons for FDM’s popularity compared to other AM methods include the ease of use and the fact that no extra equipment is required (e.g., mold, oven, or tools), leading to low costs of machines and processes [63]. Typically, raw materials for FFF are thermoplastics in the form of solid feedstock, which are of low toxicity and are easy and safe to handle during processing [69, 70]. Besides, the nature of thermoplastics, which can be heated and reshaped, it allows the products to be recyclable and creates little waste material compared to subtractive manufacturing methods [63].

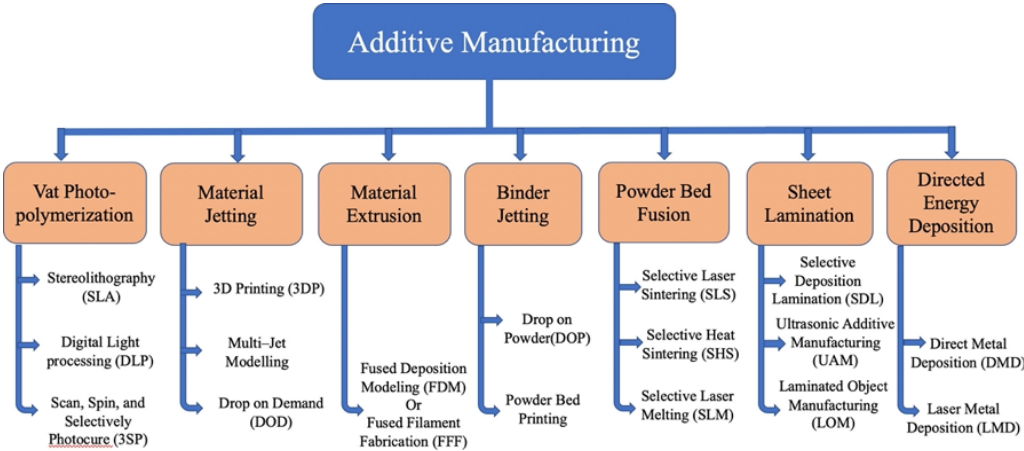


**Fig. 1.15:** Types of additive manufacturing processes and technologies [71, 72].

FFF uses a continuous filament of a thermoplastic material as a base material. A spool of filament is first loaded on to the printer. Once the nozzle has reached the desired

temperature, the filament is fed to the extrusion head and into the nozzle, where it melts. The molten material is forced out of the extruder's nozzle and is deposited first onto a 3D-printing platform, which can be heated for extra adhesion. A layer height of 200  $\mu\text{m}$  is the most commonly used, but the height can vary from 50 to 400  $\mu\text{m}$ . By mixing magnetic particles with a thermoplastic matrix material, FFF can also be used to print polymer-bonded hard or soft magnets [55, 70]. Small layer height produces smoother magnets with higher resolution and captures curved geometries more accurately. FFF has been used to print several hybrid bonded magnets, including NdFeB polymer magnets, SmCo polymer magnets, Sr-Ferrite polymer magnets, and Ba-Ferrite polymer magnets [73].

This FDM/FFF 3D printing technique has the potential to revolutionize the production of bonded magnets [62]. It's a trending technology for rapid prototyping and fabrication of net-shaped complex components which is being significantly studied for application in the manufacturing of isotropic and anisotropic permanent bonded magnets [56-61]. A major advantage of isotropic magnet is that no aligning field is required during the forming process, simplifying the fabrication process. However, anisotropic magnets are much stronger and thus can lift more or provide a larger magnetic flux density than isotropic magnets. They also have a higher energy product so are much less susceptible for demagnetizing fields and have even good performance in a small form factor. For fabricating magnetic components with the 3D printing process, an efficient magnetic filament has to be (a) magnetically strong (b) flexible enough for printing and (c) preferably light weight. The main difficulty in the development of the magnetic filament is to find the right proportions to mix. To achieve a magnetic behavior that competes at the level of conventional permanent magnets, the loading level of magnetic particles and the qualitative and quantitative dispersion of powder in the host polymer is crucial [56]. Typically, the more the magnetic powder is added to the plastic pellets, the more the magnetization increases. However, for large packing fraction, the filament gets more brittle though. In addition to packing fraction, the mechanical properties also depend on the shape of the particles or fibers included in the composite. Hence, it is crucial to find a good balance between magnetic moment, density and flexibility of the composite.

## 1.5 Organization of the Thesis

This thesis is organized in the following structure:

Chapter 1, provides a general introduction of magnetic materials, different magnetic properties, magnetic reversal mechanism and additionally magnet manufacturing techniques.

In chapter 2, the concept of Magnetic Field Assisted Additive Manufacturing (MFAAM) is introduced and a detailed background literature study of the magnetic polymer composite AM technique is presented. The challenges associated with the existing manufacturing techniques towards scaling up of the permanent bonded magnet manufacturing. Research questions are presented, and the scope of this dissertation is outlined.

In chapter 3, the major manufacturing and characterization tools and techniques used in this research are introduced. The instruments include imaging tools, optical characterization tools, magnetic characterization tools, thermal analysis tools and filament manufacturing and magnetic field assisted additive manufacturing (MFAAM) techniques. In addition, the “*structural, morphological and thermal analysis*” measurement results of the composite filaments are presented and discussed.

In chapter 4, the experimental study of the “*Biaxial time dependent measurement*” or vector magnetic viscosity of the manufactured magnetic polymer composite filaments is presented. Also included is a discussion about the time dependent measurement of pristine and field-annealed magnetic polymer composite filaments.

In chapter 5, the results of the experimental study of the “*Temperature dependent measurement*” of the manufactured magnetic polymer composite filaments are presented and discussed. Included are a simple model describing the rotation of the ferrimagnetic particles in a softened or molten plastic matrix exposed to a magnetic field. Results to simulate the alignment of the particles above and below the melting point during the 3D printing MFAAM process are presented and discussed.

In chapter 6, the experimental study of the “*Torque or angular dependent measurement*” of the manufactured pristine as well as field annealed magnetic polymer composite filaments are presented and discussed.

In chapter 7, the conclusion of the dissertation research are summarized and suggestions for future potential research are proposed.

## REFERENCES

- [1] B. D. Culity and C.D. Graham, "Introduction to Magnetic Materials", second edition, chapter 14: hard magnetic materials, pp. 477–504, 2008. <https://doi.org/10.1002/9780470386323.ch14>
- [2] K. J. Overshott, "Soft magnetic materials," Phys. Technol., vol. 6, no. 6, pp. 280–281, 1975.
- [3] Maximum energy product. Retrieved January 31, 2023, [Online]. Available: <https://www.reed-sensor.com/glossary/maximum-energy-product/>
- [4] Johann Fischbacher, Alexander Kovacs, Markus Gusenbauer, Harald Oezelt, Lukas Exl, Simon Bance, and Thomas Schrefl, "Micromagnetics of rare-earth efficient permanent magnets", J. Phys. D: Appl. Phys. 51 (2018) 193002, (17pp).
- [5] Hard and Soft Magnets. (2021, June 10). Retrieved January 31, 2023, [Online]. Available: <https://chem.libretexts.org/@go/page/189204>
- [6] G. Chatzipirpiridis et al., "3D Printing of Thermoplastic-Bonded Soft- and Hard-Magnetic Composites: Magnetically Tuneable Architectures and Functional Devices," Adv. Intell. Syst., vol. 1, no. 6, p. 1900069, 2019.
- [7] Magnetic properties of AlNiCo magnets. Retrieved December 22, 2022, [Online]. Available: <https://www.magnetexpert.com/magnetic-properties-of-alnico-magnets-i698>
- [8] Permanent Magnets. Retrieved December 22, 2022, [Online]. Available: <https://idealmagnetsolutions.com/knowledge-base/samarium-cobalt-vs-neodymium-magnets/>
- [9] M.S. Thesis of Camila Beldeque, "Development of Strontium Ferrite/Polyamide 12 Composites for Magnetic Devices Using Additive Manufacturing", Texas State University, May (2021).
- [10] Daily metal price. Retrieved December 22, 2022, [Online]. Available: <https://www.dailymetalprice.com/metalpricecharts.php?c=co&u=lb&d=0>
- [11] Current strategic metal price. Retrieved December 22, 2022, [Online]. Available: <https://strategicmetalsinvest.com/current-strategic-metals-prices/>

- [12] Chemical elements by market price. Retrieved December 22, 2022, [Online]. Available: [http://www.leonland.de/elements\\_by\\_price/en/list](http://www.leonland.de/elements_by_price/en/list)
- [13] Coercivity of NdFeB-based sintered permanent magnets: experimental and numerical approaches, [Online]. Available: <http://www.theses.fr/2019GREAY071>.
- [14] Presentation of Physics Colloquium at Texas State University by Dr. Ikenna Nlebedim, Ames Laboratory, USA.
- [15] L. H. Lewis and F. Jiménez-Villacorta, “Perspectives on permanent magnetic materials for energy conversion and power generation,” *Metall. Mater. Trans. A Phys. Metall. Mater. Sci.*, vol. 44, no. SUPPL. 1, 2013.
- [16] P. K. Deheri, V. Swaminathan, S. D. Bhame, Z. Liu, and R. V. Ramanujan, “Sol-gel based chemical synthesis of Nd<sub>2</sub>Fe<sub>14</sub>B hard magnetic nanoparticles,” *Chem. Mater.*, vol. 22, no. 24, pp. 6509–6517, 2010.
- [17] V. V Jadhav, R. S. Mane, and P. V Shinde, *Bismuth- Ferrite-Based Electrochemical Supercapacitors*. 2020.
- [18] M. F. de Campos and D. Rodrigues, “High technology applications of barium and strontium ferrite magnets”, *Mater. Sci. Forum*, vol. 881 MSF, pp. 134–139, 2017.
- [19] T. Sembiring, Y. B. Zebua, and Muljadi, “Analysis of crystal structure and magnetic character strontium ferrite (SrFe<sub>12</sub>O<sub>19</sub>) powder made of stoichiometry and non-stoichiometry compositions,” *AIP Conf. Proc.*, vol. 2221, pp. 1–6, 2020.
- [20] A. Goldman: *Modern Ferrite Technology*, Second Edition, 2006.
- [21] Magnetic and electronic properties of strontium hexaferrite SrFe<sub>12</sub>O<sub>19</sub> from first-principles calculations, C M Fang, F Kools, R Metselaar, G de With, and R A de Groot, *J. Phys.: Condens. Matter* 15 (2003) 6229–6237
- [22] J. J. Went, G. W. Rathenau, E. W. Gorter, and G. W. Van Oosterhout, “Hexagonal iron-oxide compounds as permanent-magnet materials,” *Phys. Rev.*, vol. 86, no. 3, pp. 424–425, 1952.
- [23] Z. F. Zi, Y. P. Sun, X. B. Zhu, Z. R. Yang, J. M. Dai, and W. H. Song, “Structural and magnetic properties of SrFe<sub>12</sub>O<sub>19</sub> hexaferrite synthesized by a modified chemical co-precipitation method,” *J. Magn. Magn. Mater.*, vol. 320, no. 21, pp. 2746–2751, 2008.

- [24] Coey, J. (2010). Ferromagnetism and exchange. In *Magnetism and Magnetic Materials* (pp. 128-194). Cambridge: Cambridge University Press. doi:10.1017/CBO9780511845000.006
- [25] P. E. Kazin, L. A. Trusov, D. D. Zaitsev, and Y. D. Tret'Yakov, "Glass crystallization synthesis of ultrafine hexagonal M-type ferrites: Particle morphology and magnetic characteristics," *Russ. J. Inorg. Chem.*, vol. 54, no. 14, pp. 2081–2090, 2009.
- [26] V. Bilovol and R. Martínez-García, "Phase transformation of strontium hexagonal ferrite," *J. Phys. Chem. Solids*, vol. 86, pp. 131–137, 2015.
- [27] C. Granados-Miralles, M. Saura-Múzquiz, E. D. Bøjesen, K. M. Ø. Jensen, H. L. Andersen, and M. Christensen, "Unraveling structural and magnetic information during growth of nanocrystalline SrFe<sub>12</sub>O<sub>19</sub>," *J. Mater. Chem. C*, vol. 4, no. 46, pp. 10903–10913, 2016.
- [28] S. V. Ketov, Y. D. Yagodkin, and V. P. Menushenkov, "Structure and magnetic properties of strontium ferrite anisotropic powder with nanocrystalline structure," *J. Alloys Compd.*, vol. 509, no. 3, pp. 1065–1068, 2011.
- [29] L. K. Lagorce and M. G. Allen, "Magnetic and mechanical properties of strontium ferrite," *Journal of Microelectromechanical systems*, vol. 6, no. 4, 1997.
- [30] B. D. Culity and C.D. Graham, "Introduction to Magnetic Materials", second edition, chapter 7: Magnetic Anisotropy, pp. 197-239, 2008. <https://doi.org/10.1002/9780470386323.ch7>
- [31] Robert C. Pullar, Hexagonal ferrites: A review of the synthesis, properties and applications of hexaferrite ceramics, *Progress in materials Science* 57 (2012) 1191-1334
- [32] M. Jean, V. Nachbaur, J. Bran, J.M. Le Breton, Synthesis and characterization of SrFe<sub>12</sub>O<sub>19</sub> powder obtained by hydrothermal process, *J alloys Compd* 496 (2010) 306-312.
- [33] B. S. Zlatkov, A study of magneto-crystalline alignment in sintered barium hexaferrite fabricated by powder injection molding, *J. Magn. Magn. Mat* 321 (2009) 330-335.

- [34] F-Z Mou, J-G Guan, Z-G Sun, X-A Fan, G-X Tong, In situ generated dense shell-engaged Ostwald ripening: A facile controlled-preparation for BaFe<sub>12</sub>O<sub>19</sub> hierarchical hollow fiber arrays, *J. Sol. State Chem* 183 (2010) 736-743.
- [35] Robert C. Pullar, Hexagonal ferrites: A review of the synthesis, properties and applications of hexaferrite ceramics, *Progress in Mat. Sc.* 57 (2012) 1191-1334.
- [36] B. Moskowitz, "Hitchhiker's Guide to Magnetism," 2002.
- [37] B. C. Dodrill, J. R. Lindemuth, and J. K. Krause, "Magnetic Anisotropy: Measurements with a Vector Vibrating Sample Magnetometer Theory: Anisotropy Constants from Vector Magnetization Data," pp. 1–7.
- [38] G. W. Fernando, "Chapter 4 Magnetic Anisotropy in Transition Metal Systems," *Handb. Met. Phys.*, vol. 4, pp. 89–110, 2008.
- [39] B. T. Shirk, W.R. Buessem, "Temperature Dependence of Ms and K1 of BaFe<sub>12</sub>O<sub>19</sub> and SrFe<sub>12</sub>O<sub>19</sub> Single Crystals", *J. Appl. Phys.* 40, 1294-6 (1969).
- [40] Demagnetizing Field. Retrieved January 31, 2023, [Online]. Available: [https://en.wikipedia.org/wiki/Demagnetizing\\_field](https://en.wikipedia.org/wiki/Demagnetizing_field)
- [41] Hysteresis in Magnetism, Giorgio Bertotti, Chapter 10- Magnetization Curves, Academic Press, pages 297-346, 1998.
- [42] G. M. Yang et al., "Loading effects of self-biased magnetic films on patch antennas with substrate/superstrate sandwich structure," *IET Microwaves, Antennas Propag.*, vol. 4, no. 9, pp. 1172–1181, 2010.
- [43] P. Bradford, "The aggregation of iron oxide nanoparticles in magnetic fields," doctoral dissertation, University of Birmingham, April 2010.
- [44] O. Perales-Pérez and Y. Cedeño-Mattei, "Optimizing Processing Conditions to Produce Cobalt Ferrite Nanoparticles of Desired Size and Magnetic Properties," *Magn. Spinels - Synth. Prop. Appl.*, 201
- [45] J. Mohapatra and J. P. Liu, *Rare-Earth-Free Permanent Magnets: The Past and Future*, 1st ed., vol. 27. Elsevier B.V., 2018.
- [46] J. S. Lee, J. M. Cha, H. Y. Yoon, J. K. Lee, and Y. K. Kim, "Magnetic multi-granule nanoclusters: A model system that exhibits universal size effect of magnetic coercivity," *Sci. Rep.*, vol. 5, no. November 2015.

- [47] E.C. Stoner, and E.P. Wohlfarth, "A mechanism of magnetic hysteresis in heterogeneous alloys", *Philosophical Transactions of the Royal Society A: Physical, Mathematical and Engineering Sciences*, 240 (826), 599,1948.
- [48] M. S. thesis of Elco Sterringa, University of Twente, Netherlands.
- [49] Marcos Flavio de Campos, Jose Adilson de Castro, An overview on nucleation theories and models, *J. Rare Earths* 37 (2019) 1015-1022
- [50] D.V. Ratnam, W.R. Buesem, Angular Variation of Coercive Force in Barium Ferrite, *J. Appl. Phys.* 43 (1972) 1291.
- [51] P. Bradford, "The aggregation of iron oxide nanoparticles in magnetic fields," doctoral dissertation, University of Birmingham, April 2010.
- [52] J. Cui et al., "Manufacturing Processes for Permanent Magnets: Part II—Bonding and Emerging Methods," *Jom*, vol. 74, no. 6, pp. 2492–2506, 2022.
- [53] Tech brief: Bonded Magnet Materials and Processing Options, *Magnetic Applications*, Retrieved December 22, 2022, [Online]. Available: <https://www.mpcomagnetics.com/blog/bonded-magnet-materials-and-processing-options/>.
- [54] L. Li et al., "Big Area Additive Manufacturing of High Performance Bonded NdFeB Magnets," *Sci. Rep.*, vol. 6, no. October, pp. 1–7, 2016.
- [55] J. Ormerod and S. Constantinides, "Bonded permanent magnets: Current status and future opportunities (invited)," *J. Appl. Phys.*, vol. 81, no. 8 PART 2B, pp. 4818–4820, 1997.
- [56] C. Huber, S. Cano, I. Teliban, S. Schuschnigg, M. Groenefeld, D. Suess, Polymer-bonded anisotropic SrFe<sub>12</sub>O<sub>19</sub> filaments for fused filament fabrication, *J. Appl. Phys.* 127 (2020), 063904.
- [57] C. Huber, C. Abert, F. Bruckner, M. Groenefeld, O. Muthsam, S. Schuschnigg, K. Sirak, R. Thanhoffer, I. Teliban, C. Vogler, R. Windl, and D. Suess, 3D print of polymer bonded rare-earth magnets, and 3D magnetic field scanning with an end-user 3D printer, *Appl. Phys. Lett.* 109 (2016), 162401.

- [58] L. Li, A. Tirado, B.S. Conner, M. Chi, A.M. Elliott, O. Rios, H. Zhou, M. P. Paranthaman, A novel method combining additive manufacturing and alloy infiltration for NdFeB bonded magnet fabrication, *J. Magn. Magn. Mater.* 438 (2017) 163–16.
- [59] L. Li, A. Tirado, I.C. Nlebedim, O. Rios, B. Post, V. Kunc, R.R. Lowden, E. LaraCurzio, R. Fredette, J. Ormerod, T.A. Lograsso, M.P. Paranthaman, Big area additive manufacturing of high performance bonded NdFeB magnets, *Sci. Rep.* 6 (2016) 36212.
- [60] E.A. P´erigo, J. Jacimovic, F. Garca Ferr’e, L.M. Scherf, Additive manufacturing of magnetic materials, *Addit. Manuf.* 30 (2019), 100870.
- [61] A. Sarkar, M.A. Somashekara, M. P. Paranthaman, M. Kramer, C. Haase, I. C. Nlebedim, Functionalizing magnet additive manufacturing with in-situ magnetic field source, *Addit. Manuf.* 34 (2020), 101289.
- [62] H. A. Khazdozian, J. S. Manzano, K. Gandha, I. I. Slowing, and I. C. Nlebedim, “Recycled Sm-Co bonded magnet filaments for 3D printing of magnets,” *AIP Adv.*, vol. 8, no. 5, 2018.
- [63] N. Krajangsawadi, L. G. Blok, I. Hamerton, M. L. Longana, B. K. S. Woods, and D. S. Ivanov, “Fused deposition modelling of fibre reinforced polymer composites: A parametric review,” *J. Compos. Sci.*, vol. 5, no. 1, 2021.
- [64] W. Zhang et al., “Interfacial bonding strength of short carbon fiber/acrylonitrile-butadiene-styrene composites fabricated by fused deposition modeling,” *Compos. Part B Eng.*, vol. 137, no. October 2017, pp. 51–59, 2018.
- [65] X. Wang, M. Jiang, Z. Zhou, J. Gou, and D. Hui, “3D printing of polymer matrix composites: A review and prospective,” *Compos. Part B Eng.*, vol. 110, pp. 442–458, 2017.
- [66] J.M. Gardner, G. Sauti, J.-W. Kim, R.J. Cano, R.A. Wincheski, C.J. Stelter, B.W. Grimsley, D.C. Working, E.J. Siochi, “Additive Manufacturing of Multifunctional Components using High Density Carbon Nanotube Yarn Filaments”; NASA Langley Research Center: Hampton, VA, USA, 2016.

- [67] M. Ivey, G. W. Melenka, J. P. Carey, and C. Ayranci, “Characterizing short-fiber-reinforced composites produced using additive manufacturing,” *Adv. Manuf. Polym. Compos. Sci.*, vol. 3, no. 3, pp. 81–91, 2017.
- [68] Inventor of FDM 3D Printing and Co-Founder of Stratasys, Scott Crump, inducted in to the TCT Hall of Fame. Retrieved January 31, 2023, [Online]. Available: <https://investors.stratasys.com/news-events/press-releases/detail/418/inventor-of-fdm-3d-printing-and-co-founder-of-stratasys#:~:text=Scott%20Crump%20invented%20the%20technology,in%202012>.
- [69] P. Geng et al., “Effects of extrusion speed and printing speed on the 3D printing stability of extruded PEEK filament,” *J. Manuf. Process.*, vol. 37, no. November 2018, pp. 266–273, 2019.
- [70] W. Wu, P. Geng, G. Li, D. Zhao, H. Zhang, and J. Zhao, “Influence of layer thickness and raster angle on the mechanical properties of 3D-printed PEEK and a comparative mechanical study between PEEK and ABS,” *Materials (Basel)*, vol. 8, no. 9, pp. 5834–5846, 2015.
- [71] 3D Printing / Additive Manufacturing Using Polymers - Complete Guide. Retrieved December 22, 2022, [Online]. Available: <https://omnexus.specialchem.com/selection-guide/3d-printing-and-additive-manufacturing-polymers-and-processes>
- [72] I. Peko, N. Gjeldum, and B. Bilić, “Application of AHP, fuzzy AHP and PROMETHEE method in solving additive manufacturing process selection problem,” *Teh. Vjesn.*, vol. 25, no. 2, pp. 453–461, 2018.
- [73] H. Wang, T. N. Lamichhane, and M. P. Paranthaman, “Review of additive manufacturing of permanent magnets for electrical machines: A prospective on wind turbine,” *Mater. Today Phys.*, vol. 24, p. 100675, 2022.

## 2. LITERATURE REVIEW AND MOTIVATION OF THE RESEARCH

*“It doesn't matter how beautiful your theory is, it doesn't matter how smart you are. If it doesn't agree with experiment, it's wrong.”*

- Richard Feynman

### 2.1 Introduction

3D printed additive manufactured magnetic materials have attracted tremendous attention from both the research and industrial communities. Recently, there is increased interest for magnetic materials suitable for printable electronics, including new ferro- and ferri-magnetic filaments and inks that can be used to print magnets for transformers, motors, and inductors [1-6]. AM is a trending technology for rapid prototyping and fabrication of net-shaped complex components which is being significantly studied for application in the manufacturing of isotropic and anisotropic permanent bonded magnets. Anisotropic bonded magnet must apply orientation field during the printing process which totally unlike the isotropic bonded magnet. The majority of magnetic moment will be aligned in the specific direction and thus exhibit maximum output. Hence, the anisotropic magnets are much stronger and provide a larger magnetic flux density than the isotropic one.

The application of external magnetic field during the 3D printing process in order to induce texture to realize magnetic anisotropy is termed as **Magnetic Field Assisted Additive Manufacturing (MFAAM)**. The application of a local field during the deposition of the material allows one to vary the magnetic properties as a function of the position on a mesoscopic scale realizing 3D magnetic structures with complex well-defined easy axis and/or magnetic dipole distribution functions that have new and enhanced magnetic properties. MFAAM process allows field induced anisotropy during the extrusion process to realize a magnetic anisotropy and increasing the material's energy product and remanence, thus yielding stronger permanent magnets.

In this chapter, we briefly discuss about the work done in AM magnetic materials and the alignment of magnetic particles during the printing process by various research groups and present challenges and also objectives for our research.

## 2.2 Broader Impact and Applications of MFAAM

Applications of MFAAM materials and processes include

(1) 3D printed Halbach cylinders to replace superconducting magnets in portable MRI equipment. Recent published Halbach cylinder designs based on discrete magnets have a limited field homogeneity and it is expected that MFAAM Halbach cylinders will result in more homogeneous fields and thus better MRI imaging. In a study, Kallaste et al., 2012 [7] investigated how to replace fully dense magnets with Halbach array made of strontium ferrite composites for wind generators. This set up maintains the magnetic energy required by the system without increasing the weight. If only strontium ferrite were used, the amount of material needed to generate an energy density compared to that NdFeB would be too large. Although the fabrication of Halbach device is not detailed, FFF can be used to print it by adding an electromagnet with which a printing field can be applied and the easy axis of the magnetic particles in the molten composite can be manipulated into the desired directions [7].

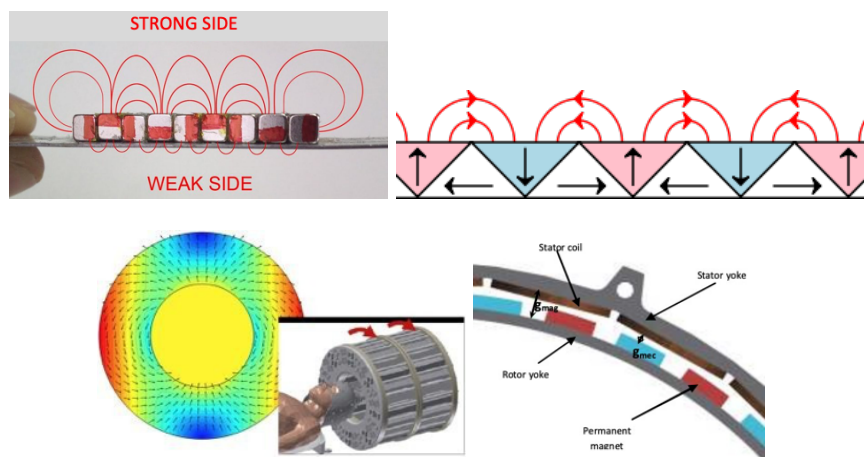


**Fig. 2.1:** Identified applications for MFAAM deposition: Superior field homogeneity of 3D printed Halbach cylinders for application in portable MRI equipment compared to currently considered cylinders using discrete magnets [10].

(2) soft magnetic flux-guides for 3D printable magnetic transformers, magnetic shielding and wireless charging applications. Preliminary results on soft magnetic composite showed that the susceptibility of soft magnets can be increased with a factor 2 by printing in a magnetic field [8].

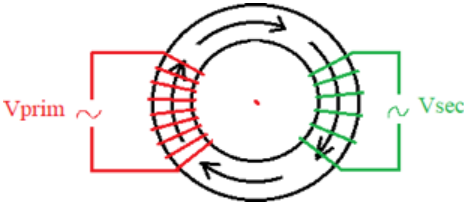


**Fig. 2.2:** Identified applications for MFAAM deposition: flux guides for printable electronics and waveguides [8].

(3) magnetic nanocomposites with intelligence to be applied in novel waveguides, actuators, and robots for drug delivery. A permanent magnetic dipole distribution function encoded in a silicone-based nanocomposite during MFAAM deposition will allow one to locally deform the material with an external magnetic field providing mobility to these structures; as remotely controlled micro-robots they can roll, crawl, and walk, and even can move small objects around [9].

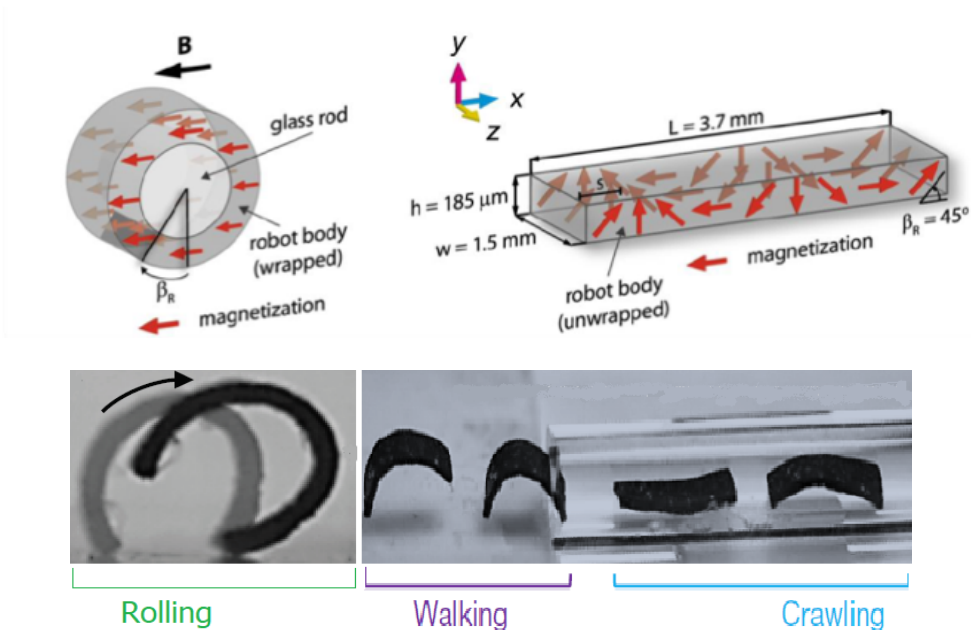


**Fig. 2.3:** Identified applications for MFAAM deposition: Magnetic robots for biomedical applications [9, 11].

## 1.4 Literature Review

Initial work published on additive manufacturing (AM) involving magnetic materials was done by three different approaches, i.e. Inkjet printing [1], Fused Deposition Modeling (FDM) [3], and Stereo Lithography (SLA) [4]. Since permanent magnets are frequently composed of rare earth elements, most of which are defined as critical materials, AM could potentially offer an effective way to reduce the usage of critical materials during bonded magnets fabrication.

Huber et al. [12] used an end-user 3D printer to fabricate isotropic NdFeB bonded magnets. The density of the printed parts was  $3.57 \text{ g/cm}^3$ , which is lower than that of the injection molded magnets ( $4.35 \text{ g/cm}^3$ ), leading to reduced remanence.

Ling et al. [1] investigated the room temperature magnetization of Big Area Additive Manufacturing (BAAM) and injection molded (IM) NdFeB/Nylon-12 bonded magnets. BAAM is a large-scale additive manufacturing or 3D printing technology which has applications in automotive, aerospace and consumer market sectors. The results are summarized in Fig. 2.4.

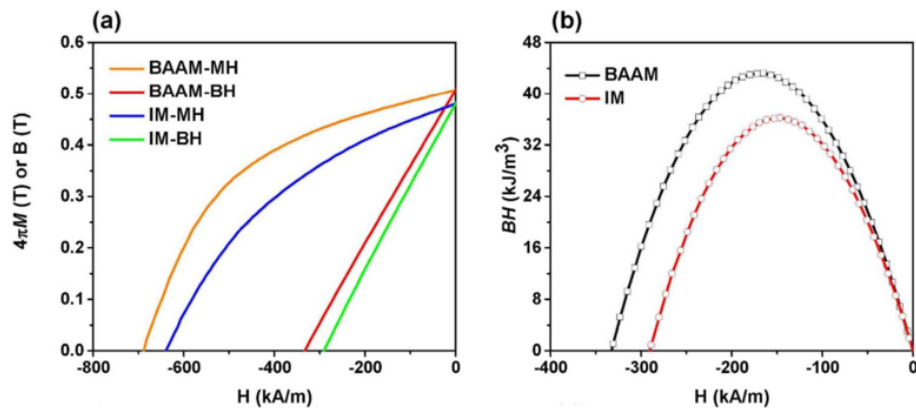


**Fig. 2.4:** Magnetic properties of Big Area Additive Manufacturing (BAAM) and Injection Molding (IM) fabricated NdFeB bonded magnets. (a) room temperature de-magnetization curves (MH and BH) for both BAAM and IM magnets; (b) room temperature maximum energy product for BAAM and IM magnets [1].

The magnets were produced with isotropic Nd-Fe-B powder mixed with 35% volume fraction of Nylon-12 binder. Fig. 2.4a shows the de-magnetization curves for

BAAM and IM magnets. The density of the BAAM and IM magnets are  $4.8 \text{ g/cm}^3$  and  $4.9 \text{ g/cm}^3$  respectively and both magnets retain the hard-magnetic behavior of the original pellets. Moreover, the BAAM magnet shows a slightly better hysteresis loop shape in the second quadrant of the demagnetization plot, and higher  $H_c$  and  $B_r$  compared to the injection molded magnets. Fig. 2.4b presents the maximum energy product  $(BH)$  vs.  $H$  for the BAAM and injection molded Nd-Fe-B magnets, whereby  $(BH)_{\max}$  was determined as the maximum point in the plot.  $(BH)_{\max} = 43.49 \text{ kJ/m}^3$  and  $36.17 \text{ kJ/m}^3$  are obtained for big area AM and IM magnets respectively. The energy product  $(BH)_{\max}$  quantifies the magnetostatic energy a permanent magnet material can store and therefore characterizes how strong the magnet is. So, Li et al. show that the AM magnets can have a better  $(BH)_{\max}$  than the IM magnets. We expect that this might be due to flow induced anisotropy which is more consistent for AM and difficult to control for IM production processes.

Shen et al. [4] report the 3D printing of polymer-bonded magnets using highly concentrated suspensions of non-spherical intrinsic NdFeB magnetic particles. Using SLA printing, bonded magnets with a loading level as high as 65% by volume, or 93% by weight, were realized. The resulting magnet had a density of  $5.2 \text{ g/cm}^3$ , an intrinsic coercivity ( $H_{ci}$ ) of  $747.232 \text{ kA/m}$ , a remanence ( $B_r$ ) of  $0.588 \text{ T}$  and an energy product of  $57.77 \text{ kJ/m}^3$ , marking it the highest values reported for 3D printed polymer-bonded magnets.

FDM also has been used to print rare-earth free magnets [13]. Ho et al. created Sr-ferrite PM with a commercial FDM printer [14]. Palmero et al. created ferrite PMs using extruded strips or filaments [15]. Peng et al. used extrusion free-forming FDM to create Ba ferrite PMs [16]. Palmero et al. printed MnAlC particles with Acrylonitrile butadiene styrene (ABS) into magnets; however, they reported the magnetic properties of their extruded filaments rather than those of the printed magnet [17].

3D print of soft magnetic materials also have been studied. Bollig et al. [18, 19] investigated the magnetic properties of Fe/Polylactic acid composite to 3D print the core of a transformer and explore the effect of infill fraction and pattern on the performance of the printed transformer core. Their results indicate a low susceptibility, not enabling enough flux coupling between the primary and secondary coil. As efficient transformer

cores are normally highly textured by rolling the material and inducing a well-defined anisotropy axis. Henderson et al. applied a magnetic field during the printing process and showed appreciable effects on the magnetic properties of soft magnetic Fe/PLA. They [8] explored the use of a magnetic field applied during the FDM printing process of Fe/PLA composite and were able to induce a texture and enhance the susceptibility of the soft magnetic polymer composite with a factor 2. In addition, they showed that printing in a magnetic field (MFAAM) can induce an anisotropy in the susceptibility. Susceptibility parallel and perpendicular to the print field appeared to differ by a factor 2.8. So, MFAAM was shown to also enhance the properties of soft-magnetic materials.

A magnetic field applied during the printing process has also shown noticeable effects on the magnetic properties of the hard-magnetic 3D printed composites [20-23], inducing a magnetic anisotropy and increasing the material's energy product and remanence, thus yielding stronger permanent magnets.

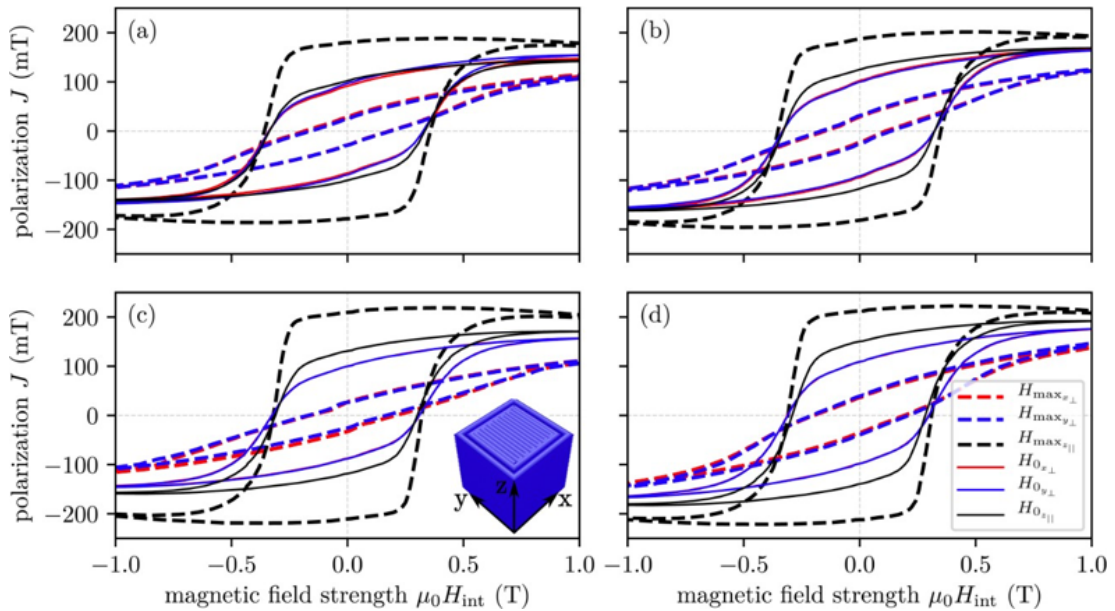


**Fig. 2.5:** Hysteresis measurements for isotropic (no external field  $H_0$ ) and anisotropic (maximum external field  $H_{max}$ ) printed magnets in all magnetization directions. Filling fraction: (a) 40 vol.%, (b) 45 vol.%, (c) 50 vol.%, and (d) 55 vol.% [21].

Huber et al. [21] 3D printed PA12 Strontium-Ferrite composites in a magnetic field of 0.5 Tesla to realize anisotropic permanent magnets. Cubic samples were printed without

an external field and under the effect of an external field (MFAAM) to obtain magnetically anisotropic samples. The remanence values for the latter were 40% higher than those of the samples printed in zero field, whereas the coercivity of the same specimens slightly decreased with print-field. Fig. 2.5 shows the hysteresis loop of these materials increasing in area and adopting a squared shape when they are under the effect of the external magnetic field. This squareness is also observed to improve with higher filler concentration.

Recently M. Suppan et al. [22] investigated in-situ alignment of the easy axis single-crystal magnetic particles inside a polymer matrix using fused filament fabrication (FFF). Explored magnetic composites are, (i) anisotropic strontium hexaferrite inside a PA6 matrix, fill grade: 49 vol.% and (ii) Samarium iron nitride inside a PA12 matrix, fill grade: 44 vol.%.

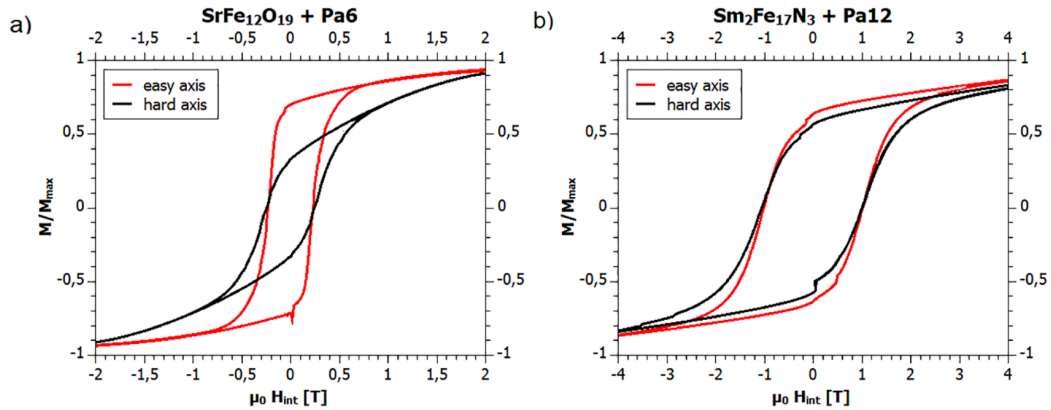


**Fig. 2.6:** Hard axis and easy axis hysteresis loops of the (a)  $\text{SrFe}_{12}\text{O}_{19}$  (Strontium hexaferrite) and (b)  $\text{Sm}_2\text{Fe}_{17}\text{N}_3$  3D printed samples. Here the easy axis loop denotes the direction that is parallel to the applied field during the printing process [22].

In the presence of the external alignment field of 1100 mT, the strontium hexaferrite particles inside the PA6 matrix can be well aligned with a ratio of remnant magnetization to saturation magnetization along the easy axis of 0.7. No significant alignment for samarium iron nitride could be achieved. The results show the feasibility to fabricate magnets with arbitrary and locally defined easy axis using FFF since the permanent magnets (or alternatively an electromagnet [20]) can be mounted on a rotatable platform. Sonnleitner et al. [23] successfully used FDM/FFF to create Sr-ferrite

and SmFeN magnets. And also applied external applied field and providing an external alignment field produces better results.

Palmero et al. [15] investigated the effect of a magnetic field while manufacturing a magnetic filament and measured the stray field of magnetic strips extruded in a transverse magnetic field with a Hall probe. They noticed that the magnetic properties of the produced filament were affected.

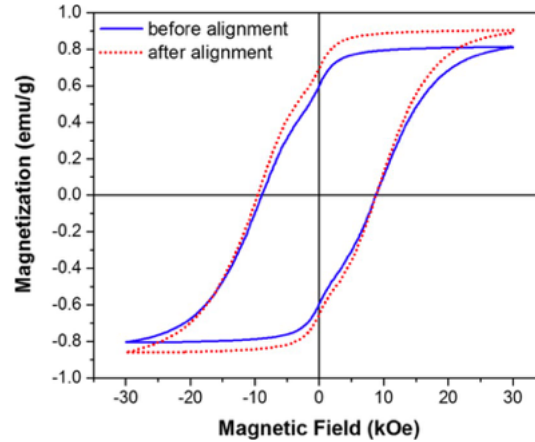


**Fig. 2.7:** Magnetic hysteresis of recycled Sm-Co powder in epoxy measured under applied magnetic field of 3 T at 400 K [24].

Khazdozian et al. [24] fabricated bonded magnetic filaments using extrusion of recycled Sm-Co powder and noticed that the recycled Sm-Co filament exhibit a different magnetic anisotropy than the raw material which they believe is due to the extrusion process. The magnetic hysteresis of the un-extruded Sm-Co powder was measured before and after applying a magnetic field of 3 T at 400 K (Fig. 2.7). Some particle rotation likely occurred, improving the remanence and coercivity of the recycled Sm-Co powder.

It has also been shown by Sakar et al. [20] that incorporating an in-situ magnetic field source into a 3D printing process allows for an in-situ magnetic pre-alignment of particles in the molten magnetic composite. A non-axisymmetric electromagnet-type field source architecture was designed, modelled, constructed, installed on a fused filament commercial 3D printer, and tested (Fig. 2.8).

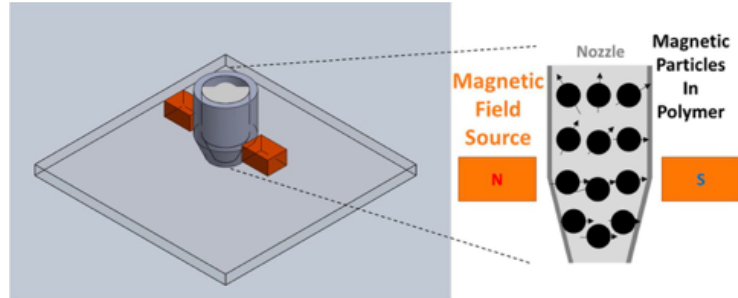


**Fig. 2.8:** Schematic of in-situ alignment mechanism for 3D printed magnetic materials [20].

The testing was performed by applying a magnetic field while printing composite anisotropic NdFeB + SmFeN powders bonded in Nylon-12 (65 vol.%) and recycled Sm-Co powder bonded in PLA (15 vol.%).

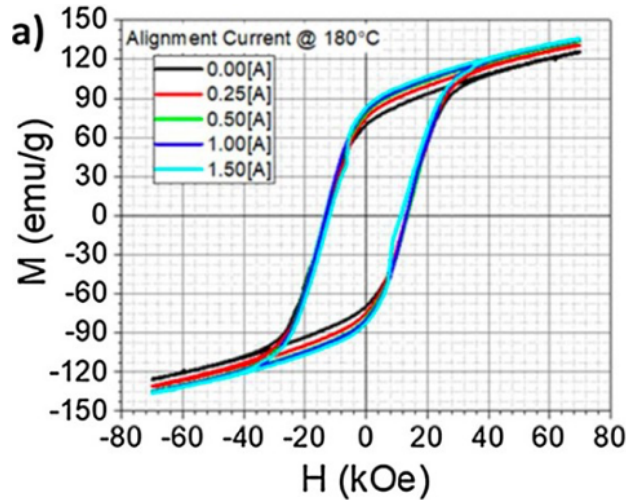


**Fig. 2.9:** Magnetic characterization of Nd-Fe-B + Sm-Fe-N/Nylon-12 65 vol.% sample printed at 180 °C nozzle temperature under varying alignment current [20].

Magnetic characterization indicated that the degree-of-alignment of the magnet powders increased both with alignment field strength (controlled by the electric current applied to the electromagnet) and the printing temperature. Both coercivity and remanence were found to be strongly dependent on the degree-of-alignment, except for printing performed below but near the Curie temperature of NdFeB (310 °C). At an applied field of 0.15 kOe, Sm-Co and hybrid NdFeB/SmFeN printed samples showed degrees-of-alignment of 83% and 65%, respectively. This work verified that integration

of magnetic field sources into 3D printing processes result in magnetic alignment of particles while ensuring that other advantages of 3D printing are retained.

Belduque et al. [25] also recently showed that good alignment can be obtained for material with a low packing fraction of strontium ferrite in PA12 matrix composite, at much lower print-fields. Anisotropic magnets with S-factors close to 1 were realized with fields well under a kOe [25].

## **1.5 Challenges and Objective of the Research**

### **2.4.1 Problem Statement**

In iterative product development, conventional magnet manufacturing methods with long lead times are a significant bottleneck for fast testing and validation. This holds true especially for the development of products that use magnets, where the fabrication of custom magnet shapes by e.g., sintering, hot-pressing, or injection molding is time and cost-intensive and requires special tooling [26]. Injection molding offers significant design freedom, but the technique cannot be used to form parts with a complex combination of materials. Sintered magnets require the use of pressing tools, which limit the complexity of the parts. Post processing machining is also challenging, as hard-magnetic materials are usually brittle, pyrophoric, and prone to cracking [27].

By exploiting the capabilities of 3D printing and rapid prototyping process, high-performance composite bonded magnets can be precisely patterned in arbitrary shapes and architectures. AM of magnetic components delivers the opportunity to shift to agile and test-driven development in early prototyping stages, minimizes the waste of critical materials, as well as new possibilities for complex designs [28]. Since permanent magnets are frequently composed of rare earth elements, most of which are defined as critical materials, AM could potentially offer an effective way to reduce the usage of critical materials during bonded magnets fabrication [1].

However, currently the only commercially available magnetic filament is magnetic Iron/PLA by Protopasta, which has been studied by several groups [29-31]. These investigations agree on that PLA is filled with 40 wt.% of Iron with a particles

size of around 40  $\mu\text{m}$  [31]. Mechanically, such material shows a brittle behavior, which highly complicates the 3D printing process. Note that this composite is soft magnetic, so its magnetic properties are limited and cannot be used to create permanent magnets. Application in transformers has shown to be limited through poor flux coupling when used to make a transformer core [18] although a factor 2 in flux coupling can be obtained when printing in a magnetic field [8].

Although 3D printing of hard magnetic objects is being explored by various research labs in the US and elsewhere, no commercial product is yet on the market. Hence, there is no commercially available filament to print permanent magnets. Hard magnetic materials being explored by others for FDM 3D printing include NdFeB and SmCo powder. Long-term supply and cost of critical Rare Earth Elements (REEs) like Sm and Nd and Dy are potential concerns for the magnet industry. Due to the large amount of REE in NdFeB (30%), it is currently one of the more expensive magnets. For the SmCo magnets, the Sm supply is not currently considered critical; however, cobalt is one of the more expensive elements and mining operations are limited to a few locations resulting in price instabilities in the past. The Congo is the the global provider of approximately 60% of the cobalt market [32]. Research efforts on addressing critical materials seek to provide solutions through materials conservation, recycling, and investigating alternative materials. Though NdFeB powder has the highest energy product, some of other drawbacks of NdFeB are their low curie temperature ( $T_c$ ), brittle behavior, and their sensitivity to corrosion. As NdFeB powder is very abrasive, special wear resistant coatings are usually needed, resulting in cost increases of the production [33]. In addition, the price of Nd has largely increased from 2020 to 2022, being significantly more expensive than Co in 2022 (see also Fig. 1.4).

### **2.4.2 Objective and Proposed Solutions**

Therefore, in this dissertation we explore the properties of hard magnetic composites that could be used for MFAAM. Focus is on a filament containing non-REE magnetic powder, specifically strontium ferrite in order to get improved magnetic performance with lower processing cost for 3D printing purpose.

As strontium ferrite powder is anisotropic a magnetic monofilament containing this powder can be used for 3D printing of anisotropic bonded magnets. Anisotropic magnets are much stronger and provide a larger magnetic flux density than isotropic magnet, hence have a higher energy product so less material would need to be used to create a specific performance. To realize the magnetic anisotropy the composite will be loaded with particles that have magnetic anisotropy and during the printing process an external magnetic field will be applied to the suspension in the printer.

Most of the MFAAM work has been done using FFF 3D printing. Note that FFF can be easily adapted by adding an external field source through a 3D-printer. Anisotropic magnets have better properties than isotropic magnets at the same loading level. Note that an additional gain can be obtained by printing an anisotropic magnet whose easy axis distribution varies with position resulting in magnets that are even stronger than homogenous anisotropic magnets. This is best explained by comparing the field created by an anisotropic magnet with the field created by a linear Halbach array.

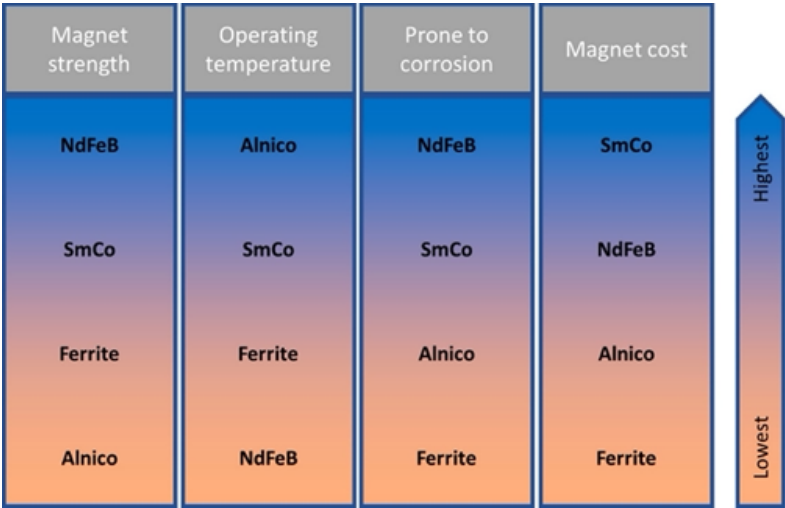


Fig. 2.10: Selection matrix of permanent magnets [34].

Due to appropriate magnetic properties, corrosion resistivity, chemical stability, and low cost compared with rare-earth compounds, Strontium Ferrite ( $\text{SrFe}_{12}\text{O}_{19}$ ) has attracted extensive interests in the past decades [35] and has been recognized that it can be used as permanent magnets. The main goal of this study is to manufacture  $\text{SrFe}_{12}\text{O}_{19}$ /PA12 composite filaments for FFF purposes by using a co-rotating twin screw

extruder.  $\text{SrFe}_{12}\text{O}_{19}$  has been chosen because of its chemical stability, which avoids oxidation issues as encountered in composites using NdFeB particles. For the magnetic particles in the composite, OP-71  $\text{SrO}(\text{Fe}_2\text{O}_3)_6$  powder obtained from Dowa Electronics Materials Co. is used. Besides being a widely used material to create bonded magnets, strontium ferrite particles are very stable, non-toxic and reinforce the polymeric matrix. The average particle size of the OP-71 powder is 1.39  $\mu\text{m}$ . Particles are platelets that have a hexagon shape with a long axis to short axis ratio of approximately a factor 3. Although it is not clear if the particles are single crystalline, particles are magnetically anisotropic with an easy axis parallel to the particle's short axis and favor strong anisotropic behavior.

Vestosint® 3D Z2773 from Evonik is used as the matrix of the filaments. It is a high-quality Nylon (PA-12) with high mechanical properties and excellent chemical behavior certified for 3D printing. It was chosen because of its low water absorption and high melt flowability, which allows for high loading concentrations of magnetic particles compared to other polymers. Its high melt flowability, allows it to be filled with approximately 60 wt.% - 80 wt.% loading level of magnetic particles. The highest loading level for strontium ferrite in PA12 that is published as of today is 85 wt.% (or 55 vol.%) by Huber group [21]. Nylon PA-12 is one of the most common plastics used in 3D printing. The effect of loading level and processing temperature and how they affect the magnetic anisotropy of 3D printed samples is studied for this dissertation research. PA-12 (nylon) and OP-71 Strontium Ferrite ( $\text{SrO}(\text{Fe}_2\text{O}_3)_6$ ) powder (1.39  $\mu\text{m}$ ) were used to realize different wt.%  $\text{SrO}(\text{Fe}_2\text{O}_3)_6/\text{PA-12}$  3D printer filaments with an average diameter of 1.5 mm. The 3D printer filaments were produced using a Thermo Fisher Process 11 co-rotating twin-screw extruder. Details on the manufacturing process is described in section 3.2.1. These manufactured 3D printer filaments were used for the MFAAM process.

Literature on 3D printed bonded permanent magnet is scarce [1, 4, 12] and recently the alignment of magnetic particles during the printing process is being studied [12, 15, 22]. It is expected that this work leads to development of new magnetic devices as currently no other manufacturing techniques exists that can realize such devices.

## **2.5 Conclusion**

This chapter presented work done of various research groups on hard magnetic composites that can be used to 3D print permanent magnets. Also, MFAAM was introduced and how it can enhance the materials properties and magnetic performance of 3D printed magnets with a distinct anisotropy distribution function. Furthermore, the challenges with the existing magnet manufacturing techniques towards scaling up of the polymer composite bonded magnets were discussed. In particular the issues that need further attention were introduced. Research questions and the scope of this dissertation were presented.

## REFERENCES

- [1] L. Li et al., “Big Area Additive Manufacturing of High Performance Bonded NdFeB Magnets,” *Sci. Rep.*, vol. 6, no. October, pp. 1–7, 2016.
- [2] B. G. Compton, J.W. Kemp, T.V. Novikov, R.C. Pack, C.I. Nlebedim, C.E. Duty, O. Rios, M.P. Paranthaman, Direct-write 3D printing of NdFeB bonded magnets, *Mater. Manuf. Process.* 33 (2016) 109–113.
- [3] C. Huber, C. Abert, F. Bruckner, M. Groenefeld, O. Muthsam, S. Schuschnigg, K. Sirak, R. Thanhoffer, I. Teliban, C. Vogler, R. Windl, and D. Suess, 3D print of polymer bonded rare-earth magnets, and 3D magnetic field scanning with an end-user 3D printer, *Appl. Phys. Lett.* 109 (2016), 162401.
- [4] A. Shen, X. Peng, C. P. Bailey, S. Dardona, and A. W. K. Ma, “3D printing of polymer-bonded magnets from highly concentrated, plate-like particle suspensions,” *Mater. Des.*, vol. 183, p. 108133, 2019.
- [5] K. Bilal, K. Lappe, D. Noetzel, K. Pursche, T. Hanemann, A 3D-printable polymer-metal soft-magnetic functional composite development and characterization, *Materials* 11 (2018) 189.
- [6] E. M. Palmero, D. Casalez, J. de Vicente, J.H. Vent, S. Lopez-Vidal, E. Rmiro, A. Bollero, “Composites based on metallic particles and tuned filling factor for 3D-printing by Fused Deposition Modeling”, *Comp. Part A: Appl. Sci. Manuf.* 124 (2019) 105497.
- [7] A. Kallaste, A. Kilk, A. Belahcen, T. Vaimann, and K. Janson, “Demagnetization in permanent magnet slotless generator using halbach array,” *Proc. 13th Int. Sci. Conf. Electr. Power Eng. 2012, EPE 2012*, vol. 2, no. January, pp. 1053–1057, 2012.
- [8] L. Henderson et al., “Altering magnetic properties of iron filament PLA using magnetic field assisted additive manufacturing (MFAAM),” *J. Magn. Magn. Mater.*, vol. 538, no. July, p. 168320, 2021.
- [9] A. de O. Barros and J. Yang, “A review of magnetically actuated milli/micro-scale robots locomotion and features,” *Crit. Rev. Biomed. Eng.*, vol. 47, no. 5, pp. 379–394, 2019.

- [10] D. Jiang, F. Ning, and Y. Wang, "Additive manufacturing of biodegradable iron-based particle reinforced polylactic acid composite scaffolds for tissue engineering," *J. Mater. Process. Technol.*, vol. 289, no. August 2020, p. 116952, 2021.
- [11] W. Hu, G. Z. Lum, M. Mastrangeli, and M. Sitti, "Small-scale soft-bodied robot with multimodal locomotion," *Nature*, vol. 554, no. 7690, pp. 81–85, 2018.
- [12] C. Huber, G. Mitteramskogler, M. Goertler, I. Teliban, M. Groenefeld, and D. Suess, "Additive manufactured polymer-bonded isotropic ndfeb magnets by stereolithography and their comparison to fused filament fabricated and selective laser sintered magnets," *Materials (Basel)*, vol. 13, no. 8, pp. 1–8, 2020.
- [13] H. Wang, T. N. Lamichhane, and M. P. Paranthaman, "Review of additive manufacturing of permanent magnets for electrical machines: A prospective on wind turbine," *Mater. Today Phys.*, vol. 24, p. 100675, 2022.
- [14] M. Ho et al., "Additive Manufacturing with Strontium Hexaferrite-Photoresist Composite," *IEEE Trans. Magn.*, vol. PP, pp. 1–1, 2020.
- [15] E. M. Palmero et al., "Magnetic-polymer composites for bonding and 3d printing of permanent magnets," *IEEE Trans. Magn.*, vol. 55, no. 2, pp. 1–4, 2019.
- [16] E. Peng, X. Wei, T. S. Heng, U. Garbe, D. Yu, and J. Ding, "Ferrite-based soft and hard magnetic structures by extrusion free-forming," *RSC Adv.*, vol. 7, no. 43, pp. 27128–27138, 2017.
- [17] E. M. Palmero et al., "Effect of particle size distribution on obtaining novel MnAlC-based permanent magnet composites and flexible filaments for 3D-printing," *Addit. Manuf.*, vol. 33, 2020.
- [18] L. M. Bollig, P. J. Hilpisch, G. S. Mowry, and B. B. Nelson-Cheeseman, "3D printed magnetic polymer composite transformers," *J. Magn. Magn. Mater.*, vol. 442, pp. 97–101, 2017.
- [19] L. M. Bollig, M. V. Patton, G. S. Mowry, and B. B. Nelson-Cheeseman, "Effects of 3-D Printed Structural Characteristics on Magnetic Properties," *IEEE Trans. Magn.*, vol. 53, no. 11, 2017.

- [20] A. Sarkar, M.A. Somashekara, M. P. Paranthaman, M. Kramer, C. Haase, I. C. Nlebedim, Functionalizing magnet additive manufacturing with in-situ magnetic field source, *Addit. Manuf.* 34 (2020), 101289.
- [21] C. Huber, S. Cano, I. Teliban, S. Schuschnigg, M. Groenefeld, D. Suess, Polymer-bonded anisotropic SrFe<sub>12</sub>O<sub>19</sub> filaments for fused filament fabrication, *J. Appl. Phys.* 127 (2020), 063904.
- [22] M. Suppan et al., “In-situ alignment of 3D printed anisotropic hard magnets,” *Sci. Rep.*, vol. 12, no. 1, pp. 1–7, 2022.
- [23] K. Sonnleitner et al., “3D printing of polymer-bonded anisotropic magnets in an external magnetic field and by a modified production process,” *Appl. Phys. Lett.*, vol. 116, no. 9, pp. 3–8, 2020.
- [24] H. A. Khazdozian, J. S. Manzano, K. Gandha, I. I. Slowing, and I. C. Nlebedim, “Recycled Sm-Co bonded magnet filaments for 3D printing of magnets,” *AIP Adv.*, vol. 8, no. 5, 2018.
- [25] C. Belduque, T. Ahmed, W. J. Geerts, J. Tate, “Magnetic Moment and Magnetic Anisotropy Analysis of 3D printed Strontium Ferrite/PA12 filament under a Magnetic Field”, *SPE-Automotive Composite Conference & Exhibition*, September 9-11, Detroit.
- [26] K. von Petersdorff-Campen et al., “3D printing of functional assemblies with integrated polymer-bonded magnets demonstrated with a prototype of a rotary blood pump,” *Appl. Sci.*, vol. 8, no. 8, 2018.
- [27] G. Chatzipirpiridis et al., “3D Printing of Thermoplastic-Bonded Soft- and Hard-Magnetic Composites: Magnetically Tuneable Architectures and Functional Devices,” *Adv. Intell. Syst.*, vol. 1, no. 6, p. 1900069, 2019.
- [28] T. N. Lamichhane, L. Sethuraman, A. Dalagan, H. Wang, J. Keller, and M. P. Paranthaman, “Additive manufacturing of soft magnets for electrical machines— a review,” *Mater. Today Phys.*, vol. 15, p. 100255, 2020.
- [29] C. Huber et al., “Additive Manufactured and Topology Optimized Passive Shimming Elements for Permanent Magnetic Systems,” *Sci. Rep.*, vol. 8, no. 1, pp. 1–8, 2018.

- [30] R. Tino, A. Yeo, M. Brandt, M. Leary, and T. Kron, “The interlace deposition method of bone equivalent material extrusion 3D printing for imaging in radiotherapy,” *Mater. Des.*, vol. 199, no. February, p. 109439, 2021.
- [31] ProtoPlant, makers of Proto-pasta. (n.d.). Magnetic Iron PLA. Protopasta. Retrieved November 11, 2020, from <https://www.protopasta.com/products/magnetic-iron-pla>.
- [32] M. S. thesis of Camila Beldeque, “Development of Strontium Ferrite/Polyamide 12 Composites for Magnetic Devices Using Additive Manufacturing”, Texas State University, May (2021).
- [33] L. H. Lewis and F. Jiménez-Villacorta, “Perspectives on permanent magnetic materials for energy conversion and power generation,” *Metall. Mater. Trans. A Phys. Metall. Mater. Sci.*, vol. 44, no. SUPPL. 1, 2013.
- [34] V. Chaudhary, S. A. Mantri, R. V. Ramanujan, and R. Banerjee, “Additive manufacturing of magnetic materials,” *Prog. Mater. Sci.*, vol. 114, no. February 2019, p. 100688, 2020.
- [35] Z. F. Zi, Y. P. Sun, X. B. Zhu, Z. R. Yang, J. M. Dai, and W. H. Song, “Structural and magnetic properties of SrFe<sub>12</sub>O<sub>19</sub> hexaferrite synthesized by a modified chemical co-precipitation method,” *J. Magn. Magn. Mater.*, vol. 320, no. 21, pp. 2746–2751, 2008.

### **3. MANUFACTURING & CHARACTERIZATION TECHNIQUES AND ANALYSIS**

*“The true laboratory is the mind, where behind illusions we uncover the laws of truth.”*

— Sir Jagadish Chandra Bose

#### **3.1 Introduction**

On the way to fabricate magnetic polymer composite filament for 3D printing purpose different characterization techniques have been employed at different steps of the research. These techniques include imaging, structural, morphological, thermal and magnetic measurements. This chapter is dedicated for a brief overview of the used manufacturing technique of fabricating the 3D printer filament and the various measurement techniques used to characterize the samples. Moreover, the necessary technical specifications of the tools used in the research are provided.

#### **3.2 Manufacturing Techniques**

This section provides information on the systems used to fabricate the magnetic polymer composite filament and the 3D printed samples.

##### **3.2.1 Twin-Screw Extruder**

The composite filaments were made using a Thermo-Fisher Process 11 Co-rotating Twin Screw Extruder, shown in Fig. 3.1(a) below.

It consists of two feeders, a twin extruder, a water bath tray to cool down the extruded filament and an automatic spooling unit. The main process parameters include the temperature distribution in the barrel, the extrusion speed, and the speed of the feeders with which magnetic powder and thermoplastic nylon are fed into the barrel. The system measures the back pressure.

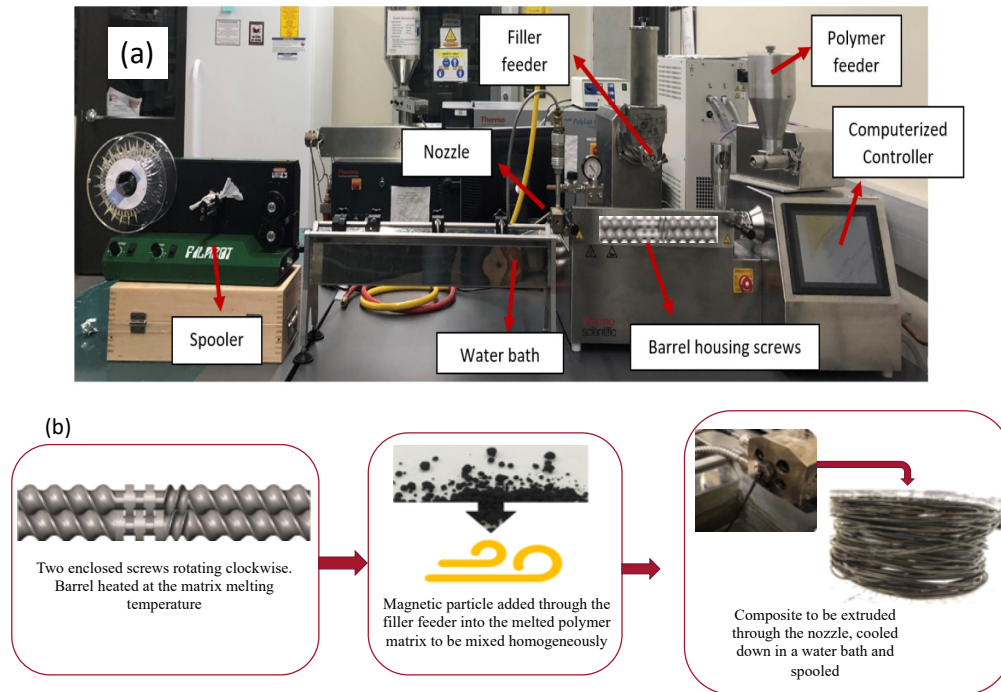


**Fig. 3.1:** (a) Thermo Fisher Process 11 Twin Screw Extruder [1] (b) Schematic of the manufacturing process.

From the computer interface, parameters such as the temperature range, and the rpm of the screws and feeders are controlled. Eight temperature zones ( $Z$ ) are monitored during the fabrication of strontium-ferrite/nylon composite filament. Zone 1,  $Z1$ , is permanently cooled and cannot be controlled.  $Z2$  to  $Z6$  go from  $220^{\circ}\text{C}$  to  $240^{\circ}\text{C}$ , at this stage of the process, the magnetic particles are added into the melted matrix.  $Z7$ ,  $Z8$  and the die go from  $240^{\circ}\text{C}$  to  $230^{\circ}\text{C}$  for extrusion. A vacuum pump connected to  $Z7$  of the extruder was used to prevent the formation of air voids in the magnetic filament, which is extruded through a 2 mm nozzle and cooled down in a water bath. The matrix feeder rate is 22 rpm, filler hopper is 80 rpm and extruder speed is 80 rpm for the fabrication of  $\sim 1.5$  mm diameter strontium-ferrite/nylon composite filament. Consequently, the filament is spooled by an automatic spooling unit [1].

**Table 3.1:** Manufactured 3D-printer filament with different concentration of SrFe<sub>12</sub>O<sub>19</sub> in PA12 by twin screw-extruder.

Number	Manufactured 3D-printer filaments
1.	Neat PA12
2.	5 wt.% SrFe <sub>12</sub> O <sub>19</sub> /PA-12
3.	26 wt.% SrFe <sub>12</sub> O <sub>19</sub> /PA-12
4.	40 wt.% SrFe <sub>12</sub> O <sub>19</sub> /PA-12
5.	70 wt.% SrFe <sub>12</sub> O <sub>19</sub> /PA-12

### 3.2.2 3D Printing or Additive Manufacturing (AM)

In our experiments, a water-cooled ROVA 3D printer of ORD solutions (Fig. 3.2) was used to 3D print samples using our fabricated magnetic polymer composite 3D-printer filament.

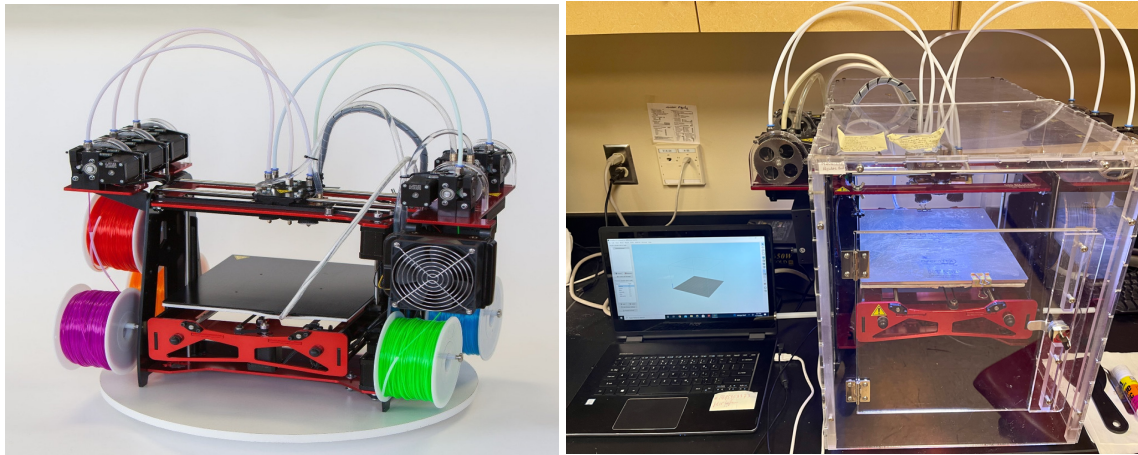


**Fig. 3.2:** A water-cooled ROVA 3D printer of ORD solutions and ROVA 3D printer of ORD solutions at Texas State University.

The ORD Solutions RoVa3D is a desktop 3D printer made by ORD Solutions. The ORD Solutions RoVa3D offers 5 extruders in a single 3D printer where all nozzles possess Bowden-style extruders. All metal hot ends are capable of printing at temperatures up to 450°C. All hot ends are water cooled to prevent jamming and for improved performance [2]. The 3D printer of ORD solutions in our lab is equipped with a print nozzle of 0.5 mm in diameter. To print samples an extrusion temperature of 200~230°C and a bed

temperature of  $\sim 45\text{ }^{\circ}\text{C}$  was usually used. Ethylene-vinyl acetate (EVA) was used to improve the adhesion of the 3D printed material to the print-bed. A computer is connected to the 3D printer to create/fabricate 3D objects using computer-aided design (CAD) model by stacking material in a layer-by-layer arrangement (Complete-Ease).

### 3.2.3 Magnetic Field Assisted Additive Manufacturing (MFAAM)

A magnetic field can be applied during the 3D printing process as a means to induce texture and enhance remanence and susceptibility. This process is referred to as magnetic field assisted additive manufacturing (MFAAM).

To orient the magnetic particles, various magnetic fields can be applied during the printing process by printing on top of different Neodymium (NdFeB) permanent magnets of grade N52. Using 1" cube NdFeB magnets an applied field of 5000 Oe perpendicular (Fig. 3.3b) or 8000 Oe parallel (Fig. 3.3c) to the print field could be realized. Using thinner NdFeB magnets smaller print fields were realized. The print field allows for the magnetic particles to be oriented in a well-defined direction resulting in the realization of anisotropic magnetic with a well-defined easy axis direction. Printing on top of a linear Halbach array results in an inhomogeneous anisotropic magnet that has a complex easy axis distribution: easy axis varies with position on a mesoscopic scale.

Pictures of the MFAAM printing process are included in Fig. 3.3 below:

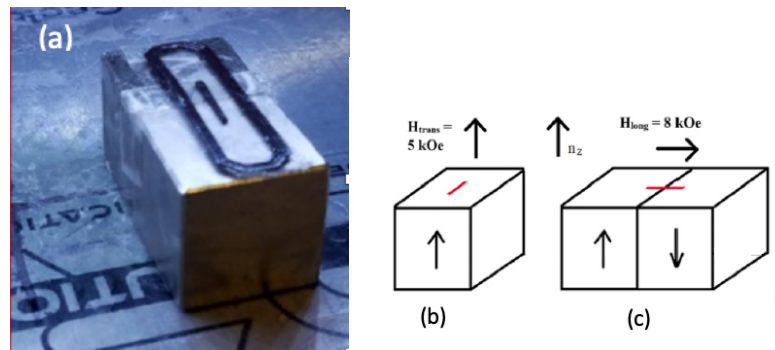


**Fig. 3.3:** (a) MFAAM sample printed on NdFeB permanent magnets on top of ROVA3D’s print bed and schematics of MFAAM printing method for (b) transverse ( $H_{trans}$ ) and (c) longitudinal ( $H_{long}$ ) print-fields. Also indicated is the direction of the print normal “ $n_z$ .”

Currently MFAAM process is done in our lab by printing on top of external permanent magnets. However, in the future this will be done by using an electromagnet or permanent magnets positioned around the extruder nozzle to make the manufacturing process more facile.

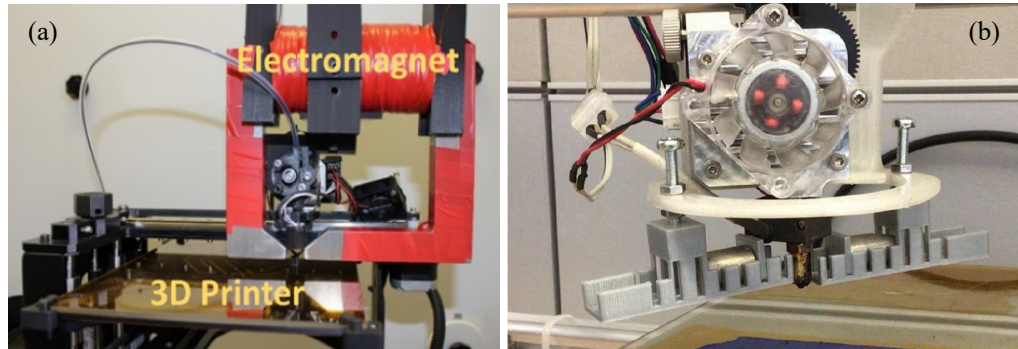


**Fig. 3.4:** (a) Specialized designed 3D printer with electromagnet positioned around the extruder nozzle at Ames laboratory [3] and (b) modified 3D-printer showing the extruder including the nozzle and the flexible fixing unit for the permanent magnets by Suppan et al. [4].

Design and development of a water-cooled electromagnet with small form factor that can be installed on top of a 3D printer and will allow us to apply a longitudinal or perpendicular field to the print surface will be a main challenge. The electromagnet would need to contain a ferrite or iron core to obtain higher fields, and the coil would need to be water cooled to not affect the temperature near the print head. Such electromagnet should contain a rather large pole piece gap to guarantee a homogeneous magnetic field across a large enough area where the composite is still drying to freeze in the magnetic anisotropy. The use of electromagnet will allow us to explore the dynamics of the alignment process including the effect of print-speed, temperature, and field changes. It is clear from Fig. 3.4a above that such system will add a lot of weight to a 3D printer head which will require to reduce the print speed significantly. Several groups are currently exploring the use of a permanent magnet carefully positioned around the print nozzle as such an approach allows for a much smaller form factor.

The magnitude of the applied field is limited by the homogeneity of the field created by the field unit as the field gradient results in exerting a force on the extruded material. At large field values, the large field gradient will exert a large force on the extruded material attracting the material to the pole pieces of the electro- or permanent-

magnet [5]. So, part of the design challenge is to create a system with small field gradients such is currently being designed by Mandesh Khadka a masters student working with Dr. Tate.

### **3.3 Characterization Techniques for Filaments**

Surface morphology in this thesis is studied by Scanning Electron Microscopy (SEM) with embedded Energy Dispersive Spectroscopy (EDS) and Hirox optical microscope. For the structural investigation, an X-ray diffractometer (XRD) was used while additional information on the polymer matrix was obtained through Fourier Transfer Infrared Spectroscopy (FTIR). The thermal analysis was done by Thermogravimetric analysis (TGA) and Differential Scanning Calorimetry (DSC). The time, temperature and angular dependent magnetic investigations were performed using a biaxial Vibrating Sample Magnetometer (VSM) and Torque Magnetometer (TM). The following sections present the working principle and technical specifications of the tools mentioned above. We also added the analysis of EDS, FTIR, XRD, TGA and DSC measurement results of our composite filaments in the corresponding sections.

#### **3.3.1 Biaxial Vibrating Sample Magnetometer (VSM) and Torque Magnetometer (TM)**

The primary equipment for this dissertation is the MicroSense EZ-9 Biaxial Vibrating Sample Magnetometer (VSM) which contain a true torque head TM option as well. The VSM option was used in this research to measure the hysteresis curves, saturation magnetization and the time dependence of the magnetic moment of the samples at room temperature for different field angles. The biaxial coil set allowed for the measurements of the sample's magnetic moment parallel to the applied field (along the X-axis,  $M_x$  signal) and perpendicular to the applied field (along the Y axis,  $M_y$  signal). For temperature dependent magnetic measurements at elevated temperatures, the furnace was raised up around the vibrating sample. Argon (Ar) gas was flown during the measurements. Although the furnace allows for measurements from -203 to 727 °C, all measurements done

in this dissertation were done below 290 °C, the onset of decomposition of the PA-12 matrix. The field anneal experiments, the magnetic rotation studies and the magnetic anisotropy studies, were all done using this VSM. The MicroSense™ option was implemented to study the RT anisotropy of a 3D printed sample and a freely extruded sample.

### ***3.3.1.1 Theory of VSM Operation***

A VSM is used to measure the magnetic properties of magnetic materials at high and low magnetic fields, as well as a wide range of temperatures. This technique can uncover a lot about a sample's magnetic behavior, including magnetic anisotropy, susceptibility, remanence, and coercivity of the material. A VSM operates by first placing the sample to be studied in a constant magnetic field. If the sample is magnetic, this constant magnetic field will magnetize the sample by aligning the magnetic domains, or the individual magnetic spins, with the field. The stronger the constant field, the larger the magnetization will be. The magnetic dipole moment of the sample will create a magnetic field around the sample, sometimes called the magnetic stray field.

As the sample is moved up and down, this magnetic stray field is changing as a function of time and can be sensed by a set of pick-up coils. The alternating magnetic field will cause an electric field in the pick-up coils according to Faraday's Law of Induction [6]. This induces a voltage in the detection coils surrounding the sample which can be described using "Faraday's Law of Induction", given below [7]:

$$\varepsilon = -N \frac{d\phi}{dt} \quad (3.1)$$

Where "ε" is the induced voltage (or emf), "N" is the number of turns in the coils, "φ" is the magnetic flux, and "t" is time. So, the amount of voltage induced in the pickup coils is proportional to the changing coupled magnetic flux through the coils over time and therefore proportional to the magnetic moment of the sample. However, even though the applied magnetic field itself is not changing, the sample's magnetic flux through the detection coils is changing and is therefore time dependent. Keeping this in mind, the magnetic flux can be described in terms of the surface area in which the flux passes through and the magnetic flux density [7]:

$$\phi = BA \cos \theta \quad (3.2)$$

where “B” is the magnetic flux density, “A” is the surface area perpendicular to the magnetic field, and “ $\theta$ ” is the angle between the direction of the sample’s magnetic stray field and the normal of the detection coils’ surface area. The sample is mounted in the VSM so that it’s normal is parallel with direction of the magnetic field, so the cosine term disappears. Substituting this definition of magnetic flux into Faraday’s law yields [7, 8]:

$$\varepsilon = -N \frac{d(BA)}{dt} = -NA \frac{d(B)}{dt} \quad (3.3)$$

Therefore, for the case of a VSM, the change in the sample’s position with respect to the detection coils placed around the sample creates a changing magnetic flux over time that in turn generates an induced voltage in those pickup coils. This current will be proportional to the magnetization of the sample. The larger the sample’s magnetization, the larger the induced current. The induction current is amplified by a transimpedance amplifier and a lock-in amplifier. The various components are hooked up to a computer interface. Using controlling and monitoring software, the system can tell you how much the sample is magnetized and how its magnetization depends on the strength of the constant magnetic field [6].

### ***3.3.1.2 Schematics of MicroSense VSM Head Option***

The components of the MicroSense EZ-9 VSM pertaining to this dissertation are comprised of the VSM motor/vibrator head, electromagnet, stationary pick-up coils, the chiller and a control rack consisting of the lock-in amplifiers, gaussmeter, and the magnet power supply. For the temperature dependent measurements, the oven and temperature controller will be used in addition to the components listed above. Also included is the true torque magnetometer head. The images below highlight the parts that will be utilized in this research:

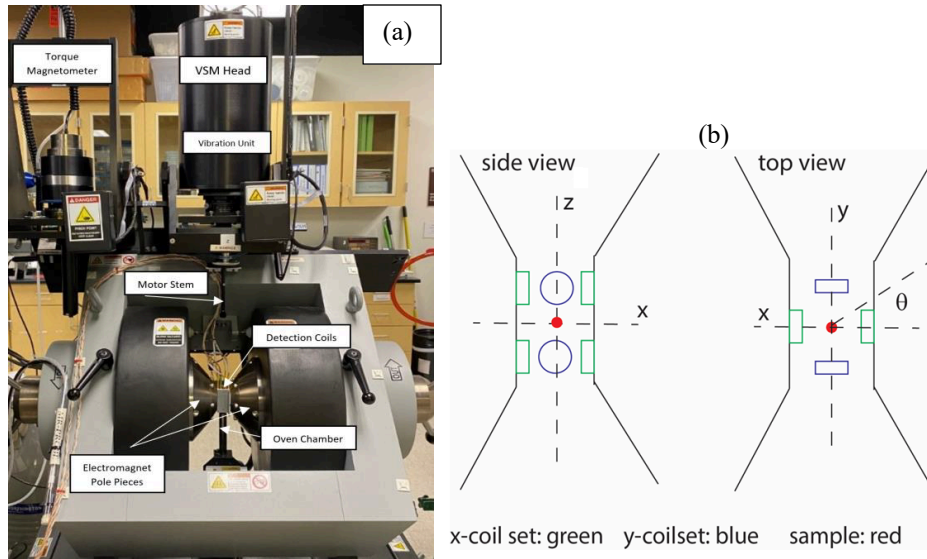


**Fig. 3.5:** a) Setup of the Bi-axial MicroSense EasyVSM at Texas State University. Also shown is the torque magnetometer. b) Configuration of biaxial coil set used to measure the components of the magnetic dipole vector parallel and perpendicular to the applied field; the red dot represents the sample [8].

The MicroSense VSM allows for a magnetic field range of  $-2.35$  T to  $2.35$  T, a full  $360^\circ$  field angle range, and a temperature range of  $-203$  to  $727$  °C [9]. The samples being measured can be mounted on a variety of rod holders, such as pyrex or quartz rods, both of which have perpendicular and transverse holder options. For temperature dependent measurement we used Pyrex hollow cylindrical sample rod holder. Adhesives such as museum wax, superglue, high temperature silicone glue, or ceramic cement can be used to attach the samples to the rod holder of choice depending on the desired temperature. Once the samples are mounted to the desired rod holder, the sample/holder mechanism is attached to a motor/vibrator stem (seen above in Fig 3.5) that is connected to the VSM head. This motor stem vibrates the sample in the z-direction at a fixed frequency and amplitude while an electromagnet applies a uniform magnetic field through two pole pieces, directly magnetizing the vibrating sample. This sample sits secured in a “chamber” consisting of eight vector coils, four measuring the magnetic moment parallel to the external magnetic field (deemed the x-direction or  $M_x$  signal) and four measuring the moment perpendicular to the external field (deemed the y-direction or  $M_y$  signal). The sample begins to experience a changing magnetic flux, inducing a voltage that is picked up

by these surrounding vector coils. The coils are connected to lock-in amplifiers, which act as narrow bandpass amplifiers and allow for a high signal-to-noise ratio by enhancing the sensitivity. The amplifiers use this signal to obtain a magnetic moment value that is read by the user through a data analysis software. This process can be employed for a range of magnetic field values in either a step mode measurement option or sweep mode measurement option [8].

### 3.3.1.3 Schematics of Torque Magnetometer (TM)

While the MicroSense VSM head allows for an indirect method of measuring torque using the perpendicular component of the magnetization picked up by the vector coils [10, 11], MicroSense also offers the option to employ a torque magnetometer. The TM uses a direct method in measuring the torque felt on a sample to determine the anisotropic direction in magnetic materials. The following diagram displays the inner workings of the MicroSense torque magnetometer head:

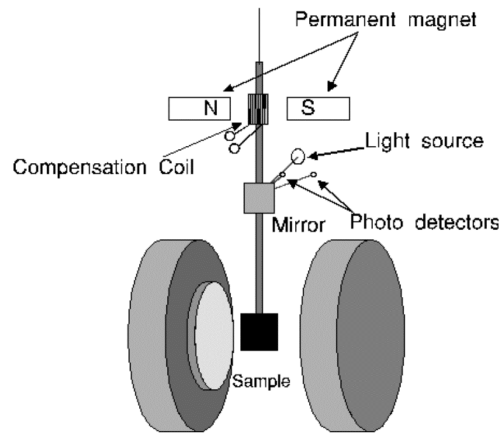


**Fig. 3.6:** Diagram of the MicroSense torque magnetometer including sensors, coils, and magnets [9].

The MicroSense TM is equipped with automatic recording of torque curves using active sensing. Within the torque head is a near frictionless air bearing in which the sample hangs from. Also attached to this rod are the compensation coils situated between a permanent magnet and a mirror which reflects a specific amount of light picked up by the

photodiodes. The sample is centered between an electromagnetic which supplies the external magnetic field. Once this field is applied, the sample is free to rotate, and the field works against the intrinsic force that tries to pull the sample back to its easy axis. As the sample rotates, the light source, mirror, and photodiodes within the torque head provide a feedback signal based off the amount of light that is reflected off the mirror and sensed by the photodiodes. Depending on the amount of light detected, a specific amount of current is then run through the coils within the torque head to supply a balancing torque. The amount of current running through the coils is directly proportional to the torque being exerted on the sample. This process is repeated for angles  $-180^\circ$  to  $180^\circ$  to create a torque vs. field angle plot using the MicroSense software in which the anisotropy constants and easy and hard directions can be derived from.

There are pros and cons of both methods; using the biaxial VSM to measure the torque curve allows measurements as a function of the temperature [8], which is not possible with the torque head due to the sensitivity of the torque sensor. The torque head makes use of an ultra-low friction air bearing to suspend the samples, and the gas flow from the cryostat necessary for temperature-dependent measurements disturbs this process by introducing noise into the data being collected, so the biaxial VSM method is more reliable when temperature-dependent torque measurements are desired.

However, the biaxial VSM method completely relies on the signal being picked up by the vector coils which causes issues regarding calibration of the sample, as well as the quality of data taken. Since no magnetic field can be applied in the perpendicular direction, the calibration in this direction is always an indirect approach and affects the sensitivity of the signal in the pick-up coils, especially for asymmetric samples as measurements in this case are now angular-dependent [12]. As the sample approaches saturation, the signal becomes less reliable because at this point, the sample's magnetic moment is almost completely lined up with the magnetic field and the perpendicular signal from the coils in the y-direction becomes very small, making the torque difficult to measure at high fields. Therefore, the quality of the signal is dependent on the calibration of the coils and the collected data can only be as credible as calibration allows, making the TM the ideal choice for accurate torque measurements. Torque curves measured by biaxial VSM furthermore suffer from a large  $2\theta$  background originating from slight misalignments of the sample on

the sample rod. This background cannot be easily distinguished from the  $2\theta$  signal originating from a uniaxial magnetic anisotropy.

#### ***3.3.1.4 VSM Data Analysis Software***

After the data is collected, MicroSense employs the data analysis software to enhance and correct the measured data using a myriad of data manipulation files. The voltage measured by the sensor coils can be attributed to more than just the signal coming from the sample, so the data analysis software allows for correction and elimination of these outside sources to isolate the signal coming from the sample and allow for higher accuracy in the measured data. The manipulation files that will be used on the samples for this dissertation are the image effect correction and the sweep field lag correction. These data manipulation corrections are explained in detail below.

##### **3.3.1.4.1 Image Effect Correction**

The first correction used on the VSM data compensates for the extra signal that is acquired due to what is called the “image effect.” When a sample becomes magnetized, the sensor coils pick up the magnetic flux coming from the magnetic image charges on the sample. The magnetic stray field from the charges on the sample affects the magnetization of the electromagnet pole pieces (made of soft magnetic iron) and induces image magnetic dipole charges on these pole pieces. Therefore, the coils also pick up the flux from the image charges resulting in a higher sensitivity for low magnetic field values. This is known as the “image effect.” This effect occurs when a sample is placed near a material that has a higher permeability than air, and as the sample is magnetized, it induces equal and opposite “image” charges on the surface of the highly permeable material as described above. The flux from the image charges is picked up by the sensor coils and adds to the total signal being read. At higher field values, specifically above 1.5 Tesla, the pole pieces saturate and the flux contribution from the image charges disappears, distorting the saturation level of the sample being measured. This phenomenon can be seen in Fig 3.7.

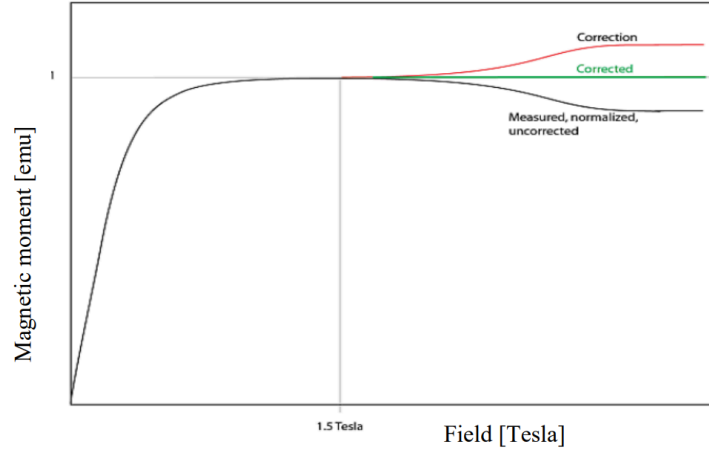


**Fig. 3.7:** Magnetization vs. field plot from MicroSense manual depicting the image effect correction employed at fields above 1.5 Tesla [13].

To compensate for this drop-in signal, the image effect correction measures a calibration sample with a known saturation magnetization as a function of the applied field above 1.5 Tesla. The signal is then normalized, and its inverse is applied to correct for the sample’s actual saturation level for fields above 1.5 Tesla [13]:

$$M(\text{Corrected}) = \frac{1}{\left[\frac{M(H)}{M(1.5 T)}\right]} \quad (3.4)$$

### 3.3.1.4.2 Sweep Field Lag Correction

When the VSM takes measurements, there are two modes applicable for data collection: step field mode and sweep field mode. Step field mode allows for a “stop and go” approach when taking data points, as it allows the system to pause at each specified magnetic field value for some time interval to allow the electronics of the system to catch up with the changed magnetic signal, collect the measurement, and then move on to the next point by changing the field value. Sweep field mode takes a more gradual approach when running measurements by continuously running through the set of desired points and collecting data without allowing time between magnetic field changes and actual data collection. Sweep field mode is incredibly time efficient, as this mode allows hysteresis curves to be measured within minutes, whereas step mode measurements can take much longer. However, due to the electronic time constant of the lock-in amplifier, the signal

being read in by the amplifier falls behind the actual signal being detected by the pickup coils during sweep field mode as the system is not allotted enough time to catch up to the true signal. Remove sweep field lag corrects for this fallback by using the sweep rate that was used during measurement and the time constant of the amplifier to shift the measured curve back over the calculated curve. Since sweep field mode was used in measuring the samples in this dissertation, the “remove sweep field lag” correction was implemented on all data to accommodate for this lag in signal [8, 13].

### **3.3.2 Optical Microscopy**

The distribution of the particles in the filaments was characterized by using optical and electron microscopy systems. The objective of this microscopy study is to analyze the dispersion and orientation of the particles in the nylon matrix and we expect to have a good adhesion between the matrix and the strontium ferrite. It will also help to get an idea on how the flow during the extrusion process will impact the orientation and dispersion of the magnetic particles in the polymer matrix filaments.

The Hirox digital microscope (DM), is a microscope that has a camera (CMOS) attached instead of an eyepiece and displays the digitally acquired image on a large monitor. In addition to direct observations, the system can also be used for dimension measurements, recording of still and moving images, the creation of z-stacks that will increase the depth of field by digital image processing, and assembling large area high magnified images by stitching individual images together in one large composition [14]. For this research, the Hirox digital microscope of Texas State University shown in Fig. 3.8 was used.



**Fig. 3.8:** Hirox Digital Microscope at Texas State University.

The Hirox DM is a system with a main unit containing a motorized xy-stage to which a lens camera unit is attached. This lens-camera unit is also motorized and allows for auto-focus and can be tilted with respect to the xy-stage to facilitate inclined optical microscopy. Furthermore, Auto Calibration Select (ACS) communications makes it possible to control speed based on lens information, instant measurement on the monitor, automatic judgment of shooting conditions according to the operation of an operator, and to observe, capture, and measure by intuitive operations of the user [4]. It has two optical zoom lenses, i.e. MXB-2016 (6-320x) Zoom Lens (Fig. 3.9a) and MXB-2500 (35-2500x) Zoom Lens (Fig. 3.9b). The latter has three objectives and allows for higher magnifications. A full set of adapters for different lighting conditions is available.

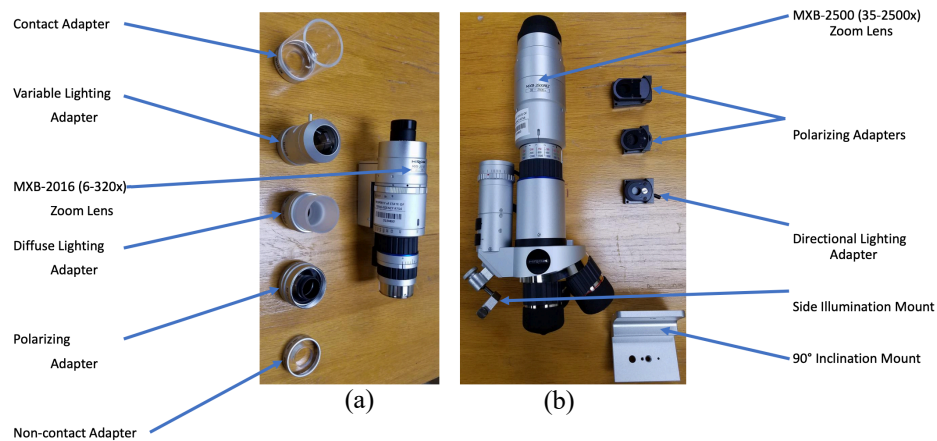


**Fig. 3.9:** (a) MXB-2016 (6-320x) Zoom Lens (left) and (b) MXB-2500 (35-2500x) Zoom Lens (right).

### ***3.3.2.1 Optical Microscopy Image Analysis***

For the optical image measurements, the samples were prepared in two different methods: (1) by cutting along the radial axis with a knife at room temperature; (2) by looking at the ends of samples field annealed above the melting temperature. Note that the thermal contraction upon solidification results in concave ends. Under the Hirox optical microscope we were able to see nice periodic patterns in the 40 wt.% Strontium-ferrite/PA12 composite filament which was magnetically annealed at 22kOe at 250 °C prior. Initially we concluded from the optical micrographs that clear chaining of the magnetic particle took place in these field annealed strontium ferrite in PA12 filaments (Fig. 3.10a and 3.10b). The optical micrographs were taken of different areas of the ends of the sample and periodic pattern was observed. Although initially it was concluded that the observed patterned proved strong chaining of particle at higher temperatures where the viscosity decreases, SEM images taken of the same samples did not show any strontium ferrite particles (Fig 3.10c and 3.10d). It is currently not clear what causes the pattern observed by optical microscopy. Note that the average diameter of the strontium ferrite particles is around 1.4  $\mu\text{m}$  which is at the limit of what can be resolved with the Hirox DM when using the high-resolution objectives. Hence for all microscopy studies performed for the research reported in this dissertation scanning electron microscopy was used which has a much higher resolution.

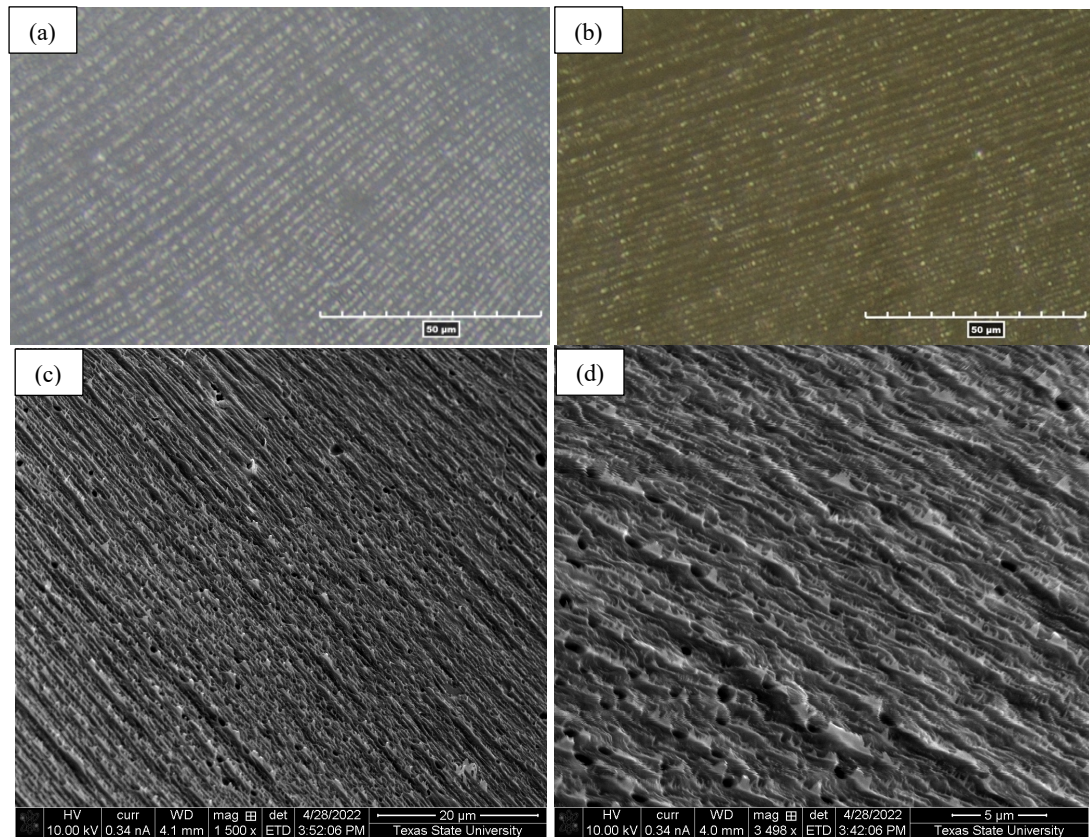


**Fig. 3.10:** (a) and (b) Optical microscopy images of 40 wt.% Strontium-ferrite/PA12 annealed filament showing periodic pattern of particles. (c) and (d) Corresponding SEM images shows no particles.

### 3.3.3 Scanning Electron Microscopy (SEM)

The objective of the Electron microscopy studies is to determine the dispersion and orientation of the particles in the nylon matrix and also check the size and orientation of clusters or agglomerates of particles. The objective is to investigate the morphological alignment in terms of texture or chaining (very ordered clustering) in field annealed samples.

A scanning electron microscope (SEM) is a type of electron microscope that produces images of a sample by scanning the surface with a focused beam of electrons. The electrons interact with atoms in the sample, producing various signals that contain information about the surface topography and composition of the sample. SEM is capable of imaging the surface morphology with a nanometer scale resolution and allows for much higher magnifications than optical microscopy. A SEM system consists of an electron gun,

condenser lenses, scanning coil, objective lenses, detector and a display unit [15, 16]. The components are organized as shown in the Fig. 3.11a.

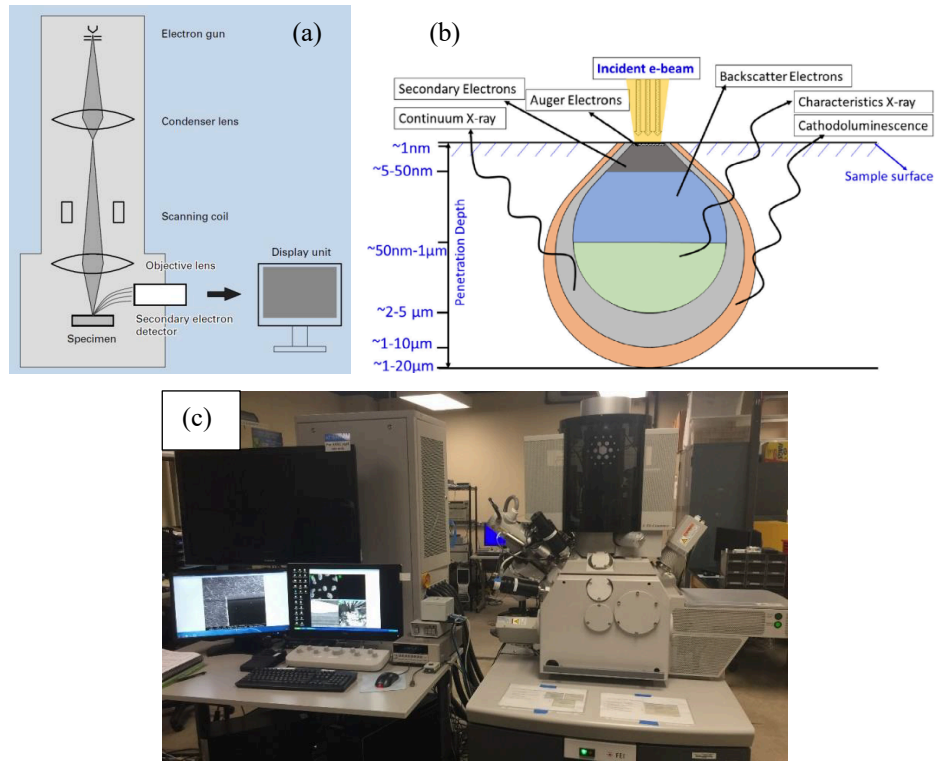


**Fig. 3.11:** (a) Schematic diagram of a scanning electron microscope [15] (b) Different type of signal generated from the irradiated spot of the sample along with corresponding depth from the surface [17], (c) FEI Helios NanoLab 400 DualBeam field emission scanning electron microscope of Texas State University [16].

Both electron gun and the sample are required to be in a high vacuum chamber. The electron gun can be thermionic or field-emission type. Images of the samples are obtained by scanning the surface using a finely focused beam of electrons. Based on the type of sample, secondary electrons, backscattered electrons, Auger electrons, light, and X-rays or a combination thereof may be released (Fig. 3.11b). The FEI Helios NanoLab 400 Dual Beam field-emission SEM of Texas State University was used for the research in this dissertation has separate detectors for backscattered and secondary electrons (SE). The signals are collected and processed by a computer to generate the image and other valuable information about the sample [17]. To image the topography of the filaments, the SE signal was used. SEs originate from the surface or the near-surface regions of the sample. They

are a result of inelastic interactions between the primary electron beam and the sample and have lower energy than the backscattered electrons. They are very useful for the inspection of the topography of the sample's surface [18]. The electric potential of the incident energy beam of the system can be varied between 8 kV-10 kV. A typical beam current of 0.34 nA was used for the imaging studies reported on in this dissertation. SEM imaging of magnetic polymer composite filaments is challenging as the nylon polymer is non-conductive resulting in charging issues (see Fig.3.12). Furthermore, during the research at times grains in the sample (specifically Nylon) were observed to separate upon hitting the surface with a high energy electron beam. It requires a suitable selection of voltage and beam current to obtain high-quality image. Best images were obtained by a typical acceleration voltage of 8 kV and a beam current of 0.34 nA. To avoid charging issues and to get improved resolution of our filament SEM images, all samples were coated with a conductive 4 to 6 nm layer of Iridium (Ir) deposited by an Imaging Sputter Coater (detailed in section 3.3.5). Detailed information on imaging of filaments are presented in section 5.3.2 of chapter 5.

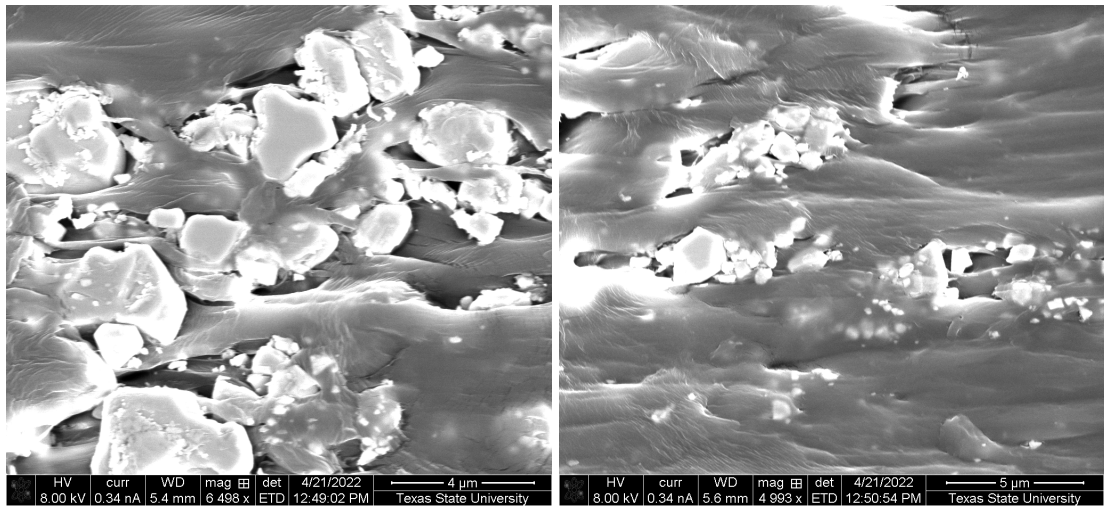


**Fig. 3.12:** Charging issue under electron microscope before coated with Iridium.

### 3.3.4 Electron Dispersive X-ray Spectroscopy (EDS)

The SEM system of Texas State University is also equipped with an Energy Dispersive X-ray Spectroscopy (EDS) system to provide elemental analysis. EDS gives the information on the elemental composition of the sample. The EDS system is used to

identify the elements from the characteristics X-ray released from the sample after its atoms are excited by the incident electron beam [16, 19]. However, EDS generally does not work for elements with a low atomic number. Hydrogen and helium both only have an  $n=1$  shell, meaning there aren't core electrons to be removed that can allow for X-ray emission. Hence, lighter elements (atomic number,  $Z < 11$ ) cannot be routinely analyzed by EDS. Hydrogen ( $Z = 1$ ) and He ( $Z = 2$ ) do not have Characteristic X-rays, and the Li ( $Z = 3$ ) K X-rays are of too low energy to be detected by EDS.

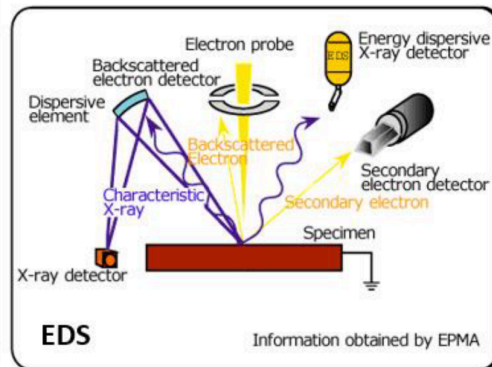
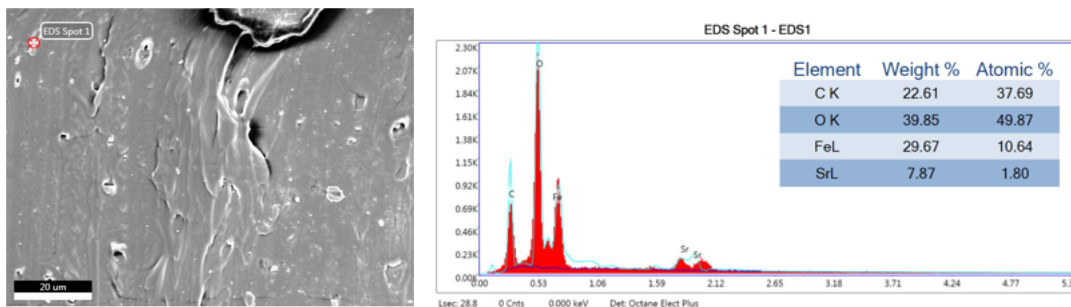
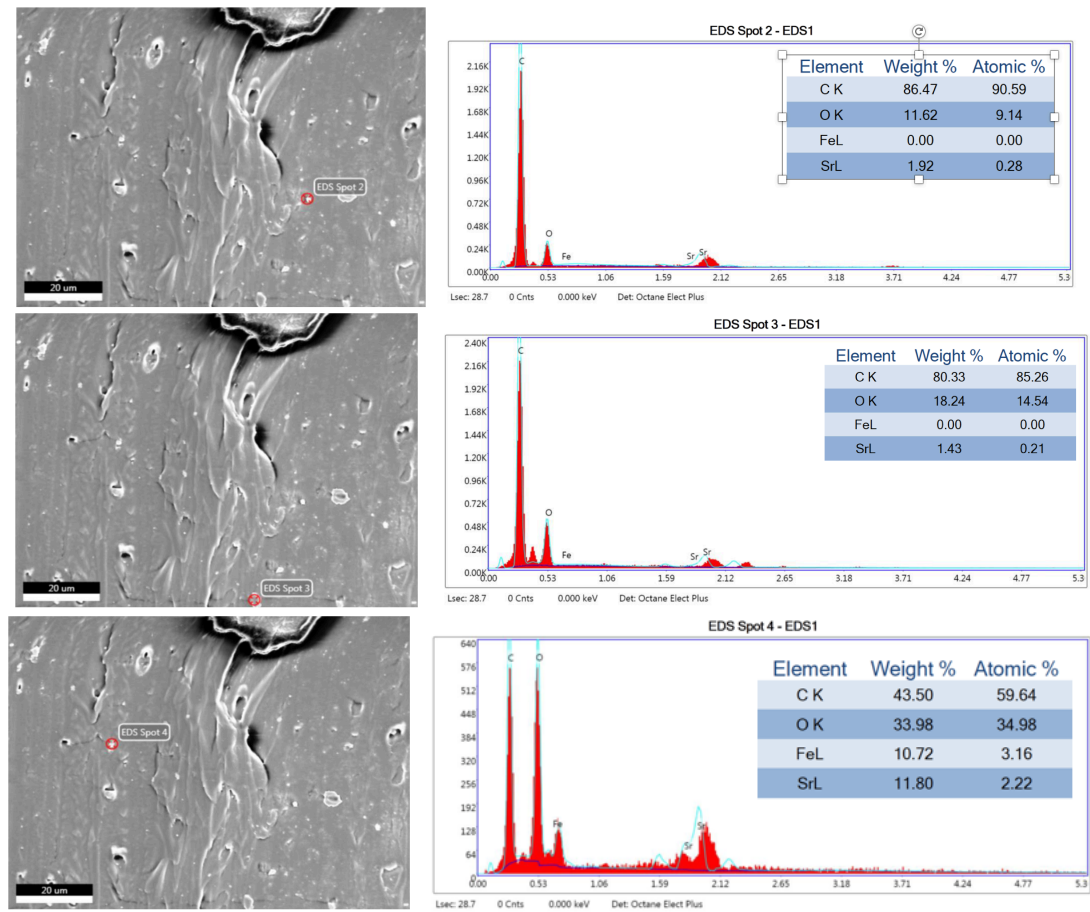


Fig. 3.13: Schematic of EDS systems for detection [23].

### 3.3.4.1 EDS Spectra Analysis

The SEM system of Texas State University is also equipped with an Energy Dispersive X-ray Spectroscopy (EDS) system to provide elemental analysis. SEM and EDS were run on the magnetic polymer composite filament samples. Firstly, the SEM images were created, and then EDS was used to verify composition of the samples.

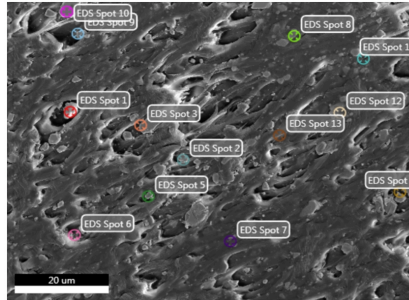




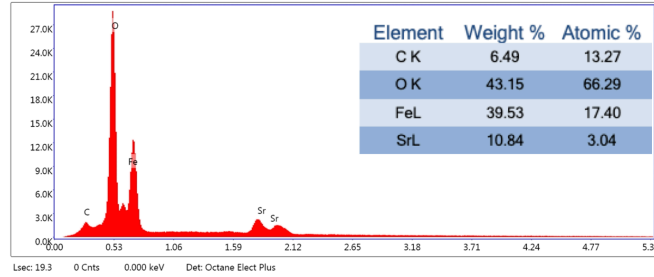
**Fig. 3.14:** EDS spectra of 5 wt.% filament (cross-section along the radial direction).

EDS gives the information on the elemental composition of the sample. Notably, the distribution of some components in the whole material often affects the final various properties of the polymer composites, meaning that EDS becomes a more important tool for polymer composite science [21, 22].

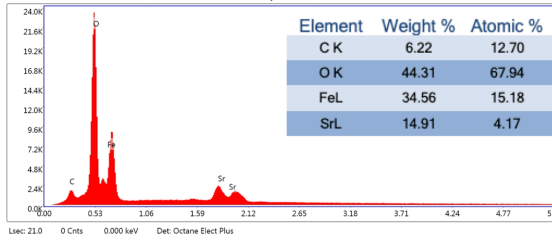
EDS for our composite filaments were done at 8 kV energy. Fig. 3.14 shows the EDS SEM image on the 5 wt.% composite filament sample and the EDS beam was scanned in random areas of the sample. The EDS SEM image (Fig. 3.14) shows the 40 wt.% composite filament sample. The EDS (Fig. 3.14 and Fig. 3.15) confirms the composition of the constituent elements are present in the composite filament. And confirms that magnetic particles are homogeneously distributed in the fabricated composite. According to the spectrum, the sample mainly consisted of C, O, Fe and Sr components. We can see small peak between C and O and it is assuming Nitrogen (N) from the PA12's N-H group. There are no any impurities index in the compounds.



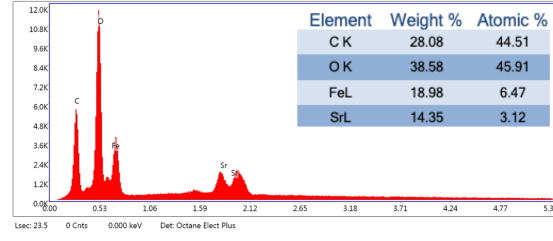
EDS Spot 1 - EDS1



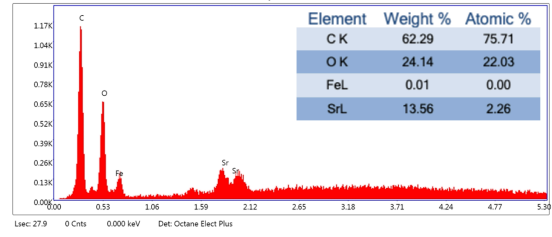
EDS Spot 2 - EDS1



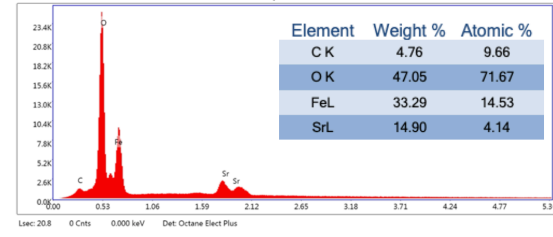
EDS Spot 3 - EDS1



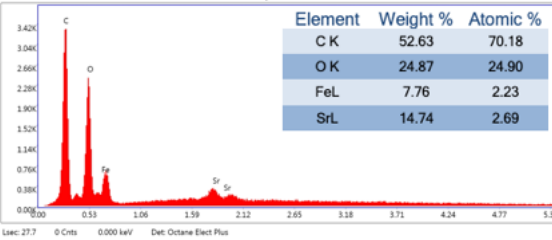
EDS Spot 4 - EDS1



EDS Spot 5 - EDS1



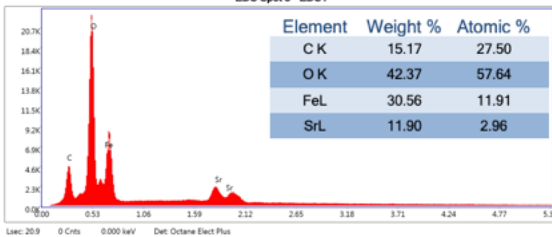
EDS Spot 6 - EDS1



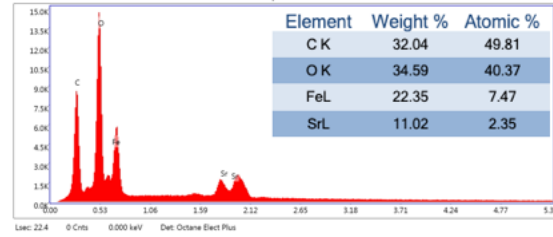
EDS Spot 7 - EDS1



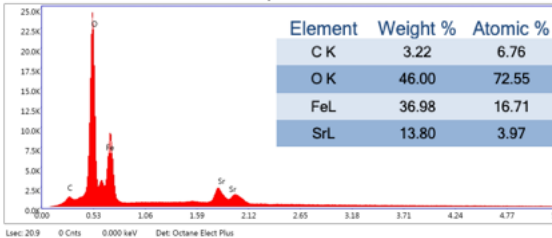
EDS Spot 8 - EDS1



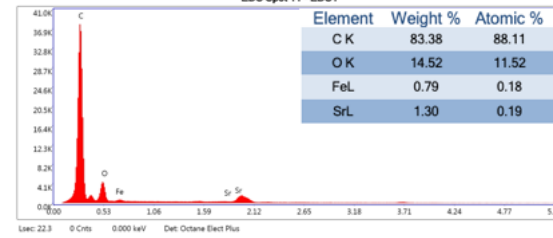
EDS Spot 9 - EDS1



EDS Spot 10 - EDS1



EDS Spot 11 - EDS1



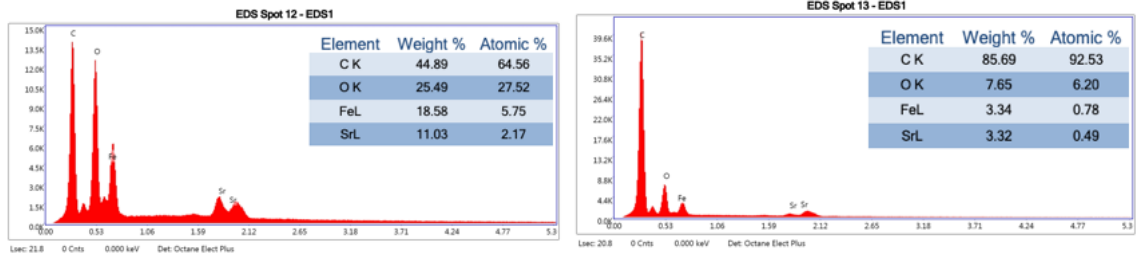


**Fig. 3.15:** EDS spectra of 40 wt.% filament (cross-section along the radial direction).

### 3.3.5 Imaging Sputter Coater

Sputter Coaters are used in SEM research to apply an electrically conductive thin film on non-conductive samples and avoid charging effects. The coating needs to be thin, so the coated film is representative of the surface topography of the original sample. Such films inhibit 'charging', reduce thermal damage, and enhance secondary electron emission [23].



**Fig. 3.16:** Imaging Sputter Coater of Texas State University.

The EMS150T system is a versatile sputter coater/turbo evaporator (see Fig. 3.16). This sputter coater is capable of producing coatings that are much thinner than standard Au/Pd sputter coaters, which can result in higher-resolution images [24]. The unique feature of the EMS150T is a rotating sample table which ensures even depositions (typically 2-5nm). It uses standard 57 mm targets, avoiding the necessity of special large profile targets. A Head/shutter assembly is fitted as standard, which allows sputter cleaning of oxidizing targets. The EMS150T fitted with a film thickness monitor (FTM), which

measures the coating thickness on a crystal in the chamber, to control the coating applied to the sample. It will automatically terminate a coating cycle when the required thickness has been achieved.

In order to improve the resolution of our filament SEM images, all samples were coated with a conductive 4 to 6 nm layer of Iridium (Ir) deposited by above-described coater. Both Au and Ir provide a conformal conductive layer for SEM imaging. The main advantage to an Ir coating is that it has a smaller grain size than Au, so depending on the feature size, Ir would help produce a higher resolution image for our samples. Hence, the ideal coating is a thin layer that has crystallites smaller than the feature size(s) present in the sample, while providing a conductive path for the electrons so that the sample will not experience “charging” or drift during e-beam imaging. See the images below that illustrate the differences in grain size of Au and Ir. As we can see, Ir is a more uniform, fine-grained deposition as compared to Au.

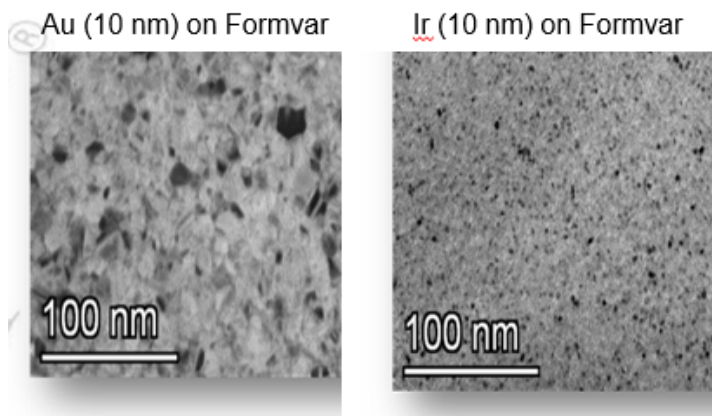


**Fig. 3.17:** TEM images for the illustration of the difference between the two coatings based on the grain size of Au and Ir [ARSC document of Texas State University].

### 3.3.6 Fourier Transformed Infrared Spectroscopy (FTIR)

Fourier transformed infrared spectroscopy (FTIR) is an analytical technique that uses incident radiation in the IR spectrum. The IR spectrum includes wavelengths of light from  $12800$  to  $10\text{cm}^{-1}$  and is typically divided into three regions, the near infrared ( $12800$ - $4000\text{cm}^{-1}$ ), the mid-infrared ( $4000$ - $200\text{cm}^{-1}$ ) and the far-infrared region ( $50$ - $1000\text{cm}^{-1}$ ). The most common measured region is the mid-infrared due to most molecules absorbing IR radiation at these wavelengths.

Infrared radiation causes bonds between atoms to vibrate and the wavelength are characteristic of specific bonds. Thus, the FTIR spectrum of a molecule provides information about the organic functional groups present in a molecule such as alcohols, ketones, amines and others. The IR energy changes the dipole moment found between bonding atoms as well as increases the vibrational energy of the bonds. Since each bonding pair has the same energy, the resulting IR spectrum gives a unique fingerprint of a molecule. A common FTIR setup is shown in Fig. 3.18a. The incident light enters a Michelson interferometer where the light is split into two beams. The movable mirror then translates through the wavelengths and an interferogram is created by the detector. A Fourier transformation is then performed on the data to translate the interferogram into spectrum of wave numbers.

To aid in signal strength and detection for samples an attenuated total reflectance (ATR) crystal is often used. ATR enhances signal strength by allowing the incident beam to interact with the sample multiple times. The incident IR beam is sufficiently high power to allow for multiple absorption events without totally absorbing all light. This ATR method increases the signal to noise ratio of the tool in particularly for low absorbing materials. The ATR crystal and beam path are shown in Fig. 3.18a.

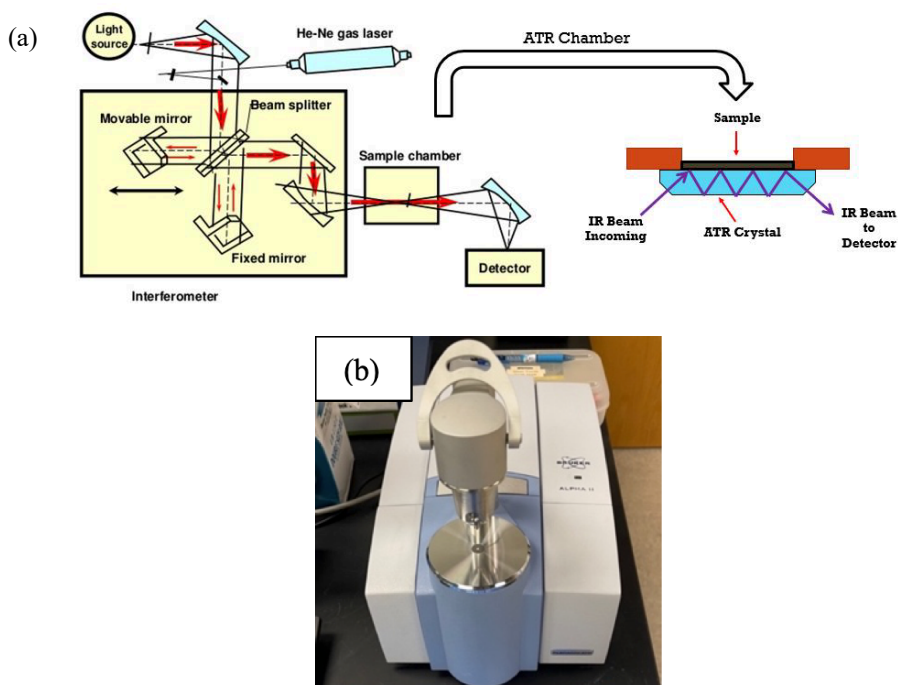


**Fig. 3.18:** (a) FTIR basic operation principle and beam amplification effect of the ATR system (top) [19]  
 (b) Fourier Transformed Infrared Spectroscopy (FTIR) of Texas State University (bottom).

Fourier transform infrared spectroscopy (FTIR) is used extensively for the characterization of quantitative analysis of composite materials (polymer blends), for the identification of their compatibility via intermolecular hydrogen bonding, and also to investigate their degradation processes.

For the FTIR measurement, we prepare the sample by cutting along the radial axis of the filament with a knife at room temperature. Background spectra taken at the beginning and end to ensure no artifacts were introduced. Samples were taken using attenuated total reflection (ATR) mode and the Germanium crystal was used. Samples were pushed onto the ATR with the same source during the measurement using the standard sample holder fixture of the Nicolet 6700.

### ***3.3.6.1 FTIR Spectra Analysis***

Fourier Transform Infrared spectroscopy (FTIR) was used in this work to analyze functional groups of neat PA12 filament and further characterize the different wt.% (5, 26, 40 and 70 wt.%) of SrFe<sub>12</sub>O<sub>19</sub>/PA12 composite filament and collected infrared spectra for the structural analysis. This analysis was carried out using a Bruker Alpha II FTIR spectrometer. The conditions of measurement were as follows: spectral region of 4000–400 cm<sup>-1</sup>; spectral resolution of 4 cm<sup>-1</sup>.

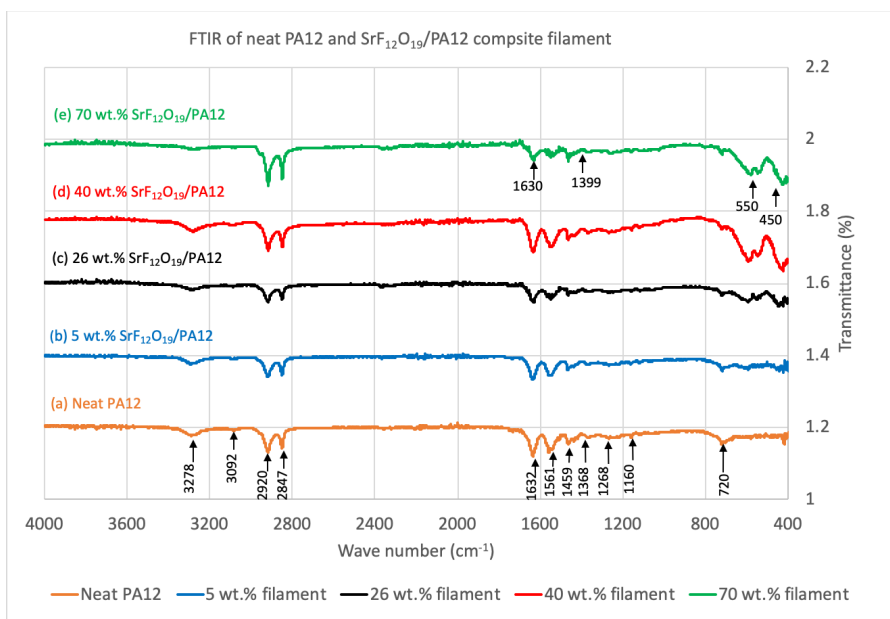


**Fig. 3.19:** FTIR spectra of (a) neat PA12 and (b) 5, (c) 26, (d) 40, and (e) 70 wt.% SrFe<sub>12</sub>O<sub>19</sub>/ PA-12 composite filament (cross section along the radial direction).

From the Fig. 3.19a we can see the infrared spectra of neat PA12 filament, a stretching vibration of N–H and C=O bonds, which occur at 3278 cm<sup>-1</sup> and 1632 cm<sup>-1</sup>, respectively [25] and the moderate amide B band at 3,092 cm<sup>-1</sup> with weak intensity of  $\alpha$ -PA12 [26, 27]. The CH<sub>2</sub> asymmetric stretching which occurs at 2920 and 2847 cm<sup>-1</sup>, which were also observed in each curve of Fig. 3.19. The N-H bending occurs at 1561 cm<sup>-1</sup>, 1368cm<sup>-1</sup> corresponds to CH<sub>2</sub> twisting vibration [28], C-N stretching at 1268 cm<sup>-1</sup> and N-H out of plane bending occurs at 720 cm<sup>-1</sup> [29, 30]. However, with the increase of the loading concentration of the SrFe<sub>12</sub>O<sub>19</sub>, most of the peaks related to the N–H functional groups disappeared in the FTIR spectrum of SrFe<sub>12</sub>O<sub>19</sub>/PA12 composites (Fig. 3.19b to 3.19e) [31]. The FTIR spectrum of SrFe<sub>12</sub>O<sub>19</sub> has been well reported in the literature [26] and FTIR spectrum of SrFe<sub>12</sub>O<sub>19</sub> reveals that the marked peaks in the range of 400–650 cm<sup>-1</sup> (Fig. 3.19b, c, d and e) SrFe<sub>12</sub>O<sub>19</sub>/PA12 composite filaments are intrinsic vibrations of the tetrahedral and octahedral sites for the M SrFe<sub>12</sub>O<sub>19</sub>, respectively [32, 33]. The peak occurring at 1630 cm<sup>-1</sup> are assigned to the O–H bending vibration of chemically adsorbed water and 1399 cm<sup>-1</sup> the O–H stretching mode of the adsorbed free water molecules, respectively [33, 34].

### 3.3.7 X-Ray Diffraction (XRD)

XRD is a powerful technique to investigate the crystallographic properties of materials. Performing XRD analysis on samples of polymers or composites provides important solid-state structural information such as the degree of crystallinity, crystalline form, crystalline perfection, preferred orientation, and texture. It is used in this dissertation to study the degree of crystallinity for the semi-crystalline, amorphous polymeric matrix and verify the crystal structure and texture of the magnetic strontium ferrite particles [35].

XRD is a nondestructive technique for the material system studied in this dissertation. The measurements can be performed in a normal atmosphere without any special sample preparation. Although X-ray diffractometry also can be done in a special environment such as, at elevated temperature or high pressure with special arrangement, here all XRD measurements are performed at RT under standard atmospheric pressure. This technique is used for studying lattice constants, crystal structure, crystal orientations, preferred orientations including orientation distributions, strain, crystal defects, grain size, film thickness, and film density [36].

Crystals contain a regular array of atoms. The spacings between the atomic planes are comparable with the X-ray wavelength. Therefore, a crystalline material can be considered as a three-dimensional diffraction grating for X-rays. When X-rays are incident at a certain angle on a crystalline sample, they interact with the material and the X-ray beam is diffracted as illustrated in the Fig. 3.20a. Based on the atomic spacing between the planes, angle of incidence and wavelength of the incident X-rays, the interference between the diffracted X-ray beam may be constructive or destructive. Constructive interference occurs when the parameters satisfy the Bragg's condition below.

$$n\lambda=2d \sin\theta \quad (3.5)$$

Here,  $n$  is an integer,  $d$  is the atomic spacing,  $\lambda$  is the wavelength of X-ray and  $\theta$  is the diffraction angle. In a  $\theta/2\theta$  measurement, the X-ray beam incident on the sample at an angle  $\theta$  and the detector collects the diffracted X-rays at an angle  $2\theta$ . Typically, the angle is varied from  $5^\circ$  to  $80^\circ$ , and the detector collects the diffracted X-rays. Peaks are observed for certain positions of  $2\theta$  in an X-ray count versus  $2\theta$  plot, from which crystallographic information are extracted.

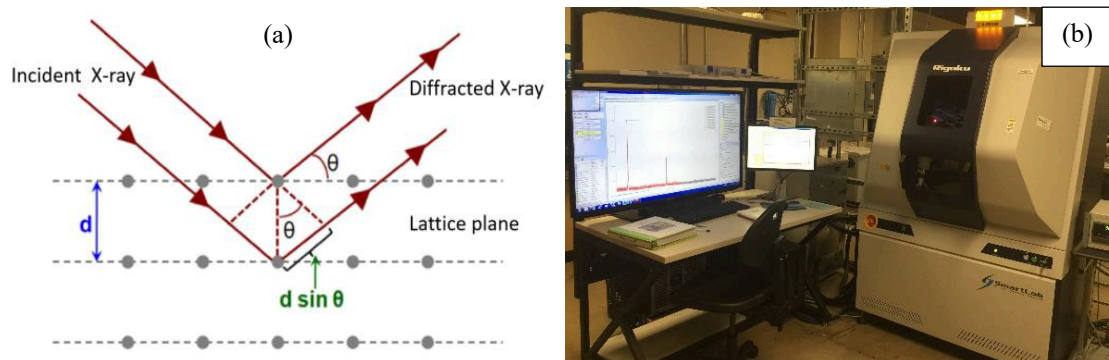


**Fig. 3.20:** (a) Diffraction of X-ray at crystal planes (b) Rigaku Smartlab diffractometer of Texas State University [16].

For this research, XRD measurements were conducted using the Rigaku Smartlab high-resolution X-Ray diffractometer using the Smartlab Guidance software. The components of the system are an X-ray tube, an X-ray detector, a goniometer, an incident optical system, and a receiving optical system. The SmartLab diffractometer is a 5-axis tool. The position of the sample can be manipulated with a rotation stage and two goniometers and the detector can be moved along two circles as shown in the Fig. 3.20 [37].  $\theta$ - $2\theta$  measurements can detect the plane parallel to the sample surface. Typically, a  $\theta/2\theta$  scan is performed for identification of phase and crystal structure. A Cu  $K\alpha$  X-ray source (1.76kW) [38] operating at 40 kV and 44 mA used as the incident radiation source and operated in the Bragg-Brentano high resolution configuration. The  $\theta$ - $2\theta$  XRD spectrum scanned with a  $2\theta$  range of 5-90°.

### 3.3.7.1 XRD Measurement Analysis

X-ray diffractometer (XRD) is a powerful tool used to analyze the atomic or molecular structure of materials. XRD was used here to identify the phase constituent of neat PA12 filament and SrFe<sub>12</sub>O<sub>19</sub>/PA-12 composite filaments. A Rigaku Smartlab high-resolution XRD was used to perform the X-ray Reflectivity measurement using a standard anode Cu  $K\alpha$  source (1.76 kW) to generate the X-ray beam. Fig. 3.21 show XRD patterns of the neat PA-12 and different wt.% (5, 26, 40 and 70 wt.%) of SrFe<sub>12</sub>O<sub>19</sub>/PA-12 composite filament. For the XRD measurements (Fig. 3.21), the samples were prepared by

cutting along the radial axis with a knife and attaching those filaments with wax as adhesive to a glass slide horizontally as shown in the insert of Fig. 3.21 below. Data was acquired over the range of ( $2\theta$ ) 0–90° with a step size of 0.0017 and a scan rate of 7° min<sup>-1</sup> at room temperature.

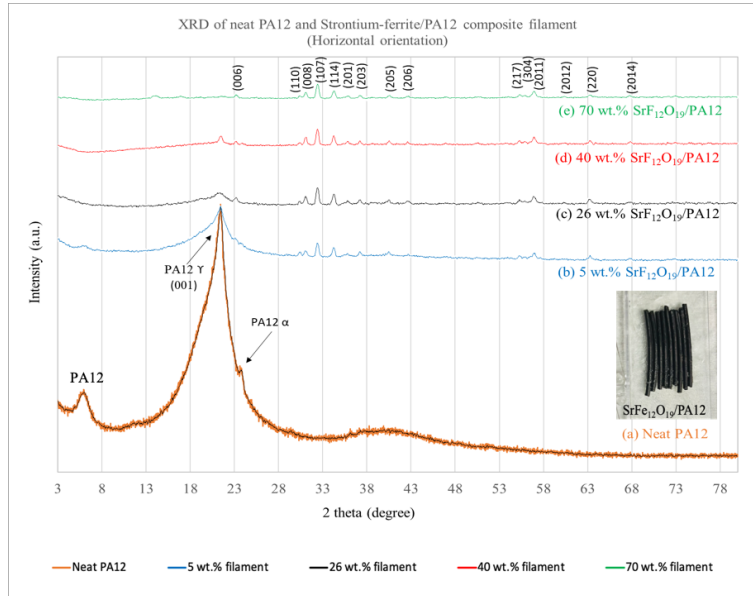


**Fig. 3.21:** XRD patterns of (a) neat PA12 and (b) 5, (c) 26, (d) 40, and (e) 70 wt.% SrFe<sub>12</sub>O<sub>19</sub>/ PA-12 composite filament (horizontally).

The  $\theta$ - $2\theta$  XRD spectra show weak nylon peaks around 6°, 11.2°, 21.5°, 23.8°, and a small very wide peak around 41°. In the neat PA12 filament both crystalline  $\alpha$  and  $\gamma$  phases were observed with their corresponding peaks. The peak at 23.8°  $2\theta$  corresponds to the  $\alpha$  phase. Peaks at 11.2° and 21.5°  $2\theta$  correspond to the  $\gamma$  phase [39, 40]. These characteristic peaks are for the  $\gamma$  and  $\alpha$ -phases of nylon and indicate that the nylon matrix in our samples is semi-crystalline. Position of the peaks are in good agreement with results reported on by others [27, 30, 41, 42].

As shown in Fig. 3.21, a sharp peak at  $2\theta=21.5^\circ$  can be indexed to the (001) crystallographic plane of the neat PA12. However, it eventually almost vanished with the increase of the loading level of the strontium ferrite particle in the PA12 matrix for SrFe<sub>12</sub>O<sub>19</sub>/PA12 composites (Fig. 3.21b to 3.21e). The characteristic crystallographic diffraction peaks of strontium ferrite appeared in the spectra (Fig. 3.21 b, c, d and e) of the magnetic composite samples. Strontium ferrite diffraction peaks were observed at  $2\theta=$

30.83°, 32.40°, 34.36°, 35.47°, 37.07°, 40.63°, 42.82°, 55.05°, 57.01°, and 63.05° in the SrFe<sub>12</sub>O<sub>19</sub>/PA12 composite samples. These peaks correspond to the typical M type SrFe<sub>12</sub>O<sub>19</sub> characteristic peaks as observed by other [31-33, 43, 44] and which were indexed to be the (110), (107), (114), (201), (203), (205), (206), (217), (304), and (220) lattice planes, respectively [44]. The sharp diffraction peaks and high intensity indicate the good crystallinity of our composites which firmly proves the successful formation of in SrFe<sub>12</sub>O<sub>19</sub>/PA12 composite.

To check the texture of the filaments, we also did XRD measurements (Fig. 3.22), filament samples with a different orientation. The filaments were cut with a knife perpendicular to the cylindrical axis the radial axis and attached with wax to a glass slide vertically like the tree trunk type of arrangement shown in the inset of Fig 3.22 below. Data were acquired over the range of (2θ) 0–90° with a step size of 0.0017 at room temperature.

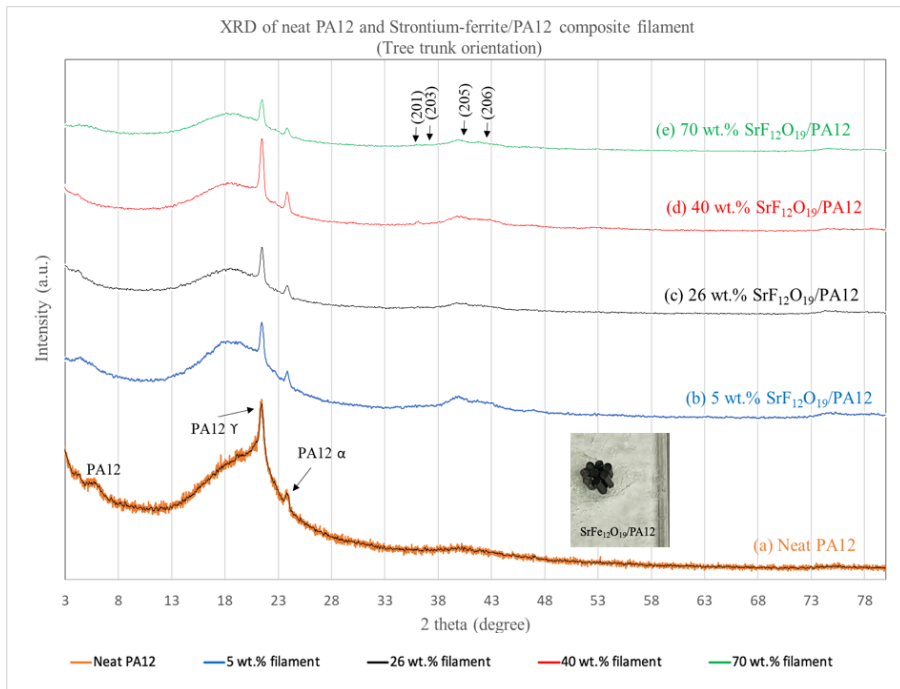


**Fig. 3.22:** XRD patterns of (a) neat PA12 and (b) 5, (c) 26, (d) 40, and (e) 70 wt.% SrFe<sub>12</sub>O<sub>19</sub>/ PA-12 composite filament (tree trunk).

In the neat PA12 filament tree trunk XRD spectra, both crystalline  $\alpha$  and  $\gamma$  phases were observed. PA12  $\alpha$  and  $\gamma$  peaks were observed for all loading levels. The peak at 21.5° 2θ corresponds to the  $\gamma$  phase and the 23.8° 2θ corresponds to the  $\alpha$  phase [39, 40]. Although the intensity of the PA12 peaks decreases with strontium ferrite loading level

even the 70 wt.% sample show clear PA-12 peaks indicative that even at the highest loading level the PA12 is semi-crystalline. Wide strontium ferrite peaks of low intensity are visible between 35 and 45 degrees for all loading levels although the largest intensity peaks are visible in the spectra of the lower loading level composites (Fig. 3.22b to 3.22e). The absence of the other strontium ferrite peaks in the tree trunk sample suggest that the strontium ferrite particles in our filaments are textured. Also, the PA-12 diffracts more strongly in certain directions. So, it confirms that also the PA-12 is textured for our manufactured filaments.

### 3.3.8 Thermo-Gravimetric Analysis (TGA) and Differential Scanning Calorimetry (DSC)

Thermal analysis is an important analytical tool used to study the properties of materials as the temperature is changed. Differential scanning calorimetry (DSC) and thermogravimetric analysis (TGA) are two of the most widely used thermal analysis techniques in the characterization of crystalline and amorphous materials [45].

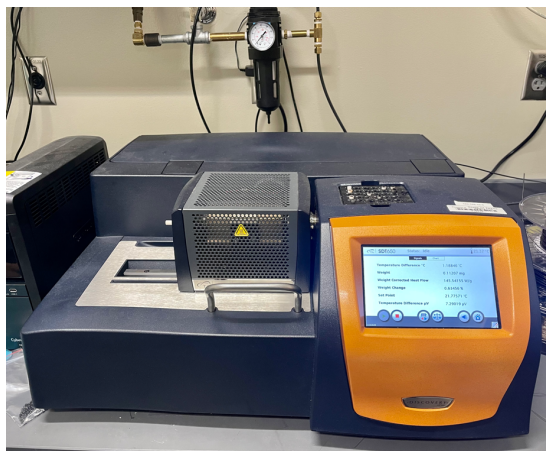


**Fig. 3.23:** An SDT 650 Simultaneous Thermal Analyzer of TA Instruments to perform Thermo-Gravimetric Analysis (TGA) and Differential Scanning Calorimetry (DSC) analysis at Texas State University.

DSC measures various thermal transitions associated with a material when it is heated or cooled in a controlled manner. The thermal transition could be due to a physical transformation or a chemical reaction. Physical transformations, such as melting, crystallization, polymorph conversion, desolvation, and dehydration, are always associated

with a change in enthalpy. This change of enthalpy is detected as a heat-absorbed (endothermic) or heat-released (exothermic) event in the DSC measurement graph. The thermal events associated with melting, dehydration, or desolvation are directly related to the crystal structure of a material, and therefore, provide fundamental information related to its crystal structure. DSC monitors the change of heat flow as the sample is heated or cooled and reveals any change in heat capacity that occurs during any solid-state transition, and is, therefore generally useful for determining the glass transition temperature of amorphous materials [45]. TGA measures changes in sample mass with temperature within a controlled environment. Such measurement provides information concerning the content of volatile materials, such as residual solvent or moisture. It also provides information of the degradation temperature, the level organic and inorganic component in the materials, decomposition points, and combustion of solvent residues [46].

An SDT 650 Simultaneous Thermal Analyzer of TA Instruments was used to perform Thermo-Gravimetric Analysis (TGA) and Differential Scanning Calorimetry (DSC) analysis on the filaments to showing a glass transient temperature, the melting temperature and how the multiple annealing cycle effect the thermal behavior of the filaments.

#### ***3.3.8.1 TGA Measurement Analysis***

The thermogravimetric study is a thermo-analytical technique which is crucial in monitoring the thermal stability of the composites by measuring the weight loss as a function of temperature. There is a close relationship between the thermal stability and the structural integrity of materials which require understanding the decomposition kinetics of our material in a temperature-controlled environment [47].

The thermogravimetric data obtained from the simultaneous differential thermal experiment on the neat PA12, pristine strontium-ferrite/PA12 composite filament and multiple temperature cycle annealed strontium-ferrite/PA12 composite filament and presented in Table 3.3. The multiple temperature cycle annealed strontium-ferrite/PA12 composite filament was prepared by increasing temperature ascending series first four scans (150 °C, 175 °C, 200 °C, 225 °C) under exposure of 500 Oe field and the next four

scans descending temperature series (225 °C, 200 °C, 175 °C, 150 °C) on respectively the 5 and 40 wt.% sample. An SDT 650 is used to perform simultaneous differential thermal experiment and all tests were ramped with a heating rate of 10 °C/min up to 600 °C in a nitrogen environment. Fig. 3.24 shows the TGA curve which illustrates the thermal degradation behavior exhibited by the composites. The decomposition temperature and weight loss obtained from the thermogravimetric data are thermal properties that can be used to deduce the thermal stability of the composite.

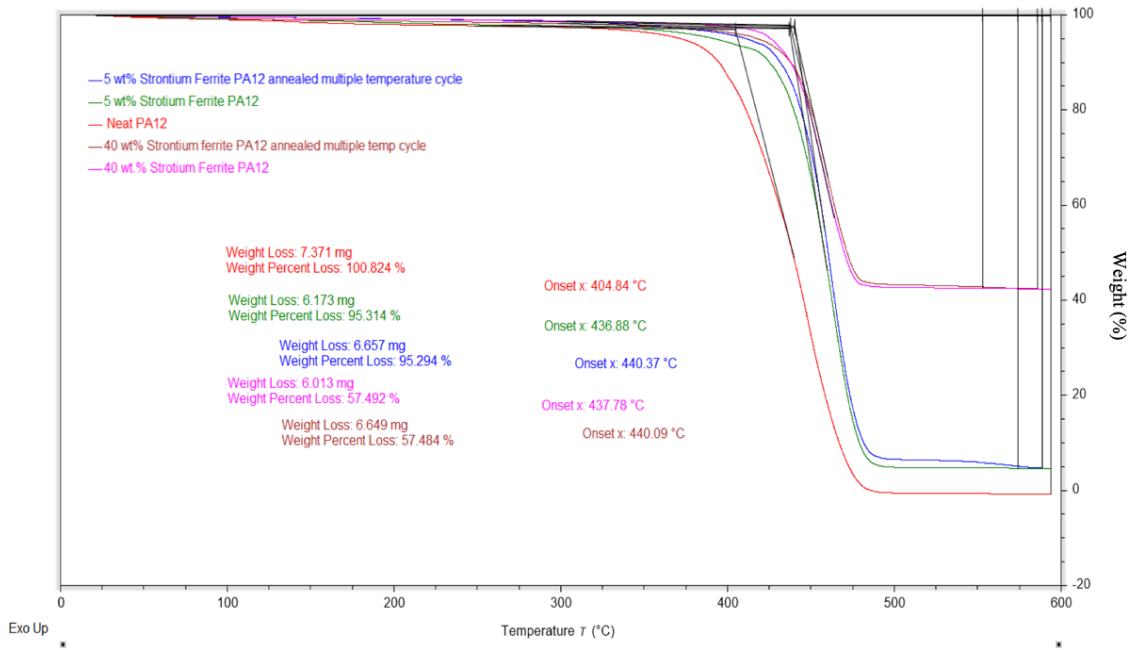


**Fig. 3.24:** TGA curves of neat PA-12, Strontium-Ferrite/PA-12 (5 and 40 wt.%) composites and multiple temperature cycle annealed Strontium-Ferrite/PA-12 (5 and 40 wt.%) composites.

The TGA curve in Fig. 3.23 shows the onset decomposition temperature and the weight percent loss at the end of the heating profile. The extrapolated onset temperature signifies the temperature at which the weight loss begins which is an indication of the thermal stability of the material. There are three thermal degradation stages noticeable on the TGA curve of the nanocomposite shown in Fig. 3.24. Prior to the appreciable mass loss changes, there is an evaporation of bound water molecules in the recurring polar amide groups of the Polyamides 12, which typically takes place at temperature up to ~125 °C. This is not far-fetched since polyamides are typically known to be highly hygroscopic due to their high moisture sensitivity [48, 49].

The first noticeable decomposition stage observed between  $\sim 125\text{--}380$  °C could be attributed to onset of the depolymerization of polyamide to  $\epsilon$ -caprolactam [50]. The second degradation stage was observed between  $\sim 380\text{--}475$  °C which is characterized by thermo-oxidative destruction and highlighted by a significant mass loss [48]. This region represents the major degradation and the onset of the decomposition temperature presented in Table 3.3 was extrapolated in this region. The decomposition temperature is a measure of the thermal stability of the magnetic polymer composite, and it could be observed that the decomposition temperature of the neat PA12 was increased with the increase of the loading level of the magnetic filler platelets (magnetic polymer composite) and also with multiple temperature cycle annealed magnetic polymer composite samples. Furthermore, no major degradation was observed with inclusion of magnetic filler on the TGA curve and the thermal stability of the composites was sustained throughout the scanning temperature. The third degradation stage between  $\sim 475\text{--}600$  °C represents the *combustion of carbonized residue* of the thermally degraded nanocomposite and the amount of residue can be evaluated from the weight % loss measurements. The weight loss percentages at the final temperature reduces with increasing magnetic filler loading and the pristine nylon being the highest with 100%. It is noteworthy that the residue amount was about the weight fraction of the strontium-ferrite incorporated in the PA12 matrix which clearly indicates that the strontium-ferrite was not thermally degraded due to the inert atmosphere employed in the thermal experiment. Overall, it could be observed that 40 wt.% strontium-ferrite addition has the most significant thermal stability on the PA12 matrix considering the reduction in the weight % loss measurements of the host polymer.

**Table 3.2:** Mass loss ( $\Delta m/m_{\text{initial}}$ ) % of neat PA12 and strontium-ferrite/PA12 composites:

Transition Temperatures (°C)	Neat PA12 Mass loss (%)	Pristine 5 wt.% Strontium-ferrite/PA12 composites Mass loss (%)	Multiple temperature cycle annealed 5 wt.% Strontium-ferrite/PA12 composites Mass loss (%)	Pristine 40 wt.% Strontium-ferrite/PA12 composites Mass loss (%)	Multiple temperature cycle annealed 40 wt.% Strontium-ferrite/PA12 composites Mass loss (%)
RT to 125 °C	1.2	0.95	0.56	0.56	0.97
125 °C -380 °C	4.8	3.2	2.5	1.4	2
380 °C -475 °C	96	84	82	54	52
475 °C -486 °C	100	-	-	-	-
475 °C -600 °C	100	69	73	6.5	9.5

**Table 3.3:** TGA data of Strontium-ferrite/PA12 composites:

Transition parameters	Neat PA12 filament	Pristine 5 wt.% Strontium-ferrite/PA12 composites filament	Multiple temperature cycle annealed 5 wt.% Strontium-ferrite/PA12 composites filament	Pristine 40 wt.% Strontium-ferrite/PA12 composites filament	Multiple temperature cycle annealed 40 wt.% Strontium-ferrite/PA12 composites filament
Decomposition temperature, $T_g$ (°C)	404	436	440	437	440
Weight % loss	100	95	95	57	57

### 3.3.8.2 DSC Measurement Analysis

The thermal properties data of the magnetic polymer composites that was evaluated from the DSC studies are reported in Table 3.3. DSC is an important technique that was used to qualitatively and quantitatively characterize the thermal transitions unique to a material [47]. The thermal properties measured are thermal transitions such as glass transition ( $T_g$ ), melting ( $T_m$ ), peak crystallization temperature, and the enthalpy of crystallization which was used to evaluate the degree of crystallinity of the neat PA12 and magnetic polymer composite. The DSC curves presented in Fig. 3.25 exhibits different exothermic and endothermic peaks that signifies observable transitions in the thermal profile of the composite. It is noteworthy that, the peaks facing upward are exothermic and that endothermic peaks proceed downward on the DSC curves (Fig. 3.25).

The glass transition temperature ( $T_g$ ) is the first thermal transition observable in the DSC scan of the composites. The glass transition is represented as the first endothermic peak (Fig. 3.25), which indicates the temperature region at which the amorphous portion of the semi-crystalline PA12 matrix experience changes from the rigid glassy to a more flexible, rubbery state. The glass transition temperature ( $T_g$ ) of the neat PA12 matrix occurs at 47.34 °C and a minimal increase to 47.55 and 48.10 °C was observed at 5 and 40 wt.% reinforcement respectively. Hence, it could be observed that the glass transition temperature slightly increases with increasing magnetic filler addition. This can be traced to the enhancement of the bonding strength along the matrix-filler interface induced by the strontium-ferrite platelets. The incorporated strontium-ferrite reduces the free volume between the molecular chains of the polyamide 12 and consequently promote restriction of segmental motion of the polymer [48]. Multiple temperature cycle annealed (5 and 40 wt.%) composite's  $T_g$  slightly decreases than the pristine (5 and 40 wt.%) composites.

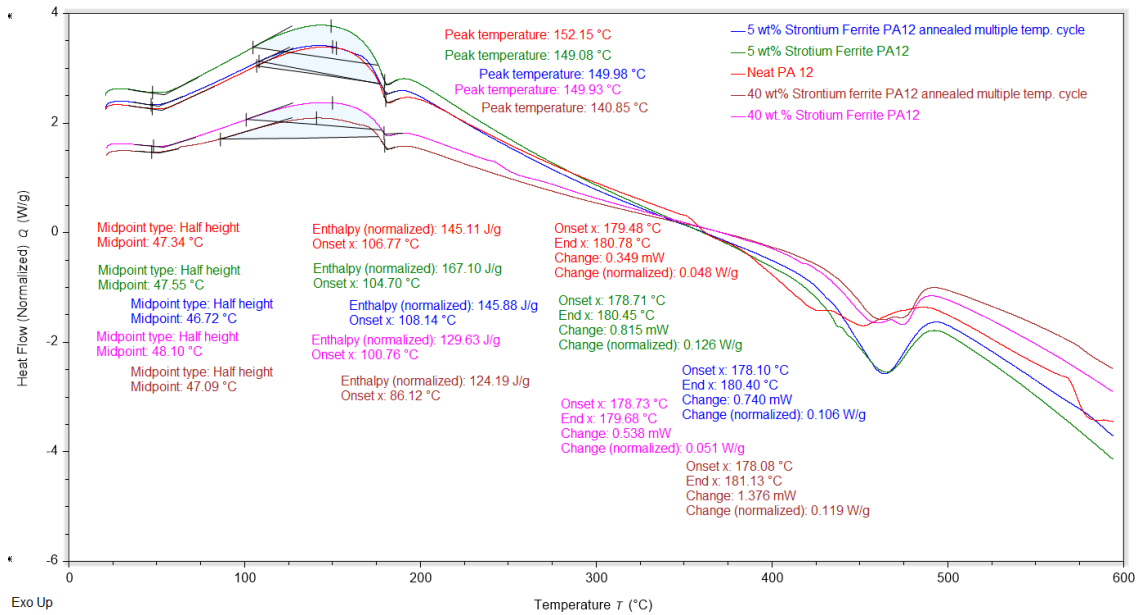


**Fig. 3.25:** DSC curves of neat PA-12, Strontium-Ferrite/PA-12 (5 and 40 wt.%) composites and multiple temperature cycle annealed Strontium-Ferrite/PA-12 (5 and 40 wt.%) composites.

The transition peak after the  $T_g$  illustrates the crystallization behavior of the investigated material system. The peak crystallization temperature was observed to be highest for the neat Nylon matrix, however, there was an early onset of crystallization at 5 and 40 wt.% respectively. This is expected, and it is consistent with the Hoffman's nucleation theory which describes polymer crystallization in terms of kinetics and thermodynamics of surface nucleation [51]. The addition of magnetic filler creates new surfaces in the nylon matrix thereby reducing the total surface energy of nuclei formation and consequently promoting heterogeneous nucleation which possesses a lower Gibbs free energy for crystallization. The heat of crystallization is the enthalpy associated with the crystallization process and could be used to determine the degree of crystallinity in the investigated material according to the following equation [52].

$$X_c (\%) = (\Delta H_m / (1 - \phi) \Delta H_o) \times 100 \quad (3.6)$$

where  $\Delta H_m$  is the enthalpy of crystallization melting shown in the figure above,  $\phi$  is the weight fraction of strontium-ferrite magnetic filler,  $\Delta H_o$  is the consensual value reported in literature for the enthalpy of fusion of 100 % crystalline PA12, given as 209 J/g [53].

**Table 3.4:** DSC data of Strontium-ferrite/PA12 composites:

Transition parameters	Neat PA12 filament	Pristine 5 wt.% Strontium-ferrite/PA12 composites filament	Multiple temperature cycle annealed 5 wt.% Strontium-ferrite/PA12 composites filament	Pristine 40 wt.% Strontium-ferrite/PA12 composites filament	Multiple temperature cycle annealed 40 wt.% Strontium-ferrite/PA12 composites filament
Glass transition temperature, $T_g$ (°C)	47	47	46	48	47
Melting temperature, $T_m$ (°C)	179	178	178	179	178
Heat of crystallization, (J/g)	145	167	146	130	124
Degree of crystallinity, (%)	69	84	73	100	99

Using the equation above,  $X_c$  (%) values have been computed as 69.38%, 84.11% and 102.87% for 0, 5 and 40 wt. % respectively of  $SrFe_{12}O_{19}$  loading. The observed increasing trend affirms the heterogeneous nucleation promoted by the magnetic fillers. It is suspected that the higher degree of crystallinity experienced at 5 and 40 wt.% loading levels translated into the improvement of thermal stability and mechanical properties. However, the deterioration of crystallinity of multiple temperature cycle annealed 5 and 40 wt.% composite could be due to possible weak interfacial strength vis-à-vis agglomeration effects [47].

The melting transitions illustrates the onset of melting of the investigated material system. It could be observed that the onset of melting temperature slightly decreases with increasing strontium-ferrite loadings. The presence of second phase strontium-ferrite could promote increase in dislocation movements in the nylon matrix in form of interstices. These interstices could be perceived as weak impurities which could lower the melting temperature of the nylon/ strontium-ferrite composites [47, 54].

Summarizing: Upon multiple anneal cycles  $T_g$ ,  $T_m$ , heat of crystallization and degree of crystallinity slightly decreased of the 5 wt.% and 40 wt.% PA-12/strontium-

ferrite composites. An increase of  $T_g$  and  $T_m$  that would confirm a significant increase of the average length of the polymer molecules was not observed.

### **3.4 Conclusion**

We have briefly introduced and discuss the major manufacturing and characterization tools and techniques used in this research. The instruments include manufacturing tools, imaging tools, optical characterization tools, thermal analysis tools and magnetic characterization tools. We briefly explained the used fabrication method to realize 3D-filaments with different loading level of hard-magnetic particles. The used Magnetic Field Assisted Additive Manufacturing (MFAAM) setup was also discussed briefly with a discussion on the used printing parameters. Additionally, measurement results on the structural, morphological and thermal properties of the realized composite filaments were presented.

## REFERENCES

- [1] T. N. Ahmed, M. C. Belduque, Binod D.C., J. Tate, W. Geerts, AIP Advances 11, 015048 (2021).
- [2] Available Online: <https://www.aniwaa.com/product/3d-printers/ord-solutions-rova3d-5-extruder/>
- [3] A. Sarkar, M.A. Somashekara, M. P. Paranthaman, M. Kramer, C. Haase, I. C. Nlebedim, Functionalizing magnet additive manufacturing with in-situ magnetic field source, Addit. Manuf. 34 (2020), 101289.
- [4] M. Suppan et al., "In-situ alignment of 3D printed anisotropic hard magnets," Sci. Rep., vol. 12, no. 1, pp. 1–7, 2022.
- [5] Presentation in Physics Colloquium at Texas State University by Dr. Ikenna Nlebedim, Ames Laboratory, USA.
- [6] Vibrating Sample Magnetometer Home Page. Retrieved December 25, 2022. Available Online: <https://gato-docs.its.txst.edu/jcr:7543b8ec-f619-49c3-888f-01c3ad13c7da/vsm.pdf>
- [7] Jiles, D. C. (1990). Introduction to Magnetism and Magnetic Materials (1st ed). Springer.
- [8] M.S. Thesis of Lauren Henderson, "Magnetic Characterization of Fe/PLA 3D Printed Filaments and Fe-doped Ga<sub>2</sub>O<sub>3</sub> Thin Films", Texas State University, August (2022).
- [9] MicroSense LLC. (n.d.). VSM Options and Accessories. MicroSense. Retrieved January 26, 2022, from <http://www.microsense.net/products-vsm-accessories.htm>
- [10] Erik Samwel, Ph.D. dissertation, University of Twente, 1995.
- [11] B. C. Dodrill, J.R. Lindemuth, J. K. Krause, Lake Shore Cryotronics, Inc., 575 McCorkle Blvd., Westerville, Ohio, USA.
- [12] MicroSense LLC. (n.d.). Torque Magnetometer. MicroSense. Retrieved December 26, 2022, Available Online: <http://www.microsense.net/products-vsm-torque-magnetometer.htm>

- [13] MicroSense EasyVSM: Operating software for the microsense vibrating sample magnetometer. Retrieved December 26, 2022, Available Online: <http://www.microsense.net/products-vsm-ez11.htm>
- [14] Hirox Digital Microscope. Retrieved December 26, 2022, Available Online: <https://www.hirox-usa.com/products/3d-digital-microscope/>
- [15] Jeol Ltd, "SEM Scanning Electron Microscope A to Z Basic Knowledge for Using the SEM Construction of Instrument Electron Gun Construction of Lens Condenser Lens and Objective Lens Specimen Stage Secondary Electron Detector Image Display and Recording Vacuum System," Jeol Ltd, pp. 1–32, 2009.
- [16] M. Hasan, "Methylammonium Acetate Assisted Deposition of Hybrid Halide Perovskite for Efficient Devices, " Ph.D. Thesis, Texas State University, San Marcos, USA (May-2019).
- [17] M. Mazumder, R. Ahmed, A. Wajahat Ali, and S. J. Lee, "SEM and ESEM techniques used for analysis of asphalt binder and mixture: A state of the art review," *Constr. Build. Mater.*, vol. 186, pp. 313–329, 2018.
- [18] Thermo fisher Scientific " SEM: Types of Electrons and the Information They Provide". Retrieved, December 26, 2022, Available Online: <https://www.thermofisher.com/blog/materials/sem-signal-types-electrons-and-the-information-they-provide/#:~:text=Secondary%20Electrons,-Unlike%20BSEs%2C%20SEs&text=They%20are%20a%20result%20of%20in-elastic%20interactions%20between%20the%20primary,topography%20of%20the%20sample's%20surface.>
- [19] C. E Manspecker, "Role of The Cation in Hybrid Organic-Inorganic Perovskite Solar Materials", Ph.D. Thesis, Texas State University, San Marcos, USA (August-2018).
- [20] Energy Dispersive X-Ray Spectroscopy. Retrieved 26 December 2022, Available Online: <https://sciencetech.tistory.com/17>
- [21] D. Son, S. Cho, J. Nam, H. Lee, and M. Kim, "X-ray-based spectroscopic techniques for characterization of polymer nanocomposite materials at a molecular level," *Polymers (Basel)*., vol. 12, no. 5, 2020.

- [22] P. Phengchan, A. Chaijaruwanich, W. Nakkiew, and S. Pitjamit, “Characterization and fabrication of bio-composite filaments for fused deposition modeling 3D printing,” *IOP Conf. Ser. Mater. Sci. Eng.*, vol. 639, no. 1, 2019.
- [23] Quorum Technologies “Q150T S/E/ES Sample Preparation System Instruction Manual”. Retrieved 26 December 2022, Available online: [https://www.stonybrook.edu/commcms/cryo/\\_pdf/EM150T\\_Manual.pdf](https://www.stonybrook.edu/commcms/cryo/_pdf/EM150T_Manual.pdf)
- [24] Quorum Technologies EMS 150 T ES Iridium Sputter Coater. Retrieved December 26 2022, Available Online: <https://cmrf.research.uiowa.edu/quorum-technologies-ems-150-t-es-iridium-sputter-coater>
- [25] S. Li, Y. Yang, X. Zha, Y. Zhou, W. Yang, and M. Yang, “Nanoscale morphology, interfacial hydrogen bonding, confined crystallization and greatly improved toughness of polyamide 12/polyketone blends,” *Nanomaterials*, vol. 8, no. 11, 2018.
- [26] N. Ma et al., “Crystal transition and thermal behavior of Nylon 12,” *E-Polymers*, vol. 20, no. 1, pp. 346–352, 2020.
- [27] P. Chen, M. Tang, W. Zhu, L. Yang, S. Wen, C. Yan, Z. Ji, Hai Nan Yusheng Shi, “Systematical mechanism of Polyamide-12 aging and its micro-structural evolution during laser sintering”, *Polymer Test.* 67 3701-379 (2018).
- [28] G. S. Martynkova, A. Sliva, G. Kratosova, K. C. Barabaszova, S. Studentova, J. Klusak, S. Brozova, T. Dokoupil, and S. Holesova, “Polyamide 12 Materials Study of Morpho-Structural Changes during Laser Sintering of 3D Printing Polymers”, 13, 810 (2021).
- [29] A. El Magri, S. E. Bencaid, H. R. Vanaei, and S. Vaudreuil, “Effects of Laser Power and Hatch Orientation on Final Properties of PA12 Parts Produced by Selective Laser Sintering,” *Polymers (Basel)*, vol. 14, no. 17, 2022.
- [30] R. Kuracina, Z. Szabova, E. Buranska, A. Patierova, P. Gogola, and I. Buransky, “Determination of Fire Parameters of Polyamide-12 Powder for Additive Technologies”, *Polymers* 13, 3014 (2021).
- [31] W. Chen, Q. Liu, X. Zhu, and M. Fu, “One-step in situ synthesis of strontium ferrites and strontium ferrites/graphene composites as microwave absorbing materials,” *RSC Adv.*, vol. 7, no. 64, pp. 40650–40657, 2017.

- [32] X. Meng, Y. Zhu, S. Xu, and T. Liu, “Facile synthesis of shell-core polyaniline/SrFe<sub>12</sub>O<sub>19</sub> composites and magnetic properties,” *RSC Adv.*, vol. 6, no. 6, pp. 4946–4949, 2016.
- [33] F. Bavarsiha, M. Rajabi, and M. Montazeri-Pour, “Synthesis of SrFe<sub>12</sub>O<sub>19</sub>/SiO<sub>2</sub>/TiO<sub>2</sub> composites with core/shell/shell nano-structure and evaluation of their photo-catalytic efficiency for degradation of methylene blue,” *J. Mater. Sci. Mater. Electron.*, vol. 29, no. 3, pp. 1877–1887, 2018.
- [34] C. L. Yuan and Y. S. Hong, “Microwave adsorption of core-shell structure polyaniline/SrFe<sub>12</sub>O<sub>19</sub> composites,” *J. Mater. Sci.*, vol. 45, no. 13, pp. 3470–3476, 2010.
- [35] X-Ray Diffraction for Polymers and Composites. Retrieved December 26 2022, Available Online: <https://www.intertek.com/polymers/x-ray-diffraction-composites/>
- [36] A. A. Bunaciu, E. gabriela Udriștioiu, and H. Y. Aboul-Enein, “X-Ray Diffraction: Instrumentation and Applications,” *Crit. Rev. Anal. Chem.*, vol. 45, no. 4, pp. 289–299, 2015.
- [37] Keigo Nagao, “X-ray thin film measurement techniques - Pole figure measurement,” vol. 27, no. 2, p. 2, 2014.
- [38] T. N. Ahmed, C. Belduque, M. Y. Chen, J. S. Tate, and W. J. Geerts, “Dynamic viscosity of strontium ferrite–nylon composite below the melting temperature,” *AIP Adv.*, vol. 12, no. 9, p. 095223, 2022.
- [39] G. V. Salmoria, R. A. Paggi, A. Lago, and V. E. Beal, “Microstructural and mechanical characterization of PA12/MWCNTs nanocomposite manufactured by selective laser sintering,” *Polym. Test.*, vol. 30, no. 6, pp. 611–615, (2011).
- [40] Y. Liu, L. Zhu, L. Zhou, and Y. Li, “Microstructure and mechanical properties of reinforced polyamide 12 composites prepared by laser additive manufacturing,” *Rapid Prototyp. J.*, vol. 25, no. 6, pp. 1127–1134, (2019).
- [41] G. S. Martynkova, A. Sliva, G. Kratosova, K. C. Barabaszova, S. Studentova, J. Klusak, S. Brozova, T. Dokoupil, and S. Holesova, “Polyamide 12 Materials Study of Morpho-Structural Changes during Laser Sintering of 3D Printing Polymers”, 13, 810 (2021).

- [42] N. Ma, B. Liu, L. Ma, S. he, H. Liu, Z. Zhang, A. un, M. Huang, C. Zhu, *e-Polymers* 20, 346-352 (2020).
- [43] K. Hedayati, A. Zahra, and D. Ghanbari, "Preparation and characterization of various morphologies of SrFe<sub>12</sub>O<sub>19</sub> nano-structures: investigation of magnetization and coercivity," *J. Mater. Sci. Mater. Electron.*, vol. 28, Jan. (2017).
- [44] G. Mohammadi Ziarani, Z. Kazemi Asl, P. Gholamzadeh, A. Badiei, and M. Afshar, "Sol-gel auto-combustion production of SrFe<sub>12</sub>O<sub>19</sub> magnetic nanoparticles and its application in the synthesis of spirooxindol-quinazolinone derivatives," *J. Sol-Gel Sci. Technol.*, vol. 85, no. 1, pp. 103–109, 2018.
- [45] S. R. Byrn, G. Zografı, X. Chen, "Differential Scanning Calorimetry and Thermogravimetric Analysis", pp. 124-141, (2017). DOI: 10.3139/9781569906446.007
- [46] Thermal Analysis Service. Retrieved December 26 2022, Available Online: [https://triclincilabs.com/page-directory/materials-analysis-services/thermal-materials-characterization-techniques-services-from-triclincilabs.html?utm\\_term=thermo%20gravimetric%20analysis&utm\\_campaign=THE+RMAL+Q3+2019&utm\\_source=adwords&utm\\_medium=ppc&hsa\\_acc=4485589874&hsa\\_cam=2069619741&hsa\\_grp=76131671213&hsa\\_ad=380048448629&hsa\\_src=g&hsa\\_tgt=kwd-786864644830&hsa\\_kw=thermo%20gravimetric%20analysis&hsa\\_mt=b&hsa\\_net=adwords&hsa\\_ver=3&gclid=Cj0KCQiAyracBhDoARIsACGFcS5QnIRsMSBSvEqJwpKVdcpptoR1K6qFNQOw8ScaAXXrsNAy85W33R8aAhKAEALw\\_wcB](https://triclincilabs.com/page-directory/materials-analysis-services/thermal-materials-characterization-techniques-services-from-triclincilabs.html?utm_term=thermo%20gravimetric%20analysis&utm_campaign=THE+RMAL+Q3+2019&utm_source=adwords&utm_medium=ppc&hsa_acc=4485589874&hsa_cam=2069619741&hsa_grp=76131671213&hsa_ad=380048448629&hsa_src=g&hsa_tgt=kwd-786864644830&hsa_kw=thermo%20gravimetric%20analysis&hsa_mt=b&hsa_net=adwords&hsa_ver=3&gclid=Cj0KCQiAyracBhDoARIsACGFcS5QnIRsMSBSvEqJwpKVdcpptoR1K6qFNQOw8ScaAXXrsNAy85W33R8aAhKAEALw_wcB)
- [47] O. K. Arigbabowo and J. S. Tate, "Additive manufacturing of polyamide nanocomposites for electrostatic charge dissipation applications," *Mater. Sci. Eng. B Solid-State Mater. Adv. Technol.*, vol. 271, no. April, p. 115251, 2021.
- [48] O. K. Arigbabowo, L. Omer, and J. Tate, "Fused filament fabrication of polyamide 6 nanographene composite for electrostatic discharge applications," *Mater. Sci. Eng. B*, vol. 287, no. February 2022, p. 116086, 2023.

- [49] N. Jia and V. A. Kagan, “Mechanical Performance of Polyamides with Influence of Moisture and Temperature – Accurate Evaluation and Better Understanding,” *Plast. Fail. Anal. Prev.*, no. May 2019, pp. 95–104, 2001.
- [50] A.C. Draye, O. Persenaire, J. Brožek, J. Roda, T. Košek, P. Dubois, “Thermogravimetric analysis of poly ( $\epsilon$ -caprolactam) and poly [( $\epsilon$ -caprolactam)-co-( $\epsilon$ -caprolactone)] polymers”, *Polymer* 42 (20), pp. 8325–8332, 2001.
- [51] S. Z. D. Cheng and B. Lotz, “Enthalpic and entropic origins of nucleation barriers during polymer crystallization: The Hoffman-Lauritzen theory and beyond,” *Polymer (Guildf.)*, vol. 46, no. 20, pp. 8662–8681, 2005.
- [52] A. K. Barick, and D.K. Tripathy, “Preparation and characterization of carbon nanofiber reinforced thermoplastic polyurethane nanocomposites,” *J. Appl. Polym. Sci.*, vol. 124, no. 1, pp. 765–780, 2011.
- [53] K. Chen et al., “Effects of build positions on the thermal history, crystallization, and mechanical properties of polyamide 12 parts printed by Multi Jet Fusion,” *Virtual and Physical Prototyping*, vol. 17, no. 3. pp. 631–648, 2022.
- [54] J. Kruželák, R. Dosoudil, R. Sýkora, and I. Hudec, “Rubber composites with incorporated magnetic filler,” *Polimery/Polymers*, vol. 59, no. 11–12, pp. 819–824, 2014.

## 4. TIME DEPENDENT STUDY

*“Everything should be made as simple as possible, but not simpler.”*

- Albert Einstein

Note: Most of the contents from this chapter (sections 4.1 and 4.2) was published in AIP Advances on 28 January 2021 by the author of this dissertation along with other co-authors. DOI number of the publication is <https://doi.org/10.1063/9.0000216>. The contents taken from the published article were cited where applicable.

### 4.1 Introduction

One of the main factors to consider in a permanent magnetic material application is the time dependence of the magnetic dipole moment volume density. If the magnet is exposed to an opposing magnetic field, some domains may preferentially align with the external field, reducing the magnet's overall strength. The domains can also randomly reorient when energy is imparted to the magnet, such as when it is dropped or struck sharply. In a similar way, magnetism is gradually lost when the magnet is heated at a temperature called the Curie point [1]. Hence, the magnetization of the permanent magnets decreases with time, random temperature fluctuations, stray magnetic fields and mechanical movement will cause magnetic properties to decay [1] and its coercivity ( $H_c$ ) is affected as well [2]. Consequently, if the magnetic moment of a permanent magnet used in an electrical generator or motor changes, the motor's operation conditions change leading to performance changes. When medium-permanent magnetic materials are used in information storage applications, it is important that any stored information is not corrupted by large magnetic relaxation effects, i.e. a change of magnetization with time. In this respect, the investigation of the time dependent behavior of the magnetization serves two purposes: (i) quantifying the stability of the magnetization state against thermal excitations, and (ii) deriving a more detailed microscopic understanding of the magnetization reversal mechanism. An appreciation of these factors is essential for

tailoring hard magnetic materials with the required magnetic hysteretic behavior for specific applications [3].

Time-dependent changes in the magnetization of ferromagnetic materials are commonly referred to as magnetic viscosity or magnetic after-effects, the study of which has had a long history of both experimental and theoretical research [4]. Two types of mechanisms responsible for time dependent behavior were identified in the literature and became known as “diffusion” and “fluctuation” after-effect or magnetic viscosity. The former, the diffusion after-effect, is associated with the diffusion of ferrous ions and vacancies, i.e. thermally induced motion. The latter, the fluctuation after-effect, is a consequence of thermal activation of irreversible domain processes across an energy barrier such as domain-wall motion, coherent rotation, buckling, fanning, or the nucleation of domains of reverse magnetization [4].

Magnetic viscosity measurements are usually performed during the demagnetization of the material after its magnetic saturation. Initially, the material is saturated under a large applied field to bring the material in a well-defined state. Then the field is lowered, and the magnetic moment is monitored after the field change. The time dependent properties originate from thermally assisted processes of crossing an energy barrier that occurs when the applied field is suddenly reversed, and a significant amount of the particles is brought in a metastable state. Under a constant reverse field, the magnetization is reduced with time, given that the thermal activation of an energy barrier leads to a more stable state of reduced average magnetization [5, 6]. For a system with a single energy barrier the time dependence of the magnetization can be found from the probability per unit time that the system relaxes over the energy barrier  $\Delta E$  to the ground state using the Boltzmann factor. This results in an exponential time dependence

$$M_{irr}(t) = A + B e^{-t/\tau_o} \quad ; \quad \frac{1}{\tau_o} = f_o e^{\frac{\Delta E}{k_B T}} \quad (4.1)$$

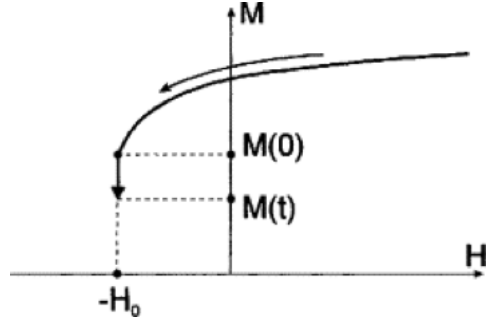


**Fig. 4.1:** A magnetic viscosity experiment at constant field. Initially, a large field is applied to the system, in order to achieve saturation. The field is then reversed and brought to some negative value  $-H_0$ , which is subsequently kept constant. During the field reversal, the magnetization decreases from positive saturation to some lower value, which gives the starting point from which the relaxation is measured. the magnetization decays in time according to a logarithmic law [7].

For a collection of particles, characterized by a distribution of energy barriers (or activation energies), the decay of  $M(t)$  is found to be not exponential but rather a logarithmic function of the time  $t$  [6, 8, 9]. For a constant distribution of energy barriers  $\Delta E$ , the  $M(t)$  is found to be

$$M(t) = M_o + S \cdot \ln \left[ 1 + \frac{t}{t_o} \right] \quad (4.2)$$

where,  $M_o$  is the magnetic moment of the material just after the applied field is changed.  $S$  is the magnetic viscosity describing the time dependence of the magnetic moment.  $S$  is a constant if the energy barrier distribution function is constant or slowly varying. If the energy barrier distribution function increases (decreases) with  $\Delta E$  the slope of the  $M(t)$  versus  $\ln(t)$  graph will increase (decrease) with  $\ln(t)$ . The parameter  $t_o$  is related to the time constant of the experiment and the materials properties but often considered a fitting constant [6]. It can be observed that the change in magnetic moment is large immediately after the field change and then decreases over time. The energy barrier depends on the magnetic reversal mechanism and is different for single domain and multidomain particles. For single domain particles that reverse via coherent rotation, the barrier distribution function can be determined from the particle size distribution function using the Stoner-Wohlfarth model. The energy barrier is a consequence of the intrinsic magnetic anisotropy of the material and the magnetic reversal mechanism. Note that the energy barrier is different for coherent and incoherent reversal mechanism in small particles. Incoherent reversal modes include fanning, buckling, or domain wall motion and

barriers depend on domain wall pinning or nucleation mechanisms which often depend on defects and can be greatly influenced by magnetostatic interaction, so there is always a distribution of such barriers in real materials [10].

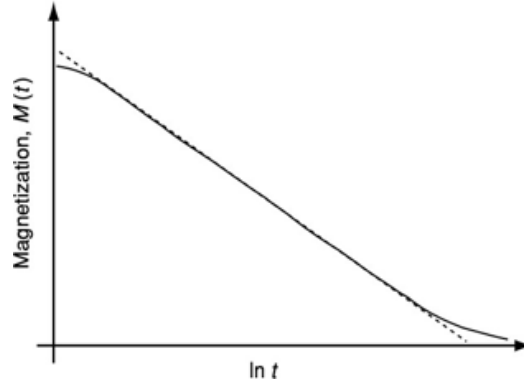


**Fig. 4.2:** The time dependence of the magnetization of a ferromagnet. The logarithmic variation is indicated by the dotted line [11].

From the logarithmic dependence of the magnetization, the viscosity

$$S = -\frac{dM}{d(\ln t)} \quad (4.3)$$

can be deduced [12].  $S$  has a sharp maximum for applied magnetic fields in the vicinity of  $H_c$  and it is much weaker when the applied field is very different from  $H_c$ .

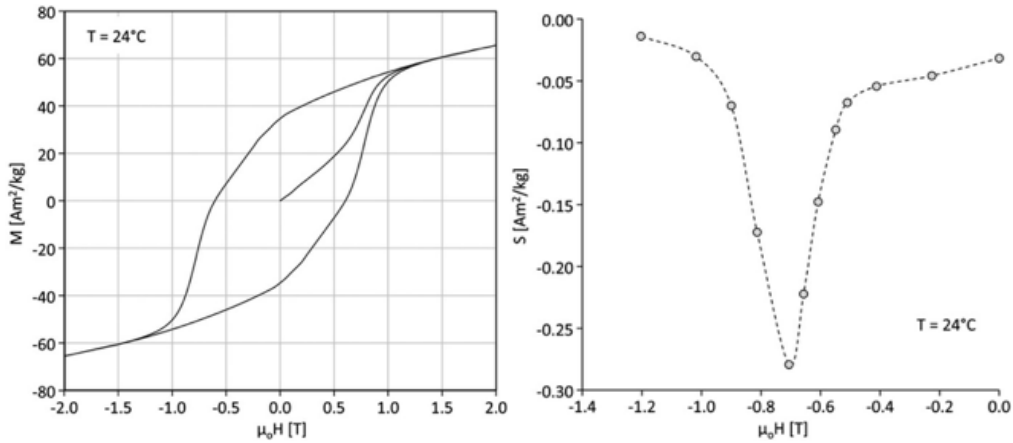


**Fig. 4.3:** (a) Major magnetization hysteresis loop for the  $\text{Sr}_{0.8}\text{La}_{0.2}\text{Fe}_{11.8}\text{Co}_{0.2}\text{O}_{19}$  hexaferrite (b) Dependence of the magnetic viscosity coefficient  $S$  on the applied reverse field by Serletis et al. 2012 [6].

Serletis et al. [6] investigated the time dependence of magnetization of  $\text{Sr}_{0.8}\text{La}_{0.2}\text{Fe}_{11.8}\text{Co}_{0.2}\text{O}_{19}$  hexaferrite. From the major magnetization hysteresis loop they

determined the magnetization at 2 T to be  $65 \text{ Am}^2/\text{kg}$ , the remanence magnetization to be  $35 \text{ Am}^2/\text{kg}$ , and the coercive field ( $\mu_0 H_c$ ) to be 0.6 T. In Fig. 4.3b, the viscosity coefficient  $S$  in relation to the applied reverse field is shown and the  $S$  attains a maximum value near -0.7 T which is at the vicinity of coercive field.

By varying the field and field angle and monitoring the time dependence of the magnetic moment it is possible to determine the activation switching volume and energy barrier. The particle which energy barrier  $\Delta E$  is small and close to  $K_B T$  will contribute to the time dependence. Because for a small barrier we expect the magnetic moment to be able to flip from a meta-stable to a ground state. The energy barrier depends on different factors. Most important are the materials properties, specifically the intrinsic properties such as saturation magnetization ( $M_s$ ), anisotropy ( $K$ ), and exchange stiffness ( $A$ ) (represents the strength of direct exchange interactions among neighboring spins), but also on extrinsic properties such as defects, crystal boundaries, and correlates to some extent with the coercivity. Other factors that determine the energy barriers are (2) the size and shape of the particles, (3) the orientation of the particles with respect to the magnetic field and (4) the interaction between the particles. Note that doubling the size of a particle can decrease the probability to flip from the metastable to the ground state with more than a factor 1000, so only particles for which the  $\Delta E$  is small will contribute to the time dependence (for Stoner Wohlfarth particles this is close to the field where the hysteresis closes: for particles with a square hysteresis curves this means a field close to the coercivity). Therefore, if the percentage of particles whose energy barrier is small is high, then the time dependence will be large. Not all the particles will contribute to the time dependence. Particles that have a large  $\Delta E$ , their magnetic moment will take forever to flip and will not contribute to the time dependence. Which particles contribute to the time dependence depends on the applied field.

Time dependent measurements are typically done with a scalar instrument monitoring the sample's moment parallel to the applied field over time after a field change [13]. In this work for the first time, a biaxial VSM is employed to monitor both the  $M_x$  and  $M_y$  signal as a function of time. This is the first time that magnetic viscosities are studied with a vector VSM.

## 4.2 Pristine Filament Time Dependence Study

In this section, the hysteresis curve and time dependence of Strontium Ferrite/PA12 filament composites for 3D printing purposes with 5 and 26 wt.% filling fractions are reported on.

### 4.2.1 Experimental Procedure

A MicroSense LLC/EZ9-HF VSM with a biaxial modified Mallinson coil set was used to determine the hysteresis curve and the time dependence of the magnetic moment of the filament samples at room temperature for different field angles.

The biaxial coil set allowed for the measurements of the sample's magnetic moment parallel to the applied field (along the X-axis,  $M_x$  signal) and perpendicular to the applied field (along the Y axis,  $M_y$  signal). The magnetic hysteresis curves for both the  $M_x$  and  $M_y$  signals were measured in a field range from -22000 to 22000 Oe. The image effect correction is applied to all the measured hysteresis curves to compensate for the loss of magnetic signal as a function of the field when the pole pieces saturate at values higher than 1.5 T. Additionally, the sweep field lag was removed. This effect is the product of the lag in the data measured by the lock-in-amplifier. The magnetic moment of the sample rod is believed to be at least a factor 100 times smaller than the sample's magnetic moment and was not corrected for in the presented data. This vector approach allows for the determination of the magnetic anisotropy axis from the hysteresis data.

Time dependent measurements were done as a function of the reverse field and field angle. After saturation of the sample at 22000 Oe, the field was lowered to  $-H_a$  and  $M_x$  and  $M_y$  were monitored for 300 seconds. The auto range functions of the lock-in-amplifier were used to guarantee an optimum sensitivity range and reduce the influence of digital noise. When analyzing the data, the values obtained during the first 10 seconds were ignored to remove the effect of the field transient on the measurement results [14]. The time constants of the lock-in amplifiers were set to 0.1 seconds and data was accumulated over 2 seconds for each data point.

## 4.2.2 Results and Discussion

To check the homogeneity of our samples, the saturation magnetic moment density per unit mass was measured for different parts of the filament. VSM measurements were done on samples cut at different positions along the filament. Samples were slit along the cylindrical axis analyzing both sides of the fiber. The mass of each sample was measured with a scale down to a precision of 0.1 mg and used to determine the magnetic moment per unit mass. The standard deviation of the calculated magnetic moment per unit mass of five samples is similar in two digits to what one expects based on the digital error of the scale. This indicates that inhomogeneities in our composite are less than  $\pm 3\%$ .

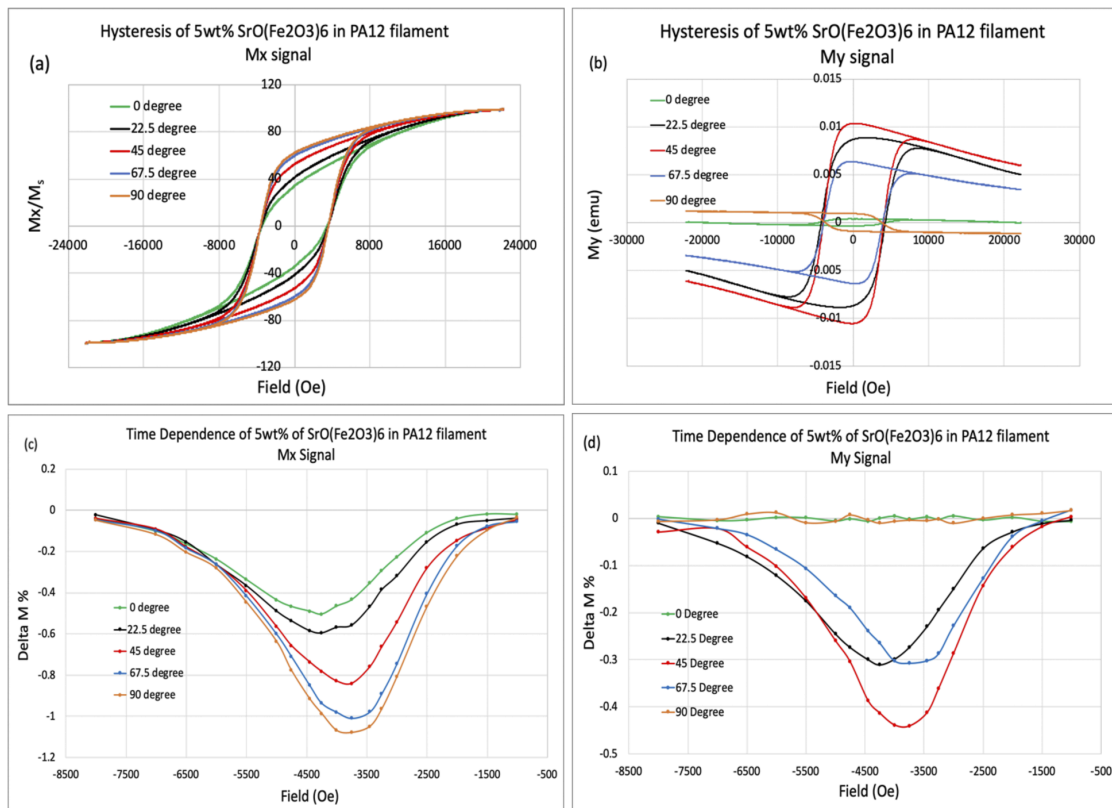


**Fig. 4.4:**  $M_x/M_s$  (a) and  $M_y$  (b) Hysteresis curves of the 5wt.% SrO(Fe<sub>2</sub>O<sub>3</sub>)<sub>6</sub>/PA12 filaments; Time dependence of  $M_x/M_s$  (c) and  $M_y /M_s$  (d) signals of 5wt.% SrO(Fe<sub>2</sub>O<sub>3</sub>)<sub>6</sub>/PA12 filaments [15].

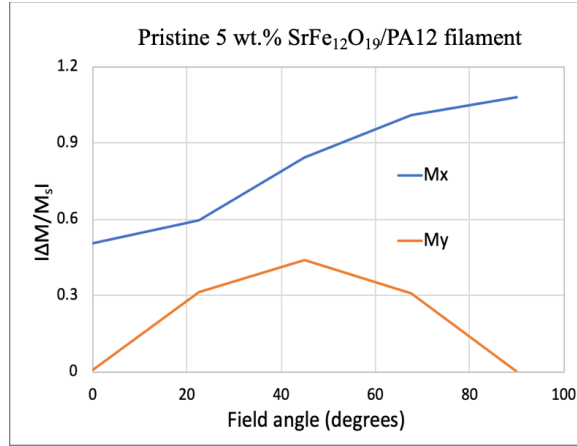
Fig. 4.4 (a) and (b) show the Hysteresis curve of the  $M_x$  and  $M_y$  signal of the 5 wt.% composite filament. The sample was positioned horizontally on the sample rod and the 0° orientation corresponds to the applied field being parallel to the cylindrical axis of the sample. The hysteresis curve of the  $M_x$  signal shows that at 90° the filament has

the highest remanence, indicating the easy axis is oriented along this direction. Additionally, at 0° the material shows the lowest remanence, which means that the hard axis is found at this orientation. This suggests that the filament has a texture with the easy axis oriented along its radial direction. The graph shown in Fig. 4.4b of the  $M_y$  signal shows that the  $M_y$  hysteresis is also angle dependent and it confirms the anisotropy axis of the sample, with a negligible signal when the field angle is parallel to the easy or hard directions. The non-zero  $M_y$  signal at 90° is due to a slight misalignment of the sample's easy axis with the field. Note that only in 0-degree position, prior to the hysteresis measurement we adjust the sample position to center the sample between the X-pick up coils which also centers them between the Y-pick up coils. Hence, the crosstalk is minimized for the data measured at zero degrees since the sample is perfectly centered. When the field angle is changed because of small misalignments of the sample on the sample-rod the perfect centering with respect to X and Y-coil set is lost introducing a non-zero cross-talk  $S_{xy}(\theta)$ . This results in the Y-coil signal being dependent on the  $M_x$  value at higher field angles [15]:

$$Y_{coil} = S_{yy}(\theta)M_y + S_{xy}(\theta)M_x \quad (4.4)$$

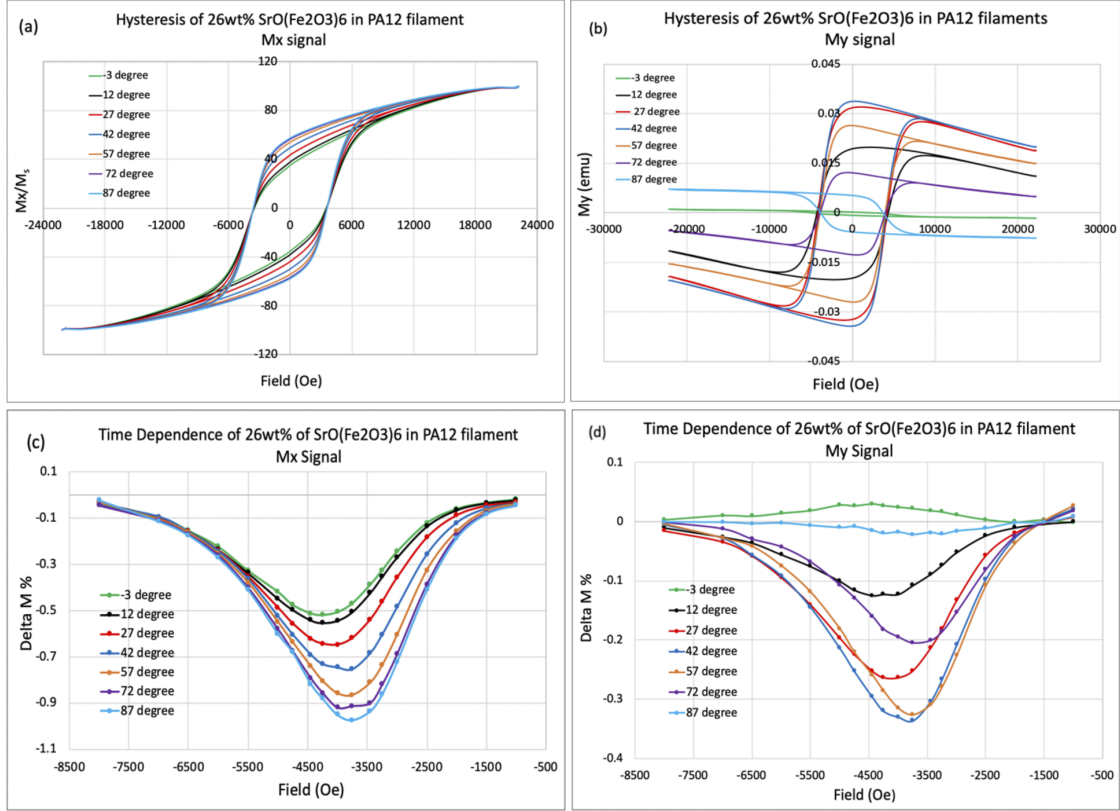
The observed macroscopic anisotropy is uniaxial with the filament's cylindrical axis perpendicular to the easy-plane and parallel to the hard axis.

Fig. 4.4 (c) and (d) show the  $\Delta M_x/M_s$  and  $\Delta M_y/M_s$  measured over the first 300 seconds of the 5 wt.% composite filaments at 0, 22.5, 45, 67.5 and 90 degrees. The time dependence is largest for  $M_x$  when the sample is oriented along the easy axis, i.e. the field is perpendicular to the cylindrical axis of the filament. The time dependence of the  $M_y$  signal is the largest when the sample is aligned at approximately 45° with respect to the easy axis and becomes zero when the field is parallel or perpendicular to the easy axis.



**Fig. 4.5:**  $|\Delta M_{\max}/M_s|$  [16] (a) and  $|\Delta M_{\max}/M|$  (b) as a function of field angle for 5 wt.% SrO(Fe<sub>2</sub>O<sub>3</sub>)<sub>6</sub>/PA12 composite filaments at room temperature (RT).

The maximum  $\Delta M_{\max}/M_s$  of each graph of Fig. 4.4 (a) and (b) is plotted against the field angle in Fig. 4.5 (a). It summarizes the field angle dependence of the time dependent measurement on the 5 wt.% filament sample at RT. The  $M_x$  magnetic viscosity is maximum for field angles close to the easy axis and decreases for angles close to the hard axis to approximately half the value. Because of the activation volume, the volume of the materials involved in the process of overcoming the energy barrier, is less at the easy axis as already particle flip its magnetic moment from metastable state to more stable state. Or the percentage of particles whose energy barrier is small is high in easy axis, they contribute to the time dependence, hence, the time dependence will be large. In addition, for most samples the time dependence correlates to the slope of the hysteresis curve and is larger when the slope of the hysteresis curve is large. At easy axis i.e at 90° angle the slope of the hysteresis is more steep, so the slope is larger and so, the  $M_x$  magnetic viscosity is maximum at easy axis and decrease at hard axis. The  $M_y$  magnetic viscosity is zero near the easy axis and hard axis and maximum for field angles of 45°.



**Fig. 4.6:**  $M_x/M_s$  (a) and  $M_y$  (b) Hysteresis curves of the 26 wt.%  $\text{SrO}(\text{Fe}_2\text{O}_3)_6/\text{PA12}$  filaments; Time dependence of  $M_x/M_s$  (c) and  $M_y/M_s$  (d) signals of 26 wt.%  $\text{SrO}(\text{Fe}_2\text{O}_3)_6/\text{PA12}$  filaments [16].

Fig. 4.6 shows the  $M_x/M_s$  (a) and  $M_y$  (b) hysteresis curves of 26 wt.% composite filament sample. The  $\Delta M_x/M_s$  (c) and  $\Delta M_y/M_s$  (d) over the first 300 seconds after the field step of the 26 wt.% composite filament samples at different field angles are shown in Fig. 4.6 (c) and (d). It can be observed that at  $87^\circ$ , the material has the highest remanence, and at  $-3^\circ$  has the lowest remanence which reveals that the anisotropy of the higher packing fraction composite filament is similar to that of the 5 wt.% filament. The non-zero  $M_y$  signal at  $87^\circ$  in Fig. 4.6b, is due to a slight misalignment of the sample's easy axis introducing a cross-talk that causes the Y-coil set to depend on  $M_x$ . This is similar to what was observed in the  $M_y$  data of the 5wt.% sample. Additionally, the sign change of the time dependence of the  $M_y$  signal at  $87^\circ$  observed in Fig. 4.6 is not physical but reflects that the cross-talk is negative (see equation 4.4).

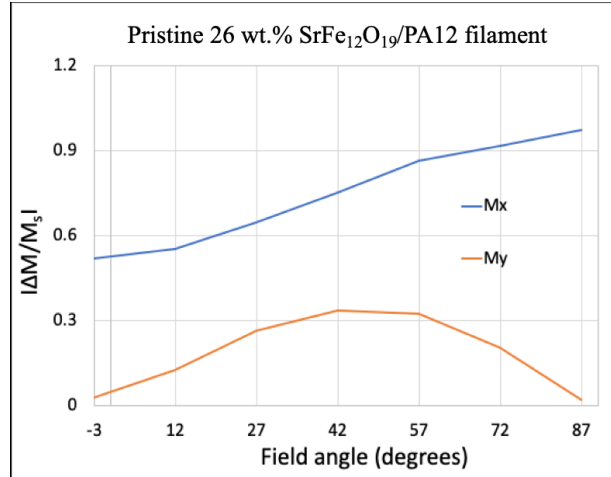


**Fig. 4.7:**  $|\Delta M_{\max}/M_s|$  (a) and  $|\Delta M_{\max}/M|$  (b) as a function of field angle for 26 wt.% SrO(Fe<sub>2</sub>O<sub>3</sub>)<sub>6</sub>/PA12 composite filaments at room temperature (RT).

The maximum  $\Delta M_{\max}/M_s$  of each graph of Fig. 4.6 (a) and (b) is plotted against the field angle in Fig. 4.7 (a). It summarizes the field angle dependence of the time dependent measurement on the 26 wt.% filament sample at RT. The  $M_x$  magnetic viscosity is maximum for field angles close to the easy axis and decreases for angles close to the hard axis to approximately half the value. The  $M_y$  magnetic viscosity is zero near the easy axis and hard axis and maximum for the intermediate field angles. It is also clear that with the increase of filler content from 5 wt.% to 26 wt.%, the time dependence does not differ significantly which indicates negligible magnetostatic interactions between the particles.

Similar experiments were performed on SrO(Fe<sub>2</sub>O<sub>3</sub>)<sub>6</sub> powder loaded in a 2 mm diameter cylindrical powder sample holder under a magnetic field of 22000 Oe. This sample differs in several ways from the magnetic composites: (1) the magnetic field induced anisotropy was much stronger and had more than one easy axis; (2) the packing fraction calculated from the sample's magnetic moment was close to 50%, so the interaction of the magnetic particles with each other can no longer be ignored. Note that also the shape (2 mm long cylinder with 1 mm radius) and orientation (cylindrical axis along the z-direction). The magnetic time dependent measurement results differ in two important ways with the composite sample: (1) The magnetic viscosity in the x-direction is less field angle dependent and (2) the magnetic viscosity in the y-direction is changing sign with the field angle.

### 4.2.3 Summary

The hysteresis curve of the 5 and 26 wt.% SrO(Fe<sub>2</sub>O<sub>3</sub>)<sub>6</sub>-PA12 pristine filaments have their easy axis parallel to the radial direction, which means the filaments have a wire texture. This wire texture originates from the flow of the molten composites during the extrusion process. The Strontium hexa-ferrite has a hexagonal crystal structure affecting the shape of the powder's particles. From SEM pictures it is noticed that the particles are platelets with the long to short axis ratio of approximately 3. The easy axis of the particles is along the short axis. Therefore, it is expected that the magnetic anisotropy and susceptibility of 3D printed samples is affected by the printing direction. This suggests that one must be able to optimize the materials properties by carefully choosing the infill direction when printing for example transformers [17].

The filament's time dependence is strongly sensitive to the field angle. The  $M_x$  viscosity collapses with a factor of 2 when the field is rotated from the easy plane to the hard axis but does not become zero as expected for a perfectly aligned composite. The extreme in the viscosity versus field curves shifts to larger field values for field angles closer to the hard axis. The interpretation of traditional scalar viscosity measurements is challenging and requires knowledge about the reversal mechanism (coherent versus incoherent reversal modes) to correctly interpret the magnetic activation volume. This might not be necessary when interpreting magnetic viscosity measurements performed with a biaxial VSM as at field angles close to the hard axis of the material, the coherent rotation is the expected reversal mechanism in the hexa-ferrite particles.

### 4.3 “Field-annealed only” and “Field-annealed and cooled” Filament Time Dependence Study

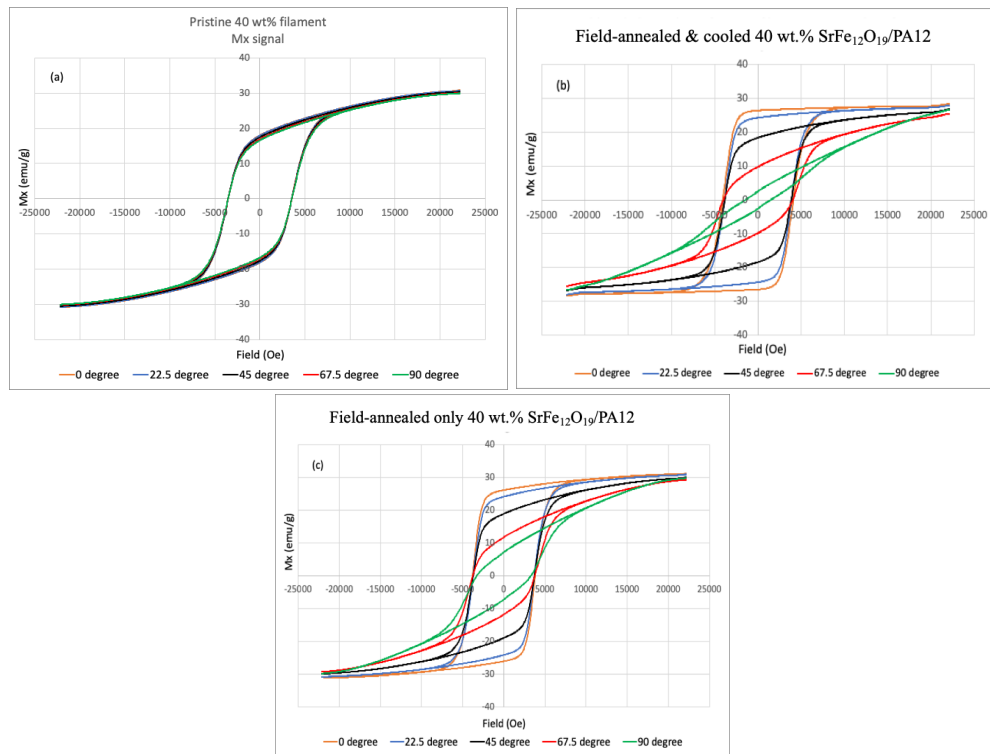
In this section the hysteresis and time dependence of the “field-annealed and cooled”, and the “field-annealed only” 40 wt.% strontium-ferrite/PA12 filament samples are discussed.

### 4.3.1 Experimental Procedure

The “field-annealed and cooled” samples were made at 230 °C by applying a field of 22 kOe for 3 minutes and then cooling it to RT (25 °C) in a magnetic field of 22 kOe. The “field-annealed only” samples were prepared at 230 °C by annealing them in a field of 22 kOe for 3 minutes and then cooling them to RT (25 °C) in zero field. So, for the “field- annealed only” sample there was no applied field when cooling down the sample to RT.

### 4.3.2 Results and Discussion

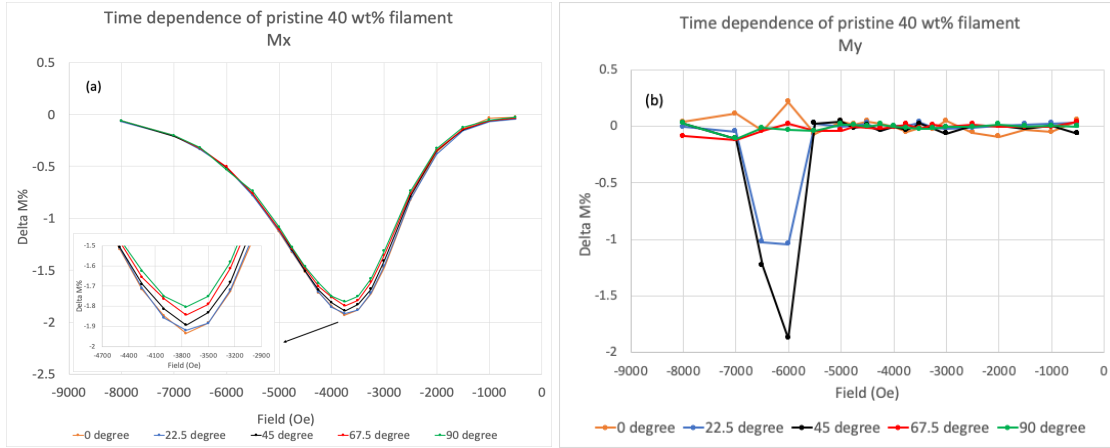
Angle dependent hysteresis measurements at RT were performed on pristine 40 wt.% and also “field-annealed and cooled” and “field-annealed only” 40 wt.% filaments. The angle dependent measurements were made from 0 to 90 degrees in 22.5-degree steps. The hysteresis curves were measured in sweep mode using a sweep rate of 400 Oe/sec. The measured hysteresis curves corrected for the field lag and image effect are shown in Fig. 4.7a, 4.7b and 4.7c.



**Fig. 4.8:**  $M_x$  hysteresis curves of (a) Pristine 40 wt.%  $\text{SrO}(\text{Fe}_2\text{O}_3)_6/\text{PA12}$  filaments; (b) “field-annealed and cooled” and (c) “field-annealed only” at 22 kOe of 40 wt.%  $\text{SrO}(\text{Fe}_2\text{O}_3)_6/\text{PA12}$  filaments at 230 °C for 3 minutes.

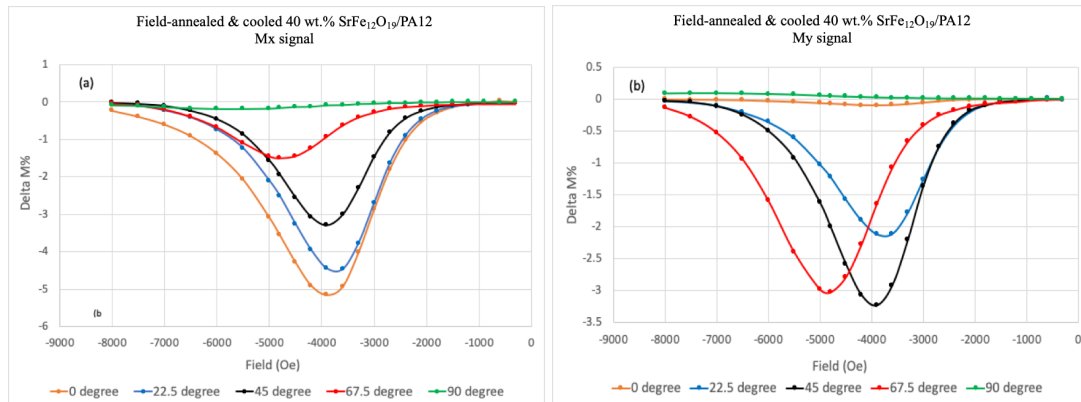
Fig. 4.8a, 4.8b and 4.8c shows the angle dependence hysteresis of the “pristine” 40 wt.% composite filament, “field-annealed and cooled” and “field-annealed only” 40 wt.% SrO(Fe<sub>2</sub>O<sub>3</sub>)<sub>6</sub>/PA12 filaments at 22 kOe of 230 °C for 3 minutes, respectively. The sample was positioned vertically in a Pyrex glass tube sample rod. For the “field-annealed and cooled” samples and the “field-annealed only” samples the 0° orientation correspond to the anneal field direction which was applied parallel to the radial axis of the filament sample. Although the initial pristine sample is isotropic as shown by the data in Fig. 4.8a which was collected when rotated along its cylindrical axis (Fig. 4.8a), the “field annealed and cooled”, and the “field-annealed only” samples showed both a strong anisotropy at room temperature with the easy axis oriented along the anneal field direction (Fig. 4.8b and 4.8c). However, the “field-annealed and cooled” sample shows more anisotropy (Fig. 4.8b) than the field-annealed only sample (Fig. 4.8c). Because the “field-annealed and cooled” sample was field annealed at 22 kOe for 3 minutes at 230 °C and then cooling it to RT (25 °C) in the presence of magnetic field of 22 kOe. So, the magnetic moment of the ferrite particles in the molten composite still aligned in the annealed field direction (22 kOe) during curing to RT. Hence, the “field-annealed and cooled” sample was exposed to magnetic field during curing unlike “field annealed only” sample. Therefore, “field-annealed and cooled” shows stronger anisotropy as exposed magnetic field longer time (Fig. 4.8b) than the field-annealed only sample (Fig. 4.8c). Additionally, the non-zero coercivity of the hard axis hysteresis curve field annealed and cooled sample and field annealed only sample are indicative of magnetostatic interaction among chained particles resulting in some kind of incoherent buckling reversal in the chained particles when measuring at 90 degrees with respect to the orientation axis.

The hysteresis curve of the M<sub>x</sub> signal shows that at 0° the filament has the highest remanence, indicating the easy axis is oriented along the applied field direction. Additionally, at 90° shows the lowest remanence and coercivity were observed, which means that the hard axis is found at this orientation. At the hard axis the field-annealed and cooled sample has a smaller but non-zero coercivity which is smaller than the hard-axis coercivity of the field-annealed only sample.



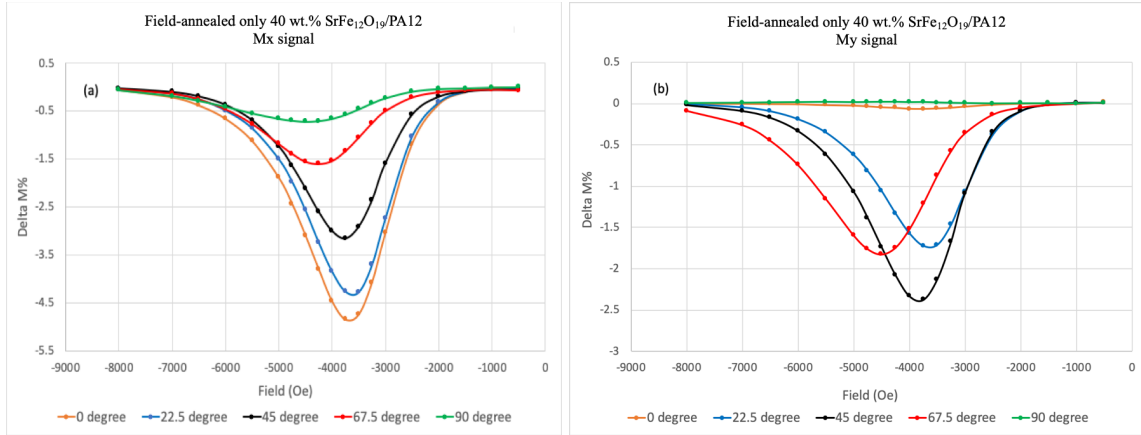
**Fig. 4.9:** Time dependence of  $\Delta M_x/M_s$  (a) and  $\Delta M_y/M_s$  (b) signals of the Pristine 40 wt.%  $\text{SrO}(\text{Fe}_2\text{O}_3)_6/\text{PA12}$  filaments.

Fig. 4.9 (a) and (b) show the  $\Delta M_x/M_s$  and  $\Delta M_y/M_s$  measured over the first 600 seconds of the pristine 40 wt.% filaments at 0, 22.5, 45, 67.5 and 90 degrees. The pristine filaments are isotropic (Fig. 4.8a), hence, there is very little time dependence observed for the sample.



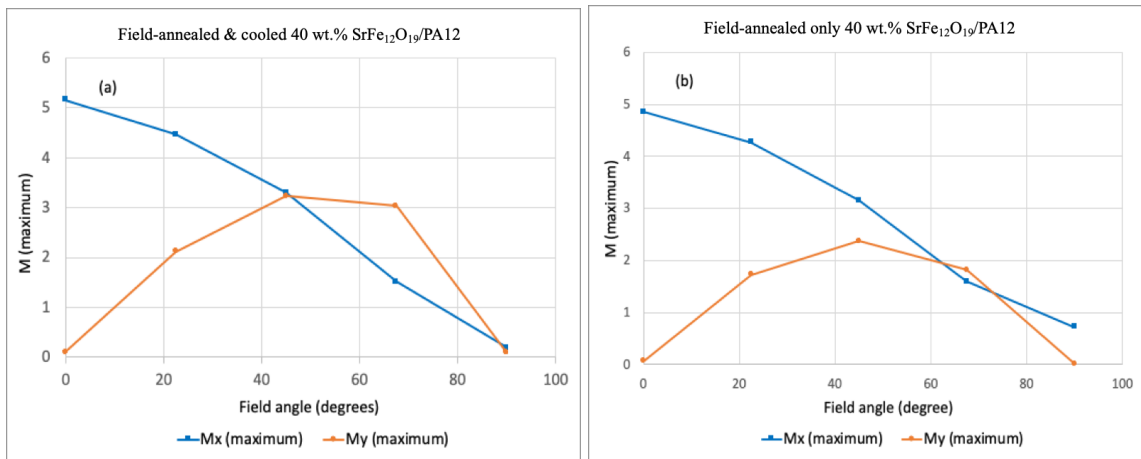
**Fig. 4.10:** Time dependence of  $M_x/M_s$  (a) and  $M_y/M_s$  (b) signals of the “field-annealed and cooled” 22 kOe of 40 wt.%  $\text{SrO}(\text{Fe}_2\text{O}_3)_6/\text{PA12}$  filaments at 230 °C 3 minutes.

Fig. 4.10 (a) and (b) show the  $\Delta M_x/M_s$  and  $\Delta M_y/M_s$  measured over the first 600 seconds of the 40 wt.% “field-annealed and cooled” filaments at 0, 22.5, 45, 67.5 and 90 degrees. The time dependence is largest for  $M_x$  when the sample is oriented along the easy axis, i.e. the annealed field direction at 0 degree. The time dependence of the  $M_y$  signal is the largest when the sample is aligned at approximately 45° with respect to the easy axis and becomes zero when the field is parallel or perpendicular to the easy axis.



**Fig. 4.11:** Time dependence of  $M_x/M_s$  (a) and  $M_y/M_s$  (b) signals of the “field-annealed only” 22 kOe of 40 wt.%  $\text{SrO}(\text{Fe}_2\text{O}_3)_6/\text{PA12}$  filaments at 230 °C 3 minutes.

Fig. 4.11 (a) and (b) show the  $\Delta M_x/M_s$  and  $\Delta M_y/M_s$  measured over the first 600 seconds of the 40 wt.% “field-annealed only” filaments at 0, 22.5, 45, 67.5 and 90 degrees. The time dependence is largest for  $M_x$  when the sample is oriented along the easy axis, i.e. the annealed field direction at 0 degree. The time dependence of the  $M_y$  signal is the largest when the sample is aligned at approximately 45° with respect to the easy axis and becomes zero when the field is parallel or perpendicular to the easy axis.



**Fig. 4.12:**  $|\Delta M_{\max}/M_s|$  of (a) field-annealed and cooled and (b) field-annealed only at 22 kOe of 40 wt.%  $\text{SrO}(\text{Fe}_2\text{O}_3)_6/\text{PA12}$  filaments at 230 °C 3 minutes.

Fig. 4.12 summarizes the field angle dependence of the time dependent measurement on the 40 wt.% “field-annealed and cooled” and “field-annealed only” filament at RT. The  $M_x$  magnetic viscosity is maximum for field angles close to the easy axis for both “field-annealed and cooled” sample and “field-annealed only” sample and

decreases more for angles close to the hard axis for the “field-annealed and cooled” samples than for the “field-annealed only” samples. The maximum  $M_y$  magnetic viscosity is zero near the easy axis and hard axis and maximum for intermediate field angles of  $45^\circ$  for both samples. However, the “field-annealed and cooled” samples have higher  $\Delta M_y$  value in the intermediate field angles of  $45^\circ$  than the “field-annealed only” samples. A non-zero  $M_x$  viscosity for “field-annealed only” sample is observed for measurement performed along the hard axis. We believe this is because during curing to RT at zero field, the ferrite particles undergo Brownian rotation in the molten PA12. This results in loss of alignment, leading to a lower magnetic anisotropy. This is accompanied by the introduction of a non-zero  $M_x$  magnetic viscosity along the hard axis.

### **i. Summary**

The hysteresis curve of the 40 wt.%  $\text{SrO}(\text{Fe}_2\text{O}_3)_6$ -PA12 “field-annealed and cooled” filaments and the “field-annealed only” filaments have their easy axis parallel to the anneal field direction, hence, show strong anisotropy. In contrast, the pristine 40 wt.% filament is isotropic. The  $M_x$  magnetic viscosity is maximum for field angles close to the easy axis for both “field-annealed and cooled” samples and “field-annealed only” samples and decreases more for angles close to the hard axis. For the “field-annealed and cooled” samples the time dependence is higher than the “field-annealed only” samples. The  $M_y$  magnetic viscosity is zero near the easy axis and hard axis and maximum for intermediate field angles of  $45^\circ$  for both samples. However, the field-annealed, and cooled samples have higher  $M_y$  value in the intermediate field angles of  $45^\circ$  than the field-annealed only samples. The “field-annealed and cooled” samples have a zero magnetic viscosity approximating when the field is applied perpendicular to the anneal field direction while the “field-annealed only” filaments have a non-zero magnetic viscosity perpendicular along the anneal field direction. As for “field-annealed only” samples after annealing at 22 kOe at  $230^\circ\text{C}$  then during curing to RT, no field was present. So, during curing to RT after removing the field to zero, the ferrite particles undergo Brownian rotation in the molten PA12 matrix to a more stable or energetically favorable distribution that decreases the sample’s magnetic viscosity as well as the

anisotropy. The loss in magnetic anisotropy is accompanied therefore by the introduction of a non-zero magnetic viscosity along the hard axis. This picture is consistent with the magnetic viscosity of the pristine filaments. They have a non-zero magnetic viscosity for fields applied along any direction, as these pristine filaments are less anisotropic than field annealed samples.

#### 4.4 Conclusion

To my best knowledge this is the first vector time dependent measurements reported on in literature. The hysteresis measurement of pristine 5 and 26 wt.% SrO(Fe<sub>2</sub>O<sub>3</sub>)<sub>6</sub>-PA12 filaments show that they have their easy axis parallel to the radial direction, which means the filaments have a wire texture. This wire texture originates from the flow of the molten composites during the extrusion process. The vector magnetic viscosity depicts that the filament's time dependence is strongly sensitive to the field angle. The  $M_x$  viscosity collapses with a factor of 2 when the field is rotated from the easy plane to the hard axis. In addition, the magnetic viscosity of the 40 wt.% SrO(Fe<sub>2</sub>O<sub>3</sub>)<sub>6</sub>-PA12 "field-annealed and cooled" filaments and the "field-annealed only" filaments were studied to further the development of the MFAAM deposition process. The filaments were field annealed at a temperature of 230 °C to simulate the alignment of the particles during the 3D printing process. Note that this temperature is chosen in the center of the process 3D-print window between the melting point of PA-12 at 175 °C and the onset of decomposition of the PA-12 at 290 °C. The hysteresis curve of the 40 wt.% SrO(Fe<sub>2</sub>O<sub>3</sub>)<sub>6</sub>-PA12 "field-annealed and cooled" filaments and the "field-annealed only" filaments have their easy axis parallel to the anneal field direction, hence, show strong anisotropy. In contrast, the pristine 40 wt.% filament is less anisotropic. The  $M_x$  magnetic viscosity is maximum in the easy plane and decreases with a factor of 5 along the macroscopic hard axis for the "field-annealed only" sample and to almost zero for the "field annealed and cooled" sample. The  $M_y$  magnetic viscosity is nearly zero along the hard axis and in the easy plane for both the "field annealed only" and the "field annealed and cooled" samples. Similar to the  $M_x$  magnetic viscosity the  $M_y$  magnetic viscosity is larger for field angles for which the hysteresis curve is steep.

## REFERENCES

- [1] New Scientist: Does magnetism decay over time? Retrieved: 31 January 2023, Available Online: <https://www.newscientist.com/lastword/mg24732911-800-does-magnetism-decay-over-time/>
- [2] P. J. Flanders and M. P. Sharrock, “An analysis of time-dependent magnetization and coercivity and of their relationship to print-through in recording tapes,” *J. Appl. Phys.*, vol. 62, no. 7, pp. 2918–2928, 1987.
- [3] S. J. Collocott and V. Neu, “Time-dependent magnetization in epitaxial hard magnetic thin films,” *J. Phys. D. Appl. Phys.*, vol. 45, no. 3, pp. 1–37, 2012.
- [4] B. M. Moskowitz, “Magnetic viscosity, diffusion after-effect, and disaccommodation in natural and synthetic samples,” *Geophys. J. R. Astron. Soc.*, vol. 82, no. 2, pp. 143–161, 1985.
- [5] R. Street and S. D. Brown, “Magnetic viscosity, fluctuation fields, and activation energies (invited),” *J. Appl. Phys.*, vol. 76, no. 10, pp. 6386–6390, 1994.
- [6] C. Serletis and K. G. Efthimiadis, “On the measurement of magnetic viscosity,” *J. Magn. Magn. Mater.*, vol. 324, no. 16, pp. 2547–2552, 2012.
- [7] *Hysteresis in Magnetism*, Giorgio Bertotti, Chapter 10- Magnetization Curves, Academic Press, pages 297-346, 1998.
- [8] R. Street and J. C. Woolley, “A study of magnetic viscosity,” *Proc. Phys. Soc. Sect. A*, vol. 62, no. 9, pp. 562–572, 1949.
- [9] P. Gaunt and G. J. Roy, “Magnetic viscosity in ferromagnets II. Co<sub>5</sub>Ce permanent magnet particles,” *Philos. Mag.*, vol. 34, no. 5, pp. 781–788, 1976.
- [10] M. El-Hilo, K. O’Grady, and R. W. Chantrell, “The origin of non-linear ln(t) behaviour in the time dependence of magnetisation,” *J. Magn. Magn. Mater.*, vol. 109, no. 2–3, pp. 164–168, 1992.
- [11] *Magnetism and Magnetic Materials*, J. M. D. Coey, First edition, Cambridge publication.
- [12] D. Givord, P. Tenaud, T. Viadieu, and G. Hadjipanayis, “Magnetic viscosity in different Nd-Fe-B magnets,” *J. Appl. Phys.*, vol. 61, no. 8, pp. 3454–3456, 1987.

- [13] H. Nishio, H. Taguchi, F. Hirata, and T. Takeishi, "Magnetic Viscosity in Strontium Ferrite Fine Particles," *IEEE Trans. Magn.*, vol. 29, no. 6, pp. 2637–2639, 1993.
- [14] S. Kirchberg, M. Rudolph, G. Ziegmann, and U. A. Peuker, "Nanocomposites based on technical polymers and sterically functionalized soft magnetic magnetite nanoparticles: Synthesis, processing, and characterization," *J. Nanomater.*, vol. 2012, 2012.
- [15] M.S thesis of Kolton J. Dieckow, "Automatic Alignment Methods for VSM Using Magnetic Low Anisotropic Samples with Reduced Time and Higher Precision", Texas State University, May (2021).
- [16] T. N. Ahmed, M. C. Belduque, D. C. Binod, J. S. Tate, and W. J. Geerts, "Time dependence of magnetic moment of strontium-ferrite powder measured with a biaxial vibrating sample magnetometer (VSM)," *AIP Adv.*, vol. 11, no. 1, 2021.
- [17] L. M. Bollig, P. J. Hilpisch, G. S. Mowry, and B. B. Nelson-Cheeseman, "3D printed magnetic polymer composite transformers," *J. Magn. Magn. Mater.*, vol. 442, pp. 97–101, 2017.

## 5. TEMPERATURE DEPENDENT STUDY

*“If you thought that science was certain - well, that is just an error on your part.”*

— Richard Feynman

Note: The first part of the chapter’s content (Section 5.2) was presented at the MMM-2021 conference and published as a regular journal paper in AIP Advances on 22<sup>nd</sup> September 2022 by the author of this dissertation along with other co-authors. DOI number of the publication is <https://doi.org/10.1063/5.0098972>. A lot of the 2<sup>nd</sup> part of the chapter’s content (section 5.3) was presented at the MMM-2022 conference in Minnesota in Fall-2022 and published in 7<sup>th</sup> February 2023 as a conference paper for the conference proceedings of the MMM conference. DOI number of the publication is <https://doi.org/10.1063/9.0000596>. The contents taken from the published article were cited where applicable.

### 5.1 Introduction

The time dependence of the magnetic moment expressed by the magnetic viscosity coefficient  $S$  is generally a function of the applied field  $H$  and the temperature  $T$  [1]. In the low temperature range below 100 °C, the time dependence mostly originates from the effect of thermal fluctuations on the magnetic reversal process (see chapter 4) [2]. At much higher temperatures other physics can influence the time dependence of the magnetic properties including the diffusion of atoms or vacancies along grain boundaries or through the bulk [3], chemical reactions [4], precipitation [5] and phase changes [6, 7].

For magnetic composites of anisotropic particles, at elevated temperatures **near the melting point of the polymer matrix** but below the Curie temperature of the magnetic particles, a large time dependence is expected once the matrix loses its ability to fix the orientation of the magnetic particles. The alignment of the magnetic particles due to the rotation inside the matrix towards an externally applied magnetic field and the redistribution of the aligned magnetic particles due to the inhomogeneous magnetostatic

interaction field between the aligned particles often referred to as magnetic chaining, lead to a large time dependence of the sample's magnetic dipole moment upon application of a field. Note that these processes greatly depend on the melt viscosity of the polymer matrix. So total time dependence effects are similar to those observed in ferro- and rheological fluids and can be described by Néel and Brownian relaxation time constants.

**Above the melting temperature of the polymer matrix**, under the effect of an external magnetic field the suspension of magnetic particles will show rheological behavior. Here we study the rotation of the magnetic particles in the softened and molten PA12 matrix under the influence of a magnetic field at elevated temperatures (below and above the melting temperature of the nylon matrix). The study of this time dependence as a function of temperature is focused on determining (1) the critical temperature and field above which the magnetic particles will be able to rotate in the polymer matrix; (2) the time constants associated with the rotation of the particles and the redistribution of the particles in the matrix (chaining) (3) the temperature dependence of melt viscosity of the magnetic composite. A better understanding of how these properties depend on the matrix materials, particle size distribution and the density will be instrumental for the development of a MFAAM setup.

The  $\text{SrFe}_{12}\text{O}_{19}$  polymer suspension might behave similar to the magnetic colloids that have been extensively studied. Magnetic colloids are constituted by dispersions of a solid magnetic phase in a nonmagnetic semi-liquid carrier. They are traditionally classified into two groups in view of their rheological characteristics: ferrofluids (FFs) and magnetorheological fluids (MRFs) (see Fig. 5.1).

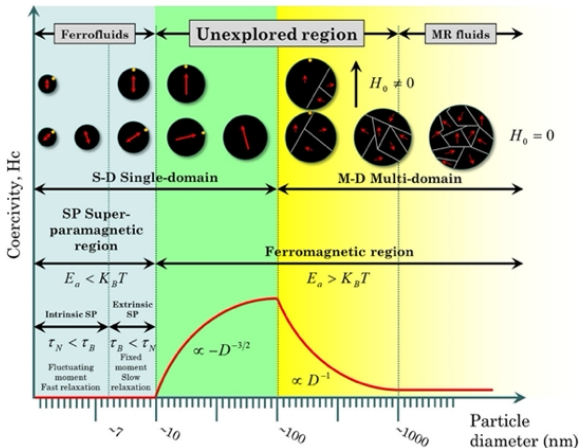
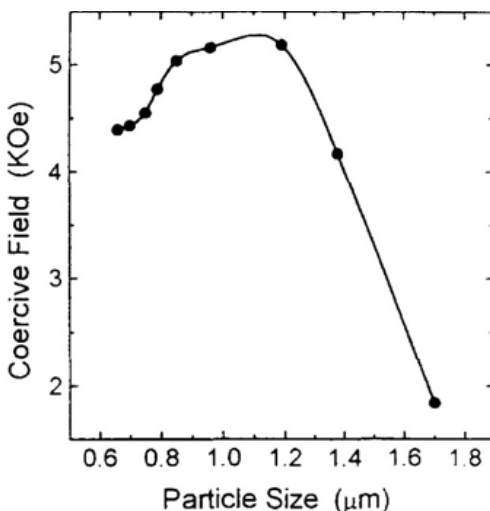


Fig. 5.1: Schematics of the size region between FFs and MRFs [8].

FF's are formed by nanosized superparamagnetic (SP) particles, typically ferrites. Because of their small size, these particles are subjected to the Brownian (thermal) motion and do not aggregate in spite of the fact that they are constituted by a single magnetic domain and hence magnetically interact even in the absence of magnetic fields [8]. In zero field the energy barrier in between two or more states is less than  $k_B T$  ( $E_a < k_B T$ ), so a suspension of these particles will have a zero average magnetic moment in zero field. Switching between states takes place by magnetic reversal in the particle (Néel process) or by rotation of the particle in the suspension (Brownian process). If  $\tau_N < \tau_B$  the latter is the main process, and the suspension is referred to as a Brownian FF. The superparamagnetic particles of a FF become stable in an applied field and are often used for magnetic domain studies or to detect microcracks in the field of non-destructive analysis. On the other hand, MRFs are constituted by micrometer-sized ferromagnetic particles, typically carbonyl iron. Because of their large size, these particles are not significantly affected by the Brownian motion and are constituted by magnetic multi-domains [9] having little hysteresis. The magnetic particles in a MRF aggregate in long chains when magnetized by an external magnetic field. This aggregation is reversible as the particles are soft magnetic and lose their magnetic moment once the external field is removed. The melt viscosity of MRFs can be greatly affected by the application of a magnetic field.

The magnetic particles used in bonded permanent magnets are mostly single domain (see Chapter 1) so are larger than the particles in FF but smaller than the particles in MRF. These particles also have a significant permanent magnetic dipole moment which makes it difficult to avoid aggregation and clustering processes are in general irreversible. Note that a molten permanent magnet composite belongs to a group of magnetic suspensions that is much less studied than FFs and MRFs (see also Fig. 5.1 above).



**Fig. 5.2:** Coercive field ( $H_c$ ) as a function of particle mean diameter ( $D$ ) of  $\text{SrFe}_{12}\text{O}_{19}$  [10].

Zai-Bing Guo et al. [10] mentioned that for  $\text{SrFe}_{12}\text{O}_{19}$ , the grain size critical dimension ( $D$ ) for single-domain configuration is  $D \cong 1.3 \mu\text{m}$ . In Fig. 5.2, their data on the  $H_c$  as a function of particle mean diameter  $D$  is reported. The figure clearly shows the correlation between grain size and  $H_c$  values. Our  $\text{SrFe}_{12}\text{O}_{19}$  particles' size is  $1.39 \mu\text{m}$  which is near critical dimension ( $D$ ) for single-domain configuration. Hence, it is here assumed that the  $\text{SrFe}_{12}\text{O}_{19}$  particles are near the single domain (SD) region and show ferromagnetic SD behavior and have a significant coercivity. As their particle size are small, these particles might be subjected to the Brownian (thermal) motion at elevated temperature and at also be subjected to Néel magnetic reversal processes. The latter will happen to some extent even at RT as was shown in the previous chapter. The magnetic colloidal suspension studied here differs from both FFs and MRFs as they constitute of single domain particles. Note that magnetic colloidal suspensions of particles in this size range are less well studied (see Fig. 5.1 above). In addition, most magnetic suspension studied contain soft magnetic particles while the molten magnetic composites during injection molding, calendaring or AM of permanent magnets consist of hard magnetic particles and are much less understood. Time dependent magnetic properties were measured at elevated temperature and are reported on here. Section 5.2 reporting on experiments done below the melting point (130-175 Celsius) and section 5.3 reporting on experiments done above the melting point.

## 5.2 Dynamic Viscosity of Strontium Ferrite–Nylon Composite Below the Nylon Melting Temperature

Here we report on the time dependence of the magnetic properties of 40 wt.% SrO(Fe<sub>2</sub>O<sub>3</sub>)<sub>6</sub>/PA-12 composite above room temperature but below the nylon melting point (128-175 °C). Within this temperature interval the PA-12 matrix softens, and the magnetic particles gain mobility allowing them to align with the field and possibly redistribute through the polymer matrix upon alignment. So, in addition to the Néel time constant originating from the magnetic viscosity of the strontium ferrite particles we expect the time dependence of the 40 wt.% SrO(Fe<sub>2</sub>O<sub>3</sub>)<sub>6</sub>/PA-12 composites to show two Brownian time constants due to chaining and rotation which depend on the shear melt viscosity and rotation melt viscosity respectively. Note that below the melting point the Néel time constant is much smaller than the Brownian time constants. The Brownian rotation time constant is inversely proportional to the applied rotation field ( $H_a$ ) and inversely proportional to the saturation magnetization of the particle ( $M_s$ ). The Brownian chaining time constant should to first order be independent of the applied magnetic field and depends mainly on the magnetostatic interaction between the particles and is thus inversely proportional to  $M_s^2$ :

$$\frac{\tau_{chaining}}{\tau_{rotation}} \propto \frac{M_s H_a}{M_s^2} = \frac{H_a}{M_s} \quad (5.1)$$

So, by choosing  $H_a \gg M_s$  and the time interval of the experiment on the order of  $\tau_{rotation}$  one can zoom in on the rotation process.

The study of this time dependence as a function of temperature is relevant for the development of Magnetic Field Assisted Additive Manufacturing (MFAAM) [11-15], i.e. 3D printing in a magnetic field. This emerging manufacturing method allows for the realization of inhomogeneous anisotropic magnetic materials that cannot be manufactured by traditional methods. In such composites the magnetic anisotropy axis can be varied as a function of position which gives them enhanced novel properties. These materials are promising for application in printable electronics and RF antennas, magnetic flux-guides for wireless charging application, artificial muscles for use in all kinds of actuators, and novel Halbach cylinders interesting for application in electromotors, generators, magnetic

gears, and other applications such as portable magnetic resonance imaging (MRI) equipment [16]. To emphasize that this study is limited to the temperatures below the melting point the term “melt” viscosity is avoided here and the word dynamic viscosity is used.

### 5.2.1 Experimental Procedure

Strontium ferrite composites are hard magnetic, have a saturation field near 19.5 kOe [6] and are biocompatible. They are currently being studied to be applied in hard magnetic 3D printer filament [11, 12] to allow for 3D printing of novel anisotropic magnets. Vestosint® 3D Z2773 PA-12 (nylon) from Evonik and OP-71 strontium ferrite ( $\text{SrO}(\text{Fe}_2\text{O}_3)_6$ ) powder (1.39  $\mu\text{m}$ ) obtained from Dowa Electronics Materials Corporation were used to realize 40 wt.%  $\text{SrO}(\text{Fe}_2\text{O}_3)_6/\text{PA-12}$  filaments with an average diameter of 1.5 mm. The filaments were produced using a Thermo Fisher Process 11 co-rotating twin-screw extruder. Details on the manufacturing process are described in [17]. An SDT 650 Simultaneous Thermal Analyzer of TA Instruments was used to perform Thermo-Gravimetric Analysis (TGA) and Differential Scanning Calorimetry (DSC) analysis on the filaments showing a glass transient temperature of 48-49 °C, a melting temperature of 184.1 °C and evidence for an exothermic reaction around 380 °C [18]. A Rigaku Smartlab high-resolution X-ray diffractometer was used to perform the X-ray Reflectivity measurement using a standard anode Cu  $K\alpha$  source (1.76kW) to generate the X-ray beam. The  $\theta$ -2 $\theta$  XRD spectra show weak nylon peaks around 6, 11, 20, 21.5, 23.5, and a small very wide peak around 41 degrees. These peaks are characteristic for the  $\gamma$  and  $\alpha$ -phases of nylon and indicate that the nylon matrix in our samples is crystalline [19-22]. A FEI Helios NanoLab 400 DualBeam SEM was used to observe the strontium ferrite particle's orientation and distribution in the filaments. To improve resolution, all samples were coated with a conductive 2 nm layer of Iridium (Ir) deposited by a Quorum Technologies EMS150T Imaging Sputter Coater. This even thin layer enhances secondary electron emission and solved the charging issue of the polymer magnetic composite samples under the electron microscope. Additional studies were done with an Hirox digital optical microscope at lower resolution.

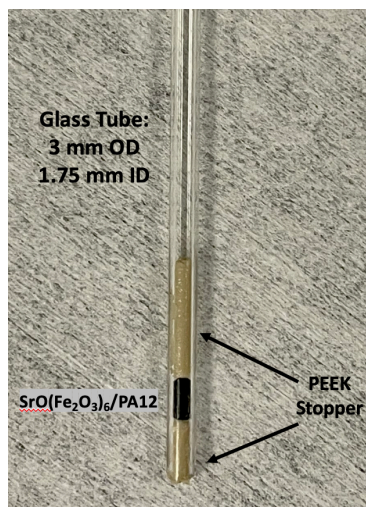


**Fig. 5.3:** 40 wt.% SrO(Fe<sub>2</sub>O<sub>3</sub>)<sub>6</sub> in PA12 cylindrical-shaped filament secured in Pyrex glass tubes [23].

Magnetic characterization was performed using a biaxial EZ-9 Vibrating Sample Magnetometer (VSM) furnished with a 70-1000 K temperature option. Samples were 4-5 mm long filaments with a diameter of 1.5 mm and typically had a mass of around 14 mg. The samples were loaded in a Pyrex glass tube with an outer diameter of 3 mm and an inner diameter of 1.75 mm. The filament was compacted with PEEK stoppers with silicone glue on both sides to secure its position and avoid direct exposure to the atmosphere while heating (see Fig. 5.3). The PEEK stoppers also prevented the molten composite to leak out the glass rod and contaminate the furnace in the event of over-heating.

### 5.2.2 Quasi Static Magnetic Measurement

Quasi static VSM measurements were performed from room temperature (RT) up to 175 °C. Argon gas was flown during the measurements above RT. The hysteresis curves were measured in sweep mode using a sweep rate of 25 Oe/sec. Measurements were made from 25 to 175 °C every 15 °C step.

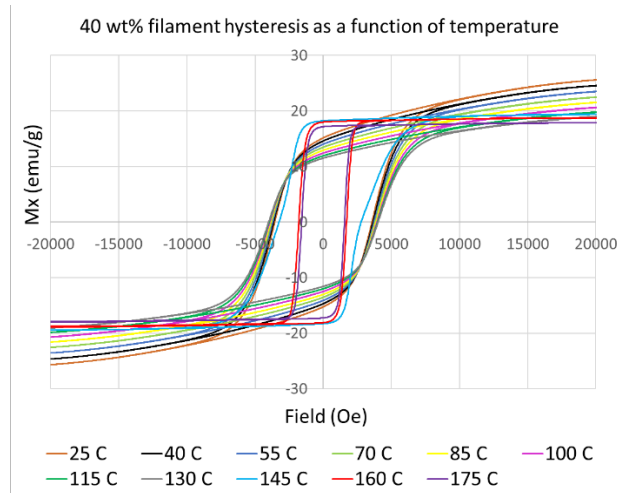


**Fig. 5.4:** Magnetic hysteresis curves above and below the softening temperature of the PA-12 matrix.

The measured hysteresis curves corrected for the field lag and image effect are shown in Fig. 5.4. Below 130 °C the coercivity of the composite is approximately 4000 Oe which is slightly larger than the coercivity of an isotropic 90 wt.% injection molded material that is listed on the datasheet of the OP-71 strontium-ferrite powder. The difference is caused by a combination of factors including (a) the lower loading level of the filaments and thus less magnetostatic interaction between the particles; (b) the presence of a small anisotropy in the filaments caused by the flow during the extrusion process (easy plane in the radial direction) [17]; (c) the demagnetizing field (estimated 134 Oe using a volume fraction of 8 % and spherical particles using the equation (3) of reference [24]) of the filament sample oriented with its long axis perpendicular to the field. Up to 130 °C the  $H_c$  increases with temperature as expected for strontium ferrite [25]. At higher temperatures, i.e. 145 °C and up, the coercivity strongly decreases. At those temperatures, the orientation of the particles is no longer fixed by the PA-12 matrix and can rotate with respect to the nylon matrix. As a consequence, the observed coercivity is much lower than for the case where the particles are secured in the polymer matrix. The observed residual magnetic hysteresis at the higher temperatures is in part due to the magnetic hysteresis of the strontium ferrite particles and in part due to mechanical friction forces between nylon and magnetic particles as the strontium ferrite particles are lined-up parallel to the applied magnetic field. Furthermore, the results of Fig. 5.4 show that the  $M_s$  decreases with temperature up to 130 °C in agreement with the literature. The small increase from 130 to

145 °C is not a measurement artefact. It is hypothesized that this small increase is due to alignment of the easy axis of the particles above 130 °C parallel to the anneal field and indicates that some of the strontium ferrite particles have an  $H_k$  in excess of 22,000 Oe.

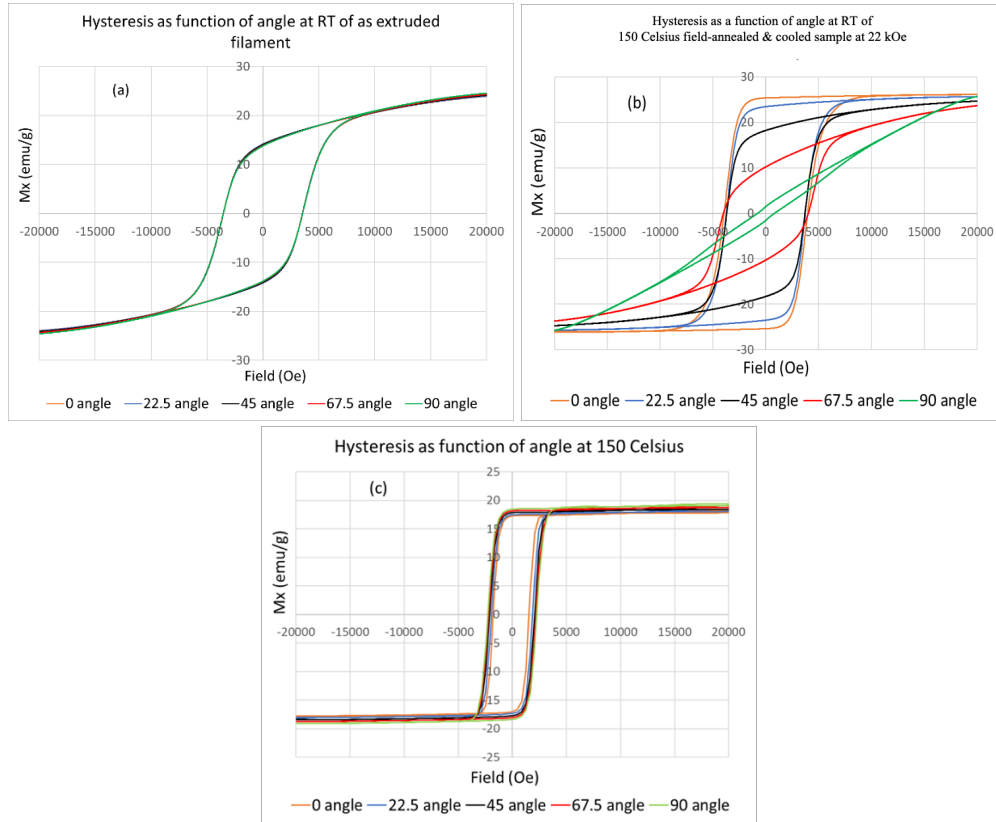


**Fig. 5.5:** Angle dependence of RT hysteresis curves before (a) and after (b) a 1 minute anneal at 150 °C in a field of 22 kOe; (c) Angle dependence of hysteresis at 150 °C [23].

To further explore the softening of the PA12 at elevated temperature, the angle dependence of the RT hysteresis curve before (Fig. 5.5a) and after (Fig. 5.5b) a 1 minute anneal at 150 °C in a field of 22,000 Oe were measured. Although the initial sample is isotropic when rotated along its cylindrical axis (Fig. 5.5a), the field annealed sample shows a strong anisotropy at room temperature with the easy axis oriented along the anneal field direction (Fig. 5.5b). This magnetic anisotropy disappears at elevated temperature as shown in Fig. 5.5c which shows the angle dependence of the hysteresis curve measured at 150 °C. The small angle dependence of the  $M_s$  shown in Fig. 5.5c is a measurement artifact and originates from a slight misalignment of the sample on the sample-rod which makes the exact position of the sample between the pickup coils a weak function of the field angle.

Note that the exact sensitivity of a VSM depends on the sample position. The results of Fig. 5.5 thus provide further evidence that the particles rotate in the nylon matrix above 130 °C.

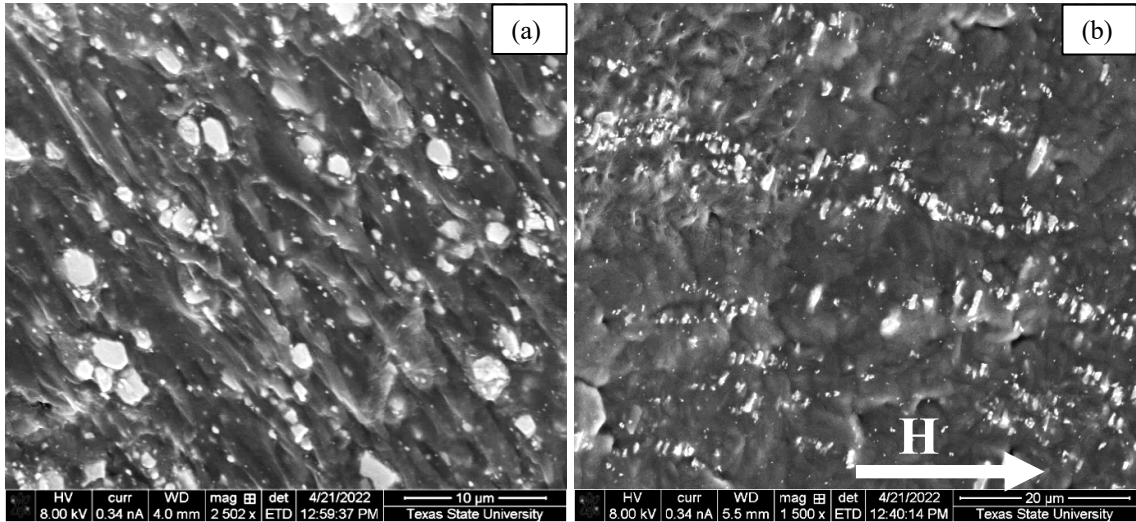


**Fig. 5.6:** 40 wt.% SrO(Fe<sub>2</sub>O<sub>3</sub>)<sub>6</sub>/PA12 composite filament (a) pristine filament (left) (b) filament annealed in a field of 22000 Oe at 175 Celsius for one minute (right) and the white arrow indicates the applied magnetic field direction [23].

SEM images of the pristine composite filament and the filament field annealed at 175 °C are shown in Fig. 5.6a and 5.6b respectively. Sample 5.6a was cut along the radial axis (i.e. parallel to the filament base) with a surgical knife at room temperature. It is noticed that none of the larger strontium ferrite platelets have their short axis oriented parallel to the arrow. This suggests that a flow in the arrow direction might have been present or that the observed orientation of the platelets is somehow due to the cutting process. The extrusion direction for this sample is actually perpendicular to the page of the paper. A flow parallel to the plane of the paper could originate from die-swell when the suspension exits the extruder die. The orientation of the platelets due to the shear flow in the extrusion die is expected to be inhomogeneous through the filament cross section [26, 27]. The alignment due to flow is expected to be better near the outer diameter and weak near the center of the filament. Quasi-chaining or short-range order is observed parallel to the flow direction, in particularly for the larger particles. It is believed that this weak quasi-chaining is due to the combination of flow and magnetostatic interaction.

Fig. 5.6b show the surface of a sample that was field annealed at 175 °C, the platelets are oriented with their short axis parallel to the field direction and long-range order of the particles i.e. a weak chaining in the direction of applied field is observed. Note that OP-71 SrO(Fe<sub>2</sub>O<sub>3</sub>)<sub>6</sub> particles are aspherical and have a platelet shape, so they have two long and one short axis. It is expected that chaining influences the magnetic anisotropy of the samples as it induces an easy axis of magnetostatic origin parallel to the anneal field direction. For the strontium ferrite composites, this agglomeration shape anisotropy due to chaining is in addition to the crystal and shape anisotropy originating from the single crystalline particles lining up with the easy axis parallel to the print field [24]. Although some amount of chaining is observed in the samples studied here, the SEM images indicate that strontium ferrite particles are individually suspended with PA-12 in between separate ferrite particles in both pristine and field annealed samples. The samples studied here have a packing fraction of approximately 8 vol.%.

### 5.2.3 Dynamic Magnetic Measurement

To study the dynamics of the rotation of the strontium ferrite particles in the softened nylon matrix, measurements were done at elevated temperatures as a function of the time on field annealed samples. The annealing was done below the matrix melting temperature at 175 °C avoiding issues with wetting of the magnetic composite on the inside of the quartz tubes that would drastically change the shape of the filament. Above the melting temperatures, the adhesion and cohesion forces change the shape of the sample inside the sample holder tube.

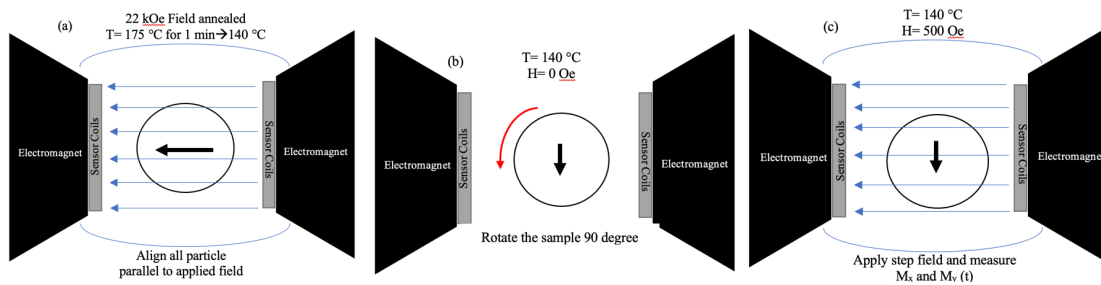


**Fig. 5.7:** Top view of the sample inside VSM chamber (a) Filament samples were annealed in a field of 22,000 Oe at 175 °C for 1 minutes, cooled down in a magnetic field to the measurement temperature; (b)

rotated over 90 degrees in the VSM so the magnetic moment of the field annealed sample is perpendicular to the field direction; (c) a step field of 500 Oe was applied at the measurement temperature while the  $M_x$  and  $M_y$  component were monitored as a function of the field temperature.

To make the sample anisotropic, the magnetic strontium ferrite particles were first oriented by annealing the sample in a magnetic field of 22 kOe at 175 °C for 1 minute. Then the sample was cooled down in a field of 22 kOe to the measurement temperature and after a 1.5 minutes stabilization period at the measurement temperature the field was lowered to 0 Oe. At zero field the sample was rotated over 90 degrees and then a small rotation field was applied. Note that this field is perpendicular to the sample's magnetic moment so will rotate the magnetic particles. The small field applied at perpendicular angle assured that only reversible magnetic rotation occurs in the particles and reversal by domain wall motion is negligible. Directly following the rotation field, the sample's magnetic moment components along ( $M_x$ ) and perpendicular ( $M_y$ ) to the field axis were monitored as a function of time using the biaxial coil signals for 300 seconds. This allowed for the calculation of the transient of the angle and magnitude of the magnetic moment vector using the following equations:

$$\theta(t) = \tan^{-1}(M_y(t)/M_x(t)) \quad (5.2)$$

$$|\vec{M}(t)| = \sqrt{(M_x(t))^2 + (M_y(t))^2} \quad (5.3)$$

Note that the torque exerted on an anisotropic particle by the magnetic field,  $\tau_H = V\mu_0\vec{M} \times \vec{H}$ , rotates the particles along the field direction. Here  $\mathbf{H}$  is the total magnetic field,  $\mu_0$  is the magnetic permeability of the vacuum,  $\vec{M}$  is the saturation magnetization of the particle and  $V$  its volume.

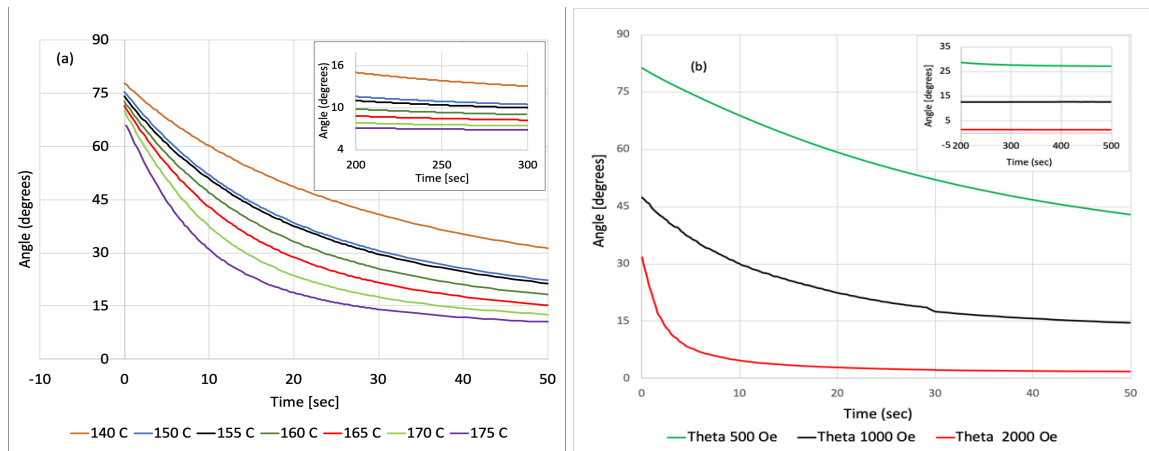


**Fig. 5.8:** Angle variation with time (a) at different elevated temperature (b) at 136 °C for different rotation fields of 40 wt.% SrO(Fe<sub>2</sub>O<sub>3</sub>)<sub>6</sub> in PA12 matrix [23].

Using the procedure outlined above, measurements were done for the fields of 500, 1000 and 2000 Oe, and at different elevated temperatures of 120, 124, 128, 132, 136, 140, 150, 155, 160, 165, 170 and up to 175 °C. Fig. 5.8a. shows the time dependence of the orientation of the sample’s magnetic moment vector for temperatures from 140 to 175 °C for a rotation field of 500 Oe. The angle decreases with time as the magnetic moment of the particles is rotating towards the field direction. For t=0 for all curves the magnetic moment angles are already below 90 degrees which is caused by a delay of the start of the data acquisition in the setup used for this experiment caused by several factors including the time it takes to rotate the sample over 90 degrees. Note that the transient becomes steeper for higher temperatures indicative of a higher initial angular velocity due by the lower dynamic viscosity at elevated temperatures.

Fig. 5.8b shows the  $\theta(t)$  transient for different rotation field values at 136 °C. The larger the applied rotation field the steeper the transients, again indicative of a larger initial angular velocity now caused by the larger initial torque exerted to the particles. At large t values the rotation stops before the magnetic moment is completely lined up along the field direction (see inserts of Fig. 5.8a and 5.8b). For smaller  $\theta$  the magnetic torque on the ferrite particles decreases and at some point, is canceled out by an elastic or friction torque caused by the interaction between the nylon and the ferrite particles. The insets in the graphs of Fig. 5.8 show that the limiting angle decreases with temperature and rotation field. The existence of a limiting angle indicates one or more of the following: (1) the nylon does not

behave as an ideal Newtonian fluid but can support a static shear stress, (2) the nylon exerts an elastic torque on the ferrite particles; (3) the strontium ferrite particles touch each other upon rotation and or interact with each other magnetostatically. The first two hypothesis are consistent with the fact that this are temperatures well below the melting point of PA-12 (178 °C). The SEM picture shown in Fig. 5.6b of the sample field annealed at 175 °C indicates that some of the particles are close enough to touch upon rotation. Two experiments were conducted to further investigate the origin of the limiting angle at low field and low temperature. After measuring the magnetic transient in 1000 Oe (Fig. 5.8b) the field was switched off and the magnetic moment was monitored for another 600 seconds. No additional transient was observed. Note that an elastic torque exerted by the nylon on the strontium ferrite particles would rotate them back after switching of the field resulting in a 2<sup>nd</sup> transient as the elastic torque would no longer be compensated for by the magnetic torque. As no significant transient was observed after the field was switched off, at these experimental conditions a significant elastic torque exerted by the nylon on the strontium ferrite particles can be excluded. To determine whether hypothesis (3) contributes to the observed limiting angle at low field and low temperature, additional experiments were performed at higher annealing temperatures and longer field annealing times that result in stronger chaining. A larger limiting angle was observed for those stronger chained samples.

#### 5.2.4 Data Analysis and Modelling

Assuming that the acceleration is negligible, i.e. steady state condition, following a similar approach as [28], the equation of motion for the orientation of a magnetic particle in a viscous medium is given by the balance of the magnetic torque, and the hydrodynamic torque:

$$L \frac{d\theta}{dt} = -V\mu_o \vec{M}_s \times \vec{H} \quad (5.4)$$

Where  $t$  is the time,  $\theta$  is the orientation of the particle defined by the angle between the field and its c-axis (easy axis),  $V$  the volume of the particle,  $\vec{M}_s$  the saturation magnetic moment of Strontium Ferrite, and  $\vec{H}$  the magnetic field felt by the particle. Note that the

effect of the static friction and direct particle to particle interaction are ignored here. The value of L depends on the volume and the shape of the particle and is given by [29-32]

$$L = \frac{8\pi\eta a^3}{F(D)} \quad (5.5)$$

where  $2a$  is the length of the particle's short axis,  $D$  is the aspect ratio,  $\eta$  is the dynamic rotation viscosity, and  $F(D)$  is a correction factor which depends on the shape and the rotation axis of the particle and can be calculated from integrating the fluid pressure and the friction forces over the surface of the particle for rotational flow [33, 34]. To simplify our model, we assume spherical particles i.e.  $F(D)=1$  in the rest of the paper. Note that  $\mathbf{H}$  in equation (5.4) is the applied field corrected for by the demagnetizing field so

$$\begin{aligned} L \frac{d\theta}{dt} &= -V\mu_o \vec{M}_s \times (\vec{H}_a - \vec{H}_d) = -V\mu_o \vec{M}_s \times (\vec{H}_a - N_d \vec{M}_s) = \\ &= -V\mu_o [\vec{M}_s \times \vec{H}_a - N_d \vec{M}_s \times \vec{M}_s] = -V\mu_o \vec{M}_s \times \vec{H}_a \end{aligned} \quad (5.6)$$

Where,  $\mathbf{H}_a$  is the applied field,  $\mathbf{H}_d$  is the particle's demagnetizing field and  $N_d$  is the particle's demagnetizing factor. Hence, the demagnetizing field actually has zero contributions to the torque because it is always anti-parallel to the particle's magnetic moment [7]. Using equation (5.5) for L, assuming uniaxial anisotropy for the ferrite particles and an angle  $\Delta\theta$  between the Magnetic moment and the easy axis of the particle equation (5.6) simplifies to:

$$8\pi\eta a^3 \frac{d\theta}{dt} = -V\mu_o M_s H_a \sin(\theta - \Delta\theta) \quad (5.7)$$

$\Delta\theta$  can be calculated from the balance between the magnetic torque and anisotropic torque of the sample [7]

$$V\mu_o M_s H \sin(\theta - \Delta\theta) = K_1 \sin(2\Delta\theta) \quad (5.8)$$

Using the magnetic properties of strontium ferrite from reference [35] the  $\Delta\theta$  was determined from equation (5.8) by plotting the left and the right side of (5.8) at  $\theta=90$  degrees versus  $\Delta\theta$ . The intersection points give us the  $\Delta\theta$  value. For H the applied field corrected for by the demagnetizing field was used. Since  $\Delta\theta$  is very small i.e. 1.4 degrees at RT and even smaller at 175 °C the term  $\sin(\theta - \Delta\theta) \sim \sin(\theta)$ , hence equation (5.7) can be approximated by,

$$8\pi\eta a^3 \frac{d\theta}{dt} = -V\mu_o M_s H_a \sin(\theta) \quad (5.9)$$

Taking the integral gives:

$$\int \frac{d\theta}{\sin(\theta)} = -\frac{\mu_o M_s H_a}{6\eta} \int dt = -\frac{1}{\tau} \int dt \quad \rightarrow \quad -\ln\left(\frac{\cos(\theta)}{\sin(\theta)} + \frac{1}{\sin(\theta)}\right) = -\frac{t}{\tau} + C \quad (5.10)$$

Taking the exponent on both sides and substituting  $e^C = \frac{\sin(\theta_o)}{\cos(\theta_o)+1}$  gives:

$$\frac{\sin(\theta)}{\cos(\theta)+1} = \frac{\sin(\theta_o)}{\cos(\theta_o)+1} e^{-t/\tau} \quad (5.11)$$

$$\text{where } \tau = \frac{L}{M_s V \mu_o H_a} = \frac{6\eta}{M_s \mu_o H_a} \quad (5.12)$$

So, it is possible to determine the viscosity from the measured time constant of a  $\frac{\sin(\theta)}{\cos(\theta)+1}$  versus t graph. For this approach the angular acceleration is neglected so assuming the particles have a negligible rotational inertia. Furthermore, the effect of the magnetic interaction on the dynamic viscosity is ignored. It is also assumed that the rotation field is large enough so  $\tau_{\text{Brownian rotation}} \ll \tau_{\text{Brownian chaining}}$  but small enough to not significantly influence the magnetization of the particles. So, the latter means it can be assumed that the magnetic moment in the particles is parallel to their easy axes. Furthermore, it is assumed that the magnetic particles are spherical and that they rotate coherently in the xy plane of the composite where x is the direction of the rotation field. The data of Fig. 5.8 was used to determine the time constant of the rotation from the initial slope of the  $\ln((\cos(\theta)+1)/\sin(\theta))$  versus t graphs. Then these time constants were used to estimate the dynamic rotation viscosity using equation (5.12). For the measurements done at 132 and 136 °C the dynamic viscosity was determined from the slope of a  $\tau$  versus 1/H graph as measurements were done for different rotation fields for these temperatures. The data is summarized in Fig. 5.9a. A kink is observed in the dynamic viscosity near 140 °C which is close to the  $\alpha_c$ ' relaxation related to the crystalline regions as observed by Salmoria et al. in PA-12 at 145 °C [31]. The steep decrease of the slopes of  $\eta(T)$  in the interval 132-150 °C, is due to a reduction of the number of cross-link bonds between the separate nylon polymer chains and a reduction of density with temperature resulting in a lower dynamic viscosity.

At large t-values, the angular velocity of the particles decreases to zero before they are lined up with the magnetic field. The magnetic torque exerted on the particles by the field is compensated for by another torque. Assuming the compensating torque to be due to a friction force that is located at the surface of the particle, one can determine the yielding

shear stress from the limit of the magnetic dipole moment angle, the applied field, and the  $M_s$ , i.e.

$$V\mu_o\vec{M}_s \times \vec{H} = \frac{4}{3}\pi R^3\mu_oM_sH\sin(\theta_\infty) = \sigma_s4\pi R^2R \quad (5.13)$$

Where  $\sigma_s$  is the yielding shear stress caused by the static friction. Reorganizing gives:

$$\sigma_s = \frac{1}{3}\mu_oM_sH\sin(\theta_\infty) \quad (5.14)$$

Note that  $\sigma_s$  is independent of the particle size.

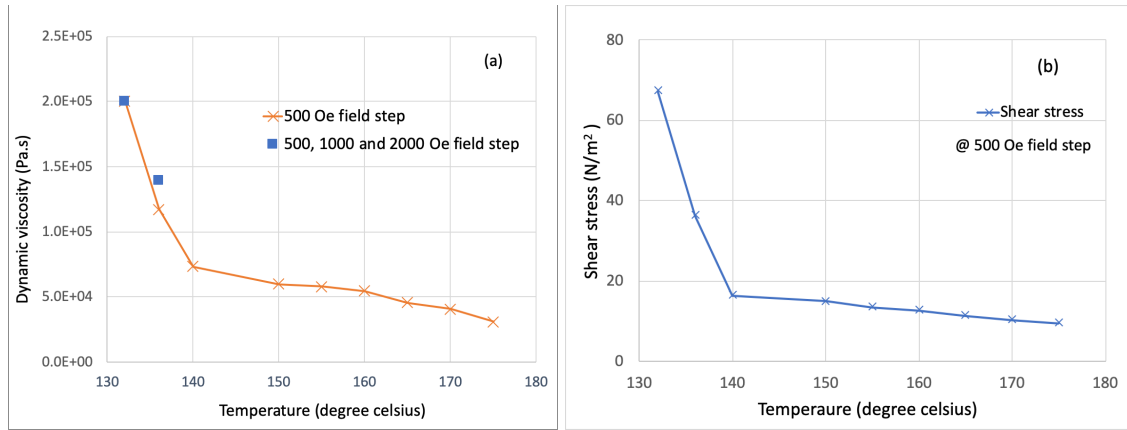


**Fig. 5.9:** (a) Dynamic viscosity and (b) Shear stress as a function of temperature for 40 wt.% SrO(Fe<sub>2</sub>O<sub>3</sub>)<sub>6</sub> particles in PA12 matrix [23].

Fig. 5.9b shows the yielding shear stress as a function of the temperature. Similarly, as for the dynamic viscosity graph a kink is observed around 140 °C. The step decrease of the slopes of  $\sigma_s(T)$  the interval 132-150 °C, is due to a reduction of the number of cross-link bonds between the nylon polymer chains and a decrease of the density of the plastic with temperature allowing for less obstruction for the rotation of the strontium ferrite particles with higher temperatures. The existence of a yielding shear stress is also observed in magnetorheological fluids (MRF) that are placed in a magnetic field. Note that the softened PA-12/ferrite composite differs from a typical MRF in that its particles have a permanent dipole moment resulting in clustering and chaining even upon removal of the alignment field and that the softened PA12 matrix has a much larger viscosity and might also contribute to the observed non-zero yielding stress similar to a Bingham plastic.

### 5.2.5 Discussion

Although the demagnetizing field will not directly impact the transients as the demagnetizing field does not provide a torque on the particles, the shape of the sample, the particles and the aggregates of particles (chaining) can impact the measured transients. The model derived in Section 5.2.4 is based on the assumption that the magnetic ferrite particles rotate coherently in the xy-plane of the composite. The sample's inhomogeneous demagnetizing field will favor rotation out of the xy-plane and/or "incoherent rotation" modes possibly including macroscopic curling and or buckling processes where the magnetic moment of different strontium ferrite particles are not parallel to each other. Evidence for a magnetic moment perpendicular to the xy-plane and or "incoherent rotation" modes are shown in Fig. 5.10 which shows that  $|\vec{M}(t)|$  is not constant but varies slightly with time. The sign of the  $|\vec{M}(t)|$  transient depends on the temperature as shown in Fig. 5.10a. Note that there is a period of approximately 16 seconds between the time that the anneal field is lowered to zero and the rotation field is applied. During this period the non-homogeneous demagnetizing field acts on the particles and causes the  $|\vec{M}(t)|$  to decrease. Preliminary experiments show that the  $|\vec{M}(t)|$  transient can be suppressed by (a) choosing a sample shape that has a low average demagnetizing field in the xy-plane as for example a disk sample or by (b) using a bias field that partly compensates for the demagnetizing field. Note that this bias field is applied in the x-direction and can only cancel out the demagnetizing field at the start of the 90-degree rotation step. As the sample is rotated the angle between the demagnetizing field and the bias field increases from 0 to 90 degrees and the cancelation is no longer perfect at the end of the rotation step. Fig. 5.10b shows that the  $|\vec{M}(t)|$  transient is almost 6.6% of  $M_s$  for a 1.5 mm diameter filament sample while for a 3.2 mm diameter disk sample the observed  $|\vec{M}(t)|$  transient is smaller than 2.7%. The bias field method can suppress the  $|\vec{M}(t)|$  transient to 3.5% as shown in Fig. 5.10b. A correction field of 134 Oe was applied on a filament sample. Both measures are not for 100% effective in eliminating the  $|\vec{M}(t)|$  transient.

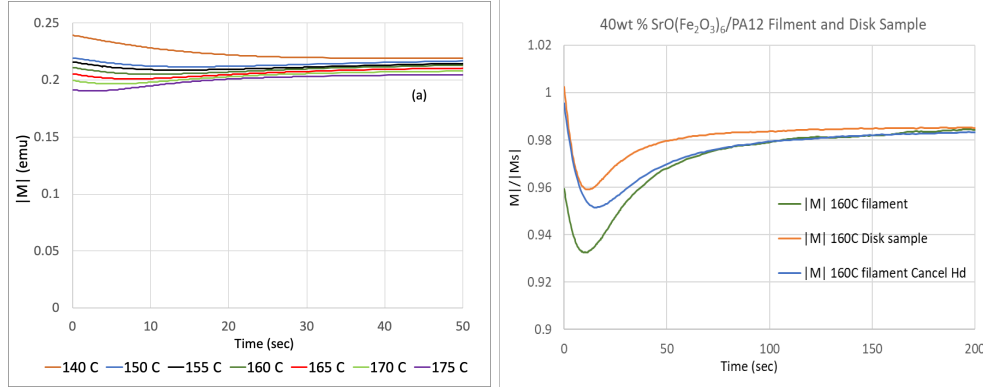


**Fig. 5.10:** (a)  $|M|$  Vs time of 40wt.% SrO(Fe<sub>2</sub>O<sub>3</sub>)<sub>6</sub>/PA12 composite filament for different temperatures (left) and (b) comparison between observed  $|\vec{M}(t)|/|\vec{M}_s|$  transient on filament and disk sample at 160 °C (right) [23].

The inhomogeneous demagnetizing field for these “incoherent rotation” modes originate from the variation of the demagnetizing field caused by the variation of the magnetostatic interaction originating from the size, shape and spatial distribution of the particles including the effect of magnetic chaining [36, 37]. Although magnetic chaining was observed, the SEM image of Fig. 5.6b shows a very moderate amount of chaining explaining the small effects observed. Larger effects are to be expected at higher packing fractions or for samples that are field annealed for longer times, and or at higher temperatures.

When doing repeated measurements on the same samples it was noticed that the measured dynamic viscosity of samples exposed to numerous thermal cycles above 200 °C slowly increases over time. It is hypothesized that the multiple annealing experiments will make the polymer chains longer and/or increase their entanglements resulting in the observed increases of the dynamic viscosity over time. The thermal annealing is expected to lower the water content of the nylon increasing the average polymer length. This effect is well known and has been observed by others for Z2773 PA12 of Evonik. Additionally, we suspect that exposing the same sample to multiple field anneal cycles increases the agglomeration of particles through chaining and increases the dynamic viscosity of the magnetic composite similarly as exposing an MRF to an external magnetic field. This hypothesis is consistent with small increases of the yielding stress of samples exposed to multiple annealing cycles above 200 °C. Attempts to directly observe those subtle

agglomerations changes by SEM or optical microscopy on the samples studied have not been successful yet. More sensitive methods to quantify agglomeration effects in magnetic composites need to be developed.

### 5.2.6 Summary

A biaxial VSM was used to study the rotation of the magnetic moment in strontium ferrite-PA12 composites in the temperature range from 120-175 °C, i.e below the matrix melting temperature. For specific applications such as permanent magnet for motor cannot operate above 150 °C [38]. To check the temperature capability of the PA12 bonded permanent magnet, it's crucial to study the below matrix meting temperature measurement. It was noticed that the strontium ferrite particles are no longer fixed in the PA-12 matrix at temperatures above 132 °C. These results show that 3D printed bonded magnets using PA-12 as a polymer cannot be used above 132 °C. Furthermore, it shows that the magnetic particles can be oriented with an external magnetic field down to 132 °C although quick orientation requires elevated temperatures and high magnetic fields. It also suggests that magnetic anisotropy can be realized by field annealing 3D printed objects at temperatures slightly above 130 °C. Exposure of 3d printed objects to these low temperatures might not significantly impact shape and form but could induce a magnetic anisotropy. It might be possible to improve the temperature stability of 3D printed PA12/strontium ferrite composites by improving the interfacial bond between the nylon matrix and the strontium ferrite filler using an adhesion promoter like Silane. Such approach could push up this critical temperature (132 °C) for this type of PA12/strontium ferrite composite bonded magnets. Another approach would be to replace PA12 with a larger melting point matrix. The melting point of nylon depends on the distance between the polyamide groups in the polymer chain (i.e. PA12, PA11, PA6). More polyamide groups per molecule means more cross links between the nylon molecules but also more possible cross links between polymer matrix and hexaferrite particles. Hence, this will affect cohesion and adhesion forces. The higher melting point will come at the expense of lower flowability of the suspension and larger water content as water will attach to the Polyamide groups. The dynamic viscosity of the strontium ferrite composite was estimated from the initial slope

of the  $\ln((\cos(\theta)+1)/\sin(\theta))$  versus  $t$  graph and decreased with temperature from  $2E5$  Pa.s at  $132$  °C to  $3.1E4$  Pa.s at  $175$  °C. Note that these viscosity values are significantly higher than the one measured above the melting temperature of PA12 by others [39]. The yield shear stress between the strontium ferrite particles and the nylon matrix was estimated from the magnetic dipole angle at large  $t$  and also decreased with temperature. Both the dynamic viscosity and the yield shear stress versus  $T$  curves show a kink near  $140$  °C. Note that this is close to the  $\alpha_c'$  relaxation observed by Salmoria et al. in a PA-12 loss tangent versus temperature graph at  $145$  °C [31]. As far as we know this is the first-time dynamic viscosity is studied with a VSM. Note that the estimate of the viscosity with the here presented method depends on the drag torque while standard viscosity measurement equipment senses the drag force. Better models describing hydrodynamic drag in suspensions under creeping flow of non-spherical particles need to be developed [40]. We also compared our results with recent modeling and experimental work done by Sarkar et al. [14] on NdFeB and SmCo nylon composites. They explored the effect of magnetic field, packing fraction, and particle size on the degree of alignment all at a printing temperature of  $230$  °C. The calculated time constant for the rotation was compared to the time the particles are exposed to the magnetic field calculated from the print speed estimating the degree of alignment of the MFAAM printed composites. Although their experiments were done for higher packing fraction up to  $65$  vol.% which is much larger than the  $8$  vol.% of our samples and for higher temperatures, i.e.  $230$  °C which is also significantly higher than the  $175$  °C used for our experiments, their results are consistent with the results presented here. Specifically, their observation that for high packing fractions and low magnetic fields the alignment field is insufficient to overcome the drag torque of the polymer binder, is similar to the friction torque we observed in Fig. 5.7b and 5.8b.

For MFAAM, here presented results suggests that one can orient the particles in the PA12/ferrite composite down to temperatures below the melting point. The required alignment field at  $175$  °C for an alignment time less than  $1$  second can be estimated from equation (5.12) and the results presented in Fig. 5.8a and is approximately  $5000$  Oe. Although such fields can be generated by permanent magnets [11, 41] or electromagnets [42] near the print head, it might be better to apply the field away from the nozzle to avoid clogging issues caused by magnetic chaining in the heated nozzle. Assuming a printing

temperature of 260 °C, a typical cool down rate of 50 °C /sec [43, 44], and a printing speed of 20 mm/sec [45], it should be possible to apply the magnetic field 1 inch away from the nozzle and still have a sufficient low alignment time. Such implementation of an MFAAM printer would avoid rheological clogging issues caused by chaining in a nozzle exposed to the magnetic print field. Although the 3D-print quality of nylon in general is improved if the filament is dried, extensive drying can largely impact the viscosity of the material and possibly affect print quality in a negative way. Although the simplified model as described in here can help to the understanding of MFAAM alignment process a more complete modelling approach that includes the combined effect of flow and magnetic field on the alignment process as well as changes of the mass density of the printed material as it solidifies is required to further develop MFAAM.

### **5.3 Magnetic Behavior and Chaining of Strontium Ferrite-Nylon Composite Above the Melting Temperature**

To better understand Magnetic Field Assisted Additive Manufacturing (MFAAM), the effect of a magnetic field on the orientation and distribution of Sr-ferrite particles in a molten PA-12 matrix study is extremely crucial. Typically, Strontium Ferrite-Nylon composite is printed at a temperature above 230 °C, so significant above the nylon melting temperature. Hence, to simulate the 3D printing process one should study the orientation and the redistribution of the magnetic particles above the melting temperature.

MFAAM, or 3D printing in a magnetic field, is a new manufacturing method that allows for the realization of new materials and devices whose magnetic anisotropy axis varies as a function of position. Such materials cannot yet be made by any other manufacturing method. Applications of hard magnetic MFAAM materials include Halbach cylinders for use in energy efficient electromotors and generators and high-performance permanent magnets for use for example in portable MRI equipment. In addition, these new MFAAM materials might replace magnetic polymer composites applied in rapid prototyping or high-performance applications. Properties of such magnetic composites depend on the particle microstructural distribution within the polymer matrix [46]. At elevated temperatures, above the softening temperature of the polymer matrix but below the Curie temperature of

the single domain magnetic particles, the polymer matrix loses its ability to fix the orientation of the non-spherical magnetic particles and individual particles rotate freely, lining up with an externally applied field [23]. This alignment process influences the distribution pattern of the magnetic particles in the suspension. The particles attract each other due to the magnetic force originating from the magnetostatic interaction, and eventually organize in long chains parallel to the direction of the applied magnetic field [47]. This interaction and chaining process is enhanced in suspensions exposed to a magnetic field. So, two effects are observed: (1) the alignment of the magnetic particles due to the rotation inside the molten matrix towards an externally applied magnetic field and (2) the redistribution of the aligned magnetic particles due to the inhomogeneous magnetostatic interaction field often referred to as magnetic chaining [23, 47-52]. If the matrix is cooled down to room temperature in a field, the frozen-in magnetic texture and chain morphology make the composite anisotropic. Here, we report on the magnetic anisotropy of 5 and 40 wt.% SrO(Fe<sub>2</sub>O<sub>3</sub>)<sub>6</sub>/PA-12 composites (read 1 vol.% and 8 vol.%) after field-anneals above T<sub>m</sub>. The rotation of magnetic dipoles during the field annealing process above T<sub>m</sub> is studied with a biaxial VSM using a similar method as described in [23]. The chaining is studied through direct SEM studies on field-annealed samples.

### 5.3.1 Experimental Procedure

OP-71 Strontium Ferrite (SrO(Fe<sub>2</sub>O<sub>3</sub>)<sub>6</sub>) powder obtained from Dow Electronics Materials Corporation and Vestosint® 3D Z2773 PA-12 (Nylon) (T<sub>m</sub> ~ 178 °C [31]) from Evonik were used to realize 5 and 40 wt.% SrO(Fe<sub>2</sub>O<sub>3</sub>)<sub>6</sub>/PA-12 composite 3D printer filaments. OP-71 powder consists of strontium ferrite platelets (Curie temperature is 477 °C) with an average diameter of 1.39 μm. SEM images of the as-received powder reveal a large spread in diameter i.e. 0.1-4.5 μm. Individual particles are platelets with a typical aspect ratio of 3. These particles do not have a perfect hexagonal shape suggesting they are polycrystalline but have a strong texture [18]. Using the M<sub>s</sub> and K data of [53] the calculated RT single domain size of strontium ferrite is approximately 0.6 μm and increases to 1.2 μm at 230 °C, the field-anneal temperature used in this study. Although these values suggest that the largest particles are multi-domain the coercivity of both studied composites

is close to 4 kOe. A Thermo Fisher Process 11 co-rotating twin-screw extruder was used to manufacture the magnetic polymer composite filaments [12, 17]. The particle's orientation and distribution in the filaments was studied with a FEI Helios NanoLab 400 DualBeam SEM. Samples were cut at RT perpendicular to the cylindrical axis using a surgical knife. All samples were coated with a conductive 4 to 6 nm layer of Iridium (Ir) deposited by a Quorum Technologies EMS150T Imaging Sputter Coater. The 5 wt.% filaments needed a thicker coating (6 nm) to avoid charging issues than the 40 wt.% filaments (4 nm) that have a higher loading level [23].

The field-anneal process and the magnetic rotation studies were all done using a MicroSense-KLA biaxial EZ-9 VSM furnished with a 70-1000 K temperature option flowing Argon (Ar) gas at 230 °C. This temperature (230 °C) was chosen to simulate the alignment of the particles during the 3D printing process as it is in the center of the process 3D-print window defined by PA-12's  $T_m$  (175 °C) and the onset of decomposition of the Nylon matrix (290-400 °C) [54]. Note that, up to 290 °C the weight loss observed in TGA graphs is negligible.

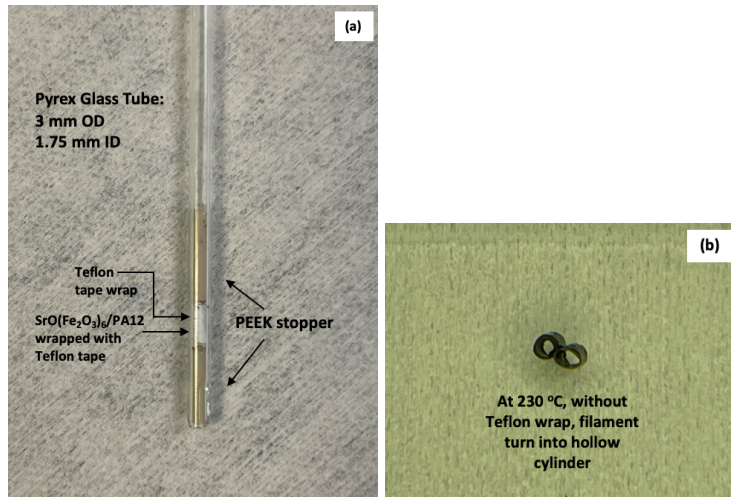


**Fig. 5.11:** (a) SrO(Fe<sub>2</sub>O<sub>3</sub>)<sub>6</sub>/ PA12 cylindrical-shaped filament wrapped with Teflon tape and secured in Pyrex glass tubes with PEEK stoppers and high temperature silicone glue (b) at 230 °C upon melting, without Teflon wrap, filament turn into hollow cylinder [55].

Samples were 4-6 mm long cylindrical filaments with an average diameter of 1.5 mm and typically had a mass of around ~14 mg. The sample's mass was measured with a C-30 Cahn microbalance that has a resolution down to 1 microgram. They were loaded in a Pyrex glass tube with an outer diameter of 3 mm and an inner diameter of 1.75 mm (Fig.

5.11a). The filament was wrapped with Teflon plumber tape that has a low surface free energy to avoid the composite to wet with the Pyrex tube upon melting and turn into a hollow cylinder at 230 °C (Fig. 5.11b). PEEK stoppers with high temperature silicone glue on both sides of the samples were used to secure the sample's position and prevent the molten composite to leak out the glass rod. The VSM's furnace was used to heat up the sample for the field-anneal and the rotation studies. This furnace operates under Ar and allows temperature rates up to 1.1 °C/sec.

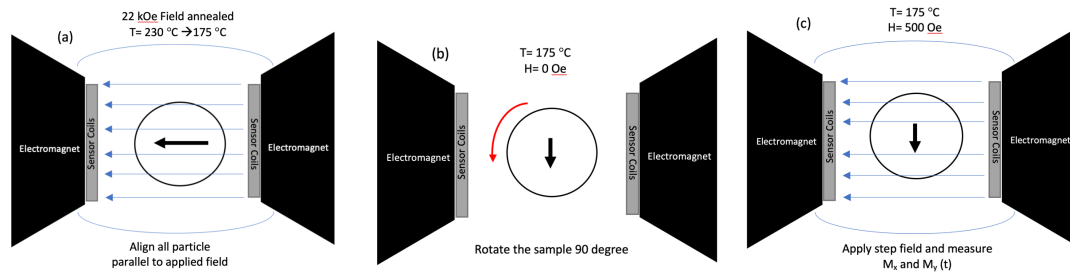


**Fig. 5.12:** Top view of the sample inside VSM chamber (a) Filament samples were annealed in a field of 22,000 Oe at 230 °C for 3 minutes, cooled down in a magnetic field; (b) rotated over 90 degrees in the VSM so the magnetic moment of the field annealed sample is perpendicular to the field direction; (c) a step field of 500 Oe was applied at the measurement temperature while the  $M_x$  and  $M_y$  component were monitored as a function of the field temperature.

The rotation of the magnetic particles in the molten suspension was studied with the biaxial VSM. Filament samples were annealed in a field of 22 kOe at 230 °C for 3 minutes and cooled down to measurement temperature in a magnetic field of 22 kOe. Then the sample was rotated in zero field over 90 degree to orient its magnetic dipole moment perpendicular to the field direction. A step field of 500 Oe was applied to exert a torque on the magnetic particles that rotates them towards the field direction. Please note that the applied field is much smaller than the coercivity and anisotropy field so thus not significantly affects the particle's magnetic dipole moment which is expected to line up close to the particle's easy axis. During the application of this field, the sample's  $M_x$  and  $M_y$  components were recorded to monitor the rotation of the particles in the nylon matrix through  $\theta(t) = \tan^{-1}(M_y(t)/M_x(t))$  [23]. This experiment was repeated for different temperatures on the same sample to explore how temperature affects the alignment process.

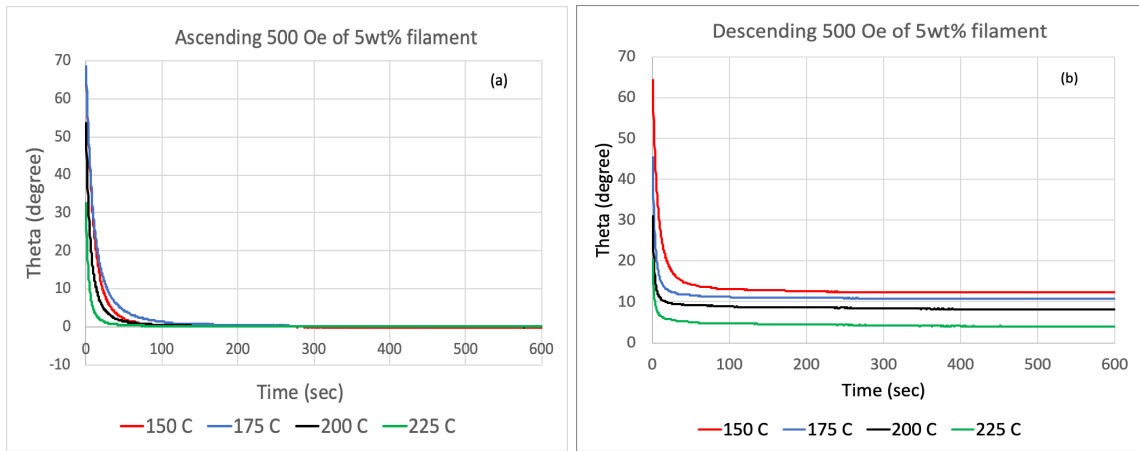
The experiment is summarized in Fig. 5.12 and more details on this novel method can be found in [23].

Directionality analysis of scanning electron micrographs was utilized as a tool to quantify the degree of filler (magnetic particle) orientation and magnetic chaining in the composite filament. Within the pristine as extruded filament, the magnetic particles were homogeneously dispersed and randomly oriented with a weak c-axis texture along the filament's r-direction originating from flow induced anisotropy [17]. When this molten suspension is subjected to an external magnetic field, magnetic moments are induced along the applied field axis, producing particle chaining that enhances magnetic properties like magnetic anisotropy along the direction of the anneal field [46, 48-52]. Such field-induced magnetic anisotropy is what makes MFAAM materials different from other isotropic or anisotropic magnetic composites and of significant interest for application in magnetic sensors actuators, and electronic devices.

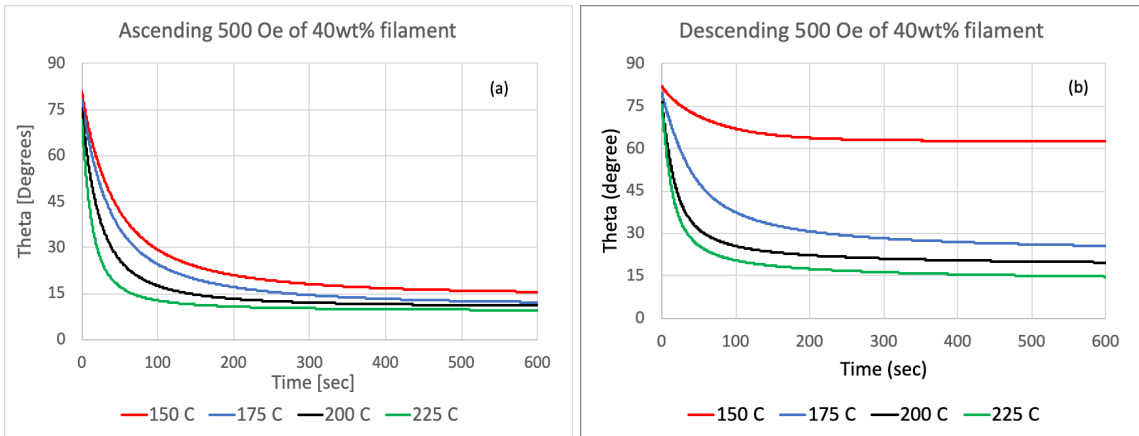
### 5.3.2 Measurement Data and SEM Image Analysis

Fig. 5.13 and 5.14 show the time dependence of the magnetic moment angle of 5 and 40 wt.% filament samples under exposure of a 500 Oe field step perpendicular to the field-anneal direction for different temperatures. All measurements were done on the same samples and in between each curve the sample was field-annealed along the same direction using the recipe mentioned in section II. The ascending series in Fig. 5.13a and 5.14a show the first four scans (150 °C, 175 °C, 200 °C, 225 °C) done on respectively the 5 and 40 wt.% sample. Fig. 5.13b and 5.14b show the next four scans (225 °C, 200 °C, 175 °C, 150 °C) on respectively the 5 and 40 wt.% sample. The observed transients depend on the temperature similar to what was observed in a previous study for field-anneals below the  $T_m$  [23]. The initial slope of the transients ( $\left. \frac{d\theta}{dt} \right|_{t=0}$ ) increases with temperature and the limiting magnetic moment angle at large  $t$ , ( $\theta(600)$ ), decreases with temperature. The transients depend strongly on the packing fraction (Fig. 5.13 and 5.14) with the initial slopes for the high packing fraction samples a factor 4 to 20 smaller indicating an increase of viscosity with packing fraction as also is observed in other composites [56]. Viscosity increases with multiple thermal cycles above  $T_m$  as seen in Fig. 5.13 and 5.14 are consistent

with what other people found for PA-12 [56, 57]. Strong particle to particle interaction in particularly for the 40 wt.% samples is shown by the large  $\theta(600)$ . In particularly after several field-anneal cycles the  $\theta(600)$  increases (Fig. 5.14). It is clear from this data that the molten composite (200 and 225 °C curves) is a non-Newtonian fluid that can support a yielding stress and that the strength of this yielding stress shows hysteresis, depends strongly on the packing fraction and is affected by the number of high temperature field-anneal cycles the sample is exposed to.



**Fig. 5.13:** Magnetic transient upon application of a 500 Oe field perpendicular to the easy axis of 5 wt.% 22 kOe field annealed at 230 °C composite (a) ascending temperature from 150 to 225 °C (left); (b) descending 225 °C to 150 °C (right) [55].



**Fig. 5.14:** Magnetic transient upon application of a 500 Oe field perpendicular to the easy axis of 40 wt.% 22 kOe field annealed at 230 °C composite (a) ascending temperature from 150 to 225 °C (left); (b) descending 225 °C to 150 °C (right) [55].

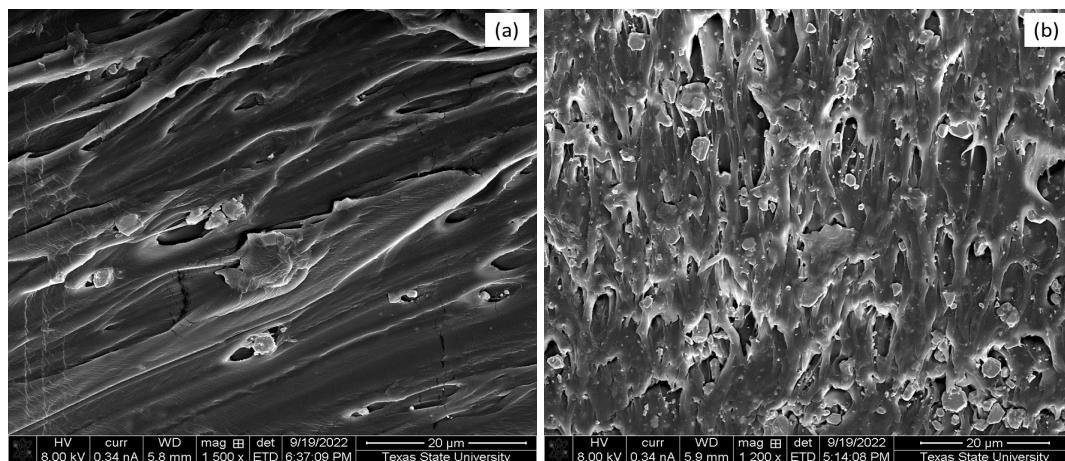


**Fig. 5.15:** SEM images of Pristine (a) 5 wt.% and (b) 40 wt.% SrO(Fe<sub>2</sub>O<sub>3</sub>)<sub>6</sub>/PA12 composite [55].

The SEM images of 5 and 40 wt.% SrO(Fe<sub>2</sub>O<sub>3</sub>)<sub>6</sub>/PA12 pristine filaments are shown in Fig. 5.15a and 5.15b, respectively. Very little agglomeration or grouping is observed in the as-extruded samples. Apparently forces originating from the shear flow in the extrusion die and/or the rotation of the extrusion screws compete with the magnetostatic interaction forces and keep the particles apart in the pristine filament. Note that the velocity in the extrusion is not constant across the extrusion die. The velocity is zero near the walls of the extrusion nozzle wall and then increases towards the middle of the channel. Such flow is referred to as shear flow. Because of the finite dimensions of the particles and the gradient of the flow across the channel, a hydrodynamic torque is exerted on the particles resulting them to spin or tumble (see Fig. 5.16). The motions of the non-spherical particles are periodic, and the axis of the spheroid describes a so-called “Jeffery orbit” in space. Although an infinite number of degenerate Jeffery orbits exist, calculations of others have shown that including inertia results removes the degeneracy. The stable Jeffery orbit of a prolate spheroid is tumbling while the stable Jefferey orbit for an oblate spheroid depend on the aspect ratio. For aspect ratios larger than 1/7 the stable Jefferey orbit is spinning while for smaller aspect ratio tumbling is again the stable state [58]. The SEM pictures show a small number of particles with their long axis parallel to the cross-sectional plane which suggests that they tumble during extrusion although this is not consistent with the observed 1/3 aspect ratio from SEM images. Comparing the SEM images of the pristine filaments of Fig. 5.15 with the field annealed samples of Fig. 5.17, one notices that the particle density is much smaller of the pristine filament indicating that most particle are

not visible and only few of the particles are parallel to the cross-sectional plane which is what is expected. Tumbling of individual particles can provide in a mechanism for chained particles to break up as a tumble results a flip of the magnetic moment and destroys the chaining ordering. Tumbling during the extrusion process then can separate particles from each other destroying agglomeration and realize a more equally dispersed distribution of particles through the pristine filament. Spinning does not usually separate the particles from agglomeration. Another mechanism that might be able to separate chained magnetic particles during the extrusion process is the effect of the hydrodynamic forces exerted by the fluid on particles of a chain.

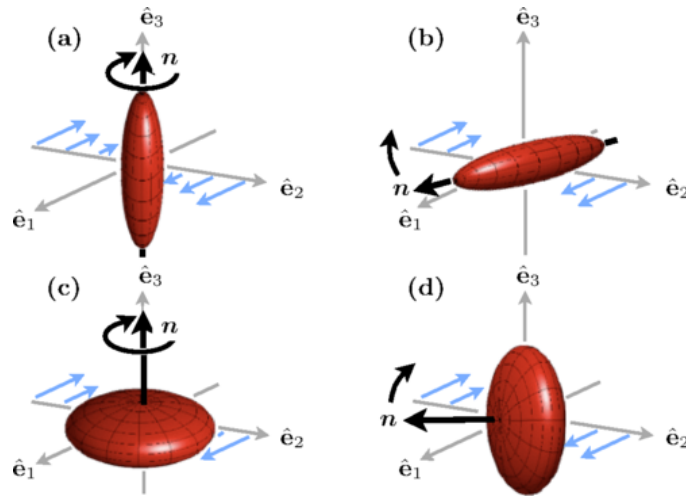


**Fig. 5.16:** (a) spinning Jeffery orbit for prolate spheroid; (b) tumbling Jeffery orbit for prolate spheroid; (c) spinning Jeffery orbit for oblate spheroid; (d) tumbling Jeffery orbit for oblate spheroid [59].

Note that the orientation and possible concentration of the platelets along the  $r$ -direction of the filament is expected to be inhomogeneous due to the shear flow in the extrusion die as shown by others [26, 27]. However, VSM hysteresis curve measurements show that the as-extruded filament has a  $c$ -axis magnetic texture along the filament's  $r$ -direction originating from a flow-induced anisotropy [17].

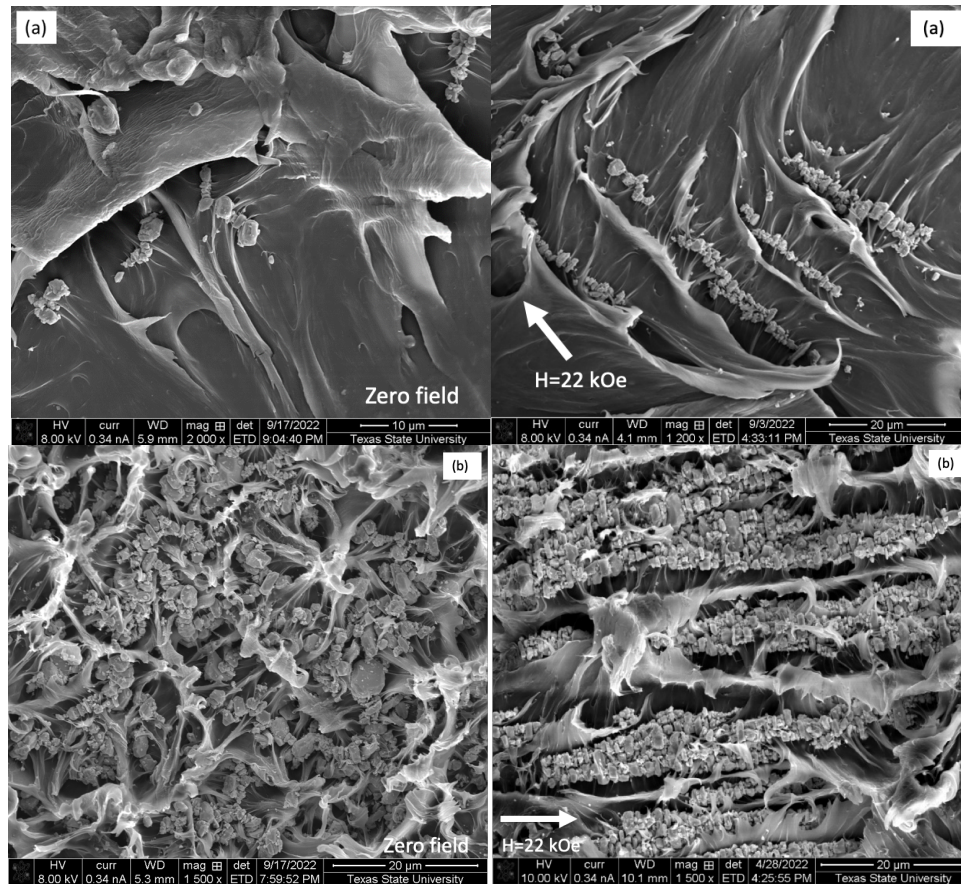


**Fig. 5.17:** Effect of anneal-field on agglomeration: SEM images of zero field and 22,000 Oe field-annealed at 230 °C for 3min for (a) 5 wt.% (top) and (b) 40 wt.% (bottom) SrO(Fe<sub>2</sub>O<sub>3</sub>)<sub>6</sub>/PA12 filament [55].

Fig. 5.17 above shows the effect of field-annealing at 230 °C on the agglomeration of the magnetic particles. These SEM micrographs depicts that, there is considerable amount of agglomeration occurring in both annealed filaments compared to the pristine filament of Fig. 5.15.

However, the shape of the agglomerates in the zero field samples is extremely random due to the absence of any applied magnetic field and chains are much shorter compared to the samples annealed in a field. Clear chaining along the applied field direction is observed in the samples field-annealed at 22 kOe. The cluster size is larger for the high packing fraction filament. Individual particles in the chains are randomly oriented in the zero field-annealed filaments. With the increase of the field to 22 kOe, the orientation of the strontium ferrite particles in the chain are more directional along the field direction (c-axis parallel to the field direction). Note that the cluster size is much higher in the 22

kOe field-annealed for both 5 and 40 wt.% SrO(Fe<sub>2</sub>O<sub>3</sub>)<sub>6</sub>/PA12 composites compared to the zero field-annealed samples.

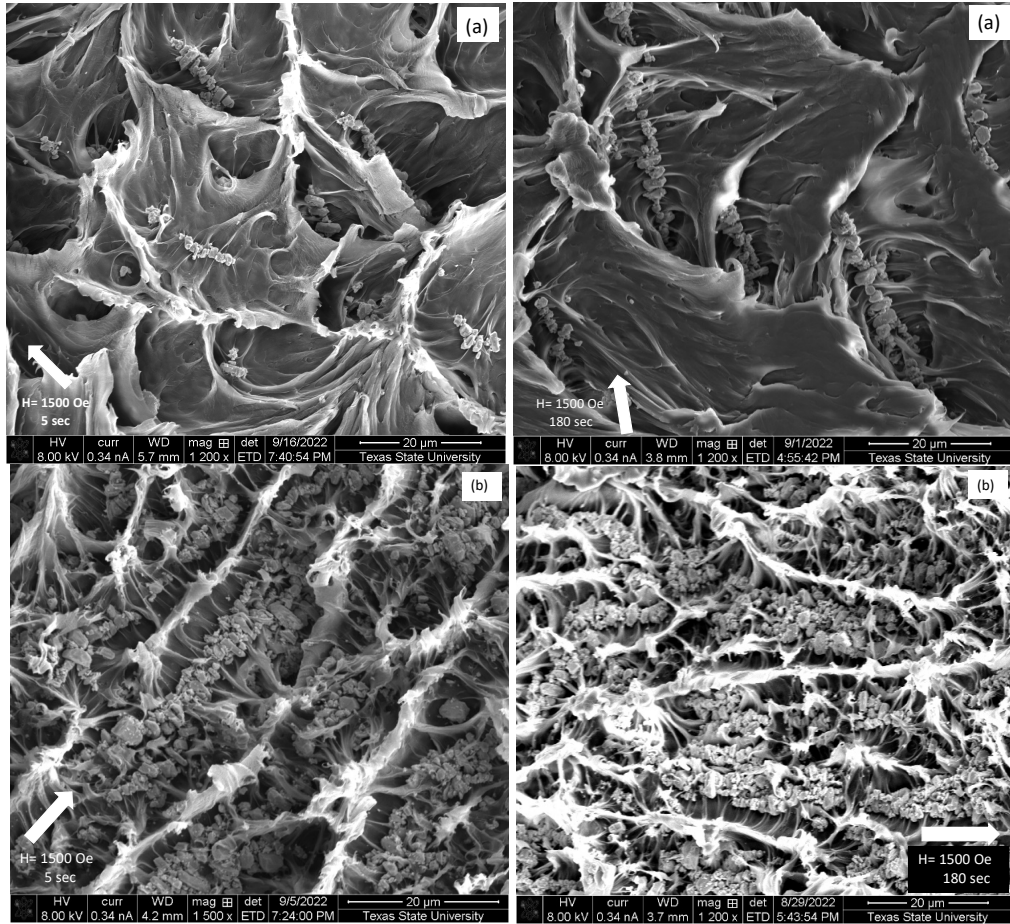


**Fig. 5.18:** Effect of anneal-time on agglomeration: SEM images of 1500 Oe field annealed at 230 °C for 5 sec and for 180 sec for (a) 5 wt.% (top) and (b) 40 wt.% (bottom) SrO(Fe<sub>2</sub>O<sub>3</sub>)<sub>6</sub>/PA12 filament [55].

The effect of the annealing time on the agglomeration and orientation is shown in Fig. 5.18. These SEM micrographs depict that, there is a considerable amount of chaining formation and particle rotation occurring for anneal-fields lower than 22 kOe. For these smaller fields the magnetic chaining is still more or less along the field direction although a larger spread in the chain and individual particle directions are observed. It was additionally observed that, higher field annealing time (180 sec) not only controlled particle agglomeration but also improves the degree of particle alignment in the field direction. Hence, there is a clear anneal-time dependence on agglomeration size and orientation distribution.

The SEM images in the previous section show significant particle agglomeration for all samples except for the pristine filament samples. The cluster size increases with anneal-field, anneal time, and packing fraction and is summarized in Table 5.1 below.

**Table. 5.1.** Cluster size of pristine and 230 °C field-annealed 5 and 40 wt.% composite [55]:

SrO(Fe <sub>2</sub> O <sub>3</sub> ) <sub>6</sub> /PA12 composite	Annealing field (Oe)	Annealing time (sec)	Avg. cluster size (number)
5 wt.%	Pristine	-	2.48
	0	0	9.0
	1500	5	15.49
	1500	180	18.87
	22000	180	26.66
40 wt.%	Pristine	-	4.90
	0	0	44.02
	1500	5	77.0
	1500	180	102.0
	22000	180	169.0

All three effects are understandable. A large anneal-field results in a strong alignment of the particles' magnetic dipole moments which increases the magnetostatic interaction and the speed with which they chain. Similarly, a larger packing fraction results in particles initially already being closer together in the pristine filament increasing the initial magnetic force the particles exert on each other speeding up the chaining process [46, 60, 61]. Additionally, longer annealing time allows for particles initially farther apart to chain-up resulting in longer chains. The strong chaining with little PA-12 left between individual Sr-ferrite particles for samples field-annealed at 22 kOe suggests that direct particle to particle interaction should contribute to the observed non-zero yielding stress shown in Fig. 5.13 and 5.14.

### 5.3.3 Summary

Biaxial VSM was also used to monitor the rotation of the magnetic moment in field-annealed samples exposed to a small field perpendicular to the field-anneal direction. The

rotation time constant, which is inversely proportional to the viscosity, decreases with temperature. At lower temperatures and smaller rotation fields, it is not possible to align the sample's magnetic dipole moment up with the rotation field direction. SEM images suggest that strong chaining limits the space available for the non-spherical particles to rotate over a full 90 degrees and is responsible for the observed non-zero yielding strength. The latter increases with packing fraction which indicates that the required MFAAM alignment fields resulting in decent alignment also increases with packing fraction. To further the development of MFAAM a model of the MFAAM deposition process [14] that also includes chaining processes [39] needs to be developed to better understand how viscosity and packing fraction affect non-spherical particle alignment processes.

Lastly, it was observed that viscosity and yielding strength increase when the composite is exposed to multiple thermal cycles above  $T_m$ . PA-12 polymers often contain reactive chain ends and these reactive end groups can react at elevated temperatures, particularly above  $T_m$ , to increase molecular weight which has a large effect on viscosity for a linear polymer as shown by others [55, 56].

## 5.4 Conclusion

A biaxial VSM was used to study the rotation of the magnetic moment in a strontium ferrite-PA12 composite below the matrix melting temperature and noticed that the strontium ferrite particles are no longer fixed in the nylon matrix at temperatures above 132 °C. These results show that bonded magnets using PA-12 as a polymer cannot be used above 132 °C. Additionally, dynamic viscosity of the strontium ferrite composite was estimated from the initial slope of the  $\ln((\cos(\theta)+1)/\sin(\theta))$  versus  $t$  graph and decreased with temperature from 2E5 Pa.s at 132 °C to 3.1E4 Pa.s at 175 °C. Although the simplified model as described in section 5.2.4 can help to the understanding of MFAAM alignment process a more complete modelling approach that includes the combined effect of flow and magnetic field on the alignment process as well as changes of the mass density of the printed material as it solidifies is required to further develop MFAAM. Biaxial VSM was also used to monitor the rotation of the magnetic moment in a strontium ferrite-PA12 composite above the matrix melting temperature. The initial slope of the transients  $(\frac{d\theta}{dt}|_{t=0})$

increases with temperature and the limiting magnetic moment angle at large  $t$ , ( $\theta(600)$ ), decreases with temperature. The transients depend strongly on the packing fraction (Fig. 5.13 and 5.14) with the initial slopes for the high packing fraction samples a factor 4 to 20 smaller indicating an increase of viscosity with packing fraction as also is observed in other composites [55]. SEM images suggest that strong chaining limits the space available for the non-spherical particles to rotate over a full 90 degrees and is responsible for the observed non-zero yielding strength.

## REFERENCES

- [1] A. M. de Witte, K. O'Grady, G. N. Coverdale, and R.W. Chantrell, *J. Magn. Magn. Mater.* 88, 183 (1990).
- [2] C. Serletis, K.G. Efthimiadis, *J. Magn. Magn. Mater.* 324, 2547-2552 (2012).
- [3] G. Richter, *Ann. Phys.* 421, 605 (1937).
- [4] Y. Li, H.E. Evans, I.R. Harris, and I. P. Jones, *Oxidation of Metals* 59, 167-182 (2003).
- [5] J. W. Cahn, *J. App. Phys.* 34, 3581 (1963).
- [6] S. Chikazumi, *Physics of Ferromagnetism* (Oxford Science Publications 1997), ISBN 0198517769.
- [7] B.D. Culity and C.D. Graham *Introduction to Magnetic Materials*, Second ed., (Wiley-IEEE, 2008), Chap.7: Magnetic anisotropy, ISBN:9780471477419.
- [8] K. Shahrivar et al., "Rheological behavior of magnetic colloids in the borderline between ferrofluids and magnetorheological fluids," *J. Rheol. (N. Y. N. Y.)*, vol. 63, no. 4, pp. 547–558, 2019.
- [9] D. Givord, P. Tenaud, T. Viadieu, and G. Hadjipanayis, "Magnetic viscosity in different Nd-Fe-B magnets," *J. Appl. Phys.*, vol. 61, no. 8, pp. 3454–3456, 1987.
- [10] Zai-Bing Guo et al., "Preparation and magnetic properties of SrFe<sub>12</sub>O<sub>19</sub> particles prepared by the salt-melt method," *J. Magn. Magn. Mater.*, vol. 175, pp. 333–336, 1997.
- [11] C. Huber, S. Cano, I. Teliban, S. Schussnigg, M. Groenfeld, D. Suess, *J. Appl. Phys.* 127, 063904 (2020).
- [12] C. Belduque, R. Robinson, A. Medina, T. Ahmed, R. Kala, W. Geerts, and J. Tate, *Society for the Advancement of Material and Process Engineering*, Long Beach, CA, 24–27 May 2021 (SAMPE, 2021), p. 686.
- [13] L. Henderson, S. Zamora, T. N. Ahmed, C. Belduque, J. Tate, M. Y. Chen, and W. J. Geerts, *J. Magn. Magn. Mater.* 538, 168320 (2021).
- [14] A. Sarkar, M. P. Paranthaman, I. C. Nlebedim, *Additive Manufacturing* 46, 102096 (2021).

- [15] C. Huber, C. Abert, F. Bruckner, M. Groenefeld, O. Muthsam, S. Schuschnigg, K. Sirak, R. Thanhoffer, I. Teliban, C. Vogler, R. Windl, and D. Suess, *Appl. Phys. Lett.* 109, 162401 (2016).
- [16] C. Huber, M. Goertler, C. Abert, F. Bruckner, M. Groenefeld, I. Teliban, D. Suess, *Sci. Rep.* 8, no. 1, pp. 1–8, (2018).
- [17] T. N. Ahmed, M. C. Belduque, Binod D.C., J. Tate, W. Geerts, *AIP Advances* 11, 015048 (2021).
- [18] M.S. Thesis of Maria Camila Belduque Correa, "Development of Strontium Ferrite/Polyamide 12 Composites for Magnetic Devices Using Additive Manufacturing", Texas State University, May (2021).
- [19] R. Kuracina, Z. Szabov., E. Buransk., A. Pastierov., P. Gogola, and I. Buranský, *Polymers* 13, 3014 (2021).
- [20] G. S. Martynkova, A. Sliva, G. Kratosova, K. C. Barabaszova, S. Studentova, J. Klusak, S. Brozova, T. Dokoupil, and S. Holesova, *Polymers* 13, 810 (2021).
- [21] N. Ma, W. Liu, L. Ma, S. he, H. Liu, Z. Zhang, A. Sun, M. Huang, and C. Zhu, *e-Polym.* 20, 346–352 (2020).
- [22] P. Chen, M. Tang, W. Zhu, L. Yang, S. Wen, C. Yan, Z. Ji, and H. N. Yusheng Shi, *Poly. Test.* 67, 370–379 (2018).
- [23] T. N. Ahmed, C. Belduque, M. Y. Chen, J. S. Tate, and W. J. Geerts, "Dynamic viscosity of strontium ferrite–nylon composite below the melting temperature," *AIP Adv.*, vol. 12, no. 9, p. 095223, 2022.
- [24] R. Skomski, G. C. Hadjipanayis, and D. J. Sellmyer, *IEEE Trans. Magn.* 43, 2956–2958 (2007).
- [25] H. Nischio and H. Yamamoto, *IEEE Trans. Magn.* 47, 3641–3644 (2011).
- [26] B. P. Heller, D. E. Smith, and D. A. Jack, *Addit. Manuf.* 12, 252–264 (2016).
- [27] J. H. Phelps, C. L. Tucker, *J. Non-Newtonian Fluid Mech.* 156, 165–176 (2009).
- [28] T. Kimura, M. Yamato, W. Koshimizu, M. Koike, and T. Kawai, *Langmuir* 16, 858 (2000).
- [29] A. Einstein, *Ann. Phys.* 19(4), 289 (1906).
- [30] G. B. Jeffery, *Proc. R. Soc. London, Ser. A* 102, 161 (1922).

- [31] G. V. Salmoria, J. L. Leite, L. F. Vieira, A. T. N. Pires, and C. R. M. Roesler, *Polym. Test.* 31,411 (2012).
- [32] F. R. Eirich, *RHEOLOGY: Theory and Applications* (Academic Press, 1967), Vol. 4.
- [33] D. Leith, *Aerosol Sci. Technol.* 6(2), 153–161 (1987).
- [34] Y. C. Chang and H. J. Keh, *Theor. Comput. Fluid Dyn.* 26, 173–183 (2012).
- [35] P. Jing, J. Du, J. Wang, J. wei, L. Pan, J. Li, and Q. Liu, *Sci. Rep.* 5, 15089 (2015).
- [36] J. E. Martin and A. Snezhko, *Rep. Prog. Phys.* 76, 126601 (2013).
- [37] L. Kaufman and P. J. Rousseeuw, *Finding Groups in Data: An Introduction to Cluster Analysis* (Wiley, New York, 1990).
- [38] K. Komeza et al., “High Temperature Permanent Magnet Synchronous Machine Analysis of Thermal Field,” *Open Phys.*, vol. 17, no. 1, pp. 631–642, 2019.
- [39] B. Haworth, N. Hopkinson, D. Hitt, and X. Zhong, *Rapid Prototyping J.* 19(1), 28–36 (2013).
- [40] S. A. Faroughi and C. Huber, *Rheol. Acta* 56, 35–49 (2017).
- [41] C. Huber, C. Abert, F. Bruckner, C. Pfaff, J. Kriwet, M. Groenefeld, I. Teliban, C. Vogler, and D. Suess, *J. Appl. Phys.* 122, 053904 (2017).
- [42] A. Sarkar, M. A. Somashekara, M. P. Paranthaman, M. Kramer, C. Haase, and I. C. Nlebedim, *Addit. Manuf.* 34, 101289 (2020).
- [43] K. Pooladvand and C. Furlong, *Mech. Compos. Multifunct. Mater.* 7, 45 (2016).
- [44] Retrieved: 31 January 2023, Available Online: See [https://www.youtube.com/watch?v=\\_SvR5Dxu0cU](https://www.youtube.com/watch?v=_SvR5Dxu0cU) for the temperature distribution simulation during the 3D printing of a part using commercially available software. Layer-by-layer fabrication of an ABS specimen with 6mm height, 5mm width, and 40 mm length is presented using the Finite Element Method (FEM).
- [45] T. Beran, T. Mulholland, F. Henning, N. Rudolph, and T. A. Osswald, *Addit. Manuf.* 23, 206–214 (2018).
- [46] B. Nagarajan, M. A. W. Schoen, S. Trudel, A. J. Qureshi, and P. Mertiny, *Polymers.* 12, no. 9., (2020).

- [47] H. Wu., Z. Xu, J. Wang, X. Bo, Z. Tang, S. Jiang, and G. Zhang, *J. Magn. Magn. Mater.* 527, 167693, (2021).
- [48] J. J. Romero, R. Cuadrado, E. Pina, A. de Hoyos. F. Pigazo, F.J. Palomares, A. Hernando, R. Sastre, and J. M. Gonzalez, *J. of App. Phys.* 99, no. 8, (2006).
- [49] J. E. Martin, E. Venturini, J. Odinek, and R. A. Anderson, *Phys. Rev. E - Stat. Physics, Plasmas, Fluids, Relat. Interdiscip. Top.* 61, no. 3, 2818–2830, (2000).
- [50] E. Joven, A. Del Moral, and J. I. Arnaudas, *J. of Magn. and Mag. Mater.* 83, pg. 548, (1990).
- [51] R. M. Erb, J. Segmehl, M. Charilaou, J. F. Löffler, and A. R. Studart, *Soft Matter.* 8, no. 29, 7604–7609, (2012).
- [52] D. Kokkinis, M. Schaffner, and A. R. Studart, *Nat. Commun.* 6, (2015).
- [53] B. T. Shirk, W.R. Buessem, *J. Appl. Phys.* 40, 1294-6 (1969).
- [54] S. V. Levchik, E. D. Weil, and M. Lewin, *Polym. Int.*, vol. 48, no. 6–7, pp. 532–557, (1999).
- [55] T. N. Ahmed, C. Selsor, J. S. Tate, and J. S. Tate, “Magnetic behavior and chaining of strontium ferrite-nylon composite above the melting temperature Magnetic behavior and chaining of strontium ferrite-nylon composite above the melting temperature,” *AIP Advances* 13, 025024, (2023).
- [56] J. Bai, R. D. Goodridge, R. J. M. Hague, M. Song, and M. Okamoto, *Polym. Test.*, vol. 36, no. July, pp. 95–100, (2014).
- [57] Ph.D. Dissertation of G. M. Craft, “Characterization of Nylon-12 in a Novel Additive Manufacturing Technology, and the Rheological and Spectroscopic Analysis of PEG-Starch Matrix Interactions by,” University of South Florida, April (2018).
- [58] J. Einarsson, F. Candelier, F. Lundell, J. R. Angilella, and B. Mehlig, “Rotation of a spheroid in a simple shear at small Reynolds number,” *Phys. Fluids*, vol. 27, no. 6, 2015.
- [59] J. Einarsson, F. Candelier, F. Lundell, J. R. Angilella, and B. Mehlig, “Effect of weak fluid inertia upon Jeffery orbits,” *Phys. Rev. E - Stat. Nonlinear, Soft Matter Phys.*, vol. 91, no. 4, pp. 1–4, 2015.

- [60] J. G. Ku, X. Y. Liu, H. H. Chen, R. D. Deng, and Q. X. Yan, *AIP Adv.* 6, no. 2, (2016).
- [61] B. F. Edwards and J. M. Edwards, *Eur. J. Phys.* 38, no. 1, 0–15, (2017).

## 6. TORQUE OR ANGULAR DEPENDENT STUDY

*“No matter what you look at, if you look at it closely enough, you are involved in the entire universe.”*

— Michael Faraday

Note: The last part of the chapter’s content (Section 6.4) was presented at the MMM-2022 conference in Minnesota in Fall-2022 and published in 7<sup>th</sup> February 2023 as a conference paper for the conference proceedings of the MMM conference. DOI number of the publication is <https://doi.org/10.1063/9.0000596>. The contents taken from the published article were cited where applicable.

### 6.1 Introduction

Torque measurements have been widely used to measure a sample’s magnetic anisotropy. One measures the torque exerted as a function of the field angle and field, and the magnetic anisotropy is determined from an inverse Fourier series analysis of the torque curve. Torque curves provide the magnetic anisotropy constant but also information on the preferential magnetization directions [1]. Although usually torque magnetometers are used, one can also indirectly measure torque with a biaxial Vibrating Sample Magnetometer (VSM) from the components of magnetic moment perpendicular to the field direction since:

$$\boldsymbol{\tau} = \mu_o \mathbf{M} \times \mathbf{H} = \mu_o M_y H_x \hat{e}_z + \mu_o M_z H_x \hat{e}_y \quad (6.1)$$

where  $M_y$  and  $M_z$  are the components of the magnetic dipole moment perpendicular to the applied field  $H_x$  [2, 3].

A torque curve is a plot of the torque required to rotate the magnetic dipole moment away from the easy direction as a function of the field angle. A field applied to a magnetic material at a certain angle, forces the magnetic dipole moment to rotate towards the field direction away from the easy axis. At the same time, a torque is exerted on the magnetic dipole moment by the anisotropy as soon as the magnetic dipole moment rotates

away from the easy-axis direction [2]. Consider first a uniaxial crystal, such as a hexagonal crystal, with an easy axis parallel to the c-axis. It is cut in the form of a thin disk with the c-axis in the plane of the disk, placed in a saturating magnetic field (usually provided by an electromagnet) directed in the plane of the disk, as in Fig. 6.1. The disk is rotated about an axis through its center, and the torque acting on the disk is measured as a function of the field angle. If the field is strong enough, the magnetic dipole moment  $m_s$  will be parallel to  $H$  and the angle between  $c$  and  $m_s$ , which we can call  $\theta$ , will be the same as the angle between  $c$  and  $H$ .

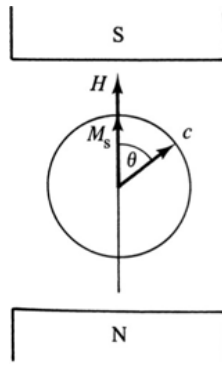


**Fig. 6.1:** Uniaxial disk sample in a saturating magnetic field produced by an electromagnet.  $c$  = easy axis [2].

The anisotropy energy per unit volume  $E$  of a uniaxial crystal depends on  $\theta$  and is given by:

$$E = K_0 + K_1 \sin^2(\theta) + K_2 \sin^4(\theta) + \dots \quad (6.2)$$

where  $K_1, K_2, \dots$  are the anisotropy constants. If  $K_2$  is negligible, the anisotropy energy per unit volume is given by

$$E = K_1 \sin^2(\theta) \quad (6.3)$$

When the energy of a system depends on the angle the magnetic dipole moment makes with the easy axis, the derivative of the energy with respect to the angle is a torque. Thus  $V \frac{dE}{d\theta}$  is the torque exerted by the crystal on  $m_s$ , and  $-V \frac{dE}{d\theta}$  is the torque exerted on the crystal by  $m_s$ . (Clockwise torques are taken as positive, and the positive direction of  $\theta$  is measured from  $m_s$  to  $c$ .) Then the torque on the crystal per unit volume

L is,

$$L = - \frac{dE}{d\theta} \quad (6.4)$$

$$L = - 2K_1 \sin\theta \cos\theta = K_1 \sin 2\theta \quad (6.5)$$

The torque per unit volume L is in dyne-cm/cm<sup>3</sup> if E is in erg/cm<sup>3</sup>, or in Nm/m<sup>3</sup> if E is in J/m<sup>3</sup>.

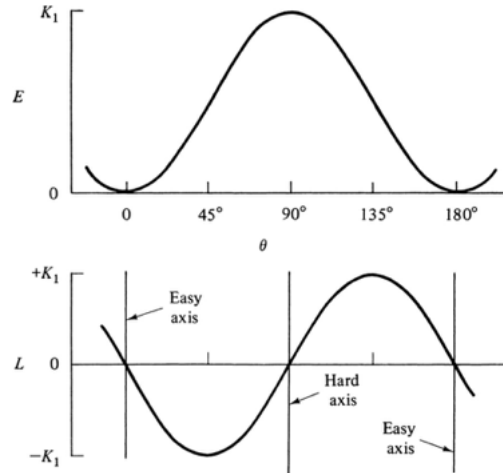


**Fig. 6.2:** Variation with  $\theta$  of the anisotropy energy  $E$  and the torque  $L (=dE/d\theta)$  for a uniaxial crystal.  $\theta$  is the angle between  $M_s$  and the easy axis [2].

Fig. 6.2 shows how  $E$  and  $L$  vary with angle. For positive  $K_1$ , the  $0$  and  $180^\circ$  positions are energy minima, and  $\theta = 90^\circ$ , which is a direction of difficult magnetization, is a position of instability. The slope of the torque curve at  $L=0$  is negative for the equilibrium angles ( $\theta=0$  and  $180^\circ$ ) and positive for the unstable equilibrium angle ( $\theta=90^\circ$ ). At a stable equilibrium angle, a clockwise (positive) rotation of the sample produces a negative (counterclockwise) torque, and vice versa. At an unstable equilibrium, a clockwise rotation of the sample produces a positive (clockwise) torque. The value of  $K_1$  can be found simply from the maximum amplitude of the torque curve ( $= \pm K_1$ ), or from the values of the slope at the zero crossings ( $= \pm 2K_1$ ), or by fitting the entire curve to Equation 6.5 with the value of  $K_1$  as a fitting parameter.

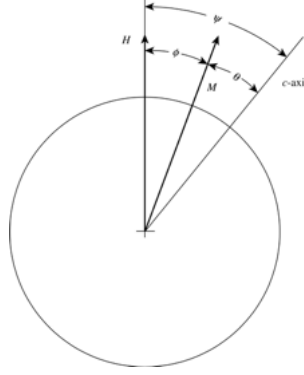


**Fig. 6.3:** For the case where  $M_s$  is not aligned with the field  $H$  [2].

The preceding analysis is valid only if the field is strong enough so that the magnetic dipole moment  $m_s$  is aligned with the field  $H$  for all values of  $\theta$ . This condition is often not met, and we have instead the situation shown in Fig. 6.3. Here  $\psi$  is the angle from the  $c$  direction to the applied field, which is known from the measurement;  $\theta$  is the angle from the  $c$  direction to the magnetic dipole moment  $m_s$ , and  $\phi (= \psi - \theta)$  is the angle from the field  $H$  to the magnetic dipole moment  $m_s$ . Neither  $\theta$  nor  $\phi$  is known directly, but the angular position of  $m_s$  is determined by the balance between the two normalized torques ( $\text{Nm/m}^3$ ),  $L_K = -K_1 \sin 2\theta$  and  $L_H = H \sin \phi * m_s / V = M_s H \sin \phi$ . Here  $L_K$  is the anisotropy torque per unit volume, acting to rotate the magnetic dipole moment toward the easy direction, and  $L_H$  is the torque per unit volume exerted by the field on the magnetic dipole moment, acting to rotate the magnetization toward the field. Since these torques are balanced, we have

$$K_1 \sin 2\theta = M_s H \sin \phi \quad (6.6)$$

We also know that the torque per unit volume exerted on the sample by the anisotropy must be balanced by the measured torque per unit volume  $L_{\text{meas}}$ , so that,

$$L_{\text{meas}} = K_1 \sin 2\theta = M_s H \sin \phi \quad (6.7)$$

So, if we measure  $L$ , and we know  $M_s$  and  $H$ , we can find  $\sin \phi$  and therefore  $\phi$  from  $\sin \phi$  from above equation. And knowing  $\phi$ , we can correct the measured value of  $\psi$  for each measured  $L$  to a value of  $\theta$ .

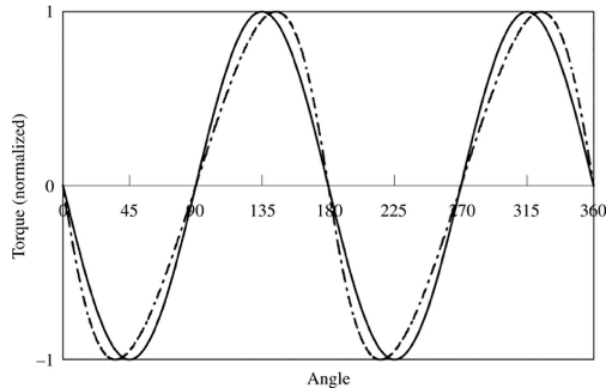


**Fig. 6.4:** Variation of torque with angle  $\psi$  between easy axis  $c$  and field  $H$  for a uniaxial crystal and the dashed curve is for  $H = 2K_1/M_s$ ; solid curve for  $H \gg 2K_1/M_s$  [2].

Fig. 6.4 shows a plot of torque  $L$  vs  $\psi$ , for uniaxial anisotropy with  $M_s H = 2K_1$  (dashed line). The corrected curve (solid line) corresponds to  $M_s H \gg K_1$ . The correction does not affect the maximum torque, but it clearly does affect the slopes at zero torque, and the general shape of the curve.

The usual method for anisotropy determinations is torque magnetometry, which directly measures the macroscopic torque exerted by an applied field on the magnetization of a sample that is not precisely aligned with the field. Although torque magnetometers enjoy the advantage of high sensitivity and accuracy, they are unsuited to measure other magnetic parameters of interest, e.g., hysteresis loops, remanence curves, etc [2].

## 6.2 Correction Strategy for Systematic Wobble Errors in VSM Torque Curves Measured on Soft Magnetic Samples

In the study of magnetic thin films, multilayers and composites, torque measurements are useful to find the magnetic anisotropy of the sample. Although traditionally torque measurements are performed with a torque magnetometer where the magnetic torque on a sample suspended from a thin wire or air bearing exposed to a magnetic field is compensated for by a torque coil, torque measurements have also been performed with other methods including a vibrating sample magnetometer [3-5]. The

torque can be indirectly sensed with a vector VSM from the components of the magnetic moment perpendicular to the field direction (equation 6.1).

The normal components of  $\mathbf{M}$  are determined with a vector VSM that in addition to the moment parallel to the field has additional pick-up coils to measure the magnetic moment components in one [2] or two directions perpendicular to the field [6-8]. For biaxial VSMs that only measure  $M_x$  and  $M_y$ , one needs to position the easy and hard axis of the sample in the  $xy$ -plane. Fourier coefficients of the  $M_yH$  versus field angle  $\theta_{\text{field}}$  or moment angle  $\theta_{\text{moment}}$  provide the magnetic anisotropy constants. Measurements are typically made as a function of the applied field and high field values are determined from the  $y$ -intercept of a plot of the Fourier coefficient versus  $1/H$ . This approach is particularly advantageous for cases where the magnetic field of the setup is not sufficient to saturate the sample in all directions. Although torque curves can be measured with a true torque magnetometer, the range of samples that can be determined with such instrument is often limited and a wider range of samples can be explored through torque curves measurements with a vector VSM. Both types of torque curves contain backgrounds. The true torque curve often contains a  $1\theta$  component torque component originating from the gravity force on the sample sample-rod combination. This is not much of a concern since for most samples no magnetic  $1\theta$  components exist, so the gravity background can be ignored or easily removed by subtracting the torque curve measured at zero field from the other curves measured at non-zero field. The vector VSM torque curve on the contrary often contains a  $2\theta$  background that is much larger than the signal due to the sample's magnetic anisotropy. Such background originates from small changes of the sample position with field angle and cannot be easily distinguished from the field angle dependence due to the sample's magnetic anisotropy. The figure below shows the torque curves of a 2 mm circular mu-metal disk sample that was misaligned with respect to rotation axis of the holder. The  $2\theta$  amplitude of the VSM torque curve is approximately 230 dyne cm while the  $2\theta$  amplitude of the true torque curve is not more than 3 dyne cm. When the field angle is rotated through 360 degrees the sample describes a circle in the  $xy$ -plane. This results in a  $\theta$ -dependence of the  $y$ -coil set signal that is not caused by a  $M_y$   $\theta$ -dependence, so not related to the torque.

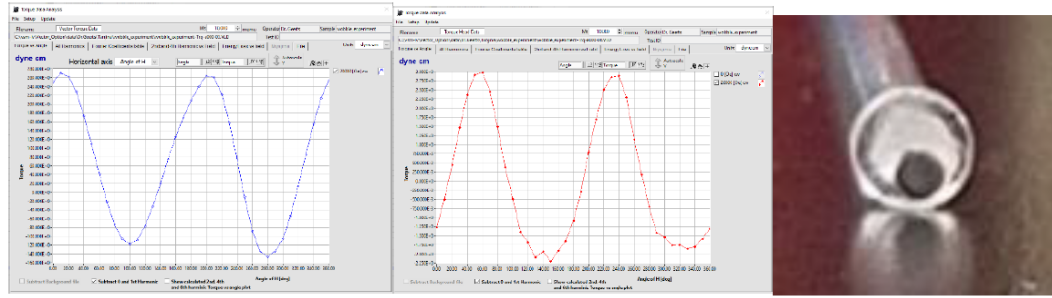


**Fig. 6.5:** Biaxial torque curve (left) and true torque curve (middle) for a 2 mm circular mu-metal foil sample misaligned on a 5 mm diameter transvers rod (right).

Although it is possible to center the sample better on the rod so smaller effects are to be expected, it is not really possible to exclude minor misalignments. Furthermore, additional background can be expected by imperfections of the sample rotation mechanism or sample-rod. Anytime the rotation axis of the system does not line-up with the sample-rod axis a change of the field angle is expected to change the sample position and to affect the background in the measured VSM torque curves. In the rest of this chapter we will refer to this effect as wobble. Here we will quantify the effect of circular wobble on biaxial torque curves in more detail and propose a method to subtract these systematic errors that works well for soft magnetic samples. The analysis will be done for a biaxial VSM that employs a Modified Mallinson coil set. Similar relations can be derived for other pickup coil sets.

### 6.2.1 Theory

For a vector VSM the coil signal vector  $\mathbf{X}$  relates to the sample's magnetic dipole moment vector  $\mathbf{m}$  as follows:

$$\vec{X} = \begin{bmatrix} X \\ Y \\ Z \end{bmatrix} = \begin{bmatrix} S_{xx} & S_{xy} & S_{xz} \\ S_{yx} & S_{yy} & S_{yz} \\ S_{zx} & S_{zy} & S_{zz} \end{bmatrix} \begin{bmatrix} m_x \\ m_y \\ m_z \end{bmatrix} = \vec{S} \cdot \vec{m} \quad (6.8)$$

Where,  $\vec{S}$  is the sensitivity matrix. We here refer to its diagonal components as sensitivities and its off-diagonal components as cross-talks. The sensitivity matrix depends on the geometry and dimensions of the coil set, the shape and size of the sample, and the position of the sample in between the pickup coils. For a biaxial VSM with the field applied along

the x-axis and a modified Mallinson coil set employing similar coils for the x and y directions this expression simplifies to:

$$\vec{X} = \begin{bmatrix} X \\ Y \end{bmatrix} = \begin{bmatrix} S_{xx} & S_{xy} & S_{xz} \\ S_{yx} & S_{yy} & S_{yz} \end{bmatrix} \begin{bmatrix} m_x \\ m_y \\ m_z \end{bmatrix} = \vec{S} \cdot \vec{m} \quad (6.9)$$

In the rest of this paper, we assume that the sample has azimuthal symmetry around the z-axis. If such sample is perfectly centered in between the pickup coils all crosstalk terms of  $\vec{S}$  are zero. For large fields for a centered sample  $S_{xx}=S_{yy}$  since the pole caps saturate at high fields and the image effect no longer contributes to the X-sensitivity at high field. When the sample is not centered the crosstalk, terms are in generally not zero. The magnetic field at field point  $\mathbf{x}$  caused by a point dipole at source point  $\mathbf{x}'$  is given by [9, 10]:

$$\vec{B} = \frac{\mu_0}{4\pi} \frac{1}{r^3} \{3(\vec{m} \cdot \hat{r})\hat{r} - \vec{m}\} \quad (6.10)$$

Where  $\mathbf{r}=\mathbf{x}-\mathbf{x}'$  with  $\mathbf{x}$  the field point and  $\mathbf{x}'$  the source point,  $\mathbf{m}$  is the sample's magnetic dipole moment vector and  $\hat{r}$  is the unit vector pointing from the source to the field point. Assuming that the sample is perfectly aligned in the z-direction and vibrating with an amplitude of  $\alpha$  at an angular frequency  $\omega$  in the z-direction we can write for the  $z'$

$$z' = \alpha \sin(\omega t) \quad (6.11)$$

For pickup coils that have a cross sectional area small compared to  $\mathbf{r}$ , we can consider the coupled flux to be linear proportional to the pickup coil's cross-sectional area  $A$  that has a number of windings  $N$ . For a coil oriented in the yz-plane at position  $(x,y,z)$  we find for the flux  $\Phi_x$  caused by  $\mathbf{m}$  positioned at  $\mathbf{x}'$ :

$$\Phi_x = NA(B_{xx} + B_{xy} + B_{xz}) = \Phi_{xx} + \Phi_{xy} + \Phi_{xz} \quad (6.12)$$

Where  $B_{xx}$ ,  $B_{xy}$ , and  $B_{xz}$  are the field in the x direction caused by the x, y, and z components of  $\mathbf{m}$  at field point  $\mathbf{x}$  in the pickup coil's position and  $\Phi_{xx}$ ,  $\Phi_{xy}$ ,  $\Phi_{xz}$  are the coupled fluxes caused by respectively the x, y, and z component of  $\mathbf{m}$  at location  $\mathbf{x}'$  in the coil located at position  $\mathbf{x}$ . These are given by the following expressions [11, 12]:

$$\Phi_{xx} = m_x \frac{NA\mu_0}{4\pi} \frac{[2(x-x')^2 - (y-y')^2 - (z-\alpha \sin(\omega t))^2]}{[(x-x')^2 + (y-y')^2 + (z-\alpha \sin(\omega t))^2]^{\frac{5}{2}}} \quad (6.13)$$

$$\Phi_{xy} = m_y 3 \frac{NA\mu_0}{4\pi} \frac{(y-y')(x-x')}{[(x-x')^2+(y-y')^2+(z-\alpha \sin(\omega t))^2]^{\frac{5}{2}}} \quad (6.14)$$

$$\Phi_{xz} = m_z 3 \frac{NA\mu_0}{4\pi} \frac{(z-\alpha \sin(\omega t))(x-x')}{[(x-x')^2+(y-y')^2+(z-\alpha \sin(\omega t))^2]^{\frac{5}{2}}} \quad (6.15)$$

The induced voltage in the coil is proportional to the negative of the time derivative. If we further assume that amplitude of vibration is much smaller than  $z$  so we can approximate  $z - \alpha \cos(\omega t)$  by  $z$  and we add the signal of the four X-coils positioned at  $(-X_c, 0, Z_c)$ ,

$(-X_c, 0, -Z_c)$ ,  $(X_c, 0, -Z_c)$ , and  $(X_c, 0, Z_c)$  we find for the first harmonics of the X-coil signal:

$$X = S_{xx}m_x + S_{xy}m_y + S_{xz}m_z \quad (6.16)$$

With

$$S_{xx}(x', y') = 6 \frac{NA\mu_0\alpha\omega Z_c}{4\pi} \left\{ \frac{4(X_c-x')^2 - y'^2 - Z_c^2}{[(X_c-x')^2 + y'^2 + Z_c^2]^{\frac{7}{2}}} + \frac{4(X_c+x')^2 - y'^2 - Z_c^2}{[(X_c+x')^2 + y'^2 + Z_c^2]^{\frac{7}{2}}} \right\} \quad (6.17)$$

$$S_{xy}(x', y') = 30 \frac{NA\mu_0\alpha\omega Z_c}{4\pi} \left\{ -\frac{(X_c-x')y'}{[(X_c-x')^2 + y'^2 + Z_c^2]^{\frac{7}{2}}} + \frac{(X_c+x')y'}{[(X_c+x')^2 + y'^2 + Z_c^2]^{\frac{7}{2}}} \right\} \quad (6.18)$$

$$S_{xz}(x', y') = \frac{6}{Z_c} \frac{NA\mu_0\alpha\omega Z_c}{4\pi} \left\{ \frac{(X_c-x')((X_c-x')^2 + y'^2 - 4Z_c^2)}{[(X_c-x')^2 + y'^2 + Z_c^2]^{\frac{7}{2}}} + \frac{(X_c+x')((X_c+x')^2 + y'^2 - 4Z_c^2)}{[(X_c+x')^2 + y'^2 + Z_c^2]^{\frac{7}{2}}} \right\} \quad (6.19)$$

Note that the sensitivity  $S_{xx}$  for small values of  $x'$  ( $y'$ ) is proportional to  $x'^2$  ( $-y'^2$ ). This property is normally used to center the sample in between the X-pickup coils, i.e. the  $x'$  sample position is adjusted to minimize the X signal, and the  $y'$  sample position is adjusted to maximize the X coil signal. Furthermore, note that these expressions are approximations as they assume the pickup coils, the amplitude of the vibration, and the size of the sample to be small compared to the sample pickup coil distance. Also, the image effect in the pole caps was ignored in the calculations and the coil set is assumed to be perfectly symmetric. Similar equations can be derived for the y-coil set with coils at  $(0, Y_c, Z_c)$ ,  $(0, -Y_c, Z_c)$ ,  $(0, Y_c, -Z_c)$ , and  $(0, -Y_c, -Z_c)$ :

$$Y = S_{yx}m_x + S_{yy}m_y + S_{yz}m_z \quad (6.20)$$

with

$$S_{yx}(x', y') = 30 \frac{NA\mu_0\alpha\omega Z_c}{4\pi} \left\{ -\frac{(Y_c-y')x'}{[x'^2 + (Y_c-y')^2 + Z_c^2]^{\frac{7}{2}}} + \frac{(Y_c+y')x'}{[x'^2 + (Y_c+y')^2 + Z_c^2]^{\frac{7}{2}}} \right\} \quad (6.21)$$

$$S_{yy}(x', y') = 6 \frac{NA\mu_0\alpha\omega Z_c}{4\pi} \left\{ \frac{-x'^2 + 4(Y_c - y')^2 - Z_c^2}{[x'^2 + (Y_c - y')^2 + Z_c^2]^{\frac{7}{2}}} + \frac{-x'^2 + 4(Y_c + y')^2 - Z_c^2}{[x'^2 + (Y_c + y')^2 + Z_c^2]^{\frac{7}{2}}} \right\} \quad (6.22)$$

$$S_{yz}(x', y') = \frac{6}{Z_c} \frac{NA\mu_0\alpha\omega Z_c}{4\pi} \left\{ \frac{(Y_c - y')((Y_c - y')^2 + x'^2 - 4Z_c^2)}{[(Y_c - y')^2 + x'^2 + Z_c^2]^{\frac{7}{2}}} + \frac{(Y_c + y')((Y_c + y')^2 + x'^2 - 4Z_c^2)}{[(Y_c + y')^2 + x'^2 + Z_c^2]^{\frac{7}{2}}} \right\} \quad (6.23)$$

To understand how a rotation of the sample-rod for a misaligned sample affects the X and Y coil signals we assume that the sample subscribes a circular trajectory in the xy-plane as the field angle is changed. It is clear that a simple misalignment of the sample on a perfectly aligned sample rod or a slight angle between sample rod axis and the rotation axis of sample rod system will result in such trajectory. So to determine the effect of circular wobble on the coil signals we substitute the coordinates of the sample position  $(x', y')$  in above expressions by [12]:

$$x' = r \cos(\theta + \theta_o) + x'_o \quad (6.24)$$

$$y' = r \sin(\theta + \theta_o) + y'_o \quad (6.25)$$

Where  $\theta$  is the field angle,  $r$  is the radius of the circle that the sample describes while rotated in the xy-plane,  $(x'_o, y'_o)$  is the wobble center around which the sample rotates, and  $\theta_o$  is the phase of the circular trajectory of the wobble and depends on the angle the sample-rod is inserted in the sample-rod holder. Assuming  $X_c^2 + Z_c^2 \gg (r \cos(\theta + \theta_o) + x'_o)^2 + (r \sin(\theta + \theta_o) + y'_o)^2$ , and  $C = 3 \frac{NA\mu_0\alpha\omega Z_c}{4\pi[X_c^2 + Z_c^2]^{\frac{7}{2}}}$  we find for the first row of  $\vec{S}$ :

$$S_{xx} = C\{8(X_c^2 + x_o'^2) - 2(y_o'^2 + Z_c^2) + 3r^2 + 4r^2 \cos(2\theta + 2\theta_o) + 16x'_o r \cos(\theta + \theta_o) - 4y'_o r \sin(\theta + \theta_o)\} = A_{dc,xx} + B_{1\theta,xx} \cos(\theta + \theta_o) + C_{1\theta,xx} \sin(\theta + \theta_o) + D_{2\theta,xx} \cos(2\theta + 2\theta_o) \quad (6.26)$$

$$S_{xy} = C\{-10r^2 \sin(2\theta + 2\theta_o) - 20y'_o r \cos(\theta + \theta_o) - 20x'_o r \sin(\theta + \theta_o) + 20x'_o y'_o\} = A_{dc,xy} + B_{1\theta,xy} \cos(\theta + \theta_o) + C_{1\theta,xy} \sin(\theta + \theta_o) + D_{2\theta,xy} \sin(2\theta + 2\theta_o) \quad (6.27)$$

$$S_{xz} = C\{(4X_c^2 + 12X_o'^2 + 8r^2 + 4y_o'^2 - 16) + 24x'_o r \cos(\theta + \theta_o) + 4y'_o r \sin(\theta + \theta_o) + 4r^2 \cos(2\theta + 2\theta_o)\} = A_{dc,xz} + B_{1\theta,xz} \cos(\theta + \theta_o) + C_{1\theta,xz} \sin(\theta + \theta_o) + D_{2\theta,xz} \cos(2\theta + 2\theta_o) \quad (6.28)$$

Similarly assuming  $Y_c^2 + Z_c^2 \gg (r \cos(\theta + \theta_o) + x'_o)^2 + (r \sin(\theta + \theta_o) + y'_o)^2$  the values of the 2<sup>nd</sup> row of  $\vec{S}$  are given by:

$$\begin{aligned}
S_{yx} &= C\{20x'_o y'_o - 20y'_o r \cos(\theta + \theta_o) - 20x'_o r \sin(\theta + \theta_o) \\
&\quad - 10r^2 \sin(2\theta + 2\theta_o)\} \\
&= A_{dc,yx} + B_{1\theta,yx} \cos(\theta + \theta_o) + C_{1\theta,yx} \sin(\theta + \theta_o) + E_{2\theta,yx} \sin(2\theta + 2\theta_o) \quad (6.29)
\end{aligned}$$

$$\begin{aligned}
S_{yy} &= C\{8(Y_c^2 + y_o'^2) - 2(x_o'^2 + Z_c^2) + 3r^2 \\
&\quad + 16y'_o r \sin(\theta + \theta_o) + 4x'_o r \cos(\theta + \theta_o) - 4r^2 \cos(2\theta + 2\theta_o)\} \\
&= A_{dc,yy} + B_{1\theta,yy} \cos(\theta) + C_{1\theta,yy} \sin(\theta + \theta_o) + D_{2\theta,yy} \cos(2\theta + 2\theta_o) \quad (6.30)
\end{aligned}$$

$$\begin{aligned}
S_{yz} &= C\{(4Y_c^2 + 12y_o'^2 + 8r^2 + 4x_o'^2 - 16) + 24x'_o r \cos(\theta + \theta_o) + \\
&\quad 4y'_o r \sin(\theta + \theta_o) + 4r^2 \cos(2\theta + 2\theta_o)\} \\
&= A_{dc,yz} + B_{1\theta,yz} \cos(\theta + \theta_o) + C_{1\theta,yz} \sin(\theta + \theta_o) + D_{2\theta,yz} \cos(2\theta + 2\theta_o) \quad (6.31)
\end{aligned}$$

Note that we omitted the phase angle of the wobble so for the most general case the  $1\theta$  terms in equations (6.26) through (6.31) contain a  $\theta_o$  term and the  $2\theta$  terms a  $2\theta_o$  term. Equations (6.26) through (6.26) can now be used to determine the effect circular wobble has on the measured torque curves. It is assumed that the wobble is small compared to the sample coil distance so  $|S_{xx}| \gg |S_{xz}|$ ,  $|S_{xx}| \gg |S_{xy}|$ ,  $|S_{yy}| \gg |S_{yx}|$ , and  $|S_{yy}| \gg |S_{yz}|$ . Furthermore, for a soft magnetic sample at large fields it can be assumed that  $m_x \gg m_y$  and  $m_x \gg m_z$ , so the signal of the X and Y-coils can be approximated by:

$$X = S_{xx}m_x + S_{xy}m_y + S_{xz}m_z \approx S_{xx}m_x \quad (6.32)$$

$$Y = S_{yx}m_x + S_{yy}m_y + S_{yz}m_z \approx S_{yx}m_x + S_{yy}m_y = Y_o + Y_{cor} \quad (6.33)$$

Where for anisotropic material  $m_x$  and  $m_y$  are function of the field angle. As shown above for a sample misaligned on the sample rod exhibiting wobble also  $S_{yy}(\theta)$ , and  $S_{xy}(\theta)$  are a function of the field angle causing systematic errors in the torque curve causing the large background shown in Fig. 6.5. At large values of the applied field the 2<sup>nd</sup> term in equation (6.33) will go to zero as  $M_y$  goes to zero and the magnetic moment lines up with the field applied in the x-direction. So only the first term is left which becomes independent of the field as  $m_x$  saturates and  $S_{yx}(\theta)$  is independent of the field but angle dependent and non-zero. So, for a soft magnetic sample that can be saturated along the applied field direction one can determine the cross-talk term ( $Y(\theta)$ ) from the Y-signal at large field and then subtract this curve from all other  $Y_{raw}(\theta)$  curves, i.e.

$$Y_o(\theta) = Y_{Hmax}(\theta) \quad (6.34)$$

$$Y_{cor,H}(\theta) = Y_{raw,H}(\theta) - Y_o(\theta) \quad (6.35)$$

If the sample cannot be completely saturated it is better to first determine the Fourier series of the measured  $Y(\theta)$  curves and extrapolate the  $\mathcal{F}\left(Y_{raw,H}(\theta)\right)$  to infinite field from the y-intersect of a  $\mathcal{F}\left(Y_{raw,H}(\theta)\right)$  versus  $1/H_a$  plot, i.e.

$$Y_o(\theta) = \mathcal{F}^{-1}\left(\frac{m_x}{m_s} \text{Lim}_{1/H_a \rightarrow 0} \left[\mathcal{F}\left(Y_{H_a}(\theta)\right)\right]\right) \quad (6.36)$$

Where,  $\mathcal{F}$  is the Fourier series function and  $\mathcal{F}^{-1}$  is the inverse Fourier series function. The  $Y_{cor,H}(\theta)$  curves no longer have the cross-talk offset but still contain a systematic error because of the field angle dependence of  $S_{yy}(\theta)$  often referred to as the angular sensitivity of the y-coils. One can correct for this if  $S_{yy}(\theta)$  is known before one converts the  $Y(\theta)$  curves to torque curves:

$$\tau_{cor,H}(\theta) = \mu_o H_a Y_{cross\ talk\ cor}(\theta) S_{yy}(\theta) \quad (6.37)$$

Note that this angular sensitivity  $S_{yy}(\theta)$  is often measured upon calibration of the system although it is time consuming. For this calibration one would need a sample that has a significant remanence for all directions. One first rotates the field angle to  $\theta=90$  degrees, applies a large magnetic field to saturate the sample, and then reduces the field carefully to zero followed by an accurate measurement of the X-coil signal. Then the  $S_{yy}(\theta)$  is calculated from  $Y(\theta)/X(\theta=90)$  creating angular sensitivity table that allows one to make correction on a sample with similar shape and similar alignment. For an anisotropic sample that has a zero remanence for some angles this method will not allow to determine  $S_{yy}(\theta)$  accurately for all field angles and the measured y-angular sensitivity has often outliers. Also, for soft magnetic materials the method fails as during rotation the magnetic moment changes. Furthermore, it should be noticed that using such approach will not correct for wobble originating from sample positioning errors on the sample rod only for wobble originating from sample rod and rotation mechanism imperfections providing one uses the same sample rod and the angular position of the sample-rod in the sample-rod holder is same during the measurement and the calibration. An alternative method would be to measure the  $S_{xx}(\theta)$  which does not require a large remanence and then calculate the  $S_{yy}(\theta)$  from the  $S_{xx}(\theta)$  using equations (6.26) and (6.30). We noticed that for soft magnetic samples  $X(\theta)$  becomes field independent at much lower fields than  $Y(\theta)$ . Assuming that the center of the x-coil set coincides with the center of the y-coil set and  $X_c=Y_c$  we see that

$D_{2\theta,yy} = -D_{2\theta,xx}$ ,  $C_{1\theta,yy} = -4C_{1\theta,xx}$ ,  $B_{1\theta,yy} = -\frac{1}{4}B_{1\theta,xx}$ ,  $A_{dc,yy} = A_{dc,xx} + 10(y'_o{}^2 - x'_o{}^2)$ ,  $x'_o = \frac{B_{1\theta,xx}}{8\sqrt{D_{2\theta,xx}}}$  and  $y'_o = \frac{C_{1\theta,xx}}{2\sqrt{D_{2\theta,xx}}}$ . So one can determine the angle dependence of  $S_{yy}(\theta)$  from the angle dependence of  $S_{xx}(\theta)$ . Fig. 6.6 shows the measured  $S_{xx}(\theta)$  and  $S_{yy}(\theta)$  for a 8 mm length Strontium-ferrite/PA-12 wire sample that is mounted horizontally on a perpendicular rod (cylindrical axis is parallel to the field at zero field angle). The figure also shows the  $S_{yx}(\theta)$ . The solid lines are a best fit for the measurement data using equation (6.26), (6.29) and (6.30). Note that strontium ferrite has a saturation field equal to 19,000 Oe and a slight anisotropy originating from the shape of the sample and the weak texture induced by the flow during the extrusion process.

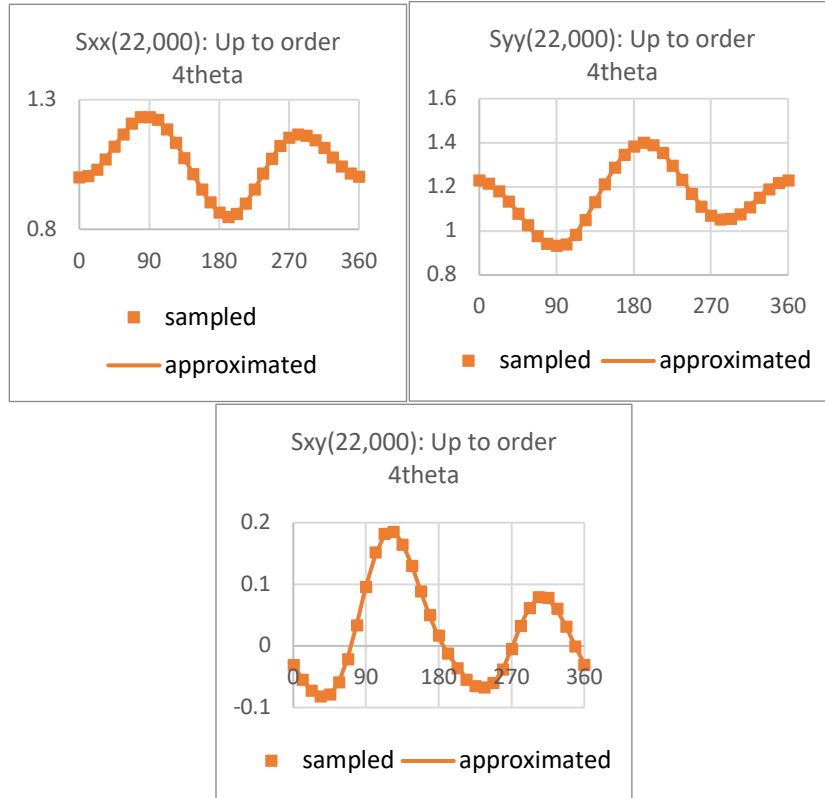
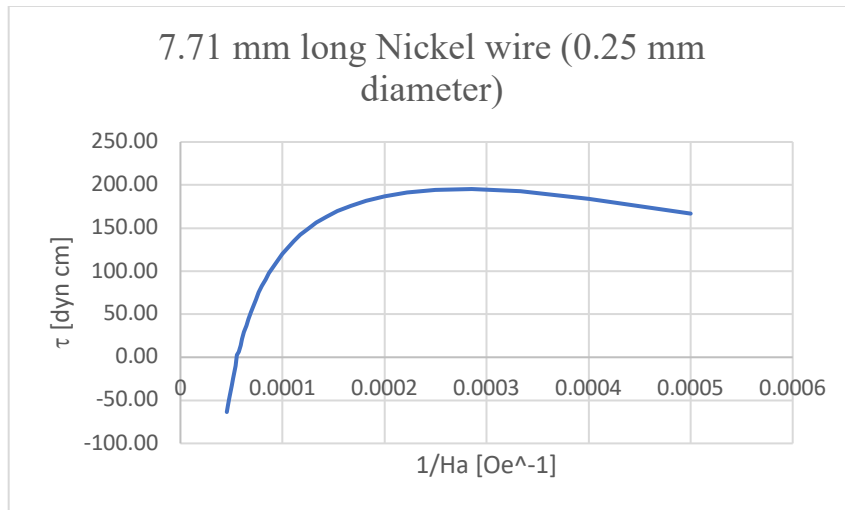


**Fig. 6.6:** Measured  $S_{xx}(\theta)$ ,  $S_{yy}(\theta)$ ,  $S_{yx}(\theta)$  for a strontium-ferrite/PA-12 filament sample mounted horizontally on a perpendicular rod. Solid lines are best fits using equations (6.26), (6.29), and (6.30).

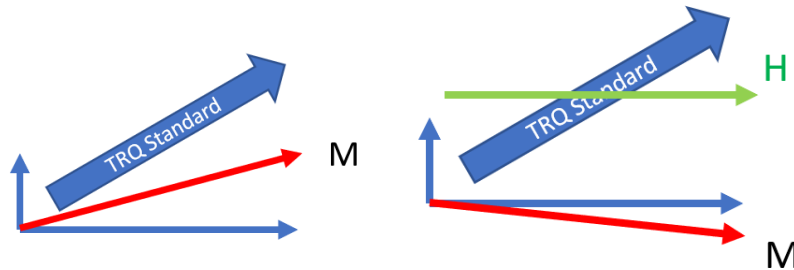
## 6.2.2 Experimental Verification

The method proposed at the end of last section was verified using a MicroSense EZ9 Vibrating Sample Magnetometer furnished with a biaxial Mallinson coil set. Measurements were done on a 7.71 mm long Nickel wire (diameter 0.25 mm) that was

provided with the torque head as a calibration sample. The nickel was positioned horizontally and lined up with the field direction for a field angle of 0 degrees. Then the sample was centered in between the X-pickup coils by adjusting Z, Y, and X to maximize, maximize and minimize the X-coil signal. This process was repeated 3 times to assure that the sample was perfectly centered in between the X-pickup coils. Then the torque curves were measured in steps of 10 degrees for different field values. Fig. 6.7 shows the magnitude of the  $2\theta$  components of the uncorrected torque curves as a function of  $1/H_a$ . Above 18,000 the torque changes sign. It is clear from Fig. 6.8 that this cannot be physical as it would mean that the angle between the magnetic moment vector and the field has opposite sign from the angle between the field and the easy axis (see also Fig. 6.8). We conclude from this that the negative torque must originate from the cross-talk term in equation (6.33).

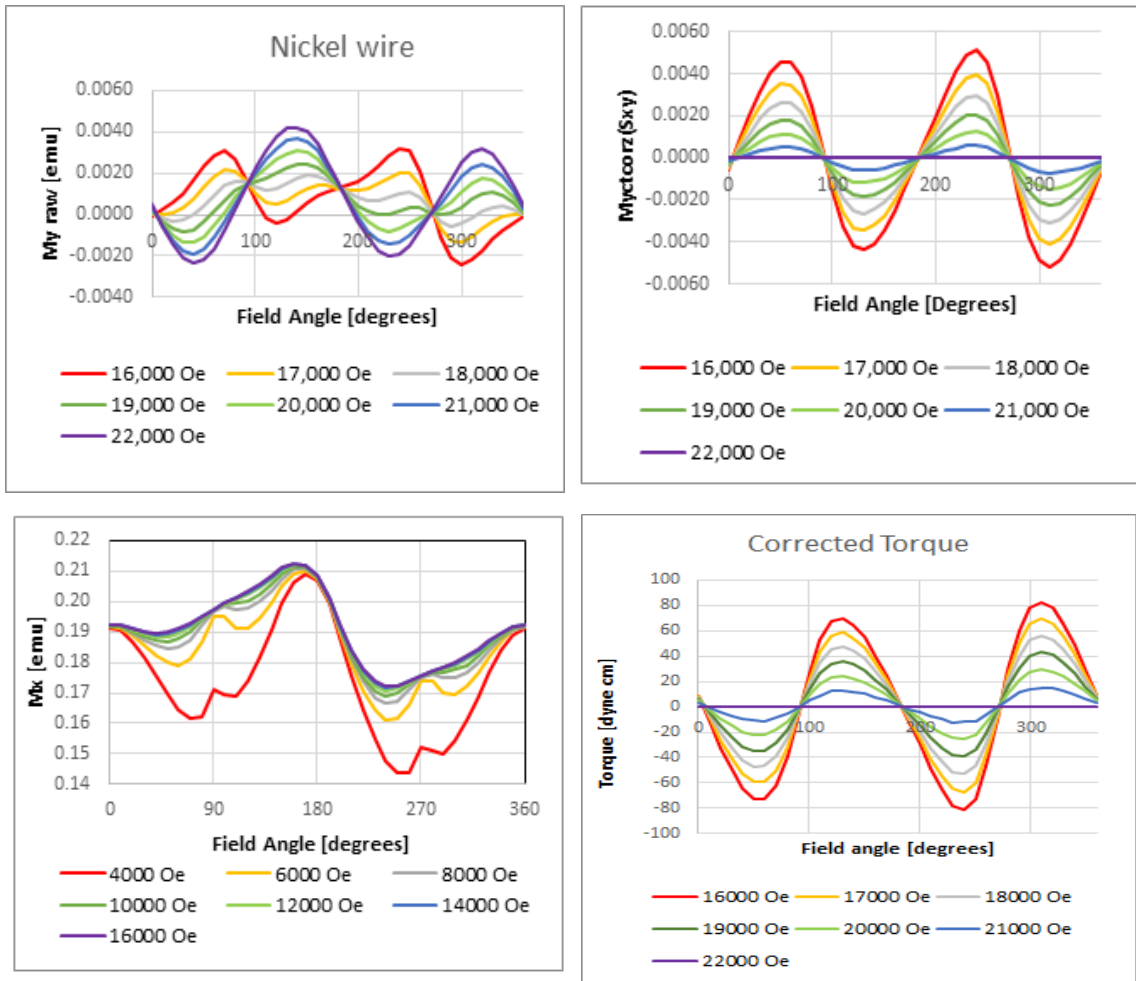


**Fig. 6.7:**  $2\theta$  component of raw torque curve as a function of the reciprocal value of the applied field.



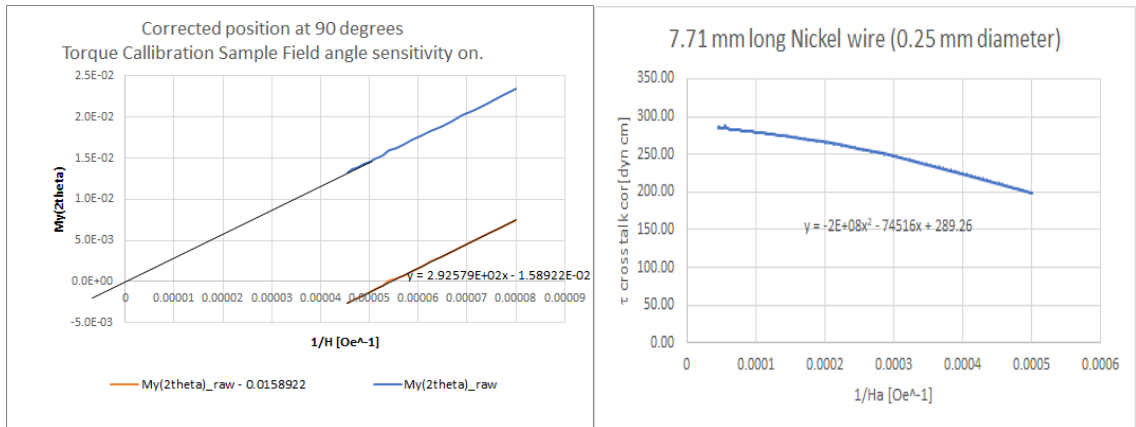
**Fig. 6.8:** Relative angles of easy axis Nickel wire (TRQ Standard), the field (H) and the magnetic moment vector (M) for values below 18000 and above 18000.

Fig. 6.9 shows the  $M_{y,raw}$ ,  $M_{y,cor}$ ,  $M_x$  and corrected torque curves of the Nickel torque calibration standard, i.e. the nickel wire of 7.71 mm long and a diameter of 0.25 mm. It was assumed that the  $M_y$  measured at the maximum applied field (22 kOe) was fully caused by the cross-talk, so this torque curve was subtracted from all other torque curves. The sample has an easy axis at 0 degrees and a hard axis at 90 degrees originating from the shape anisotropy of the sample. Note that the  $M_x$  component saturates near 14,000 Oe, with minor changes in the angular dependence for higher fields which suggest that the magnetic moment is fully oriented along the field direction. So, we do not expect any  $M_y$  component at high fields. It is clear from Fig. 6.10d that this correction for  $M_y$  is too aggressive as the measured torque still goes to zero at large field as is observed from true torque measurements.



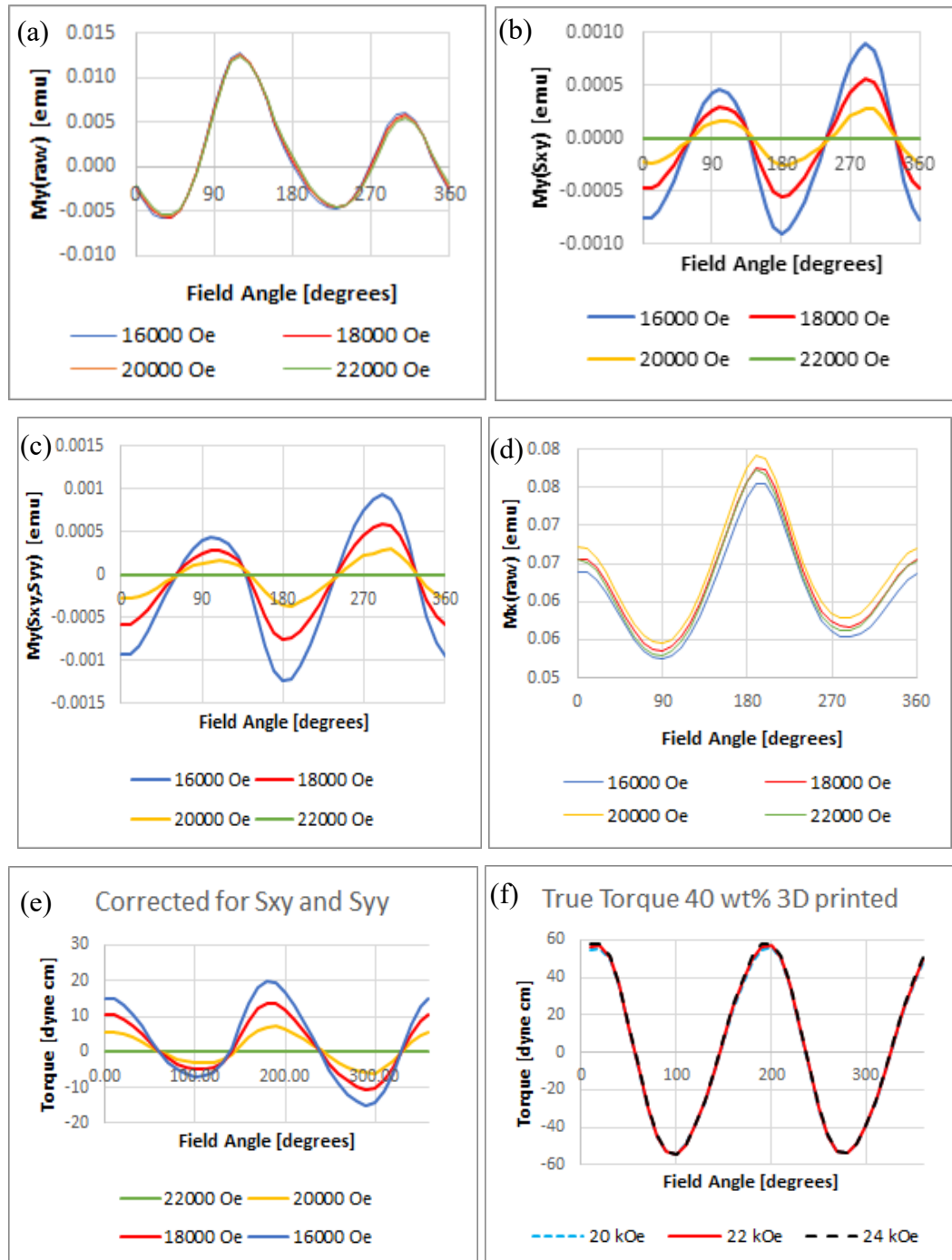
**Fig. 6.9:**  $M_{y,raw}$ ,  $M_{y,cor}$ ,  $M_x$ , and corrected torque curves of the Nickel torque calibration standard

Fig. 6.10a shows the  $2\theta$  component of the  $M_y$  signal versus  $1/H_a$  of the raw data (orange) and the data corrected for cross talk and Y-coil angular sensitivity. Fig. 6.10b shows the corrected torque curve. The torque at large field was extrapolated using a 2<sup>nd</sup> order polynomial. A torque of 289.26 dyn.cm was found which is close to the 287.086 dyn.cm estimated from the  $M_s$  Ni literature value and the size of the sample.



**Fig. 6.10:** (a)  $2\theta$  component of  $M_y$  as a function of  $1/H_a$  for raw data (orange) and data corrected for cross talk and angular sensitivity; (b) Corrected Torque versus  $1/H_a$  curve

These experiments were repeated for a Strontium Ferrite PA-12 3D printed filament (7.7 mm long). The sample was mounted horizontally on a perpendicular rod. Prior to the measurements the sample was centered in between the pickup coils following the same procedure as followed for the Ni calibration standard. Fig. 6.11 shows the raw  $M_y$  curves, the  $M_y$  curves corrected for the cross talk, the  $M_y$  curves corrected for the cross talk and the angular sensitivity, the raw  $M_x$ , and the torque curves. Note that these results suggest that the sample has an easy axis that is oriented at approximately 60 with the cylindrical axis. The orientation of this easy axis was confirmed from angular hysteresis curve measurements that showed that the S value is maximum at 60 degrees. In addition, true torque measurements were done on a similar sample and also shows this canted easy axis. Also note that the  $M_x$  curves do not saturate as was the case for the Ni calibration sample. The cross-talk correction was done by subtracting the signal measured at 22 kOe. Similar as for the nickel wire the cross-talk correction seems to be too strong and the corrected torque decreases for higher fields.



**Fig. 6.11:** (a)  $M_{y,raw}$ , (b)  $M_{y,cor}(S_{xy})$ , (c)  $M_{y,cor}(S_{xy},S_{yy})$ , (d)  $M_{x,raw}$ , and (e) torque curves of a Strontium Ferrite PA-12 3D printed filament (7.7 mm long x mm diameter) (f) shows the true torque curve of a similar sample that has a length of 4 mm.

Fig. 6.12 shows the raw and corrected  $M_y$  signals (left) and the  $\tau$  versus the reciprocal field value. Extrapolation to the y-axis suggests a torque value equal to -24 dyne

cm. Measurements with the true torque head on a similar sample that is approximately half the length shows a torque curve with the same easy and hard axis but with a different amplitude (see Fig. 6.11f). Notable is the canted easy axis at approximately 60 degrees, see also section below. At 22 kOe the torque amplitude measured with the true torque head was approximately 65 dyne cm (see Fig. 6.11f). We therefore conclude that the here presented method to subtract the wobble background from a biaxial torque curve does not results in data that is accurate enough for samples that have a long length. Note that the wobble background is proportional to the square of the wobble radius and that for 7.7 mm filaments even a small alignment of the sample on the sample rod of the order of a 0.2 mm will result in a large wobble background due to the large effective wobble radius, i.e.  $7.2/2=3.6$  mm. Therefore, all torque measurements done on samples presented in this chapter are done on filaments that are lined up with their cylindrical axis parallel to the z-direction. For such measurement configuration the  $2\theta$  background originating from the wobble is small compared to the  $2\theta$  component due to the magnetic anisotropy for the samples studied here.

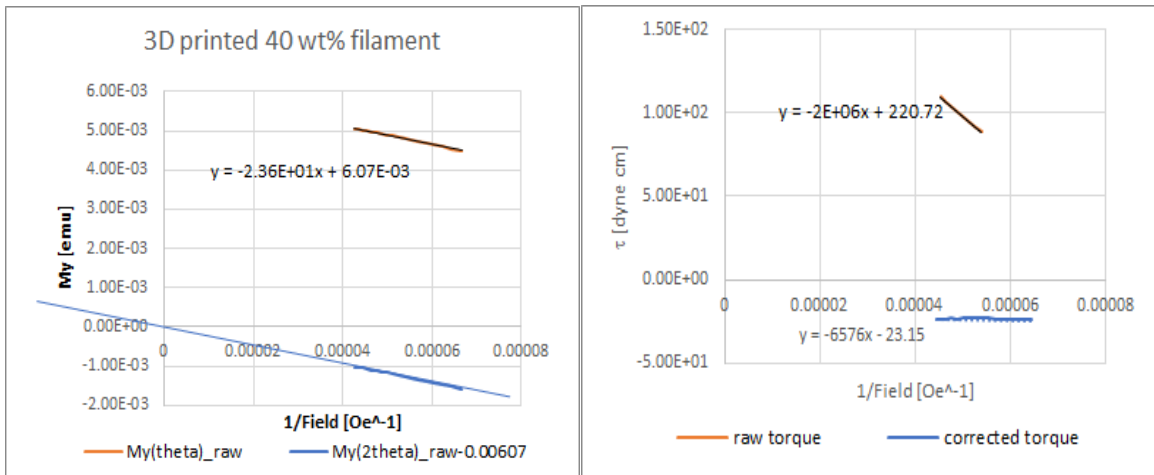


**Fig. 6.12:**  $M_{y,\text{raw}}$  and  $M_{y,\text{cor}}$  (left) and corrected and raw torque (right).

### 6.2.3 Summary

We analyzed how the signals of a biaxial VSM are affected by the position of the sample in between the pickup coils and explored how a slight misalignment of the sample on the sample holder will affect a measured biaxial torque curve. Such misalignment will cause the sample to describe a circular trajectory as the sample is rotated through a field

angle of 360 degrees and leads to systematic errors in the measured torque curves. Two type of systematic errors were identified: (1) the cross talk ( $S_{xy}$ ) between the  $M_x$  and the Y-coil set causes a non-zero angle dependence of the Y-coil signal even at fields where the sample is fully saturated along the field (x-direction); (2) the angular sensitivity ( $S_{yy}$ ) of the Y-coil set for the  $M_y$  signal also affects the angle dependence of the measured torque values. For a soft magnetic samples that has a precisely aligned sample it is possible to correct the Y-coil signal for the cross-talk by subtracting the extrapolated  $2\theta$  component at high field (at  $1/H=0$ ) from the measured  $Y(\theta)$  curves. The Y-coil angular sensitivity can be corrected for by an additional measurement at large field of the  $S_{yy}(\theta)$  using the same sample. These methods were verified by torque measurements done on a nickel wire. The magnetic anisotropy corrected for the cross-talk and Y-coil sensitivity was within 1 % of the shape anisotropy constant calculated from the literature  $M_s$  value and the sample's dimensions. Similar experiments performed on a 3D printed strontium ferrite/PA12 filament with the same dimensions as the nickel sample show that the same method does not work on such sample. The alignment of the sample on the sample-rod and or saturation issues make it difficult to get reliable results on a 7.7 mm filament that is mounted horizontal on a perpendicular rod.

### **6.3 Torque Measurements of 3D Printed Sample, Freely Extruded Sample on 3D printer, and Field-Annealed and Cooled Sample**

40 wt.%  $\text{SrO}(\text{Fe}_2\text{O}_3)_6/\text{PA-12}$  composite filament was extruded freely by the 3D printer. In freely extruded sample, the shear flow of the molten suspension causes the strontium ferrite platelets to line up with the cylindrical outer surface of the filament resulting in texture i.e. preferential orientation of the platelets in the filament. This texture results to an easy magnetization plane parallel to the radial direction of the filament. Note that this easy plane is along a direction where the demagnetizing field is large. Apparently, the flow induced texture is strong enough to compensate for shape anisotropy of the filament.

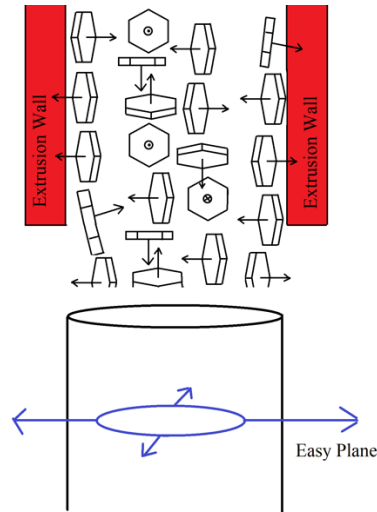


**Fig. 6.13:** Freely extruded sample on 3d printer and the shear flow of the molten suspension causes the strontium ferrite platelets to line up with the cylindrical outer surface of the filament resulting in texture i.e. preferential orientation of the platelets in the filament. This texture results to an easy magnetization plane parallel to the radial direction of the filament.

40 wt.%  $\text{SrO}(\text{Fe}_2\text{O}_3)_6/\text{PA-12}$  composite filament was 3D printed on the 3D printer and the printed samples have a more complex magnetic anisotropy and a tilted easy axis is observed that makes an angle of 60 degrees with the print bed normal (see data in Fig. 6.11f). Note that the extruded material makes a 90 degree turn when deposited on the bed of the 3D printer. Furthermore, there is now also shear flow caused by the bed of the 3D printer. This shear flow is only on one side and results in the observed easy axis or maybe easy plane that is tilted with respect to the filament's cylindrical axis.

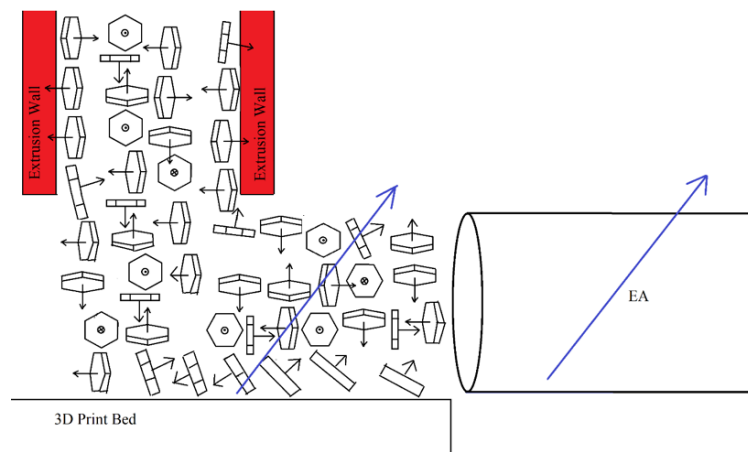


**Fig. 6.14:** 3D printed sample have a more complex magnetic anisotropy and a tilted easy axis is observed.

## 6.4 Magnetic Anisotropy Measurement of Field annealed Composite Filament Above the Nylon Melting Temperature

Here, we report on the magnetic anisotropy of 5 and 40 wt.% SrO(Fe<sub>2</sub>O<sub>3</sub>)<sub>6</sub>/PA-12 composite after field annealing the material above the melting temperature.

### 6.4.1 Experimental Procedure

The field annealing process of the 5 and 40 wt.% SrO(Fe<sub>2</sub>O<sub>3</sub>)<sub>6</sub>/PA-12 composite was done using a MicroSense-KLA biaxial EZ-9 VSM furnished with a 70-1000 K temperature option flowing Argon (Ar) gas at elevated temperatures. Samples were 4-6 mm long filaments with an average diameter of 1.3 mm and typically had a mass of around ~14 mg.

Torque measurements were done at RT using the biaxial VSM on one-time annealed samples in a field of 1.5 kOe for 1, 5 and 180 sec. Additional torque measurements were done on samples annealed for 180 seconds at 230 °C in zero field (zero-field-sample) and in 22 kOe (22 kOe-sample). Prior to the torque measurements the samples were centered in between the X-pickup coils at zero field angle. The samples were loaded in a Pyrex glass tube with an outer diameter of 3 mm and an inner diameter of 1.75 mm (Fig. 6.15). The filament was wrapped with Teflon plumber tape that has a low surface free energy to avoid the composite to wet with the Pyrex tube upon melting. PEEK stoppers with high temperature silicone glue on both sides of the samples were used to secure the sample's position and prevent the molten composite to leak out the glass rod. The VSM's furnace was used to heat up the sample for the field-anneal and the rotation studies. This furnace operates under Ar and allows temperature rates up to 1.1 °C/sec. Then the torque curves were measured at RT in steps of 10 degrees for different field values from 10 to 22 kOe with field increments of 2 kOe. The torque was determined from the y-intersect of the 1/H<sub>a</sub>-τ curve and converted to magnetic anisotropy by dividing the torque by the volume of the strontium ferrite in the sample calculated from the sample's mass, packing fraction and densities of Nylon (ρ=1 gr/cm<sup>3</sup>) and hexaferrite (ρ=5.18 gr/cm<sup>3</sup>) [12].



**Fig. 6.15:** The field-annealed  $\text{SrO}(\text{Fe}_2\text{O}_3)_6/\text{PA12}$  cylindrical-shaped filament wrapped with Teflon tape and secured in Pyrex glass tubes with PEEK stoppers and high temperature silicone glue for torque measurement.

#### 6.4.2 Measurement Results

The  $K_{\text{eff}}$  of the zero-field samples is not zero but approximately 3% of the magnetic anisotropy observed on the 22 kOe field-annealed samples. We believe that, this is a systematic measurement error originating from a circular trajectory the sample describes as the field angle is rotated through 360 degrees because of small misalignments of the sample on the sample rod. It has been recently shown that such trajectory results in a  $2\theta$  background signal in the Y-coils caused by the angular dependent cross talk term, i.e.  $S_{xy}(\theta) \cdot M_x$  [13]. Although it is possible to subtract this background signal, it is small compared to the magnetic anisotropy signal of the field-annealed samples and can be ignored for the discussion below.

**Table. 6.1:** Magnetic anisotropy of pristine and 230 °C field-annealed 5 and 40 wt.% composite [14]:

$\text{SrO}(\text{Fe}_2\text{O}_3)_6/\text{PA12}$ composite	Annealing field (Oe)	Annealing time (sec)	Anisotropy, $K_{\text{eff}}$ ( $\text{kJ}/\text{m}^3$ )
5 wt.%	Pristine	-	-
	0	0	12.4

	1500	1	96.7
	1500	5	104.0
	1500	180	116.5
	22000	180	432.3
40 wt.%	Pristine	-	-
	0	0	10.8
	1500	1	172.9
	1500	5	189.0
	1500	180	221.1
	22000	180	356.1

$K_{eff}$  increases with annealing time and annealing field. In addition to the crystal anisotropy and texture  $K_{eff}$  has three contributions due to shape, i.e. the shape of the individual particles, the shape of the agglomerates and the shape of the sample [15]. As anisotropy measurements were made in a plane perpendicular to the filament's cylindrical axis and the samples are rotation symmetric along their vertical cylindrical axes, we do not expect any contributions from the sample's macroscopic shape on the measured torque curves. When the strontium ferrite particles are far apart and do not interact at all, are single crystalline, and all of them are oriented in the same direction, the total magnetic anisotropy,  $K_{eff}$ , will be:

$$K_{eff} = K_{cr} - \frac{1}{2} \mu_0 N_d M_s^2 \quad (6.38)$$

Where  $K_{cr}$  is the crystal anisotropy of strontium ferrite which is 350 kJ/m<sup>3</sup> [16] and the 2<sup>nd</sup> term is the shape anisotropy of individual particles. For particles with an aspect ratio of 3 (OP-71),  $N_d$  is 0.64 and  $K_{eff} = 309$  kJ/m<sup>3</sup>. If the particles are not perfectly aligned or are not single crystalline the effective  $K_{eff}$  will be lower. Assuming  $N_d$  is correct, a  $K_{eff} > 309$  kJ/m<sup>3</sup> indicates the particles are chained along the anneal field direction and interact with each other. As the samples annealed in 22 kOe have an effective anisotropy beyond 350 kJ/m<sup>3</sup> (see Table 6.1) the torque measurements provide proof of chaining. The samples annealed at lower fields show all an effective anisotropy below 309 kJ/m<sup>3</sup> but still could be chained as additional shape anisotropy of the elongated agglomerates could be canceled by the poor alignment of the individual particles.

The large value of the measured  $K_{eff}$  depends on the field annealing process through induced shape anisotropy contributions originating from the shape anisotropy of the

particles and the directional agglomerates. The magnetic anisotropy increases with increase of the field annealing time for both 5 and 40 wt.% SrO(Fe<sub>2</sub>O<sub>3</sub>)<sub>6</sub>/PA12 composites.

## 6.5 Conclusion

A biaxial VSM was used to study the magnetic anisotropy of the strontium ferrite-PA12 composite induced by field annealing at 230 °C. The magnetic anisotropy depends on the field annealing process through induced shape anisotropy contributions originating from agglomerates. It increases with increase of the field annealing time for both 5 and 40 wt.% SrO(Fe<sub>2</sub>O<sub>3</sub>)<sub>6</sub>/PA12 composites. For 22 kOe field-anneals, the measured magnetic anisotropy is larger than an individual particle's  $K_{\text{eff}}$ , providing evidence for significant agglomeration along the anneal field direction. This conclusion is supported by SEM analysis showing good particle alignment and significant chaining.

## REFERENCES

- [1] Erik Samwel, Ph.D. dissertation, University of Twente, 1995.
- [2] B. D. Culity and C. D. Graham, “Magnetic anisotropy,” in *Introduction to Magnetic Materials*, 2nd ed. (Wiley-IEEE Press, 2008), Chap. 7, ISBN: 9780471477419.
- [3] B. C. Dodrill, J.R. Lindemuth, J. K. Krause, “Magnetic Anisotropy: Measurements with a Vector Vibrating Sample Magnetometer”, Lake Shore Cryotronics, Inc., 575 McCorkle Blvd., Westerville, Ohio, USA.
- [4] Hideki Miyajima, Kasuo Sato, Tadashi Mizoguchi, “Simple Analysis of torque measurement of magnetic thin films”. *J. Appl. Phys.* 47 4669 (1976).
- [5] P. Stamenov, J.M.D. Coey, “Vector vibrating-sample magnetometer with permanent magnetic flux source”, *J. Appl. Phys.* 99 (2006), 08D912-3.’
- [6] K.R. Fast, J.A. Thibault, V.T.K. Sauer, M.G. Dunsmore, A. Kav, J.E. Losby, Z. Diao, E.J. Luber, M. Belov, M.R. Freeman, “Simultaneous three-axis torque measurements of micromagnetism”, *AIP Advances* 11 (2021) 015119.
- [7] Halise Celik, Harsha Kannan, Tao Wang, Alex R. Mellnik, Xin Fan, Xinran Zhou, Daniel c. Ralph, Matthem F. Doty, Virginia O. Lorenz, and John Q. Xiao, “3D MOKE spin-orbit torque magnetometer”, <https://arxiv.org/abs/1707.08565>.
- [8] L. Benito, J.I. Arnauda, A. del Moral, “High-sensitivity vector magnetometer for measuring magnetic torque at low temperatures”, *Rev. Sc. Instrum.* 77 025101 (2006).
- [9] John David Jackson, “Classical Electrodynamics”, John Wile & Sons, 3rd edition, 1999, 978-0-471-30932-1.
- [10] David J. Griffiths, “Introduction to Electrodynamics”, Pearson, 4th edition, 2013, 0-321-85656-2.
- [11] M.S. Thesis of Binod D.C., “The Magnetic Characterization of Permalloy and Permalloy Oxide Grown by RF Magnetron Sputtering”, Texas State University, December (2019).
- [12] Sigma-Aldrich Strontium ferrite. Retrieved: 28 December 2022, Available Online: <https://www.sigmaaldrich.com/US/en/product/aldrich/480371>

- [13] M.S. Thesis of Kolton Dieckow, "Automatic alignment methods for VSM using magnetic low anisotropic samples with reduced time and higher precision", Texas State University, May (2021).
- [14] T. N. Ahmed, C. Selsor, J. S. Tate, and J. S. Tate, "Magnetic behavior and chaining of strontium ferrite-nylon composite above the melting temperature Magnetic behavior and chaining of strontium ferrite-nylon composite above the melting temperature," AIP Advances 13, 025024, (2023).
- [15] R. Skomski, G. C. Hadjipanayis, and D. J. Sellmyer, IEEE Trans. Magn. 43, no. 6, 2956–2958, (2007).
- [16] A. Z. Eikeland, M. Stingaciu, A. H. Mamakhel, M. Saura-Múzquiz, and M. Christensen, Sci. Rep. 8, no. 1, 1–9, (2018).

## 7. CONCLUSION AND FUTURE APPROACHES

*“Why do we do basic research? To learn about ourselves.”*

— Walter Gilbert

### 7.1 Conclusion

In this dissertation the fabrication and characterization of magnetic polymer composite 3D-printer filament for the development of the Magnetic Field Assisted Additive Manufacturing (MFAAM) technology is discussed. The magnetic filaments are made by adding different loading levels of magnetic  $\text{SrO}(\text{Fe}_2\text{O}_3)_6$  particles into polyamide-12(PA-12) polymer using a twin-screw extruder. This dissertation has discussed, the effects of packing fraction annealing field, annealing time, and annealing temperature on the orientation and distribution of the magnetic particles in the magnetic composite filaments. A procedure was developed to simulate and study the alignment of the particles during the 3D printing MFAAM process using a biaxial VSM. In MFAAM, an external magnetic field is applied during the printing process which allows the magnetic particles to be oriented in a well-defined direction resulting in the realization of magnetic structures with complex well-defined easy axis and/or magnetic dipole distribution functions that vary across a mesoscopic scale. The magnetic characterization done by a Bi-axial Vibrating Sample Magnetometer (VSM) to determine the hysteresis, time dependence and magnetic anisotropy of the composite filament. This is the first time a vector VSM was used to measure the magnetic viscosity of the magnetic composite 3D-printer filament. These magnetic characterization efforts have been complemented with SEM, EDS, XRD, FTIR, TGA, DSC, and Optical microscopes studies for the structural, morphological and thermal properties analysis of the composite.

In chapter 1, we discussed the permanent magnetic materials, magnetic properties, and different magnet manufacturing techniques. In addition, we have discussed trending technology for rapid prototyping and fabrication of net-shaped complex components which is being significantly studied for application in the manufacturing of anisotropic permanent bonded magnets and other magnetic materials.

In chapter 2, we introduced the MFAAM technology which is a 3D printing process that allows for an in-situ magnetic pre-alignment of particles in the molten magnetic composite. The chapter also provides and discusses about the detailed background literature study of the magnetic polymer composite AM technique. Additionally, the challenges associated with the existing manufacturing techniques of the permanent bonded magnet manufacturing are discussed. Although 3D printing of hard magnetic objects is being explored by various research labs in the US and elsewhere, currently no commercial hard-magnetic 3D-printer filament is yet on the market. For this dissertation research a non-rare earth magnetic composite with appropriate magnetic properties for 3D printing hard magnetic material was selected, specifically PA-12 filled with biocompatible and ecofriendly strontium ferrite. Furthermore, the selected composite is economical and stable and provides in a good materials system to study the MFAAM process to align the magnetic particles for the realization of texture or anisotropy to improved magnetic performance with lower processing cost for 3D printing purpose. Research questions and proposed scope of this dissertation were presented in the last section of this chapter.

In chapter 3, we discussed the major manufacturing and characterization tools and techniques used in this research. We briefly explained the used fabrication method to realize 3D-filaments with different loading level of hard-magnetic particles. The used Magnetic Field Assisted Additive Manufacturing (MFAAM) setup was also discussed briefly with a discussion on the used printing parameters. Additionally, we discussed the tools used to characterize the realized filaments including working principle. Discussed methods include imaging tools, optical characterization tools, thermal analysis tools and magnetic characterization tools. Furthermore, measurement results on the structural, morphological and thermal properties of the realized composite filaments were presented. The electron and optical microscope studies were done to investigate the dispersion and orientation of the magnetic particles in the nylon matrix in pristine filaments and field annealed filament samples. Microscopy studies focused on morphological alignment in terms of texture or chaining (very ordered clustering). The structural analysis done by XRD shows characteristic peaks for the  $\gamma$  and  $\alpha$ -phases of nylon and indicate that the nylon matrix in our samples is semi-crystalline [1-4]. The thermal analysis by TGA and DSC comparative study on pristine and multiple temperature cycled annealed filament shows of

that upon multiple anneal cycles  $T_g$ ,  $T_m$ , heat of crystallization and degree of crystallinity hardly change for samples with 5 and 40 wt.% PA-12/strontium-ferrite composites. This indicates that this composite is indeed stable which is important for applications. An increase of  $T_g$  and  $T_m$  that would confirm significant increase of the average length of the polymer molecules was not observed. The DSC and TGA study also helped to determine the printing temperature window for MFAAM (178-290 °C) defined by the PA-12's  $T_m$  (178 °C) and the onset of decomposition of the Nylon matrix (290 °C). Note that, up to 290 °C the weight loss observed in TGA graphs is negligible.

In chapter 4, we investigate the hysteresis and time dependent or magnetic viscosity of our manufactured magnetic polymer composite pristine and field-annealed filaments by a vector VSM. To my best knowledge, this is the first vector time dependent measurements reported on in literature. The hysteresis measurement of pristine filaments shows wire texture originating from the flow of the molten composites during the extrusion process. The vector magnetic viscosity depicts that the filament's time dependence is strongly sensitive on the field angle. The  $M_x$  viscosity collapses with a factor of 2 when the field is rotated from the easy plane to the hard axis for the pristine filament. The magnetic viscosity of the "field-annealed and cooled" filaments and the "field-annealed only" samples was also studied to further the development of the MFAAM deposition process. A better understanding on how viscosity and packing fraction affect non-spherical particle alignment processes is necessary to further the development of the MFAAM deposition process. The hysteresis curve of the "field-annealed and cooled" filaments and the "field-annealed only" filaments have their easy axis parallel to the anneal field direction, hence, show strong anisotropy. The  $M_x$  magnetic viscosity is maximum in the easy plane and decreases to a factor of 5 along the macroscopic hard axis for both "field-annealed and cooled" sample and "field-annealed only" of the sample. The  $M_y$  magnetic viscosity is nearly zero along the hard axis and in the easy plane and is maximum for intermediate field angles. However, the "field-annealed and cooled" samples show better anisotropy (than the field-annealed only samples. Because the "field-annealed and cooled" samples were field annealed at 22 kOe for 3 minutes at 230 °C and then cooled to RT (25 °C) in the presence of a magnetic field of 22 kOe. So, the magnetic moment of the ferrite particles in the molten composite still aligned in the anneal field direction (22 kOe) during curing to RT. Hence,

the “field-annealed and cooled” samples were also exposed to a magnetic field during curing unlike the “field annealed only” samples. Although the “field-annealed and cooled” samples and “field-annealed only” samples study also indicate that better alignment is obtained for longer field anneal times, typical cool down rates for 3D FDM printing are 50 °C providing not more than 2 seconds for the field anneal [5, 6].

In chapter 5, a simple model was presented and discussed to describe the temperature dependent experimental study of the rotation of the magnetic particles in the polymer matrix. Dynamic rotation studies were performed above and below the melting point of PA-12. It was noticed that the strontium ferrite particles are no longer fixed in the PA-12 matrix at temperatures above 132 °C which is well below the PA-12 melting point. These results show that bonded magnets using PA-12 as a polymer cannot be used above 132 °C. Furthermore, it shows that particles can be rotated with an external magnetic field down to 132 °C although quick orientation requires elevated temperatures and high magnetic fields. The dynamic melt viscosity of the strontium ferrite composite was estimated from the initial slope of the  $\ln((\cos(\theta)+1)/\sin(\theta))$  versus  $t$  graph and decreased with temperature from 2E5 Pa.s at 132 °C to 3.1E4 Pa.s at 175 °C. Note that these viscosity values are significantly higher than the one measured above the melting temperature of PA12 by others [7]. As far as we know this is the first-time dynamic viscosity is studied with a vector VSM. The magnetic rotation of the strontium ferrite particles was also studied above the nylon matrix melting temperature to simulate the alignment of the particles during the 3D printing MFAAM process. Directionality analysis of scanning electron micrographs was utilized as a tool to quantify the degree of filler (magnetic particle) orientation and magnetic chaining in the composite filament. Biaxial VSM was used to monitor the rotation of the magnetic moment in field-annealed samples exposed to a small field perpendicular to the field-anneal direction. The rotation time constant, which is inversely proportional to the viscosity, decreases with temperature. At lower temperatures and smaller rotation fields, it is not possible to align the sample’s magnetic dipole moment up with the rotation field direction. SEM images suggest that strong chaining limits the space available for the non-spherical particles to rotate over a full 90 degrees and is responsible for the observed non-zero yielding strength.

In chapter 6, the magnetic anisotropy of manufactured pristine and field-annealed magnetic polymer composite filaments measured by biaxial VSM were discussed. The magnetic anisotropy depends on the field annealing process through induced shape anisotropy contributions originating from agglomerates. It increases with increase of the field annealing time for both 5 and 40 wt.% SrO(Fe<sub>2</sub>O<sub>3</sub>)<sub>6</sub>/PA12 composites. For 22 kOe field-anneals, the measured magnetic anisotropy is larger than an individual particle's  $K_{\text{eff}}$ , providing evidence for significant agglomeration along the anneal field direction. This conclusion is supported by SEM analysis showing good particle alignment and significant chaining. Magnetic anisotropy measurements performed on 3D printed samples reveal a complex magnetic anisotropy with a tilted easy axis induced by the flow during the 3D printing process. A method to correct for systematic errors in torque measurements originating from small alignment errors of the sample on the sample-rod was presented in chapter 6 as well. The method seems to work for soft magnetic samples but not for hard magnetic samples as being studied in this dissertation.

## **7.2 Suggestions for Future Research**

### **7.2.1 Flow-induced Anisotropy**

In this dissertation, the focus has been on the use of an externally applied field to induce a magnetic anisotropy in the composite. It should also be possible to induce a magnetic anisotropy by using the shape of the particles in combination with the flow rather than a magnetic field to align the magnetic particles in the 3D printed material. Note that the magnetic anisotropy observed in the pristine PA12/strontium-ferrite filaments strongly suggest that anisotropy can also be induced by the flow of aspherical particles rather than a magnetic field. Such approach to align the magnetic particles by carefully choosing the shape of the magnetic particle and shape and size of the nozzle could provide in an easier methodology to create an anisotropic magnet. Little is known though on flow of aspherical magnetic suspensions. So, a study on the realization of inhomogeneous anisotropic permanent bonded materials is desirable and can result in a new manufacturing method that is simpler than MFAAM. This work will open a new way

to manufacture and commercialize anisotropic 3D printed bonded permanent magnets.

## 7.2.2 Installing Electromagnet or Permanent Magnet to Make MFAAM Facile

A small electromagnet or permanent magnet unit needs to be developed that can be installed on a regular FFF 3D printer in order to make the MFAAM process more facile. Design and development of a water-cooled electromagnet with small form factor that can be installed on top of a 3D printer and will allow to apply a longitudinal or perpendicular field to the print surface will be a main challenge. The electromagnet would need to contain a ferrite or iron core to obtain higher fields, and the coil would need to be water cooled to not affect the temperature near the print head. Such electromagnet should contain a rather large pole piece gap to guarantee a homogeneous magnetic field across a large enough area where the composite is still drying to freeze in the magnetic anisotropy. The use of an electromagnet will allow one to explore the dynamics of the alignment process including the effect of print-speed, temperature, and field changes. Several groups are currently exploring the use of a permanent magnet carefully positioned around the print nozzle as such approach allows for a much smaller form factor. The magnitude of the applied field is limited by the homogeneity of the field created by the field unit as the field gradient results in exerting a force on the extruded material. At large field values, the large field gradient will exert a large force on the extruded material attracting the material to the pole pieces of the electro- or permanent-magnets [8]. So, part of the design challenge is to create a system with small field gradients such is currently being designed by Mandesh Khadka a masters student working with Dr. Tate.

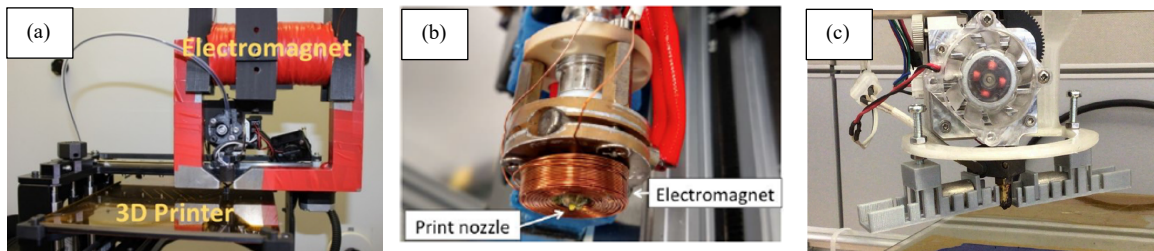


**Fig. 7.1:** Small (a) and (b) electromagnet [9] or (c) permanent magnet can be installed on a regular FFF 3D printer in order to make the MFAAM process more facile [10].

### **7.2.3 XRD Pole Figure for Texture Analysis**

Investigate the field induced morphological alignment of texture or chaining (very ordered clustering) in the 3D printed MFAAM samples by XRD pole figure. In order to get a better understanding of the orientation of the particles in the polymer matrix it might be useful to explore the use of pole figure measurements. If one obtains a more complete picture of the crystal orientation distribution one might be able to correlate the obtained texture to magnetic characterization measurement results. To identify the preferred orientation and distribution of the planes from the surface normal a pole figure study is an appropriate choice. Such study is not trivial though as it is quite challenging to create a flat 3D printed sample suitable for pole figure measurements.

### **7.2.4 Development of MFAAM a Model**

To further the development of MFAAM a model of the MFAAM deposition process [9] that also includes chaining processes [11] needs to be developed to better understand how viscosity and packing fraction affect the non-spherical particle alignment processes. Note that very little is understood how aspherical particles affect the viscosity and flow of magnetic suspensions.

## REFERENCES

- [1] P. Chen, M. Tang, W. Zhu, L. Yang, S. Wen, C. Yan, Z. Ji, Hai Nan Yusheng Shi, “Systematical mechanism of Polyamide-12 aging and its micro-structural evolution during laser sintering”, *Polymer Test.* 67 3701-379 (2018).
- [2] R. Kuracina, Z. Szabova, E. Buranska, A. Patierova, P. Gogola, and I. Buransky, “Determination of Fire Parameters of Polyamide-12 Powder for Additive Technologies”, *Polymers* 13, 3014 (2021).
- [3] G. S. Martynkova, A. Sliva, G. Kratosova, K. C. Barabaszova, S. Studentova, J. Klusak, S. Brozova, T. Dokoupil, and S. Holesova, “Polyamide 12 Materials Study of Morpho-Structural Changes during Laser Sintering of 3D Printing Polymers”, 13, 810 (2021).
- [4] N. Ma, B. Liu, L. Ma, S. he, H. Liu, Z. Zhang, A. un, M. Huang, C. Zhu, *e-Polymers* 20, 346-352 (2020).
- [5] K. Pooladvand and C. Furlong, *Mech. Compos. Multifunct. Mater.* 7, 45 (2016).
- [6] See [https://www.youtube.com/watch?v=\\_SvR5Dxu0cU](https://www.youtube.com/watch?v=_SvR5Dxu0cU) for the temperature distribution simulation during the 3D printing of a part using commercially available software. Layer-by-layer fabrication of an ABS specimen with 6mm height, 5mm
- [7] B. Haworth, N. Hopkinson, D. Hitt, and X. Zhong, *Rapid Prototyping J.* 19(1), 28–36 (2013).
- [8] Presentation in Physics Colloquium at Texas State University by Dr. Ikenna Nlebedim, Ames Laboratory, USA.
- [9] A. Sarkar, M. P. Paranthaman, I. C. Nlebedim, *Additive Manufacturing* 46, 102096 (2021).
- [10] M. Suppan et al., “In-situ alignment of 3D printed anisotropic hard magnets,” *Sci. Rep.*, vol. 12, no. 1, pp. 1–7, 2022.
- [11] S. A. Faroughi and C. Huber, *Rheol. Acta* 56, 35–49 (2017).